Study of Linear Water Wave Scattering by a Floating Structure in the Presence of Porous Breakwaters for Different Types of Sea-bed: Pattern of Scattering and Wave Force Mitigation

by

Shilpi Jain

DEPARTMENT OF MATHEMATICS
INDIAN INSTITUTE OF TECHNOLOGY GUWAHATI
GUWAHATI-781039, INDIA

January, 2025

Study of Linear Water Wave Scattering by a Floating Structure in the Presence of Porous Breakwaters for Different Types of Sea-bed: Pattern of Scattering and Wave Force Mitigation

A Thesis Submitted
in Partial Fulfillment of the Rrequirements
for the Degree of

DOCTOR OF PHILOSOPHY

by

Shilpi Jain
(Roll No: 196123113)

DEPARTMENT OF MATHEMATICS
INDIAN INSTITUTE OF TECHNOLOGY GUWAHATI
GUWAHATI-781039, INDIA

January, 2025

Dedicated To My Parents

Smt. Manju Jain

and

Shri Yogesh Kumar Jain

Declaration

I do hereby declare that this thesis entitled **Study of Linear Water Wave Scattering by a Floating Structure in the Presence of Porous Breakwaters for Different Types of Sea-bed: Pattern of Scattering and Wave Force Mitigation** is a presentation of my original research work done under the supervision of **Dr. Swaroop Nandan Bora**, Professor, Department of Mathematics, Indian Institute of Technology Guwahati for the award of the degree of Doctor of Philosophy and this work has not been submitted elsewhere for a degree.

January, 2025

Shilpi Jain
Roll No. 196123113
Department of Mathematics
Indian Institute of Technology Guwahati

Certificate

It is to certify that the work contained in this thesis entitled **Study of Linear Water Wave Scattering by a Floating Structure in the Presence of Porous Breakwaters for Different Types of Sea-bed: Pattern of Scattering and Wave Force Mitigation** has been carried out by **Shilpi Jain**, a student in the Department of Mathematics, Indian Institute of Technology Guwahati, under my supervision for the award of the degree of Doctor of Philosophy and this work has not been submitted elsewhere for a degree.

January, 2025

Dr. Swaroop Nandan Bora
Professor
Department of Mathematics
Indian Institute of Technology Guwahati

Acknowledgements

Venturing into research and working on a PhD thesis is quite challenging. Completing this thesis would not have been possible alone. Many people, whose exceptional support and guidance played a crucial role throughout this journey, deserve acknowledgment. I would like to recognize them here.

I want to express my deepest thanks to God for giving me blessings, support, strength, the ability to understand my studies, and the determination to pursue and complete my Ph.D.

I am immensely grateful to my thesis supervisor, Prof. Swaroop Nandan Bora, for his mentorship, encouragement, and invaluable feedback, which made this thesis possible. I am truly fortunate to have been selected as a research scholar under his guidance. His patience, understanding, and unwavering support were crucial throughout this journey. He always motivated me to work hard and gave me the freedom to conduct my research. This work would not have been possible without his extensive knowledge. I am deeply grateful to him for his constant support and encouragement in all aspects of my life. Thank you so much, Sir!

With great appreciation, I would like to thank my Doctoral Committee members Prof. Rajen Kumar Sinha, Prof. Bhupen Deka, and Prof. Sweta Tiwari for their continuous encouragement, helpful criticism and insightful suggestions during my Ph.D which definitely helped improve my research work. My heartfelt gratitude also goes to all the faculty members of the department who have helped me during my research work.

I want to thank my friends and seniors Sirshendu, Ashish, Deb, Deepa, Rupchand, Rik, Devang, Gopinath, Anjali, Madhab, Prakash, Shiva, Abhijit, Mahesh, Sunil, Nabanita, Sohini and Saurabh for their support and encouragement. My special thanks goes to my close friends Sirshendu, Ashish, Deb, Sagar, Anindita, Aryan and Sohini with whome I have shared best moments of this campus. I am grateful to them for all their support during my stay at IIT Guwahati; I have been fortunate enough to work with you all over the years. My sincere regards go to my seniors, Dr. Ayan Chanda and Dr. Koushik Kanti Barman, for all their help during my research work. I also want to thank my childhood friends Komal, Himanshi, Shivani, Saloni, Ritika, Sakshi, Rimjhim, Jyoti, DSG and Lucky. They always encouraged me to work hard and cared for me. I am thankful to them for being by my side through every step of this journey and beyond.

I am extremely grateful to my parents, my elder sister Mrs. Surbhi Jain, my brother-in-law Mr. Ayush Jain and my younger brother Nikhil Jain for their unconditional love, care, encouragement and moral support throughout my life which gives me the strength at every moment of my life. They have been a constant source of inspiration in my life, and I dedicate this thesis to them. I also want to thank all other family members for their

blessings and love.

I am also immensely grateful to the Ministry of Education (earlier known as the Ministry of Human Resource Development), Government of India for providing me financial assistance. I would like to thank Indian Institute of Technology Guwahati for providing me various facilities to carry out my research work.

January, 2025 **Shilpi Jain**

भारतीय प्रौद्योगिकी संस्थान गुवाहाटी
Indian Institute of Technology Guwahati

Abstract

Due to globalization and shortage of land, a significant challenge in this century is to create spaces suitable for various human activities including habitation. In this direction, therefore, there arises a great necessity for utilizing the available ocean space for accommodating numerous activities. This involves the construction and deployment of innovative floating and mobile structures such as bridges, airports, islands, habitats, entertainment facilities, etc. Subsequently, the study of the impact of water wave interaction with very large floating structures (VLFS in short) has become an important and practical issue. It has been observed that many floating structures have collapsed due to various natural hazards such as floods, cyclones and tsunamis. It is, therefore, necessary to investigate a variety of parameters with suitable values so as to bring the hydrodynamic forces acting on floating structures under reasonable control. The reduction of the hydrodynamic forces acting on floating structures can be made possible through the use of various mitigating devices, viz., floating breakwaters, air cushions, submerged barriers, and oscillating water columns. Apart form that, both refraction and diffraction in waves happen at the same time when the waves interact with the floating structure in the presence of different types of bottom topography. Due to this, the height and the direction of the wave change, and the wave field may possess some discontinuity.

In this study, we consider an incompressible and inviscid fluid with irrotational motion under the assumption of linearized water wave theory. The first work investigates the wave scattering by a floating bridge with porous wall fitted on its vertical sides. The bottom of the sea-bed is assumed to be fixed and impermeable of uniform depth. The impact of the porosity and width of the porous layer on the reflection coefficient, and horizontal and vertical forces acting on the floating bridge is studied. It is noted that, because of the rectangular porous wall, a substantial amount of wave energy gets reflected back, and the waveload thus gets reduced on the floating bridge. For the second work, we consider

an oblique wave interaction with a rigid floating structure which is placed in front of two vertical porous barriers with different porous-effect parameters and different heights. This study is done in the presence of current and no current. The sea-bed is considered flat and permeable. It provides the significant role of the porous barriers and permeable sea-bed in mitigating the wave induced forces on the floating structure. The effect of uniform current on the reflection coefficient and forces is observed. In the presence of current, a significant change in the reflection coefficient, and the horizontal and vertical forces is also observed. Next, we solve a scattering problem due to the oblique wave interaction with a floating structure placed after a porous barrier with the consideration of two types of bottom topography: (i) an elevated-type, and (ii) a trench-type, each as a separate case. The effects of both bottom topographies and the porous barrier on the reflection coefficient and hydrodynamic forces are studied. Additionally, the reflection in the presence of a trench is observed to be higher than the one due to the elevated bottom.

In the fourth work, an oblique wave interaction with a floating structure in which two porous structures are considered with each of them having different porosity, height, and width, to mitigate wave-induced forces on the floating structure, is examined. The floating structure is positioned after the porous structures which are separated by some gap. The problem is analyzed in finite ocean depth with a flat and impermeable sea-bed. The hydrodynamic coefficients, namely, reflection coefficient, transmission coefficient, dissipation coefficient and hydrodynamic forces on the floating structure are analyzed for different configurations of these thick porous structures. It is observed that the porous structures play a crucial role in mitigating waveload on the floating structure. It is also noted that, if the porosity of the second porous structure is less than that of the first porous structure, then wave energy loss increases, thereby enhancing the safety of the floating structure. In the fifth work, we examine the wave interaction with a rigid floating structure, with porous wall fitted on its vertical sides, to mitigate wave-induced forces acting on the floating structure, with the consideration of a particular type of varying impermeable sea-bed. The effect of the varying bottom is studied using modified mild slope equation (MMSE). This can be considered a significant step for handling such non-trivial issues. The reflection and transmission coefficients are determined, and then the horizontal force and vertical force acting on the floating structure are evaluated. It is noted that, by increasing the draft and thickness of the porous wall, reflection and transmission coefficients decrease. The effects of the porous wall and the varying bottom of the sea-bed are examined in mitigating the wave-induced forces acting on the floating structure. It is observed that the horizontal force and vertical force acting on the structure are reduced when the slope of the sea-bed is milder.

In all works, the results are validated against available results for verifying the effectiveness of each model presented here, which can be used for problems involving floating structures or other floating facilities.

भारतीय प्रौद्योगिकी संस्थान गुवाहाटी
Indian Institute of Technology Guwahati

Contents

भारतीय प्रौद्योगिकी संस्थान गुवाहाटी
Indian Institute of Technology Guwahati

List of Figures

भारतीय प्रौद्योगिकी संस्थान गुवाहाटी
Indian Institute of Technology Guwahati

List of Tables

CHAPTER 1

Introduction

1.1 Preamble

A fluid is a substance that deforms continuously under an applied shear stress or that does not have a preferred shape. Fluid mechanics deals with the behaviour of fluids (both liquids and gases) in rest or in motion, and the subsequent effects of the fluid on the boundaries, which may be either solid surfaces or other fluids at the boundaries. The mechanics of fluids is very interesting and important part of the recent interdisciplinary activities concerning engineering and science, especially in applied mathematics. The applications of fluids in engineering are vast and diverse: rockets go up, insects fly, blood flows through arteries and veins, the human heart acts like a pump, breathing, swimming, fans, wind turbines, airplanes, ships, windmills, pipes, missiles, engines, filters, jets, and sprinklers, to name a few. Many natural phenomena such as the rain cycle, weather patterns, the rise of ground water up to tree tops, ocean waves, and current in large water bodies are also controlled by the principles of fluid mechanics. The most fundamental approaches of applied mechanics, related to the conservation of mass, energy and momentum, are utilized to analyze the behaviour of fluids. Properties of fluid such as density, viscosity, volume, temperature, pressure, etc., are defined by the concept of the *Continuum Hypothesis*. According to the continuum hypothesis, fluid properties are point functions, and these properties vary continuously with no jump discontinuities. This hypothesis is valid if the size of the system with which we deal is significantly larger than the space between the molecules. At a solid boundary, the fluid velocity is equal to the velocity of the boundary. In other words, the outermost molecules of fluid tend to stick to the solid. This concept is known as *no-slip condition*.

There are two methods to describe the fluid motion. The first, known as the *Lagrangian Method*, involves tracing of the kinematic behaviour of every individual fluid particle from an initial location. The second method is *Eulerian Method*, which corresponds to a fixed coordinate system in space, and fluid properties vary with time as the flow passes through fixed spatial locations. Although Lagrangian Method is useful in certain special cases, the Eulerian method is employed in most of the fluid flow problems. The three types of curves *Streamlines, Pathlines*, and *Streaklines* are utilized in the description of Eulerian Method. These curves are often useful for understanding fluid motion, and serve as the foundation for experimental methods that monitor seed particles or dye filaments. A *streamline* is a curve that is tangent everywhere to the velocity vector for a fixed instant of time. A *streakline* is a curve obtained by connecting the locations of all the fluid particles that pass through a fixed point in the flow field at any instant of time. A *pathline* is a curve obtained by tracing the path that a particle takes while it moves. The pathlines, streaklines and streamlines are identical when the flow is steady.

Viscosity is one of the important properties of fluid that makes a fluid more resistive to shear stresses. In fluid mechanics, most theoretical investigations begin from the concept of an *ideal fluid*, where two contacting layers experience no *tangential forces* (i.e, shear stresses) but experience *normal forces* (i.e., pressure) only. It says that internal resistance does not exist in an ideal fluid. The inner layers of a *real fluid* experience both tangential and normal stresses. These tangential frictional forces in a real fluid show the existence of viscosity. Fluid flow is characterized into different categories according to its various properties. The fluid flow is called *inviscid* or *non-viscous* if the viscosity is negligible; otherwise it is called *viscous*. The fluid flow is *compressible* if the volume or density changes with a change in temperature and pressure; it is *incompressible* if the change in the volume or density is negligible. The *Mach number* (the ratio of the speed of flow to the local speed of sound in the flowing medium) of a fluid flow is utilized in order to identify compressible and incompressible flows. The *steady* flow is the one when the fluid properties do not change with time; otherwise, the flow is *unsteady*. Recirculation, swirl in the flow and the highly-disordered fluid motion is called a *turbulent* flow. A fluid flow is called *laminar* if no turbulence exists in the flow. *Newtonian* fluids (water, air, etc.) are those which satisfy a very close linear relation between stress (internal force) and strain (normalized measure of deformation); *non-Newtonian* fluids (blood, honey, etc.) do not follow any linear relation between stress and strain. Depending on the flow velocity (Mach number), the fluid flow is also classified as *subsonic, transonic* and *hypersonic*. A flow field with a velocity vector $\vec{U}$ is called *irrotational* if curl $\vec{U} = 0$; otherwise, it is called *rotational*. If a fluid flow is irrotational, then it guarantees the existence of a scalar function Φ. This scalar function is usually called the *velocity potential*. The Laplacian of the velocity potential must be zero if the flow is both irrotational and incompressible. This gives us the equation of continuity for a potential flow.

In physics, mathematics and related fields, a wave is a disturbance (change of state from equilibrium position) of one or more fields in which the field values repeatedly bounce around a stable equilibrium (resting) value. There are broadly two types of waves, namely, *mechanical* wave and *electromagnetic* wave. In a mechanical wave, the stress and strain fields vary around a point of mechanical equilibrium (water wave, sound wave, etc.). In an electromagnetic wave, the electric and magnetic fields oscillate. An electromagnetic wave consists of variable electric and magnetic fields that travel across the space. Some examples of electromagnetic waves are visible light, radio waves, infra-red radiation, ultraviolet radiation, X-rays, gamma rays, etc. Waves are also classified into two different categories corresponding to wave propagation direction; the first one is the *longitudinal wave* (water wave) in which the direction of the wave and vibration of the particles of the medium is the same, and the second one is the *transverse wave* (sound wave) which vibrates perpendicular to the direction of the wave.

A familiar example of a water wave is the one when a stone is thrown into a pond and we can observe ripples. A few more examples of water wave are the motion of wind over water surface (lake, ocean, etc.) that creates ripples, due to the motion of the ship in an ocean, etc. These waves have small amplitudes of oscillation. On the other hand, tidal waves, rogue waves and tsunami waves are waves whose amplitudes are not very small. These waves carry a huge amount of energy which may create destruction in coastal areas, structures in ocean and floating objects. To combat this kind of situation, the topic of wave-structure interaction has become a major topic of fluid mechanics.

Since porous breakwaters are highly effective in absorbing wave energy, various types of breakwaters have been proposed by many researchers. These studies are crucial for the protection of coastal regions and construction sites. Wave-induced forces can be minimized using the porous structures. Additionally, these structures are also utilized in construction of floating bridges, airports, piers, docks, wave power conversion system, etc. The use of porous structures to reduce wave forces on the floating structures has been found to be more appropriate as compared to the rigid ones. As a consequence, hydrodynamic research has focused on building optimal systems in order to find a way to mitigate hydrodynamic responses. When a problem is formulated in water wave mechanics, the water region is considered to be bounded by a free surface (in contact with the atmosphere) or a rigid surface or a porous surface or any other medium. In addition, virtual boundaries are also considered for the sake of simplification. There has been a substantial growth in the knowledge of the dynamics of ocean surface waves and their effects on the ocean structures during the past few decades. Depending on the physical problem, Laplace's equation or Helmholtz equation or modified Helmholtz equation is used to describe the wave motion within the water region. Different types of boundary condition, Dirichlet type (no derivative involved) or Neumann type (only derivative involved) or Robin type (mixture of derivative and non-derivative), are applied to the problem. A number of

methods are available to analyze water wave problems such as Fourier analysis, complex function theory, Green's function techniques, the boundary integral equation method, the least square approximation method, the wide spacing approximation method, integral transform methods, the method of stationary phase, etc.

The origin of water wave theory is a few centuries old. The history of water waves can be found in Craik [22]. Sir Isaac Newton was the first one who presented a theory of water waves. He proposed a dubious analogy with oscillations in a U-tube, correctly deducing that the frequency of deep-water waves must be proportional to the inverse of the square root of the "breadth of the wave" in *Book II*, *Prop. XLV* of *Principia* (1687). Wilhelm-Jacobs Gravesande (1721) and Charles Bossut (1786) also repeated Newton's argument. Much later, Joseph Louis Lagrange (1781, 1786) obtained the linearized governing equations for small-amplitude waves, and found the solution in the limiting case of long plane waves in shallow water. The almost same theory was established in *Mechanique Analitique* (1788). For shallow-water waves, Lagrange (1786) claimed that "the speed of propagation of waves will be that which a heavy body would acquire in falling from ... half the height of the water in the canal"; that is, $(gh)^{1/2}$ where g is the acceleration due to gravity and h is the liquid depth. Before the year 1800, some other works discussed wave motion. M. Flaugergues (1793) and Francois de la Coudraye (1796) carried out exceptional works, which were later summarized by Weber & Weber (1825).

The first exact nonlinear solution for waves of finite amplitude in deep water was provided by Franz Joseph von Gerstner (1802). Since the wave motion is not irrotational in general, the Gerstner wave solution was long overlooked; even today it is usually regarded more as a curiosity rather than a result of practical importance. W.J. Macquorn Rankine (1863) revived interest in it and discovered it independently. In December 1813, the *French Academie des Sciences* announced a mathematical prize competition on the propagation of surface waves in a fluid of infinite depth. In July 1815, 25-year-old Augustin-Louis Cauchy submitted his entry, and, in August, Simeon D. Poisson, one of the judges, deposited a memoir of his own to record his independent work. Cauchy was awarded the prize in 1816, Poisson's memoir was published in 1818, and Cauchy's work eventually appeared in 1827, with an astonishing 188 pages of additional notes. Horace Lamb in *Hydrodynamics* presented Cauchy-Poisson analysis but it was restricted to two-dimensional disturbances. The first edition of his book (published in 1895) was brief, incomplete and relegated to small print, but he revised it in 1916 for a more comprehensive treatment in the fourth edition. The Cauchy-Poisson analysis is now acknowledged as an important milestone in the mathematical theory of initial value problems.

Ernst Heinrich Weber and Wilhelm Eduard Weber published a very different work on waves in Leipzig: *Wellenlehre auf Experimente gegrundet* (1825). This book includes the Webers' careful laboratory experiments on plane periodic wave trains in a channel, together with extracts from, and comments on such theoretical works as were then avail-

able. John Scott Russell and Sir John Robison [67] published a remarkable work in 1837 on the wave characteristics of ocean, river and canals. The nonlinear solitary wave was discovered by Russell's experiments. They distinguished four types of waves: waves of translation, including their newly found solitary waves, tides, and bores; oscillatory waves, or periodic wave trains; capillary waves; and corpuscular waves, which are compressive sound waves propagating through water. The following year, an exemplary analysis of the effects of slow depth and width, though limited to the long linear shallow water wave, was demonstrated by George Green [34]. Philip Kelland [41] analyzed the wave motion in a fluid of finite depth, on the hypothesis of parallel sections, and correctly obtained the result of the wave speed. In 1847, Samuel Earnshaw [32] studied the representation of a solitary wave by discontinuous expressions. He pointed out the conspicuous lack of success in obtaining general solutions to the equations of hydrodynamics, and emphasized the need to limit theoretical studies to restricted classes of motions, based on hypotheses suggested by experiments. Toward the end of that year, a nonlinear theory attempted by him failed which George Gabriel Stokes [85] developed. Benard Rayleigh [64] obtained the correct approximate solution, and also discovered that Earnshaw's solution was not irrotational. In 1841, George Biddell Airy's long and famous article "Tides and Waves" was published in the *Encyclopaedia Metropolitana*. When it got published, Airy's scientific reputation as mathematician and astronomer was already well-known. Airy's article has long been recognized as a major contribution to water wave theory.

The boundary value problems related to water wave scattering are set up with Laplace's equation as the governing equation, and sometimes with Helmholtz equation or modified Helmholtz equation. The available boundary conditions and matching conditions are utilized to solve the problem. Subsequently, the required quantities, such as forces and hydrodynamic coefficients can be calculated, and these quantities are analyzed for various parameters. In the following section, a brief description of the basic equations and conditions in linearized water wave theory for the case of finite ocean depth are presented.

1.2 Relevant equations and conditions

In this section, we present a number of equations and definitions related to water waves. The description of these equations and definitions will help in understanding the fundamentals of water wave theory. We consider linearized water wave theory to describe different boundary conditions. We consider the irrotational motion of an incompressible, homogeneous and non-viscous fluid. The sea-bed is assumed to be flat and impermeable. The water depth across which waves propagate, and the height and length of the water waves are important parameters to be considered. All other parameters, such as wave-induced water velocities and accelerations, can be obtained theoretically using the values

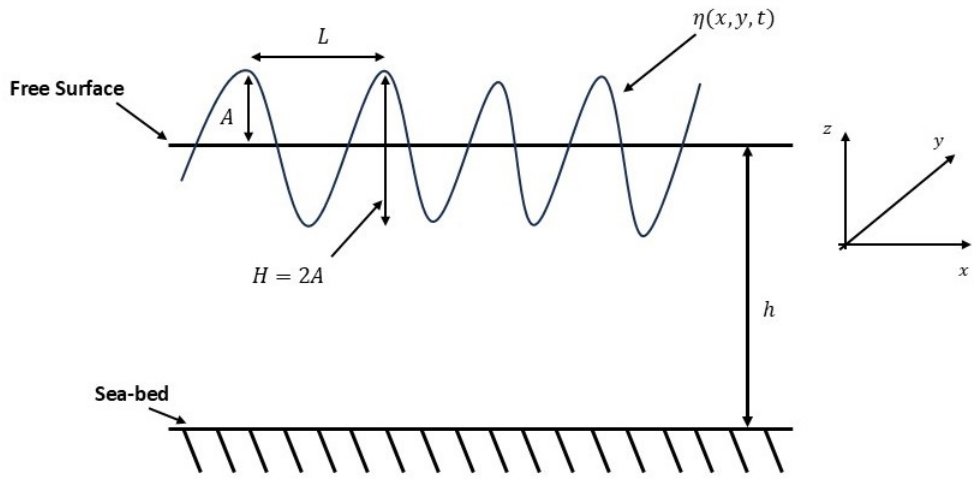

Figure 1.1: Schematic diagram of wave propagation

of these parameters. Figure 1.1 represents a right-handed Cartesian coordinate system, where the xy-plane represents the laterally unbounded ocean surface and the z-axis represents the vertically upward direction. A *crest* is a point on a surface wave where the wave displacement is at its maximum. A *trough* is the opposite of a crest, meaning it is minimum or the lowest point in a wave cycle. The horizontal distance between two successive wave crests or troughs is the *wavelength* L. The following are the standard notations associated with water waves:

h: water depth which is measured from mean water level to the sea-bed,

$\eta(x, y, t)$: vertical displacement of water surface above mean water level,

H: wave height,

$A = \frac{H}{2}$: wave amplitude,

T: wave period,

$k = \frac{2\pi}{L}$: wavenumber,

$\omega = \frac{2\pi}{T}$: wave angular frequency.

Ocean waves in nature are always irregular and random. The superposition of several regular waves (wave components) with different frequencies and amplitudes forms irregular waves. A regular wave (wave component) is defined by a single frequency (wavelength) and wave amplitude (height). *Wind waves* and *swells* are some examples of regular water waves. The examples of irregular waves are *surf, beats, harbour resonance, seiche* and *tsunamis*. According to the relative depth of the ocean water, waves are classified into three main categories. The relative depth is defined as h/L. When the relative depth is less than $\frac{1}{20}$, then the ocean depth is considered small in comparison with the wavelength, and the waves are called *shallow water* waves or *long* waves. Tidal waves, tsunami waves are some examples of shallow water waves. If the relative depth is greater than $\frac{1}{2}$, the waves are called *deep water* waves or *short* waves. Rogue waves fall into deep water wave

category. For $\frac{1}{20} < h/L < \frac{1}{2}$, the waves are termed *intermediate depth* waves. When the wave amplitude is assumed to be small compared to the wavelength, then this theory is called *linearized theory of water waves*. In general, ocean waves are nonlinear. However, it has been observed that the margin of error in most of the engineering applications is quite small even if linear theory is applied instead of nonlinear theory. Therefore, small amplitude wave theory is usually employed to model the problems in water wave mechanics. In this thesis, all the problems are tackled by utilizing linearized water wave theory.

For an inviscid and incompressible fluid with velocity $\vec{U}$, the equations for conservation of mass (the equation of continuity) and momentum (Euler's equation of motion) are given by

$$\nabla.\vec{U} = 0, \tag{1.1}$$

$$\frac{\partial \vec{U}}{\partial t} + (\vec{U}.\nabla)\vec{U} = \vec{g} - \frac{1}{\rho}\nabla\vec{P}, \tag{1.2}$$

where ρ is the density of the water, $\vec{g}$ is the acceleration due to gravity and $\vec{P}$ is the hydrodynamic pressure.

Now, we consider an irrotational flow. Then we can find a potential function Φ such that

$$\vec{U} = \pm\nabla\Phi. \tag{1.3}$$

Mathematically, both positive and negative signs are correct in (1.3), but we know that the gravity waves flow from higher to lower potential, which defines loss of the energy. Following this convention, we consider negative sign in all our works in this thesis. Now, substituting (1.3) in (1.1) gives the equation of continuity for a potential flow as

$$\nabla^2\Phi = 0, \tag{1.4}$$

which is the **Laplace's equation**.

For time harmonic motions, the velocity potential can be expressed in Cartesian co-ordinates (x, y, z) as

$$\Phi(x, y, z, t) = \mathrm{Re}[\phi(x, y, z)\exp(-\mathrm{i}\omega t)], \tag{1.5}$$

with $\phi(x, y, z)$ being the complex-valued potential function and 'Re' denoting the real part of a function.

Considering gravity to be acting in the negative z-direction, it gives

$$\vec{g} = \nabla(-gz). \tag{1.6}$$

Then, equation (1.2) gives

$$\nabla\left[-\frac{\partial\Phi}{\partial t}+\frac{1}{2}\nabla\Phi.\nabla\Phi+\frac{P}{\rho}+gz\right]=0, \tag{1.7}$$

which, after integration in real time domain $[0,t]$, can be written as

$$-\frac{\partial\Phi}{\partial t}+\frac{1}{2}\nabla\Phi.\nabla\Phi+\frac{P}{\rho}+gz=C(t).$$

However, without the loss of generality, $C(t)$ can be combined with the potential $\Phi(x,y,z,t)$ which results in

$$-\frac{\partial\Phi}{\partial t}+\frac{1}{2}\nabla\Phi.\nabla\Phi+\frac{P}{\rho}+gz=0. \tag{1.8}$$

This is called the **Bernoulli's equation** (dynamic boundary condition).

The kinematic condition on the free surface $z=\eta(x,y,t)$ is given by

$$-\frac{\partial\Phi}{\partial z}=\frac{\partial\eta}{\partial t}+\frac{\partial\eta}{\partial x}\frac{\partial\Phi}{\partial x}+\frac{\partial\eta}{\partial y}\frac{\partial\Phi}{\partial y}. \tag{1.9}$$

The linearised kinematic condition (1.9) becomes (after neglecting the products)

$$-\frac{\partial\Phi}{\partial z}=\frac{\partial\eta}{\partial t}\quad\text{at}\quad z=0. \tag{1.10}$$

Following small amplitude of the motion, the linearised dynamic boundary condition (1.8) at the free surface $z=\eta$ becomes

$$-\frac{\partial\Phi}{\partial t}+\frac{P}{\rho}+g\eta=0. \tag{1.11}$$

Following linearized water wave theory as mentioned earlier and using (1.5), the boundary value problem consists of the governing equation

$$\nabla^2\phi=0, \tag{1.12}$$

and the other conditions as described below. Assuming hydrodynamic pressure to be zero at the free surface, and combining (1.10) and (1.11) gives the mean free surface condition at $z=0$ as

$$\frac{\partial\phi}{\partial z}-K\phi=0, \tag{1.13}$$

where, $K=\omega^2/g$.

It may be noted that, while waves take different forms, in the small amplitude limit, they conform to the same governing equation (1.12) or one of its variants.

If S is a boundary of an obstacle through which fluid cannot pass, we define an impermeable boundary condition

$$\frac{\partial \phi}{\partial n} = 0 \qquad \text{on } S, \tag{1.14}$$

where n is the outward normal to the surface S.

If the bottom is an uneven impermeable rigid one, the bottom boundary condition reduces to

$$\frac{\partial \phi}{\partial z} + \nabla_{x,y} h \cdot \nabla_{x,y} \phi = 0 \quad \text{at} \quad z = -h(x,y), \tag{1.15}$$

where $\nabla_{x,y} = \left(\frac{\partial}{\partial x}, \frac{\partial}{\partial y}\right)$.

For a constant bottom, it reduces to

$$\frac{\partial \phi}{\partial z} = 0 \quad \text{at} \quad z = -h. \tag{1.16}$$

1.3 Water wave propagation: associated scattering, radiation and trapping

In the ocean, water waves interact with a variety of objects and structures. While some of these structures, like the platforms and breakwaters, are man-made for a variety of uses, others, like the rocks and sand formations on the ocean floor, are naturally occurring. Examining phenomena like scattering and radiation are crucial for researching how waves interact with these structures.

The normal component of the velocity on the surface of a structure must be equal to the velocity component in the same direction of an adjacent fluid particle. This relationship can generally be expressed as

$$\frac{\partial \Phi}{\partial n} = V_n, \tag{1.17}$$

where V_n represents the component of the structural velocity in the direction of the normal coordinate n, which is oriented outward from the fluid. In linearized water wave theory, this condition is applied to the equilibrium surface of the structure which is denoted by S_B. When a wave train is incident upon a floating structure, it is diffracted to produce a scattered wave field and also sets the structure in motion to generate a radiated field. By

linear superposition, the velocity potential can be decomposed into two parts as follows:

$$\Phi = \Phi_S + \Phi_R. \tag{1.18}$$

The potential Φ_S represents the solution to the scattering problem, when the structure is assumed to be fixed in the waves. This potential can be further decomposed as

$$\Phi_S = \Phi_{\text{inc}} + \Phi_D, \tag{1.19}$$

where Φ_{inc} is the incident wave train and Φ_D corresponds to the diffracted waves. When the structure is kept fixed, the appropriate boundary condition is

$$\frac{\partial \Phi_S}{\partial n} = 0 \ \text{ on } \ S_B. \tag{1.20}$$

When a train of surface (or internal) waves travelling from a large distance is incident on an obstacle submerged or partially immersed in water, a part of the wave is reflected by the obstacle, which is known as the *reflected wave*. Meanwhile, another portion of the wave is transmitted over or below it, which is known as the *transmitted wave*. These reflected and transmitted waves are called outgoing waves as they move away from the obstacle after interacting with it. During this process, damping of waves occurs, which leads to a reduction in the amplitude of the waves. The scattering process is characterized by two key physical quantities: *reflection coefficient* and *transmission coefficient*. These coefficients are crucial in the mathematical analysis of water wave scattering problems since they quantify the amounts of reflected and transmitted waves. The reflection coefficient R and transmission coefficient T are, respectively, given by

$$R = \frac{\text{Amplitude of the reflected wave}}{\text{Amplitude of the incident wave}},$$
$$T = \frac{\text{Amplitude of the transmitted wave}}{\text{Amplitude of the incident wave}}.$$

The potential Φ_R in equation (1.18) represents the solution of the radiation problem, in which the structure is forced to oscillate in the absence of an incident wave, and it satisfies

$$\frac{\partial \Phi_R}{\partial n} = V_n \ \text{ on } \ S_B. \tag{1.21}$$

In general, the normal velocity V_n is determined from the equation of motion of the structure (Newman [58], Chapter 6) and will depend, in particular, on the forces that result from any incident wave.

A rigid floating structure in the ocean can experience six degrees of freedom: three translational motions along the x-, y- and z-directions, known as surge, sway, and heave,

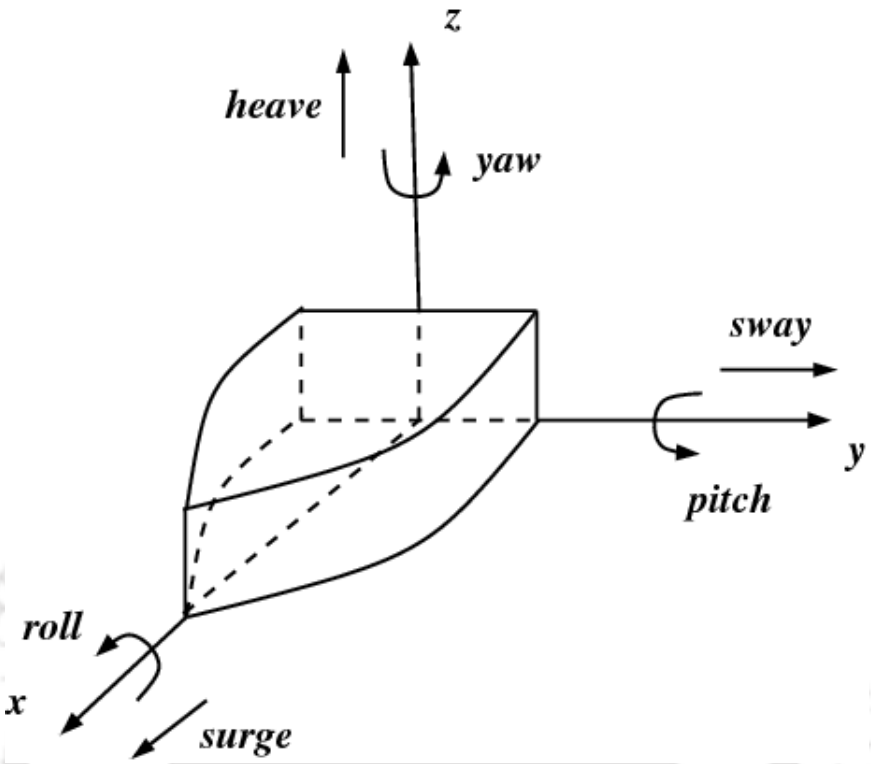

Figure 1.2: Motions of a floating body [63]

respectively, and three rotational motions about the x-, y- and z-axes, referred to as roll, pitch and yaw, respectively (Figure 1.2). Typically, the motion of the structure will be a combination of movements in all of these directions and the velocity of a point on the surface, measured normal to the surface, can be expressed as

$$V_n = \vec{U}.\vec{n} + \vec{\Omega}.(\vec{r} \times \vec{n}), \tag{1.22}$$

where $\vec{r}$ is the position vector of the point measured from the centre of rotation and $\vec{n}$ is a normal vector to the surface of the structure directed out of the fluid. Here, the translational velocity vector

$$\vec{U} = (U_1, U_2, U_3) \tag{1.23}$$

has components corresponding to surge, sway, and heave motions, respectively, and the rotational velocity vector

$$\vec{\Omega} = (U_4, U_5, U_6) \tag{1.24}$$

has components corresponding to roll, pitch, and yaw, respectively. The normal velocity

V_n given by (1.22) may be rewritten as

$$V_n = \sum_{\mu=1}^{n} U_\mu n_\mu, \tag{1.25}$$

where n_μ; $\mu = 1, 2, 3$ are the x, y, z components of the unit normal to the structure defined by the direction cosines

$$\begin{aligned} n_1 &= \cos(n, x), \\ n_2 &= \cos(n, y), \\ n_3 &= \cos(n, z), \end{aligned}$$

whereas n_μ; $\mu = 4, 5, 6$ are the corresponding components of $(\vec{r} \times \vec{n})$. If a point on the surface of the structure has coordinates (x, y, z), and if (x', y', z') is the equilibrium position of the centre of rotation, then

$$\begin{aligned} n_4 &= (y - y')n_3 - (z - z')n_2, \\ n_5 &= (z - z')n_1 - (x - x')n_3, \\ n_6 &= (x - x')n_2 - (y - y')n_1. \end{aligned}$$

For time harmonic motions, each velocity component may be written as

$$U_\mu = \mathrm{Re}(u_\mu e^{-\mathrm{i}\omega t}) \tag{1.26}$$

by linear superposition of the radiated velocity potentials, defined in

$$\Phi_R = \mathrm{Re}(\phi_R(r, \theta, z)e^{-\mathrm{i}\omega t}).$$

It may be decomposed as

$$\phi_R = \sum_{\mu=1}^{6} u_\mu \phi_\mu,$$

where u_μ is the complex amplitude of the oscillations in mode μ. The potential ϕ_μ describes the wave field due to the oscillations in mode μ with unit velocity amplitude. The boundary condition (1.21) can be rewritten as

$$\frac{\partial \phi_\mu}{\partial n} = n_\mu \ \text{ on } \ S_B \ \ \mu = 1, 2, ..., 6. \tag{1.27}$$

To obtain a unique solution of the diffracted potential Φ_D and the radiated potential Φ_R,

each must satisfy a radiation condition, ensuring that the waves associated with these potentials propagate away from the structure. For Φ, representing either Φ_D or Φ_R, this radiation condition can be expressed as follows (known as the Sommerfeld radiation condition):

$$\lim_{r\to\infty}\sqrt{r}\left[\frac{\partial\Phi}{\partial r}-\mathrm{i}k\Phi\right]=0, \tag{1.28}$$

in three dimensions, where k is the wavenumber, r is the horizontal polar coordinate.

Once the total velocity potential is determined and the pressure on the surface of the structure is calculated by using Bernoulli's equation, the total force $\vec{F}$ exerted on the body and moment $\vec{M}$ of this force in vector notation can be obtained from the following formulas:

$$\vec{F}=-\int\int_{S_B}p\vec{n}\,\mathrm{d}S,$$
$$\vec{M}=-\int\int_{S_B}p\,(\vec{r}\times\vec{n})\,\mathrm{d}S,$$

where S_B is the submerged surface of the body. Now, the hydrodynamic pressure due to the radiated potential is obtained from linearized Bernoulli's equation as

$$p_j=\mathrm{i}\rho\omega\phi_{R,j}(r,\theta,z). \tag{1.29}$$

Here, $\phi_{R,j}$ represents the radiated or forced potentials resulting from the structure's oscillation in the j-th mode. The radiated force refers to the force generated by the motion of the body. This force can be calculated from the radiated potential, and the general expression for the radiated force on the body due to the j-th motion is given as follows:

$$F_{j,l}=-\mathrm{i}\rho\omega\int\int_{S_B}\phi_{R,j}(r,\theta,z)n_l\,\mathrm{d}S, \tag{1.30}$$

where $F_{j,l}$ represents the radiated force acting on the body in the l-th direction, with its amplitude in the j-th direction, and n_l denotes the component of the unit normal vector pointing toward the cylinder at the cylinder surface. This expression can be rewritten as (Rahman [63])

$$F_{j,l}=\mathrm{i}\omega\left(\chi_{jl}+\mathrm{i}\frac{\Lambda_{jl}}{\omega}\right). \tag{1.31}$$

The first term in equation (1.31) corresponds to the component that is in phase with the acceleration in mode j, and the second term represents the component that is in phase with the corresponding velocity. Here, the notations χ_{jl} and $\frac{\Lambda_{jl}}{\omega}$ refer to the added mass

and damping coefficient, respectively. Using equations (1.30) and (1.31), we can now write this as

$$\left(\chi_{jl} + \mathrm{i}\frac{\Lambda_{jl}}{\omega}\right) = -\rho \int\int_{S_B} \phi_{R,j}(r,\theta,z) n_l \, \mathrm{d}S. \tag{1.32}$$

From equation (1.32), the added mass and damping coefficient can be determined by considering the real and imaginary parts of the right hand side, respectively. In physical sense, the added mass refers to the weight added to a system in a fluid because of the fact that an accelerating or decelerating body must move some volume of the surrounding fluid with it as it moves. Damping, on the other hand, is a force that acts within or upon an oscillatory system to reduce, restrict or prevent its oscillations. Any body accelerating in a fluid will be affected by added mass. However, since added mass depends on the density of the fluid, the effect is often negligible for dense bodies moving through much less dense fluids. For situations where the density of the fluid is comparable to or greater than the density of the body, the added mass can often be greater than the mass of the body. This phenomenon also applies to ships, submarines, and offshore platforms. For ships, the added mass can be as much as 3 to 4 times the mass in heave mode, and up to 2 times the mass in surge mode. Damping models describe how energy is dissipated during vibrations. These models play a crucial role in maintaining the stability of a moving structure and controlling its vibration amplitudes. Damping may originate from both the structure itself and the surrounding fluid.

When a wave gets trapped around an obstacle, it results in standing or localized waves. This is in addition to any scattering process that is involved. A trapped mode is a solution of the corresponding homogeneous boundary value problem and represents a free oscillation with finite energy of the fluid surrounding the fixed structure. These modes persist in some localized region including the free surface whilst decaying rapidly to zero as the free surface extends to infinity. Their existence implies that large amplitude motions of the fluid and structures are possible when the system is forced at a frequency close to that of the trapped mode. For a given structure, trapped modes may exist only at discrete frequencies. Mathematically, a trapped mode corresponds to an eigenvalue embedded in a continuous spectrum of the relevant operator.

The significance of study of trapping may be noted as follows:

- The variations of different parameters locate the region where trapped modes cease to exist and hence unique reflection and transmission coefficient can be determined for that specific set of geometrical configuration of the prescribed scattering problem.
- The trapped wave solutions throw some light on a number of issues related to various aspects of maintenance of the coast or breakwaters and for the creation of tranquility

zones.

- One interest in trapped wave problems is stimulated by the proposed construction of tube bridges in the Norwegian fjords which have a manifestly two-layer structure.
- Trapped mode frequencies can be used to estimate the dangerous resonant frequencies that may appear in the scattering problem in the vicinity of the submerged structures.
- Trapped waves have the potential to lead to sharp gradients in coastal sea level which help in improving the study of ocean currents. The examples are North Pacific subtropical gyre and Weddell sea near Antarctica.

1.4 Fluid flow through porous media

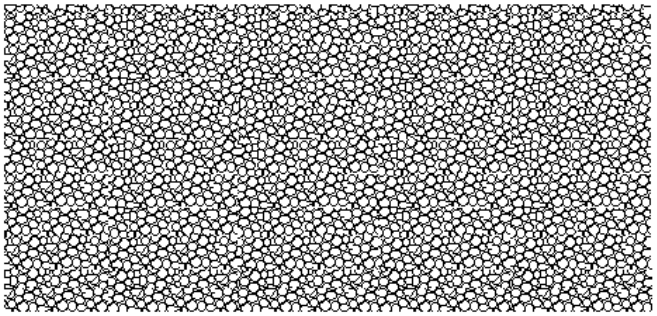

Figure 1.3: Structural model of a porous structure

We first define a porous medium and its application before discussing the flow within a porous material or medium. The porous medium is a medium that contains pores in it. The skeletal part of the medium is referred as the "matrix" or "frame". This skeletal part is usually solid, but foam-type structures are also studied by using the theory of porous media. In most cases, pores are filled with a fluid (liquid or gas). Many natural substances such as rocks and soil (e.g., aquifers, petroleum reservoirs), zeolites, biological tissues (e.g., bones, wood, cork), and man-made materials such as cements and ceramics can be considered as porous media. Only by considering them as a porous media, many of their important properties can be understood. Many areas of applied science and engineering, such as filtration, mechanics (acoustics, geomechanics, soil mechanics, rock mechanics), engineering (petroleum engineering, bioremediation, construction engineering), geosciences (hydrology, petroleum geology, geophysics), biology and biophysics, and material sciences, utilize the concept of porous media.

There are two types of porous medium, namely, *saturated* and *unsaturated* porous medium. In a saturated porous medium, all the void spaces are completely filled with fluid. In contrast, in an unsaturated porous medium, the voids are partially filled with liquid, while the remaining space is occupied by air. The term *porosity* indicates the amount of pores in a material of medium. The porosity or void fraction is a measurement of the void or empty spaces of a material. Let us consider a volume V_T of a reasonably large porous medium such that

$$V_T = V_P + V_S,$$

where V_p is the void volume (pore volume) and V_s the volume of the solid material. Porosity is defined as the ratio of pore volume to total volume. It may be denoted by ϵ and expressed as follows:

$$\epsilon = \frac{V_P}{V_T} = \frac{V_T - V_S}{V_T}.$$

Types of porosity

- Primary porosity (The porosity of a rock or any other natural porous material that happens at the depositing time.)
- Secondary porosity (The porosity that grows after deposition of the rock or any other natural porous material.)

Further, porosity can be categorized into six types depending on the size of the pores:

- Total Porosity (It is a ratio of the entire pore space in a rock to its bulk volume.)
- Effective Porosity (It is a measure of the void space that is filled by recoverable oil and gas),
  porosity$= \frac{\text{Vol. of interconnected pores + Vol. of dead end}}{\text{Total or bulk vol. of reservoir rock}}$.
- Dual porosity (It is a conceptual idea that there are two overlapping reservoirs which interact. In fractured rock aquifers, the rock mass and fractures are often simulated as being two overlapping but distinct bodies.)
- Microporosity (Pore size is smaller than 2 nanometers in diameter.)
- Mesoporosity (Pore size is greater than 2 nanometers and less than 50 nanometers in diameter.)
- Macroporosity (Pore size is greater than 50 nanometers in diameter.)

Porosity measuring method

There are several types of methods for finding porosity such as

- Direct method
- Optical method
- Computed tomography method
- Imbibition method
- Gas expansion method

Darcy's law for flow in porous media

By Darcy's law, the flow of a fluid through a porous medium may be described. Historically, Darcy's law was proposed as an empirical relationship on the basis of laboratory experiments in 1856.

The laminar stationary flow of an incompressible flow through a homogeneous porous medium can be expressed by Darcy's law as

$$\vec{U} = -\frac{\mathcal{K}}{\mu}\nabla P,$$

where, $\vec{U}$ represents the velocity and P is the fluid pressure passing through the pores. The symbol $\mathcal{K}$ denotes the permeability of the medium and μ is the dynamic viscosity. The relation between particle diameter (d_p) and porosity (ϵ) is defined by the Carman-Kozeny equation as follows:

$$\mathcal{K} = \frac{d_p^2\epsilon^2}{180(1-\epsilon)^2}.$$

Permeability has dimension of meter^2. In practical applications, the characteristic length scale for the device is denoted by $\mathcal{L}$. The dimensionless ratio defined by $\mathcal{D} = \frac{\mathcal{K}}{\mathcal{L}^2}$ is called the Darcy number. Larger Darcy numbers indicate larger particle diameters and pore sizes. Darcy number zero means that no fluid can enter the structure.

Remark

As the specific discharge increases, Darcy's law is invalid [4]. At low Reynolds numbers, there is a region where the flow is laminar, viscous forces are negligible, for which linear Darcy's law is valid. In this case, Reynolds number takes values between 1 and 10.

We know that, when a fluid flows through a perforated barrier, the fluid pressure drops. The pressure drop is calculated by the empirical formula given by Sollitt and Cross [83]. This formula contains several terms including a quadratic term. We have followed the

approach, like many others, that the quadratic term is negligibly small. However, it is not always true that the quadratic pressure drop can be neglected in the formulation. But, it is possible to ignore the quadratic pressure drop when the barrier is considered thin and at rest as assumed here.
In our work, we consider two types of porous structure:

(i) Thick porous structure,

(ii) Thin porous structure.

From modelling point of view, the mathematical treatment is different for each of them.

1.4.1 Fluid flow through a thick porous structure

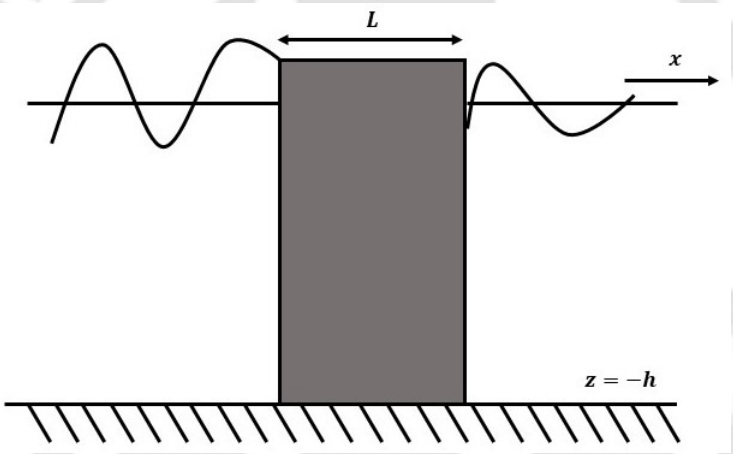

Figure 1.4: Schematic diagram of wave propagation through a thick porous structure

Sollitt and Cross [83] developed a relation between the velocity potential and the pore pressure for a time harmonic fluid flow through a homogeneous and isotropic porous medium of width L. The governing equation for a fluid motion is written as

$$\nabla^2\Phi = 0. \tag{1.33}$$

The Bernoulli's equation for fluid motion inside the porous region in terms of pore pressure P and seepage velocity $\vec{U}$ is expressed as follows:

$$m\frac{\partial\Phi}{\partial t} + \frac{P}{\rho} + gz + f\omega\Phi = 0, \tag{1.34}$$

where $\vec{U} = -\nabla\Phi$, f is a linear friction coefficient and m is an inertial coefficient defined as

$$m = 1 + \frac{(1-\epsilon)}{\epsilon}C_m, \tag{1.35}$$

with ϵ as the porosity and C_m the added mass coefficient of the grain. The kinematic boundary condition on the free-surface for the porous region is given as

$$\frac{\partial \eta}{\partial t} = \frac{\partial \Phi}{\partial z}, \tag{1.36}$$

where η is the free-surface elevation. For the time harmonic waves of angular frequency ω, the velocity potential Φ and the wave elevation can be expressed as

$$\Phi(x, y, z, t) = \mathrm{Re}[\phi(x, y, z)e^{-\mathrm{i}\omega t}], \quad \eta(x, y, t) = \mathrm{Re}[\tilde{\eta}(x, y)e^{-\mathrm{i}\omega t}]. \tag{1.37}$$

The Bernoulli's equation can be combined with the kinematic boundary condition to yield

$$\frac{\partial \phi}{\partial z} = (m + \mathrm{i}f)\frac{\omega^2}{g}\phi. \tag{1.38}$$

At the bottom of the porous medium, since the normal seepage velocity component must vanish, we have

$$\frac{\partial \phi}{\partial z} = 0. \tag{1.39}$$

Additionally, the lateral boundary conditions can be utilized to verify the continuity of mass flux and pressure across the vertical boundaries of the porous structure. These conditions are represented as

$$\frac{\partial \phi_L}{\partial x} = \epsilon \frac{\partial \phi}{\partial x}, \tag{1.40}$$

$$\phi_L = (m + \mathrm{i}f)\phi, \tag{1.41}$$

$$\frac{\partial \phi_R}{\partial x} = \epsilon \frac{\partial \phi}{\partial x}, \tag{1.42}$$

$$\phi_R = (m + \mathrm{i}f)\phi, \tag{1.43}$$

where ϕ_L and ϕ_R are the velocity potentials in the left and right hand side regions of the porous medium and they satisfy the Laplace's equation.

1.4.2 Fluid flow through a thin porous structure

Here, we discuss a boundary condition for a fluid flow through a thin porous structure, derived by Yu [95]. We consider a thin porous structure within a Cartesian coordinate system where x represents the transverse direction, y the longitudinal direction, and z the upward direction. The width of the porous structure is assumed to be very thin, such that $\gamma = b/\lambda \ll 1$, where b is the width of the porous structure and λ is the characteristic length scale of the wave motion within the porous medium in both the y- and z- directions. The thin porous structure is assumed to be non-deformable in nature. The wave motion

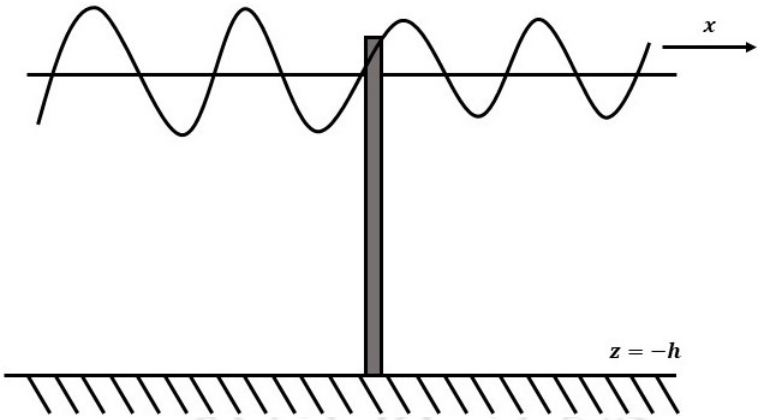

Figure 1.5: Schematic diagram of wave propagation through a thin porous structure

within the porous medium is governed by the equation of continuity and the equation of motion for the velocity $\vec{U}$ and the dynamic pressure P of the fluid, as proposed by Sollitt and Cross [83], as follows:

$$\nabla \cdot U = 0, \tag{1.44}$$

$$\frac{\partial U}{\partial t} = -\frac{\nabla P}{\rho} - f\omega U - C_m \frac{1-\epsilon}{\epsilon}\frac{\partial U}{\partial t}, \tag{1.45}$$

where t is time, ρ is the density of fluid, ω is the angular frequency of wave, ϵ is porosity of the porous medium, f is linearized resistance coefficient of porous medium and C_m is the added mass coefficient of the porous medium.

To get the harmonic solution, we can write U and P in terms of spatial functions u and p as

$$\{U, P\} = \{u, p\}e^{-\mathrm{i}\omega t}. \tag{1.46}$$

Now, substituting equation (1.46) in equations (1.44) and (1.45), we get

$$\nabla \cdot u = 0, \tag{1.47}$$

$$\nabla p + \rho\omega R u = 0, \tag{1.48}$$

where $R = f - \mathrm{i}\left(1 + C_m\frac{1-\epsilon}{\epsilon}\right)$ is the non-dimensional porous impedance parameter. The physical significance of R is that its real part refers to resistance effect of the permeable material and the imaginary part refers to inertial effect of the fluid inside the permeable material.

Since the length scale for the wave motion in the x-direction within the porous structure can be represented by b, we note by nondimensionalizing equations (1.47) and (1.48) that the gradient of the velocity and the pressure in the x-direction are predominant in

comparison with their correspondents in the other directions. Therefore, not all the terms in these equations are of the same order. Collecting all those of the leading order γ, we have

$$\frac{\partial u}{\partial x} = 0, \tag{1.49}$$

$$\frac{\partial p}{\partial x} + \rho\omega R u = 0, \tag{1.50}$$

where u is the velocity component in the x-direction. Equation (1.49) indicates that u remains the same with respect to x and hence, by integrating equation (1.50) with respect to x, we get

$$u = \frac{-(p_{b^-} - p_{0^+})}{\rho\omega b R}, \tag{1.51}$$

where, p_{0^+} and p_{b^-} denote the pressure within the porous medium at $x = 0$ and $x = b$, respectively.

Now, on matching the continuity of mass flux and pressure at $x = 0$ and $x = b$, one obtains

$$u_{0^-} = u_{b^+} = \epsilon u, \tag{1.52}$$

$$p_{0^-} = p_{0^+}, \quad p_{b^-} = p_{b^+}, \tag{1.53}$$

where the subscripts 0^+ and 0^- denote the values inside and outside the porous medium at $x = 0$, and b^- and b^+ those at $x = b$. Substituting equations (1.52) and (1.53) in equation (1.51), and with the assumption of small thickness of porous structure, it leads to the boundary condition

$$u_{0^-} = u_{0^+} = -\frac{kG}{\rho\omega}(p_{0^+} - p_{0^-}) \text{ at } x = 0^{\pm}, \tag{1.54}$$

where k is the wavenumber and $G = \frac{\epsilon}{Rkb} = G_r + \mathrm{i}G_i$ is known as the porous-effect parameter. The real part refers to the resistance effect of the porous medium against the flow while imaginary part refers to the inertia effect of the fluid inside the porous medium.

In the case of irrotational motion, using the pressure $p = \mathrm{i}\rho\omega\phi$, the porous boundary condition (1.51) may be replaced by

$$\frac{\partial \phi_L}{\partial x} = \frac{\partial \phi_R}{\partial x} = \mathrm{i}k_0 G(\phi_L - \phi_R) \text{ at } x = 0^{\pm}, \tag{1.55}$$

where ϕ_L and ϕ_R are velocity potentials on the left and right sides of the thin porous structure.

1.5 Waves with uniform current U_0

For waves in rivers or ocean currents, a first approximation to the waves and currents is to assume that the current is uniform in both depth and horizontal distance, and the flow is in the same direction as the waves.

A specific form of the velocity potential Φ can be selected to represent the uniform current speed U_0 and a progressive wave, ensuring that it satisfies the Laplace's equation:

$$\Phi = -U_0 x + A\cosh(k(h+z))\cos(kx-\omega t). \tag{1.56}$$

The form of this solution guarantees the periodicity of the wave in both space and time and also satisfies the no-flow condition at the bottom boundary. However, it is necessary to satisfy the linearized kinematic and dynamic free surface boundary conditions. The previously derived forms of these conditions cannot be directly applied, as errors would occur due to the fact that the speed U_0 is no longer necessarily small. Therefore, we must rederive the linear boundary conditions.

The dynamic free surface boundary condition:- The Bernoulli's equation about the free surface on which a zero gauge pressure is prescribed can be expanded as

$$\begin{aligned}\left[\frac{1}{2}(u^2+w^2)+gz-\frac{\partial\Phi}{\partial t}\right]_{z=\eta(x,t)} &\simeq \left[\frac{1}{2}(u^2+w^2)+gz-\frac{\partial\Phi}{\partial t}\right]_{z=0}\\ &+\eta\frac{\partial}{\partial z}\left[\frac{1}{2}(u^2+w^2)+gz-\frac{\partial\Phi}{\partial t}\right]_{z=0}+\cdots = C(t).\end{aligned} \tag{1.57}$$

Now the horizontal velocity is

$$u = -\frac{\partial\Phi}{\partial x} = U_0 + Ak\cosh(k(h+z))\sin(kx-\omega t).$$

Therefore, the u^2 term is

$$u^2 = U_0^2 + 2AkU_0\cosh(k(h+z))\sin(kx-\omega t) + A^2k^2\cosh^2 k(h+z)\sin^2(kx-\omega t).$$

For infinitesimal waves, it is expected that the wave-induced horizontal velocity component will be small (i.e., Ak is small), and therefore $(Ak)^2$ would be much smaller. We then neglect the last term in the equation above.

The linearized Bernoulli's equation (i.e., dropping all terms of order $(Ak)^2$), evaluated at $z=0$ now becomes

$$\frac{1}{2}\left[U_0^2 + 2AkU_0\cosh(kh)\sin(kx-\omega t)\right] - A\omega\cosh(kh)\sin(kx-\omega t) + g\eta = C(t),$$

or

$$\eta(x,t) = -\frac{U_0^2}{2g} + \frac{A\omega}{g}\left(1 - \frac{U_0 k}{\omega}\right)\cosh(kh)\sin(kx - \omega t) + C(t). \tag{1.58}$$

We take the spatial average of both sides of equation (1.58) to obtain the Bernoulli term $C(t)$. Since the space average of $\eta(x,t)$ is taken to be zero, it indicates that $C(t)$ = constant = $u_0^2/2g$. Furthermore, if we define a water surface displacement $\eta(x,t) = H/2\sin(kx - \omega t)$, then

$$A = \frac{gH}{2\omega(1 - U_0/C)\cosh(kh)}. \tag{1.59}$$

The kinematic free surface boundary condition:- The remaining boundary condition to be satisfied is the linearized form of the KFSBC:

$$\frac{\partial \eta}{\partial t} - \frac{\partial \phi}{\partial x}\frac{\partial \eta}{\partial x} = -\frac{\partial \phi}{\partial z}, \quad z = \eta.$$

Expanding about the still water level, we have

$$\left(\frac{\partial \eta}{\partial t} - \frac{\partial \phi}{\partial x}\frac{\partial \eta}{\partial x}\right) + \eta\frac{\partial}{\partial z}\left(\frac{\partial \eta}{\partial t} - \frac{\partial \phi}{\partial x}\frac{\partial \eta}{\partial x}\right) + \cdots = -\frac{\partial \phi}{\partial z} - \eta\frac{\partial}{\partial z}\left(\frac{\partial \phi}{\partial z}\right) + \cdots, \quad z = 0$$

or, retaining only the linear terms,

$$\frac{\partial \eta}{\partial t} + U_0\frac{\partial \eta}{\partial x} = -\frac{\partial \phi}{\partial z}, \quad z = 0. \tag{1.60}$$

Substituting for η and ϕ yields the following dispersion equation for the case of a uniform current U_0:

$$\omega^2 = \frac{gk\tanh(kh)}{(1 - U_0/C)^2}, \tag{1.61}$$

or, another form can be developed by using the relationship $\omega = kC$:

$$\omega^2\left(1 - \frac{U_0 k}{\omega}\right)^2 = gk\tanh(kh),$$

or

$$\omega = U_0 k + \sqrt{gk\tanh(kh)}. \tag{1.62}$$

The second term on the right-hand side is the angular frequency formula obtained without a current.

In terms of the celerity, the dispersion relationship can be written as

$$(C - U_0)^2 = \frac{g}{k} \tanh(kh). \tag{1.63}$$

1.6 Background and brief review of previous works

The development of floating structures using ocean space is considered necessary because of the increasing human activities and the scarcity of available land. Very large floating structures (VLFS), such as floating airports, floating bridges, entertainment provisions, floating islands, etc. ([92]), have been created for various purposes, including fish farming, offshore tourism, gas and oil exploration, and marine resource development. Consequently, the marine industry worldwide has shown great interest in examining oblique wave interactions with VLFSs over the past few decades. The study of such structures has generated a great amount of interest because of their broad range of applications. The stability of these structures depends on the ocean wave forces acting on them. However, despite all of the recent advances, many floating structures have been reported to collapse because of natural disasters like cyclones or tsunamis ([53]). Therefore, studies and analysis of various parameters with appropriate values to effectively manage the wave forces on the floating structure are necessary. Jiang et al. [38] reviewed the advancements in the modeling of VLFSs and classified them on the basis of their shapes, applications, connection systems, and mooring systems.

History of Mild-Slope Equation (MSE)

The characteristics of the waves change when they move toward the coastal areas because of the change in water depth. Changes in the sea-bed cause the height of the waves and direction to shift. This process is known as wave refraction. Finding the exact analytical solution of the Laplace's equation in regions with arbitrary bottom topography is a challenging task. Exact or analytical solutions have been obtained only for certain specific bottom shapes, particularly those with sudden changes, such as bottoms with an infinite vertical step, finite steps, a rectangular bar with two steps, or a rectangular trench. For gradually changing bottoms, like ramps with constant or varying slopes, approximate solutions have been developed. Dingemans [31] discussed several techniques such as integral equation formulation, transfer matrix formulation, matching technique, WKBJ technique to handle these bottom configurations. However, analytical methods for the solution of water wave problems with arbitrary bottom topography are not yet fully developed. One of the popular approximation methods is the mild-slope equation (MSE). Historically, Berkhoff ([7, 8]) was the first one to derive the mild-slope equation using a depth-averaging method, which simplifies a three-dimensional problem into a two-

dimensional one. The bottom has a mild-slope in the sense that the bottom gradient is very small compared to the local wavenumber, i.e., $|\nabla h|/kh \ll 1$, where h represents the undisturbed water depth, k is the associated wavenumber and $\nabla = (\partial/\partial x, \partial/\partial y)$. Based on this assumption, Berkhoff neglected the terms containing the square of bottom slope $(\nabla h)^2$ and the curvature $\nabla^2 h$ in the derivation of MSE. The MSE is a second-order linear ordinary differential equation for velocity potential with variable coefficients. The MSE was widely applied to simulate the water wave problems with arbitrary bottom topography. Later, Booij [10] conducted a number of numerical experiments to investigate the range of slopes for which the MSE could be used. From this experiment, he concluded that Berkhoff's MSE was valid for slopes up to 1:3 in predicting wave scattering. Afterward, many researchers tried to improve the accuracy of the mild-slope equation. Chamberlain and Porter [14] developed a modified version of the MSE by using variation principle with one-term approximation retaining the terms omitted by Berkhoff. Their finding demonstrated that the modified mild-slope equation (MMSE) performed effectively for bottom slopes of up to 1. Additionally, Porter and Staziker [62] extended the MMSE by incorporating a multi-mode approximation, and formulated the necessary jump conditions at the points where the bottom profile had slope discontinuities.

Different methods to solve boundary value problems

As an alternative to the above mentioned methods, a varying sea-bed can be approximated by a sequence of flat shelves separated by vertical steps. The solution for each shelf is determined using the eigenfunctions, and then the eigensolutions on the shelves are matched by the conservation of mass and momentum. This approach is referred to as the eigenfunction matching method (EMM) (O'Hare and Davies [60], Tsai et al. [88]). Besides these approaches, several other semi-analytical methods have been utilized to approximate wave scattering caused by bottom irregularities. For example, Martha and Bora [52] applied a perturbation technique, considering up to the first-order correction, to address the water wave scattering by bottom undulations. By employing Green's integral theorem and the finite cosine transform, they derived the reflection and transmission coefficients.

Water wave scattering by rigid breakwaters

In recent years, water wave scattering with VLFS has been studied extensively. The mitigation of wave forces on the floating structures can be achieved using various devices, such as floating breakwaters, submerged barriers, air cushions, and oscillating water columns ([86]). To minimize the wave impact on the floating structure, breakwaters can be installed near them. Dean [30] examined the wave interaction with a submerged vertical barrier for determining the reflection coefficient and its intensity. Ursell [91] theoretically

examined the two-dimensional reflection of normal incident waves by a vertical barrier in deep water. Abul-Azm [1] studied the scattering of water waves by thin, rigid and impermeable submerged breakwaters. He considered three types of breakwaters and utilized an eigenfunction method and the least squares method to obtain the solution. Chakrabarti et al. [13], while discussing the scattering of water waves by vertical barriers, carried out a unified analysis that involved solving multiple integral equations via a simple singular integral equation. Roy et al. [66] studied the oblique wave scattering by three thin, non-identical vertical barriers arranged asymmetrically in deep water. They considered two geometries of the barriers, and obtained the solution by employing single-term Galerkin's approximations.

Water wave scattering by permeable breakwaters

Permeable or porous breakwaters are usually chosen over impermeable ones due to the need for wave transmission with low loads and amplitudes. The cost of porous breakwaters is lower than that of impermeable breakwaters. They also permit fish migration and water circulation, which help sustain a healthy marine ecosystem. In coastal areas, the problems concerning water wave scattering with porous structures is of utmost interest from the point of view of protecting offshore facilities from different wave actions. There has been extensive research reported on the issue of interaction of water waves with porous media. Sollitt and Cross [83] can be considered to be the first ones who developed a model of wave-induced flow in a rectangular permeable breakwater for which they discussed the wave energy dissipation within the porous media. In this context, they computed the linearized friction term f by employing an iterative procedure which has found a lot of applications in many such problems. Madsen [48] studied normally incident waves interacting with a homogeneous porous structure of rectangular cross-section. Using linearized theory, he formulated the problem to obtain an explicit solution for the reflection and transmission coefficients. Madsen [49] derived a theoretical solution of shallow-water wave scattering by a vertical porous wave-absorber placed on a flat bottom. He matched the solution with unknown coefficients at the interfaces/boundaries using the continuity of mass flux and pressure at the front face of the absorber. The reflection coefficient was determined with the help of the Lorentz principle of equivalent work by considering it as a function of parameters which described the incoming waves and the absorber characteristics.

Dalrymple et al. [23] investigated the oblique wave interaction with a vertical porous structure for which they observed that the reflection of an incident wave penetrating into the structure got reduced with an increasing angle of incidence. Yu and Chwang [96] analyzed reflection, transmission, and dissipation of incident waves by a rectangular porous block using the method of matched velocity potential. Mendez and Losada [54] developed a second-order perturbation method for solving the dispersion relation - this

method is still being used by many researchers. Zhu [100] considered the propagation of waves within a porous medium placed on an undulating sea-bed and used refraction-diffraction equations in order to investigate reflection and damping. Das and Bora [27, 26, 25], in a number of works, studied water wave interaction with a vertical porous structure of rectangular shape placed on an elevated impermeable horizontal bottom and also on a multi-step bottom. Singla et al. [81] examined oblique water wave scattering by a floating porous box in finite ocean depth. They observed that the dimensions of the porous box played a very significant role in force mitigation.

Theoretical analysis of thin-type porous structures is mainly based on the theory of Chwang [20], followed by Darcy's law. He proposed a porous wavemaker theory to analyze small-amplitude water waves produced by horizontal oscillations of a vertical porous plate in the constant water depth. Yu [95] modified the Chwang's boundary condition to incorporate inertial effect of the porous medium. He analyzed the diffraction of surface gravity waves by porous breakwaters through the employment of a boundary condition for the fluid motion when the wave passed through a thin porous structure. Sahoo [72] analyzed the scattering of water waves by a surface-piercing and a fully submerged porous barrier in deep water. He employed a logarithmic singular integral equation to obtain the solution. Lee and Chwang [44] considered two-dimensional problems of scattering and radiation of small-amplitude water waves by thin vertical porous plates in finite water depth using the linearized water wave theory. They applied the eigenfunction expansion method and the least squares method to solve the boundary value problem. Sahoo et al. [73] studied the scattering of oblique incident surface waves by permeable vertical barriers in water of finite depth. Twu and Lin [90, 89] investigated the effect of a number of vertical porous plates in the reflection of small-amplitude surface waves. Many researchers (Teng et al. [87], Huang et al. [36], Liu et al. [46], Liu et al. [47]) also analyzed the wave scattering with multiple permeable barriers in different geography. Das and Bora [29] analyzed the oblique water wave interaction with two thin submerged vertical porous barriers characterized by distinct porous-effect parameters. They noticed that the maximum wave energy loss occurred when the porous barriers touched the free surface. Chanda and Bora [19, 18] extended this study for different bottom topographies.

Water wave scattering by flexible porous barrier has also been studied by many investigators. Karmakar and Soares [39, 40] investigated water wave scattering by multiple bottom-standing flexible porous barriers. Behera and Ghosh [5] investigated the scattering of waves by a flexible surface-piercing porous barrier. Koley and Sahoo [42] investigated the scattering of oblique water waves by an array of vertical partial flexible porous barriers of different configurations for both finite and infinite water depths. Sasmal and De [78] studied the problem of water wave interaction with a number of flexible porous barriers.

In coastal areas, a precise study of water wave scattering by floating structures is crucial from the perspective of protecting them. For finite depth of water, Abul-Azm and

Gesraha [2] analyzed the scattering of oblique waves by a long and stiff floating pontoon. Bhattacharjee and Soares [9] studied the oblique incident wave diffraction by a floating structure adjacent to a wall with a step-type bottom topography. They examined the hydrodynamic forces on both the structure and the wall, and the reflection coefficient, transmission coefficient and the wave elevations for various parameters. Sharma et al. [79] analyzed the oblique wave scattering by a rigid floating bridge with the consideration of a submerged rectangular and circular breakwaters along with rectangular and circular trenches. Gayathri et al. [33] solved the wave interaction problem involving oblique water waves and a floating bridge placed at some distance from a vertical permeable flexible barrier. They considered two types of barriers: a bottom-standing and a surface-piercing barriers were considered separately in their study with the conclusion that the performance of the surface-piercing barrier was more effective than the bottom-standing barrier in mitigating wave forces on the floating bridge. Sahoo et al. [70] examined the effect of a porous structure to mitigate the hydrodynamic response of an elastic plate, which was placed at a finite distance from the porous structure. Singla et al. [82] investigated the scattering of water waves by a very large floating structure with the consideration of a porous box. They studied the usefulness of the porous box in reducing the forces on the structure. Kumar et al. [43] analyzed the water wave scattering by a flexible, floating plate in the presence of a submerged bottom-mounted rectangular porous structure. Nguyen et al. [59] proposed a Finite Element-Dual Boundary Element Method (FE-DBEM) for analyzing the hydroelastic properties of a VLFS placed after a vertical perforated barrier. Sahoo et al. [71] investigated the wave scattering by an elastic plate in the presence of a bottom-standing porous structure or a surface-piercing porous structure, each considered separately, with the elastic plate placed at some distance from the sea wall.

Water wave scattering with the floating structure in the presence of current

The hydrodynamic properties of the wave interaction with floating structures can be impacted by the coupling of waves with current. Rey et al. [65] analyzed through an experimental study that, in the presence of current, reflected energy by a submerged plate was less than when there was no current. Magne et al. [50] investigated the wave scattering in the presence of a sinusoidal bottom topography under the influence of current. They observed a Doppler shift in the resonant Bragg frequency, and an enhancement in wave reflection due to the current. Huang [35] experimentally studied the impact of a steady current on the wave scattering by a vertical slotted barrier. It was observed that the current significantly increased the wave energy loss and reduced the transmission coefficient. Zhai et al. [97] employed potential theory to solve the diffraction problem of short-crested incident waves interacting with a concentric system of multiple cylinders under the influence of a uniform current, and studied the hydrodynamic properties of the

structure. Muniyappan et al. [56] reviewed the flexural gravity wave motion to investigate the relationship between the frequency and time domain problems in the presence of current. On another note, wave trapping with the consideration of current has also been studied by some researchers. Shrira and Slunyaev [80] analytically and numerically studied the nonlinear dynamics of trapped surface gravity waves due to an opposing jet current. Saha et al. [69] investigated the flexural gravity wave motion by taking into account ocean current in discussing trapping and Bragg resonance. Saha et al. [68] employed linearized water wave theory to show the existence of trapped modes due to a submerged horizontal rigid cylinder placed below a compressed ice-covered surface.

1.7 Main motivation for the current work

Many investigators have proposed various types of porous breakwaters to protect the coastal regions and construction sites. We have discussed some of the relevant works in the previous section. These structures are highly adaptable and reusable, and they may be used to develop low-cost wave attenuation and protection of systems. Due to wide range of applications of porous structures, they are generally utilized in the construction of coastal and offshore structures. Floating airports, bridges, semi-submersibles, and wave power energy conversion systems are just a few examples. A range of porous materials is used in the construction of oil rigs. Sea-cage culture is also based on the porous structures. Porous structures are used to build VLFS, such as floating airports, bridges, breakwaters, piers, docks, etc. When constructing marine structures, it is essential to consider various atmospheric factors and to accurately estimate the hydrodynamic impact on the structures. As a result, research has focused on optimizing the system to minimize substantial hydrodynamic impacts. The concept to use porous surface bodies is to reduce the impact of wave-body interaction on the body surface through the pores. Offshore wind energy, in particular, has attracted the interest of many governments seeking an alternative and reliable source of energy. South Korea has chosen to invest 9 billion dollars in the construction of a 2.5 GW offshore wind farm in the country's south west sea. As the tower height of a wind turbine increases, the foundation size must also increase, and the rotor nackle expands as the overall power generation grows. Wave forces greatly affect the substructures, making it crucial to reduce wave-induced stresses. One approach to achieve this is by using a structure with a porous surface.

The whole world went through a global oil crisis in 1970s. From then onwards, the idea of prioritising renewable energy has grown in popularity. At the same time, research and new initiatives like solar, wind, and ocean energy have also received a lot of attention. This development has made it easier to study the existing disparity between non-renewable and renewable energy sources. It was recently found that WEC (Wave

Figure 1.6: The Mutriku Wave Energy Plant (Otaola et al. [61])

Energy Converter) systems are more costly than the traditional electricity generator coal power plants. However, combining the WEC with other marine structures, such as a jetty or breakwater pier, could enhance its power. The following are the outcomes of combining a breakwater with a wave energy device over a stand-alone wave energy device (Mustapa et al., [57]):

1. Overtopping WEC-breakwater integration,
2. Oscillating water column and WEC-breakwater integration,
3. Piston-Type Porous Wave Energy Converter (PTPWEC) integration.

Figure 1.7: Siadar Wave Energy Project ([84])

"The Mutriku Wave Energy Plant" (Figure 1.6), situated in Mutriku on the northern coast of Spain between San Sebastian and Bilbao, and "Siadar Wave Energy Project" (Figure

(a) (b)

Figure 1.8: The scheme layout of the semi-circular porous breakwater; (a) breakwater structure; (b) the laying state of breakwater (Zhao et al. [98])

1.7), situated in Siadar Bay, Lewis, Scotland, are two identified current important projects in connection with breakwater integration. Another porous breakwater project involves the semi-circular breakwaters shown in Figure 1.8 and those at Miyazaki Port in Japan (Mustapa et al., [57]).

To harness offshore wind power, wind farms can be set up in any large water body, particularly in oceanic areas on the continental shelf. This wind energy can then be efficiently converted into electricity. There are numerous wind energy power resources available worldwide. The "Mar de Trafalgar", located in the sea, which runs south-west to the Gulf of Cadiz in Spain, is a notable example. Combining multiple compatible activities at a marine site can lead to more efficient use of ocean space, which is beneficial for the environment. A practical approach to investigate the economic advantages and optimized use of ocean areas through multiple compatible activities is by incorporating aquaculture within the structures of offshore wind farms. This co-location of aquaculture and wind energy production could reduce costs for both public and private sectors. The public benefits originate from the fact that a shared structural design lowers the influence on ecological services offered by the ocean area, which would otherwise require and use more space. Private benefits include cost savings obtained through common infrastructure, logistics, and operational systems. Buck and Langan [12] have addressed these topics in significant length. Sarkar and Bora [74, 75, 76, 77] investigated the hydrodynamic force due to water wave interaction with different configurations of a specific type of compound porous cylinder.

Designing a breakwater that maximizes wave reflection, minimizes transmission, and effectively dissipates energy while using minimal construction material presents a significant challenge. Numerous studies have examined different types of coastal structures, demonstrating that porous designs are highly effective at reducing wave energy, thereby

helping to regulate wave intensity in both the seaward and leeward open water areas. A practical example is the successful use of porous blocks to manage high wave impact on the Gudong and Zhuangxi Sea Dike in China's Shengli Oilfield [94]. Perforated wall breakwaters were constructed to mitigate wave impact at Dieppe, France [55] and Dalian Chemical Production Terminal, China [99].

Going by the scenario with respect to application as discussed above, in the present thesis, we are motivated to solve the scattering problems with different types of porous structures in the presence of a floating structure. Here, different types of sea-bed, such as rigid flat, rigid undulated and permeable, are considered. To protect the floating structures, various breakwaters are proposed. Since porous structures can create a tranquility zone by absorbing wave energy, both thick and thin types of porous structures are utilized in our work to mitigate wave-induced forces on the floating structures. Formulation of the boundary value problems are done by utilizing the hypothesis of linearized water wavetheory in water of finite depth. The boundary value problems related to water wave scattering with floating structures are solved using an eigenfunction expansion combined with the matching technique, due to its considerable accuracy. Therefore, mathematical problems are solved by using the standard methods of separation of variables and eigenfunction expansion. Subsequently, the required quantities, such as forces and scattering coefficients, are calculated, and these quantities are analyzed for various parameters. The results are expected to benefit researchers working in ocean engineering, especially those who study various issues related to VLFS. It is hoped that the models presented here will find precise applications in ocean and coastal engineering problems as discussed above.

1.8 Outline of the thesis

This thesis is divided into seven chapters. The present chapter deals with the basic concepts and relevant equations of the linearized theory of water waves in addition to previous major works and our motivation for doing this research. Chapters 2-6 cover the five problems studied in this research, while Chapter 7 concludes with a summary of the findings and proposes future research challenges in this area.

Chapter 2 investigates the oblique wave interaction with a floating bridge with porous walls fitted on its vertical sides by utilizing the hypothesis of linearized water wavetheory in water of finite depth. The bottom of the sea-bed is assumed to be fixed and impermeable of uniform depth. The mathematical problem is solved using the standard methods of separation of variables and eigenfunction expansion. The effect of the porous wall on force mitigation is examined and the results are compared with known results available in the literature for validation. The main objective of this work is to suggest means to be adopted for reducing wave force on the floating bridge with the assistance of a rectangular porous

wall. For mitigating waveloads on the floating bridge, the effect of various parameters, such as the width of the porous wall, porosity, friction factor, and angle of wave incidence, is studied.

Chapter 3 deals with the boundary value problem for the oblique wave interaction with a rigid floating structure which is placed in front of two vertical porous barriers with different porous-effect parameters and of different heights, in the presence of current and without current. The sea-bed is considered flat and permeable. The entire fluid region is split into five sub-domains, and the boundary value problems are set up in each of them. Utilizing the linearized water wave theory, the velocity potentials in each fluid region are obtained by employing the eigenfunction expansion method. The results of the proposed model are validated against some established results to ascertain the efficiency of the model. This study focuses on how different parameters, such as the distance between the barriers, the porous-effect parameters and the height of the barriers, influence the reflection coefficient as well as the horizontal and vertical forces. The consideration of a porous sea-bed presents a more realistic situation. The effect of such a sea-bed is analyzed. It also gives insight into the scenario when a uniform current is accounted for.

In **Chapter 4**, the interaction of oblique water waves with a floating structure placed after a porous barrier with the consideration of two types of bottom topography: (i) an elevated-type, and (ii) a trench-type, each as a separate case, is investigated. The sea-bed is considered impermeable, and the entire fluid region is split into five sub-regions in each of which relevant boundary value problems are set up. Utilizing the linearized water wave theory, the velocity potentials in each sub-region are obtained by employing the eigenfunction expansion method. This study focuses on how different parameters, such as the distance between the barrier and the floating structure, the porous-effect parameter, and the height of the barrier, influence the reflection coefficient as well as the forces acting on the floating structure. The analytical results are compared with an established result and a good agreement is observed. The main objective is to study the pattern of reflection and wave forces due to the elevation and depression of the sea-bed.

In **Chapter 5**, we examine the wave interaction with a rigid floating structure, placed after two distinct thick porous structures separated by some gap, to mitigate the wave-induced forces acting on the floating structure. The physical and mathematical consideration of the wave passing through these thick porous structures is based on the Sollitt and Cross model [83]. The problem is analyzed in finite ocean depth with a flat and impermeable sea-bed. The fluid domain, finite only in depth, is split into nine regions, and the boundary value problem associated with each region is solved by utilizing the methods of variable separable and eigenfunction expansion. The behaviour of the roots of the dispersion relation is analyzed to determine if there are situations when the eigenfunction solution fails. The energy identity is also derived. To analyze the effect of the porous breakwaters, various graphs are plotted to illustrate the reflection coefficient, transmission

coefficient, dissipation coefficient, and wave-induced forces on the floating structure. The effect of various parameters such as porosity, height, thickness and friction factor of the porous structures is analyzed. The present study concluded that a suitable arrangement of thick porous structures could efficiently mitigate the wave-induced forces acting on the floating structure.

Chapter 6 analyzes the wave interaction with a rigid floating structure, with porous walls fitted on its vertical sides, to mitigate wave-induced forces acting on the floating structure, with the consideration of a varying and impermeable sea-bed. The water waves, after interaction with the varying bottom and floating structure, are partially reflected. The fluid domain is split into nine regions, and the boundary value problem associated with each region is solved by utilizing the methods of variable separable and eigenfunction expansion. The effect of a varying bottom is examined by utilizing modified mild slope equation (MMSE). To examine the impact of the porous wall and varying bottom, various graphs are plotted to illustrate the reflection coefficient, transmission coefficient, and wave-induced forces on the floating structure. The effect of porosity, thickness, draft and friction factor of the porous wall and slope of the sea-bed is analyzed. It is observed that both reflection and transmission coefficients decrease when the sea-bed slope is milder compared to steeper slope. The horizontal and vertical forces on the floating structures is reduced when the sea-bed bottom is milder. In the presence of varying bottom, both horizontal and vertical forces acting on the floating structure are reduced compared to those on a flat bottom. The consideration of a varying bottom contributes in the stability of the floating structure.

CHAPTER 2

Oblique water wave scattering by a floating bridge fitted with a rectangular porous structure and the resulting waveload mitigation

The present work aims to study the oblique incident wave interaction by a floating bridge fitted with a rectangular porous wall with the utilization of linearized water wave theory. The bottom of the sea-bed is assumed to be fixed and impermeable of uniform depth. The mathematical problem is solved by using the standard methods of separation of variables and eigenfunction expansion. The effect of the porous wall on wave reflection and force mitigation is examined and the results are compared with known results available in the literature for validation. The main objective of this work is to suggest means to be adopted for reducing wave force on the floating bridge with the assistance of a rectangular porous wall. For mitigating waveloads on the floating bridge, the effect of various parameters, such as the width of the porous wall, porosity, friction factor, and angle of wave incidence, is studied. Simultaneously, the pattern of reflection of waves is analyzed and the effect of the porous wall is observed.

2.1 Mathematical formulation

We formulate the problem of the interaction of oblique water waves with a floating bridge which is fitted with porous wall on its vertical sides by utilizing the hypothesis of linearized water wave theory in water of finite depth. The irrotational motion of an inviscid and incompressible fluid over a flat impermeable sea-bed is assumed. A three-dimensional right-handed Cartesian coordinate system (x, y, z) is considered with the xy-plane as the horizontal plane, the positive z-axis in the upward direction, and $z = 0$ the undisturbed

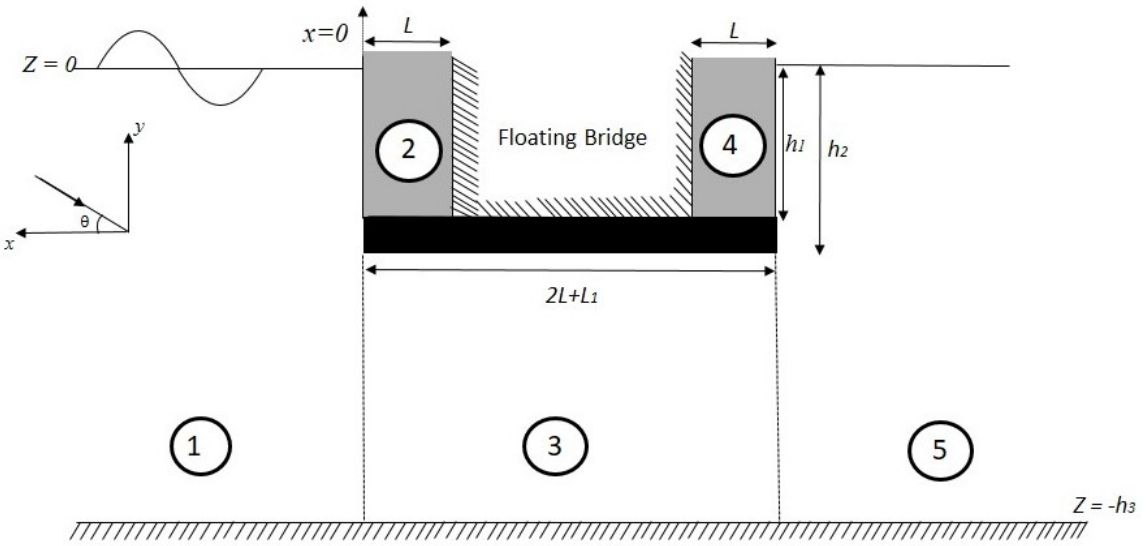

Figure 2.1: Definition sketch of the structure consisting of a rigid floating bridge fitted with a porous wall on its vertical sides.

free surface as depicted in Figure 2.1. The floating bridge under consideration is a rectangular rigid structure of finite width L_1 and draft h_1 with porous wall of width L fitted to the bridge vertically between $x = 0$ and $x = L$, and between $x = L + L_1$ and $x = 2L + L_1$. The impermeable horizontal bottom of the sea-bed is considered at $z = -h_3$ and the bottom part of the porous wall is considered at $z = -h_1$. As shown in Figure 2.1, the five regions of interest are – Region 1 (water region): $-\infty < x < 0$, $-h_3 < z < 0$; Region 2 (porous region): $0 < x < L$, $-h_1 < z < 0$; Region 3 (water region): $0 < x < 2L + L_1$, $-h_3 < z < -h_2$; Region 4 (porous region): $L + L_1 < x < 2L + L_1$, $-h_1 < z < 0$; and Region 5 (water region): $2L + L_1 < x < \infty$, $-h_3 < z < 0$. The oblique wave makes an angle θ with the x-direction.

We consider that all the motions are time harmonic along the body and also harmonic along the y-direction. We further assume that the waves propagate from the positive x-direction. Due to the wave interaction with the porous wall, some amount of waves will be reflected back. The velocity potential for the oblique water wave in each region can be considered as $\Phi_j(x, y, z, t) = \mathrm{Re}[\phi_j(x, z)e^{\mathrm{i}(k_y y - \omega t)}]$, for $j = 1, 2, 3, 4, 5$, where ω is angular frequency, $k_y = k_0 \sin\theta$, k_0 is the incident wavenumber, $\mathrm{i} = \sqrt{-1}$, and $\mathrm{Re}[\cdot]$ indicates the real quantity. The consideration of oblique waves can be seen as more general in nature since it may impinge on a structure at any inclination. The case of normal incidence can easily be obtained as a particular case from this general case. To satisfy matching conditions, the y-variation ($k_y = k_0 \sin(\theta)$) of the solution in each region must be the same (Snell's law). Therefore, the incident wave angle is uniform for all regions.

The spatial two-dimensional velocity potential ϕ_j in each fluid region satisfies the

modified Helmholtz equation

$$\left(\frac{\partial^2}{\partial x^2}+\frac{\partial^2}{\partial z^2}-k_y^2\right)\phi_j=0 \ \text{ for } \ j=1,2,3,4,5. \tag{2.1}$$

The free surface condition for Regions 1 and 5 is as follows:

$$\frac{\partial\phi_j}{\partial z}-K\phi_j=0 \ \text{ at } \ z=0, \ \ j=1,5, \tag{2.2}$$

while the condition at the mean free surface in Regions 2 and 4 is given by

$$\frac{\partial\phi_j}{\partial z}-K\gamma\phi_j=0 \ \text{ at } \ z=0, \ \ j=2,4, \tag{2.3}$$

with $K=\omega^2/g$ where g is the gravitational constant and $\gamma=m+\mathrm{i}f$ is the dimensionless porous impedance parameter where m and f, respectively, represent the inertial coefficient and the linearized friction factor as in [28]. Further, Regions 2 and 4 are assumed to possess porosity ϵ. The boundary condition on the horizontal flat bottom has the form

$$\frac{\partial\phi_j}{\partial z}=0 \ \text{ at } \ z=-h_3, \ \ j=1,3,5, \tag{2.4}$$

while the boundary condition at the bottom of the porous wall is

$$\frac{\partial\phi_j}{\partial z}=0 \ \text{ at } \ z=-h_1, \ \ j=2,4. \tag{2.5}$$

The vanishing of the vertical and horizontal velocities on the rigid horizontal and vertical sides of the floating bridge implies the following conditions:

$$\frac{\partial\phi_j}{\partial x}=0 \ \text{ at } \ x=L \ \text{ and } \ L+L_1, \ \ -h_1<z<0 \ \text{ for } \ j=2,4, \tag{2.6}$$

$$\frac{\partial\phi_3}{\partial z}=0 \ \text{ at } \ z=-h_2, \ \ 0<x<2L+L_1, \tag{2.7}$$

$$\frac{\partial\phi_j}{\partial x}=0 \ \text{ at } \ x=0 \ \text{ and } \ 2L+L_1, \ \ -h_2<z<-h_1 \ \text{ for } \ j=1,5. \tag{2.8}$$

The continuity of pressure and mass flux across the vertical boundaries $x=0$ and $x=2L+L_1$ gives the following matching conditions:

$$\phi_1=\gamma\phi_2 \ \text{ at } \ x=0, \ \ -h_1<z<0, \tag{2.9}$$

$$\frac{\partial\phi_1}{\partial x}=\epsilon\frac{\partial\phi_2}{\partial x} \ \text{ at } \ x=0, \ \ -h_1<z<0, \tag{2.10}$$

$$\phi_1=\phi_3 \ \text{ at } \ x=0, \ \ -h_3<z<-h_2, \tag{2.11}$$

$$\frac{\partial\phi_1}{\partial x}=\frac{\partial\phi_3}{\partial x} \ \text{ at } \ x=0, \ \ -h_3<z<-h_2, \tag{2.12}$$

$$\phi_5 = \gamma\phi_4 \text{ at } x = 2L + L_1, \quad -h_1 < z < 0, \tag{2.13}$$

$$\frac{\partial\phi_5}{\partial x} = \epsilon\frac{\partial\phi_4}{\partial x} \text{ at } x = 2L + L_1, \quad -h_1 < z < 0, \tag{2.14}$$

$$\phi_3 = \phi_5 \text{ at } x = 2L + L_1, \quad -h_3 < z < -h_2, \tag{2.15}$$

$$\frac{\partial\phi_3}{\partial x} = \frac{\partial\phi_5}{\partial x} \text{ at } x = 2L + L_1, \quad -h_3 < z < -h_2. \tag{2.16}$$

2.2 Method of solution

The solutions of the above boundary value problems are obtained by using eigenfunction expansion for the velocity potentials through the utilization of separation of variables method to equation (2.1) and then applying the boundary conditions on the rigid horizontal and vertical sides of the floating bridge. The continuity of mass flux and pressure is then used to match the solutions across the boundaries. Subsequently, a system of algebraic equation is obtained to evaluate the unknown coefficients appearing in the expressions of the velocity potentials. The set of algebraic equations for the unknown coefficients is solved by standard matrix techniques. After that, we can calculate the required quantities such as the reflection coefficient and wave forces.

In order to achieve our objective, we first find the velocity potentials in all sub-regions. In Region 1, the velocity potential can be obtained as

$$\phi_1(x,z) = e^{\mathrm{i}q_0 x}Z_{1,0}(k_0,z) + \sum_{n=0}^{\infty} R_n e^{-\mathrm{i}q_n x}Z_{1,n}(k_n,z), \tag{2.17}$$

where R_0 is the unknown complex reflection coefficient along with the unknowns R_n; and $Z_{1,n}(k_n,z)$ and q_n are, respectively, given by

$$Z_{1,n}(k_n,z) = \frac{\cosh(k_n(z+h_3))}{\cosh(k_n h_3)}, \quad n = 0,1,2,...,$$
$$q_n = \sqrt{k_n^2 - k_y^2}.$$

In above, k_0 is a real root and k_n's, for $n \geq 1$, are the purely imaginary roots of the dispersion relation given by [15]

$$k\tanh(kh_3) - K = 0.$$

In Region 2, the horizontal impermeable bottom is considered at $z = -h_1$. Using separation of variables technique and utilizing the boundary conditions, the general term of the scattered velocity potential takes the following form:

$$\phi_2^n(x,z) = (A_n^\star\cos(p_n x) + B_n^\star\sin(p_n x))Z_{2,n}(\mu_n,z),$$

where $A_n^\star$ and $B_n^\star$ are the unknown coefficients, and $Z_{2,n}(\mu_n, z)$ and p_n are, respectively, given by

$$Z_{2,n}(\mu_n, z) = \frac{\cosh(\mu_n(z+h_1))}{\cosh(\mu_n h_1)}, \quad n = 0, 1, 2, \ldots,$$
$$p_n = \sqrt{\mu_n^2 - k_y^2}.$$

Here, μ_n's are the complex roots of the dispersion relation [54]

$$\mu \tanh(\mu h_1) - K\gamma = 0.$$

Boundary condition (2.6) gives $B_n^\star = A_n^\star \tan(p_n L)$ and the scattered potential $\phi_2(x, z)$ can be expressed as

$$\phi_2(x, z) = \sum_{n=0}^{\infty} \phi_2^n(x, z) = \sum_{n=0}^{\infty} A_n \cos(p_n(L - x)) Z_{2,n}(\mu_n, z), \tag{2.18}$$

where $A_n = A_n^\star / \cos\ p_n L$.
In Region 3, the velocity potential has the form

$$\phi_3(x, z) = \sum_{n=0}^{\infty} \left(C_n \frac{\cosh(s_n x)}{\cosh(s_n b)} + D_n \frac{\sinh(s_n x)}{\sinh(s_n b)} \right) Z_{3,n}(r_n, z), \tag{2.19}$$

where C_n and D_n are the unknown coefficients, and $Z_{3,n}(r_n, z)$ and s_n are, respectively, given by

$$Z_{3,n}(r_n, z) = \cos(r_n(z + h_3)), \quad n = 0, 1, 2, \ldots,$$
$$s_n = \sqrt{r_n^2 + k_y^2},$$

with $r_n = n\pi/(h_3 - h_2)$ and $b = (2L + L_1)/2$.
The velocity potentials in Regions 4 and 5 are, respectively, given by

$$\phi_4(x, z) = \sum_{n=0}^{\infty} E_n \cos(p_n(L + L_1 - x)) Z_{2,n}(\mu_n, z), \tag{2.20}$$

where E_n are the unknown coefficients, and

$$\phi_5(x, z) = \sum_{n=0}^{\infty} T_n e^{\mathrm{i}q_n x} Z_{1,n}(k_n, z), \tag{2.21}$$

where T_0 is the unknown complex transmission coefficient along with the unknowns T_n. Utilization of matching conditions (2.9) and (2.11) for depths $-h_1 < z < 0$ and $-h_3 <$

$z < -h_2$, we get the following equations at $x = 0$:

$$Z_{1,0}(k_0, z) + \sum_{n=0}^{\infty} R_n Z_{1,n}(k_n, z) = \gamma \sum_{n=0}^{\infty} A_n \cos(p_n L) Z_{2,n}(\mu_n, z), \quad -h_1 < z < 0,$$
$$Z_{1,0}(k_0, z) + \sum_{n=0}^{\infty} R_n Z_{1,n}(k_n, z) = \sum_{n=0}^{\infty} C_n \left(\frac{1}{\cosh(s_n b)} \right) Z_{3,n}(r_n, z), \quad -h_3 < z < -h_2.$$

The matching conditions (2.10), (2.8) and (2.12) for depths $-h_1 < z < 0$, $-h_2 < z < -h_1$ and $-h_3 < z < -h_2$ lead to the following equations at $x = 0$:

$$\mathrm{i}q_0 Z_{1,0}(k_0, z) - \sum_{\mathrm{n}=0}^{\infty} \mathrm{i}q_n R_n Z_{1,n}(k_n, z) = \epsilon \sum_{n=0}^{\infty} p_n A_n \sin(p_n L) Z_{2,n}(\mu_{\mathrm{n}}, z), \quad -h_1 < z < 0,$$
$$\mathrm{i}q_0 Z_{1,0}(k_0, z) - \sum_{\mathrm{n}=0}^{\infty} \mathrm{i}q_n R_n Z_{1,n}(k_n, z) = 0 \ \text{ at } \ x = 0, \quad -h_2 < z < -h_1,$$
$$\mathrm{i}q_0 Z_{1,0}(k_0, z) - \sum_{\mathrm{n}=0}^{\infty} \mathrm{i}q_n R_n Z_{1,n}(k_n, z) = \sum_{n=0}^{\infty} s_n \left(\frac{D_n}{\sinh(s_n b)} \right) Z_{3,n}(r_n, z), \quad -h_3 < z < -h_2.$$

The matching conditions (2.13) and (2.15) for depths $-h_1 < z < 0$ and $-h_3 < z < -h_2$ give rise to the following equations at $x = 2L + L_1$:

$$\gamma \sum_{n=0}^{\infty} E_n \cos(p_n L) Z_{2,n}(\mu_n, z) = \sum_{n=0}^{\infty} T_n e^{\mathrm{i}q_n(2L+L_1)} Z_{1,n}(k_n, z), \quad -h_1 < z < 0,$$
$$\sum_{n=0}^{\infty} \left(C_n \frac{\cosh(s_n x)}{\cosh(s_n b)} + D_n \frac{\sinh(s_n x)}{\sinh(s_n b)} \right) Z_{3,n}(r_n, z) = \sum_{n=0}^{\infty} T_n e^{\mathrm{i}q_n(2L+L_1)} Z_{1,n}(k_n, z), \quad -h_3 < z < -h_2.$$

Similarly, the matching conditions (2.14), (2.8) and (2.16) for depths $-h_1 < z < 0$, $-h_2 < z < -h_1$ and $-h_3 < z < -h_2$ give the following equations at $x = 2L + L_1$:

$$\sum_{n=0}^{\infty} \mathrm{i}q_n T_n \mathrm{e}^{\mathrm{i}q_n(2L+L_1)} Z_{1,n}(k_n, z) = -\epsilon \sum_{n=0}^{\infty} E_n \sin(p_n L) Z_{2,n}(\mu_{\mathrm{n}}, z), \quad -h_1 < z < 0,$$
$$\sum_{n=0}^{\infty} \mathrm{i}q_n T_n \mathrm{e}^{\mathrm{i}q_n(2L+L_1)} Z_{1,n}(k_n, z) = 0, \quad -h_2 < z < -h_1,$$
$$\sum_{n=0}^{\infty} \mathrm{i}q_n T_n \mathrm{e}^{\mathrm{i}q_n x} Z_{1,n}(k_n, z) = \sum_{n=0}^{\infty} s_n \left(\frac{\sinh(s_n x)}{\cosh(s_n b)} C_n + \frac{\cosh(s_n x)}{\sinh(s_n b)} D_n \right) Z_{3,n}(r_n, z), \quad -h_3 < z < -h_2.$$

Finally, after truncating the infinite series from all of the above expressions, we get the

following equations:

$$\sum_{n=0}^{N} \alpha_{n,m} R_n - \gamma \sum_{n=0}^{N} \left(\cos(p_n L)\beta_{n,m}\right) A_n = -\alpha_{0,m}, \tag{2.22}$$

$$\sum_{n=0}^{N} I_{n,m} R_n - \sum_{n=0}^{N} C_n \left(\frac{1}{\cosh(s_n b)}\right) J_{n,m} = -I_{0,m}, \tag{2.23}$$

$$\sum_{n=0}^{N} \left(q_n \delta_{n,m}\right) R_n - \mathrm{i}\epsilon \sum_{n=0}^{N} \left(p_n \sin(p_n L)\beta_{\mathrm{n,m}}\right) A_n - \mathrm{i} \sum_{n=0}^{N} \left(\frac{s_n}{\sinh(s_n b)} J_{n,m}\right) D_n = q_0 \delta_{0,m}, \tag{2.24}$$

$$\sum_{n=0}^{N} \left(\gamma \cos(p_n L)\beta_{n,m}\right) E_n - \sum_{n=0}^{N} \left(e^{\mathrm{i}q_n(2L+L_1)} \alpha_{n,m}\right) T_n = 0, \tag{2.25}$$

$$\sum_{n=0}^{N} \left(\frac{\cosh(s_n(2L+L_1))}{\cosh(s_n b)} J_{n,m}\right) C_n + \sum_{n=0}^{N} \left(\frac{\sinh(s_n(2L+L_1))}{\sinh(s_n b)} J_{n,m}\right) D_n - \sum_{n=0}^{N} \left(e^{\mathrm{i}q_n(2L+L_1)} I_{n,m}\right) T_n = 0 \tag{2.26}$$

$$\sum_{n=0}^{N} \left(\mathrm{i}\epsilon p_n \sin\left(p_n L\right) \beta_{n,m}\right) E_n - \sum_{n=0}^{N} \mathrm{i}s_n \left(\frac{\sinh(s_n(2L+L_1))}{\cosh(s_n b)} C_n + \frac{\cosh(s_n(2L+L_1))}{\sinh(s_n b)} D_n\right) J_{n,m} - (q_m a_m e^{\mathrm{i}q_m(2L+L_1)}) T_m = 0, \tag{2.27}$$

where

$$\alpha_{n,m} = \int_{z=-h_1}^{0} Z_{1,n}(k_n, z) Z_{1,m}(k_m, z) dz$$

$$= \frac{1}{2\cosh(k_n h_3)\cosh(k_m h_3)} \left(\frac{\sinh((k_n + k_m)h_3)}{k_n + k_m} + \frac{\sinh((k_n - k_m)h_3)}{k_n - k_m} - \frac{\sinh((k_n + k_m)(h_3 - h_1))}{k_n + k_m} - \frac{\sinh((k_n - k_m)(h_3 - h_1))}{k_n - k_m}\right),$$

$$\beta_{n,m} = \int_{z=-h_1}^{0} Z_{2,n}(\mu_n, z) Z_{1,m}(k_m, z) dz$$

$$= \frac{1}{2\cosh(\mu_n h_1)\cosh(k_m h_3)} \left(\frac{\sinh((\mu_n h_1 + k_m h_3))}{\mu_n + k_m} + \frac{\sinh(\mu_n h_1 - k_m h_3)}{\mu_n - k_m} - \frac{\sinh(k_m(h_3 - h_1))}{\mu_n + k_m} + \frac{\sinh(k_m(h_3 - h_1))}{\mu_n - k_m}\right),$$

$$I_{n,m} = \int_{z=-h_3}^{-h_2} Z_{1,n}(k_n, z) Z_{1,m}(k_m, z) dz$$
$$= \frac{1}{2\cosh(k_n h_3)\cosh(k_m h_3)} \left(\frac{\sinh((k_n + k_m)(h_3 - h_2))}{k_n + k_m} + \frac{\sinh((k_n - k_m)(h_3 - h_2))}{k_n - k_m} \right),$$

$$J_{n,m} = \int_{z=-h_3}^{-h_2} Z_{3,n}(r_n, z) Z_{1,m}(k_m, z) dz$$
$$= \frac{1}{(r_n^2 - k_m^2)} \left(\frac{r_n \sin(r_n(h_3 - h_2))\cosh(k_m(h_3 - h_2))}{\cosh(k_m h_3)} \right.$$
$$\left. + \frac{k_m \cos(r_n(h_3 - h_2))\sinh(k_m(h_3 - h_2))}{\cosh(k_m h_3)} \right),$$

$$\delta_{n,m} = \begin{cases} a_n & n = m \\ 0 & n \neq m \end{cases},$$

$$a_n = \int_{z=-h_3}^{0} Z_{1,n}(k_n, z) Z_{1,n}(k_n, z) dz$$
$$= \frac{1}{2\cosh(k_n h_3)\cosh(k_m h_3)} \left(\frac{\sinh((k_n + k_m)h_3)}{k_n + k_m} + \frac{\sinh((k_n - k_m)h_3)}{k_n - k_m} \right).$$

In order to obtain the reflection coefficient and wave forces, it is required to find the unknown coefficients R_n, A_n, C_n, D_n, E_n and T_n which can be obtained from the linear system of algebraic equations

$$\mathcal{A}\mathcal{X} = \mathcal{B}, \tag{2.28}$$

where $\mathcal{X} = [R_0, R_1, ..., R_N, A_0, A_1, ..., A_N, C_0, C_1, ..., C_N, D_0, D_1, ..., D_N, E_0, E_1, ..., E_N, T_0, T_1, ..., T_N]^t$, $\mathcal{A}$ is the coefficient matrix of size $(6N + 6)$ and $\mathcal{B}$ is the right hand column vector. This gives us the coefficients required for a full-wave solution. In other words, we mathematically develop the full-wave solution for the considered problem. However, for focusing on the plane-wave solution which corresponds to the most effective propagating mode, we ignore all the infinite summations and consider only the terms corresponding to $n = 0$, that is, the plane wave approximation as in [23]. We do not focus on $n \geq 1$ which corresponds to the evanescent modes. Once the unknown coefficients are obtained, we can go ahead with determining the required quantities, viz., the reflection coefficients and the wave forces.

Having obtained the expressions for the velocity potentials, the complex-valued horizontal force X_{hf} and vertical force Y_{vf} acting on the floating bridge can be determined

by using the formulas as in [9]:

$$X_{hf} = \mathrm{i}\rho\omega \int_{-h_1}^{0} \phi_2 (L, z)\, dz, \tag{2.29}$$

$$Y_{vf} = \mathrm{i}\rho\omega \int_{0}^{2L+L_1} \phi_3 (x, -h_2)\, dx. \tag{2.30}$$

Basically, the complex-valued horizontal force and vertical force are the integrals of the pressure obtained from the linearized Bernoulli's equation. Based on what is considered in [9], for computational purpose, the horizontal and vertical forces X_{hf} and Y_{vf} can be expressed in the non-dimensional form as

$$F_h = \frac{|X_{hf}|}{\rho g A b}, \quad F_v = \frac{|Y_{vf}|}{\rho g A b}, \tag{2.31}$$

where $b = (2L + L_1)/2$ m, ρ is the density of water and $A = 1$ m is the amplitude of the incident wave.

2.3 Validation

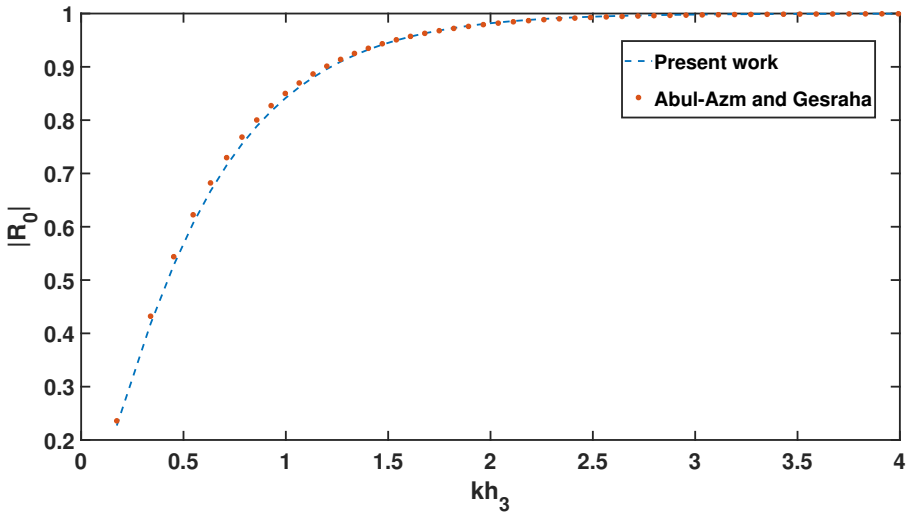

Figure 2.2: Validation of the present work with that of Abul-Azm and Gesraha [2] in the absence of the porous wall with $\theta = 0^0$, $L_1/2h_3 = 1$ and $h_1/h_3 = 0.25$.

Before presenting results based on the analytical solutions of our work, it is deemed suitable to validate our result against some similar and established result. In this direction, we take up the problem of Abul-Azm and Gesraha [2] by making some assumptions so that both models become similar. Figure 2.2 shows the plot of the reflection coefficient against the dimensionless wavenumber for both works. It is observed that the reflection coefficient

associated with the floating bridge in the absence of the porous wall (the particular case of the present model) gives the same pattern as in [2]. Figure 2.2 reveals that the current result matches with that of [2], showing that the present model is reasonably accurate and can be used for further investigation.

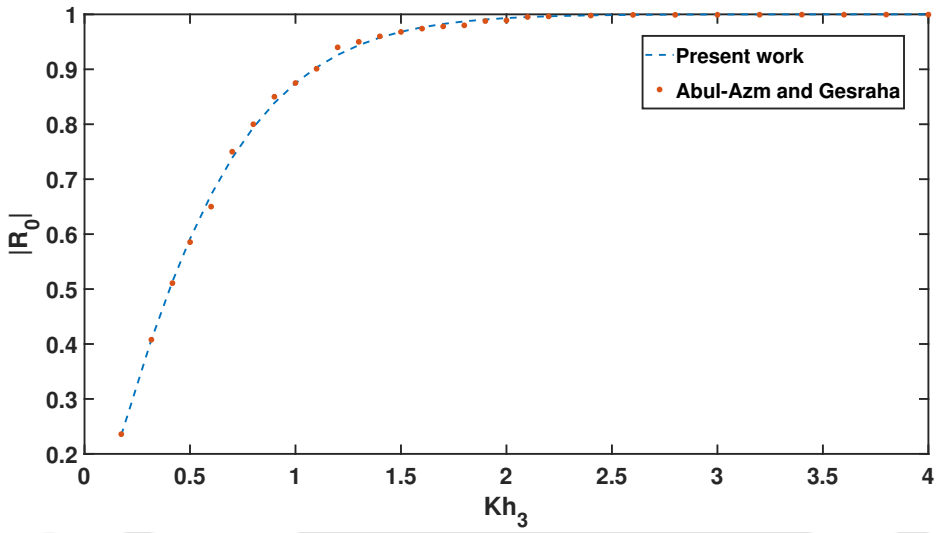

(a)

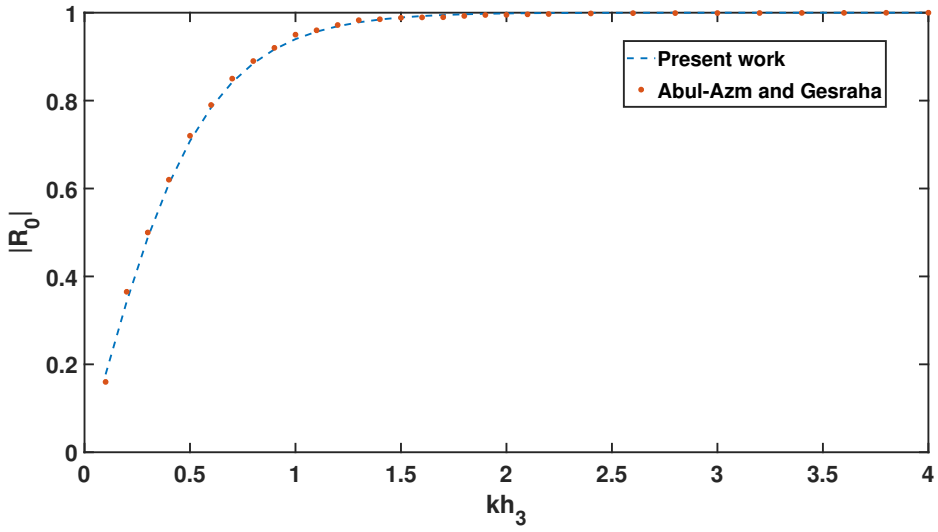

(b)

Figure 2.3: Validation of the present work with that of Abul-Azm and Gesraha [2] in the absence of the porous wall with $L_1/2h_3 = 1$ and $h_1/h_3 = 0.25$; for (a) $\theta = 30^0$, (b) $\theta = 60^0$.

Since the work in [2] presented the reflection coefficient for three angles, namely, $\theta = 0^0, 30^0, 60^0$, we further compare our reflection coefficient for the angles $\theta = 30^0, 60^0$ against their corresponding results, as can be seen in Figure 2.3. Matching of these results strengthens the validity of the present model to a large extent.

2.4 Results and discussion

Going ahead, it is now attempted to establish the effect of the porous wall in reducing the waveload on the floating bridge. For solving the system of linear equations given by (2.28), MATLAB is used. In order to compute various results, some specific values of the parameters are considered: the gravitational constant $g = 9.81$ m/s^2; the water depth $h_3 = 15$ m; the draft of the bridge $h_1 = 3$ m; $h_2 = 3.5$ m; the incident wave angle $\theta = 30°$; the porous impedance parameter $\gamma = 1 + \mathrm{i}$; the porosity $\epsilon \in [0.5, 0.7]$; the width of the porous wall $L = 1$ m; the width of the floating bridge $L_1 = 2$ m. These values of the parameters are kept fixed unless otherwise stated. The reflection coefficient and hydrodynamic forces can then be computed and assessed.

2.4.1 Effect of the porous wall in reflecting waves

In this subsection, the role of the porous wall in reflecting or damping the waves is studied.

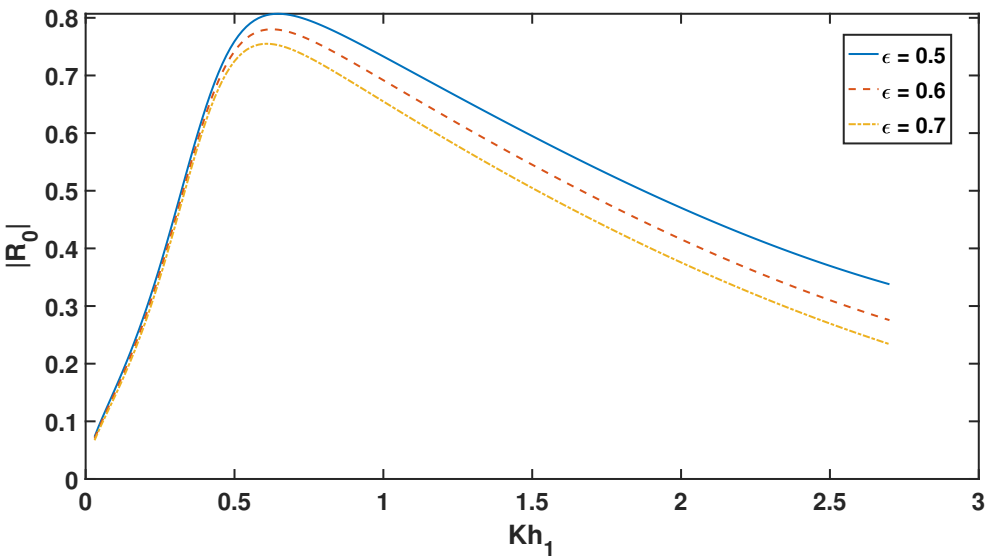

Figure 2.4: Variation of $|R_0|$ against Kh_1 for different porosity ϵ with $h_1 = 3$ m, $h_2 = 3.5$ m, $h_3 = 15$ m, $L = 1$ m, $L_1 = 2$ m and $\theta = 30°$

Figure 2.4 illustrates the effect of porosity on the reflection coefficient against the wavenumber. It can be noticed that reflection coefficient $|R_0|$ has an increasing trend as wavenumber Kh_1 increases, and it starts decreasing with a further increase of the wavenumber for approximately $Kh_1 > 0.5$. It also shows that, for relatively long wave ($Kh_1 < 0.4$), the value of the reflection coefficient is the same for all the values of porosity, but as the value of wavenumber increases, the porosity affects the reflection coefficient. It can be noted that, as the porosity is increased, the value of reflection coefficient $|R_0|$ decreases because, for higher values of the porosity, the wave mostly passes through the

porous wall. Therefore, we get lower reflection coefficient. Here, for $\epsilon = 0.7$, we get the minimum value of the reflection coefficient.

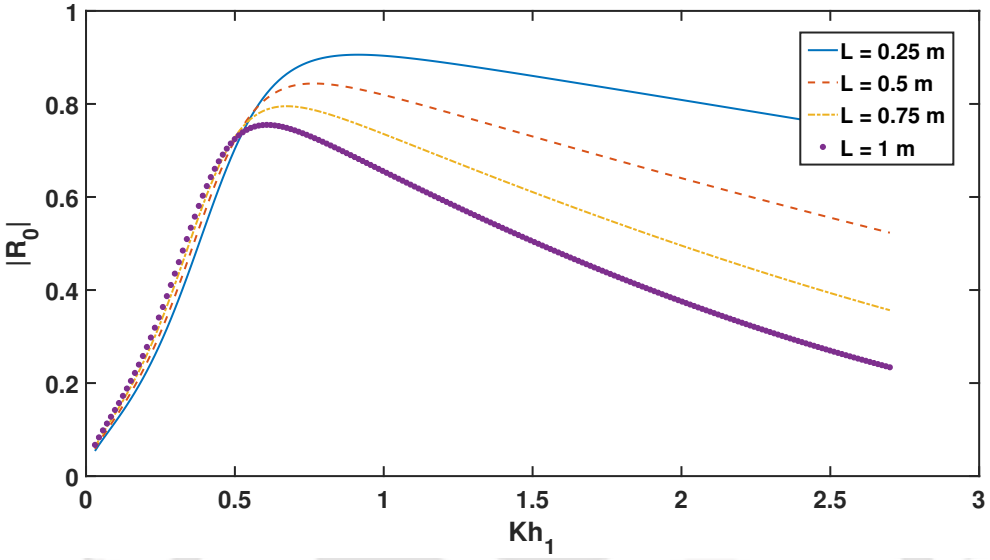

Figure 2.5: Variation of $|R_0|$ against Kh_1 for different width L of the porous wall with $\epsilon = 0.7$, $h_1 = 3$ m, $h_2 = 3.5$m, $h_3 = 15$ m, $L_1 = 2$ m and $\theta = 30°$

Figure 2.5 depicts the effect of the wavenumber on the reflection coefficient for different widths of the porous wall. It is noted that, for relatively long wave ($Kh_1 < 0.4$), there is a minor difference in the reflection coefficient corresponding to the width of the porous wall, but as the wavenumber increases, lower values in reflection are observed for higher values of the width of the porous wall. It is also observed that, as the width of the porous wall increases, the reflection coefficient decreases. It is justified since, as the width of the porous wall is increased, the waves are mostly absorbed by the porous wall and therefore, we get lower reflection coefficient.

In Figure 2.6, we plot reflection coefficient $|R_0|$ against wavenumber Kh_1 corresponding to different values of the incident wave angle. Here, we consider four different incident angles, viz., $\theta = 0°$, $\theta = 10°$, $\theta = 20°$ and $\theta = 30°$. It is observed that, as the wavenumber increases, the reflection coefficient increases, but a further increase in the wavenumber leads to lower reflection coefficient. For relatively long waves ($Kh_1 < 0.5$), the incident angle does not affect the reflection coefficient, but for shorter waves, the impact of θ on the reflection is significant. As the incident angle increases, lower reflection coefficient is observed. At $\theta = 30°$, we get the minimum reflection compared to other values of the incident wave angle.

In Figure 2.7, we plot graphs of reflection coefficient $|R_0|$ against incident wave angle θ for different values of the porosity. It is observed that, for the highest value of porosity ($\epsilon = 0.7$), the reflection is minimum because the waves mostly pass through the porous wall. The reflection coefficient decreases corresponding to increasing values of incident

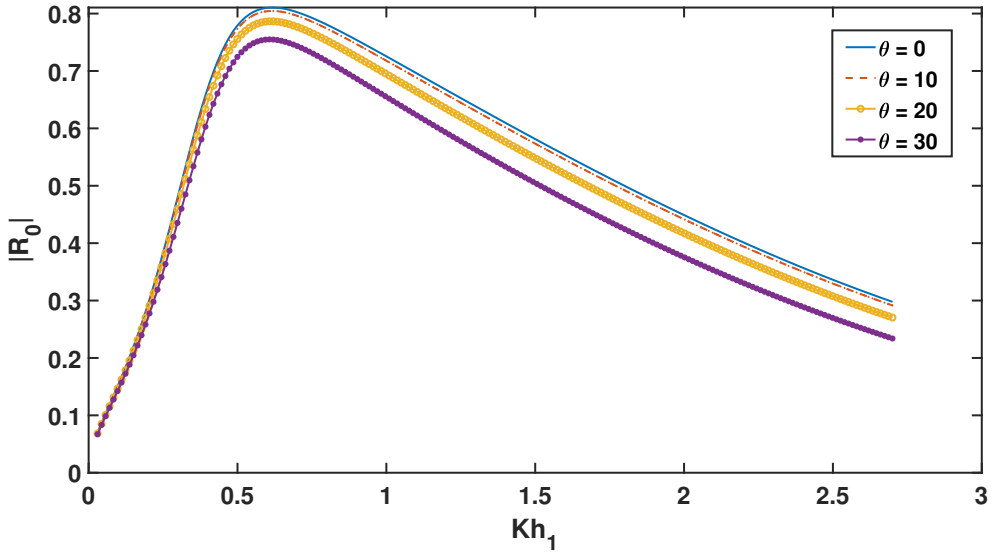

Figure 2.6: Variation of $|R_0|$ against Kh_1 for different incident wave angle θ with $\epsilon = 0.7$, $h_1 = 3$ m, $h_2 = 3.5$m, $h_3 = 15$ m, $L = 1$ m and $L_1 = 2$ m

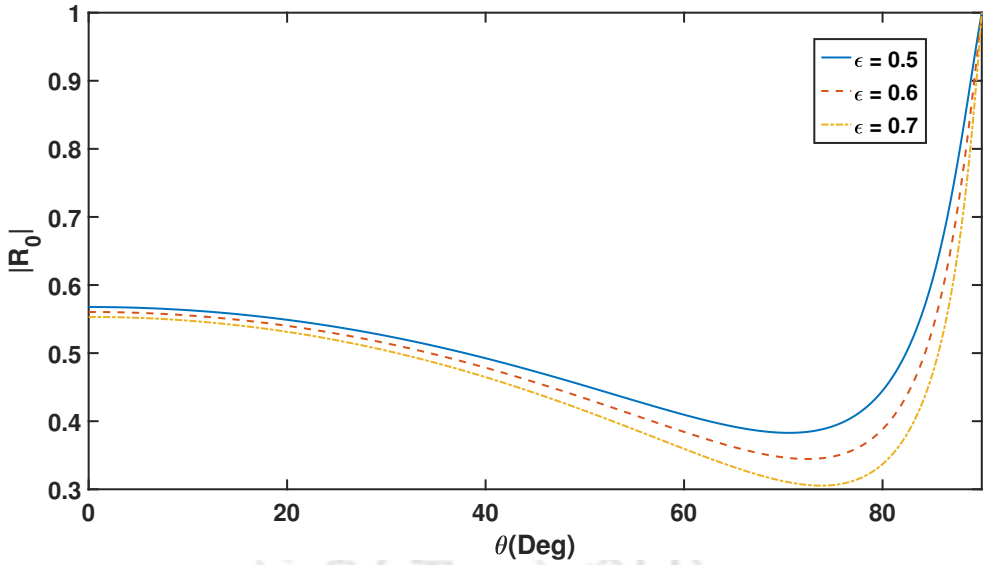

Figure 2.7: Variation of $|R_0|$ against θ for different porosity ϵ with $h_1 = 3$ m, $h_2 = 3.5$ m, $h_3 = 15$ m, $L = 1$ m and $L_1 = 2$ m

angle θ. After reaching the minimum value, all graphs of $|R_0|$ start increasing before converging to each other and reach $|R_0| = 1$ at $\theta = 90°$. This can be justified since, at $\theta = 90°$, the wave is tangential to the porous wall and therefore, there is no spike inside the porous wall which results in full reflection.

Figure 2.8 displays the effect of the draft of the floating bridge on the reflection coefficient where reflection coefficient $|R_0|$ is plotted against incident wave angle θ. Here also, we can observe that, as the incident angle increases, the reflection coefficient decreases, and after reaching the minimum value, the reflection coefficient starts to increase up to

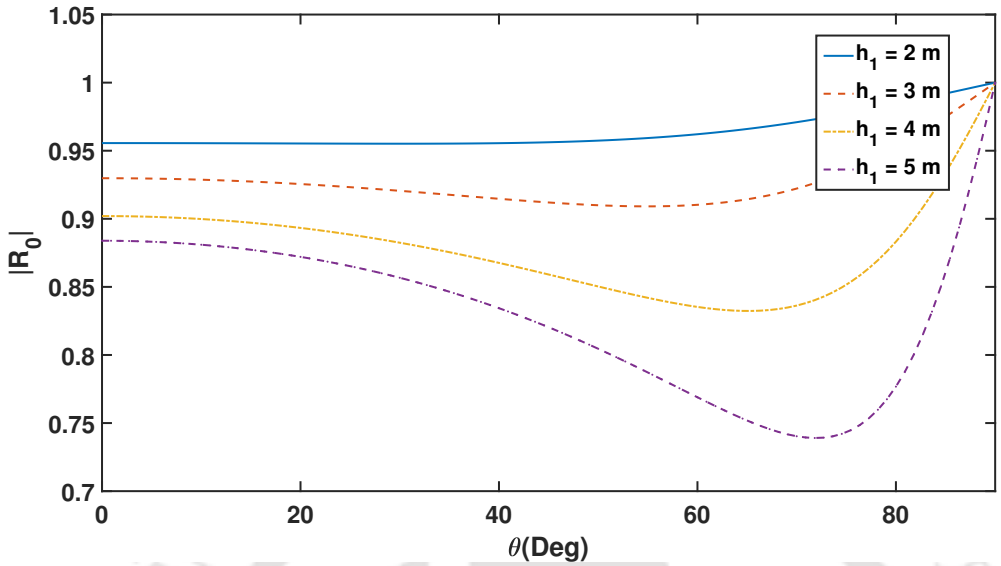

Figure 2.8: Variation of $|R_0|$ against θ for different draft h_1 with $\epsilon = 0.7$, $h_2 = h_1 + 0.5$ m, $h_3 = 15$ m, $L = 1$ m and $L_1 = 2$ m

$|R_0| = 1$. It is an implication that the porous wall with a large draft gives a lower reflection coefficient which is an obvious fact since the porous wall with a large draft absorbs most of the waves. Therefore, we get a lower reflection coefficient. Here, for $h_1 = 5$ m, we get the minimum reflection and for $h_1 = 2$ m, we observe the maximum reflection.

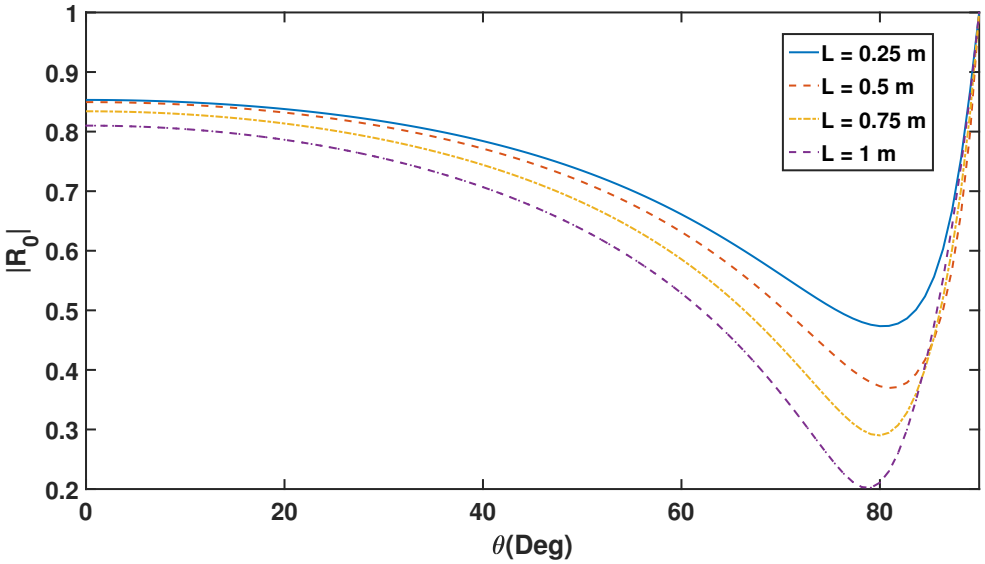

Figure 2.9: Variation of $|R_0|$ against θ for different width L of the porous wall with $\epsilon = 0.7$, $h_1 = 3$ m, $h_2 = 3.5$ m, $h_3 = 15$ m and $L_1 = 2$ m

Figure 2.9 shows the effect of incident angle θ on reflection coefficient $|R_0|$ for various widths of porous wall. With an increase in the incident angle, the reflection coefficient decreases and attains its lowest value. After reaching the minimum value, $|R_0|$ starts

increasing up to $|R_0| = 1$ at $\theta = 90°$. Here, it can be observed that, as the width of the porous wall is increased, we get lower reflection coefficient. This happens because, when the width of the porous wall is increased, more waves are absorbed by the porous wall resulting in lower reflection coefficient. Here, for $L = 1$ m, we get the minimum reflection coefficient.

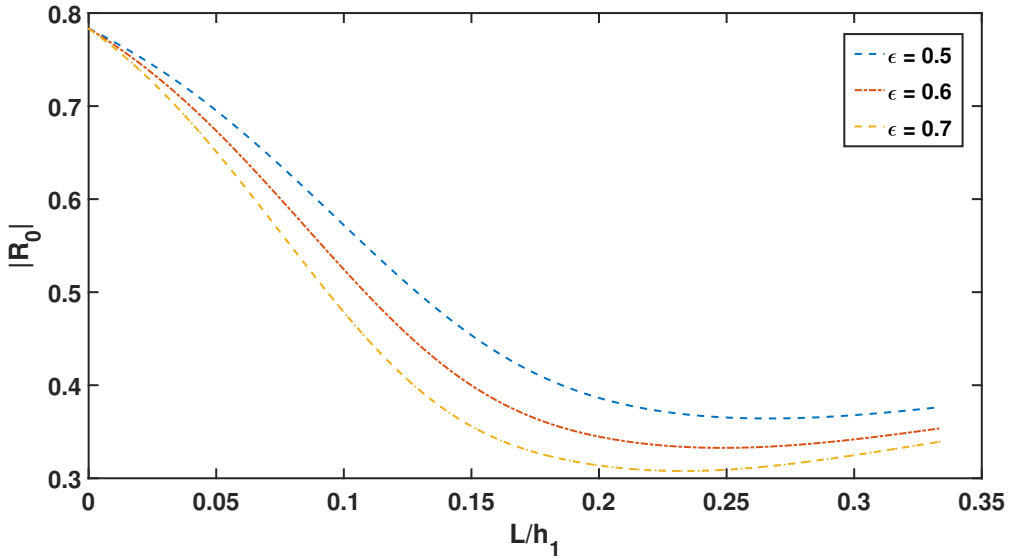

Figure 2.10: Variation of $|R_0|$ against non-dimensional width L/h_1 of the porous wall for different values of the porosity with $h_1 = 3$ m, $h_2 = 3.5$ m, $h_3 = 15$ m, $L_1 = 2$ m and $\theta = 30°$

Figure 2.10 depicts the effect of the porosity on the reflection coefficient when reflection coefficient $|R_0|$ is plotted against different values of dimensionless width L/h_1 of the porous wall. We notice that, with increasing porosity values, lower values of the reflection coefficient are observed. Here, for $\epsilon = 0.7$, the lowest reflection coefficient value is obtained. It is also observed that, as the non-dimensional width of the porous wall is increased, the value of the reflection coefficient starts decreasing because, as the width of the porous wall increases, the porous wall absorbs more waves. Therefore, the minimum in reflection is obtained.

We also study the effect of friction factor f on reflection coefficient $|R_0|$. Figure 2.11 shows the graph of $|R_0|$ against non-dimensional width L/h_1 of the porous wall. It is observed that, as the value of friction factor f is increased, the value of reflection coefficient $|R_0|$ decreases. This is what is expected since friction always introduces damping.

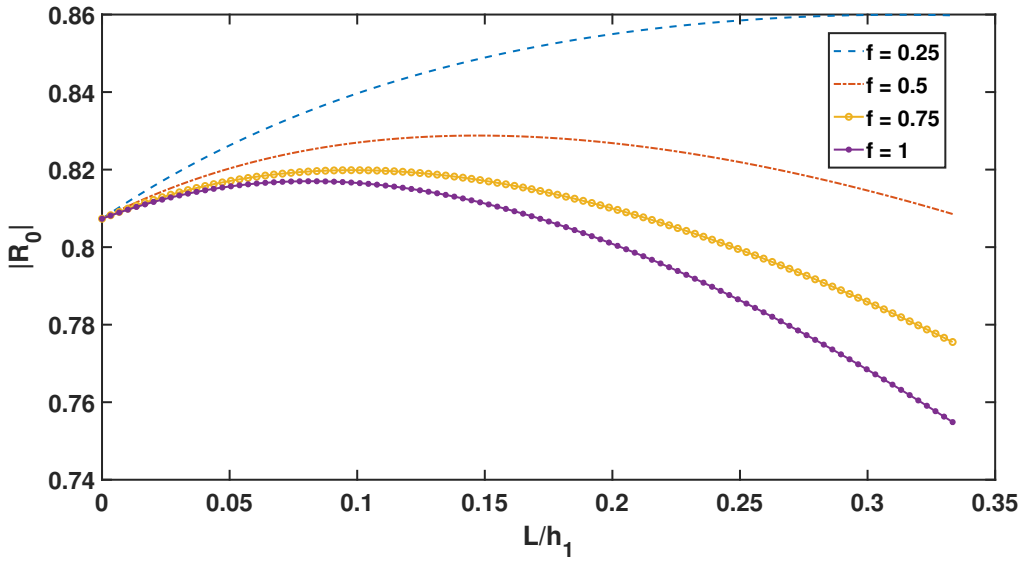

Figure 2.11: Variation of $|R_0|$ against non-dimensional width L/h_1 of the porous wall for different friction factor f with $\epsilon = 0.7$, $h_1 = 3$ m, $h_2 = 3.5$ m, $h_3 = 15$ m, $L_1 = 2$ m and $\theta = 30°$

2.4.2 Effect of the porous wall in mitigating forces on the floating bridge

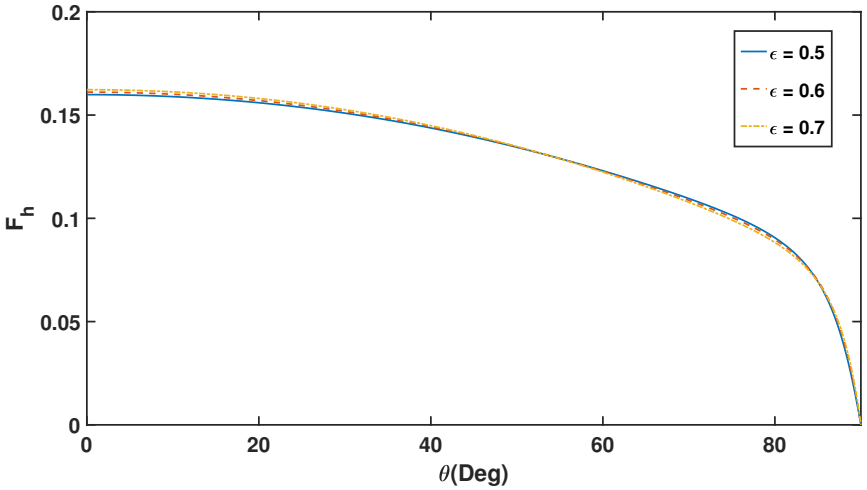

Figure 2.12: Variation of horizontal force F_h against θ for different porosity ϵ with $h_1 = 3$ m, $h_2 = 3.5$ m, $h_3 = 15$ m, $L = 1$ m and $L_1 = 2$ m

Now, we plot horizontal force F_h against incident wave angle θ for different porosity values. In Figure 2.7, the reflection is plotted against the incident angle. The horizontal force in Figure 2.12, similar to Figure 2.7, is plotted. Here, we also consider the same range of angles as in Figure 2.7. It is observed that the value of the porosity, which returns a higher value of the reflection, turns out to cause less load on the bridge and the other

way around. At $\theta = 90°$, we have $F_h = 0$ since at $\theta = 90^0$, the value of the reflection coefficient is 1.

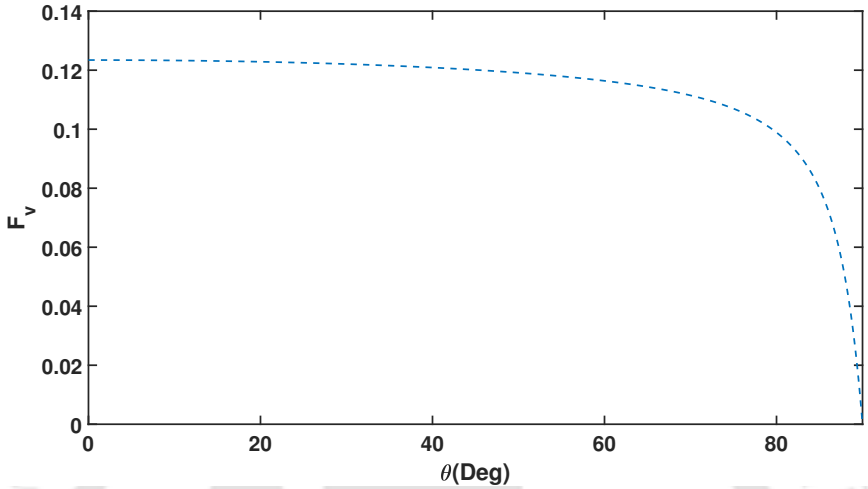

Figure 2.13: Variation of vertical force F_v against θ with $\epsilon = 0.7$, $h_1 = 3$ m, $h_2 = 3.5$ m, $h_3 = 15$ m, $L = 1$ m and $L_1 = 2$ m

The vertical force is plotted against the incident wave angle in Figure 2.13. As θ increases, the vertical force acting on the floating bridge decreases monotonically, and at $\theta = 90°$, we have $F_v = 0$ because at $\theta = 90^0$, the reflection is full. From Figures 2.12 and 2.13, we observe that the magnitude of the horizontal force is less than the vertical force.

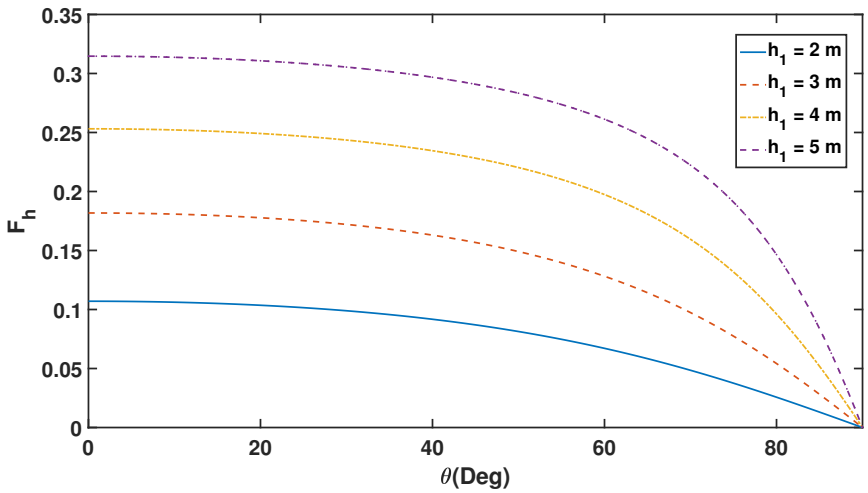

Figure 2.14: Variation of horizontal force F_h against θ for different draft h_1 with $\epsilon = 0.7$, $h_3 = 15$ m, $L = 1$ m, $L_1 = 2$ m and $\theta = 30°$

Figure 2.14 shows the graph of the horizontal force on the floating bridge plotted against the incident wave angle corresponding to different values of draft h_1 of the bridge. The horizontal force decreases monotonically as the incident wave angle increases from 0°

to 90°, and at $\theta = 90°$, we have $F_h = 0$. It is also observed that, as draft h_1 increases, the floating bridge experiences higher horizontal force since a porous wall with a large draft absorbs more waves which enhances the force at $x = L$. Here, for $h_1 = 5$m, we get the highest value of the horizontal force.

2.5 Conclusions

We have carried out a complete analysis of a problem in which an oblique wave strikes a floating bridge fitted with a porous wall on its two vertical sides. The sea-bed was assumed to be fixed and impermeable. The method of eigenfunction expansion was used to determine velocity potential in each region with the help of the variable-separable method to the modified Helmholtz equation. We had evaluated the reflection coefficient and hydrodynamic forces for various parameter values. The impact of the porosity of the porous layer on reflection and wave forces had been thoroughly studied. It was observed that, due to the presence of the porous wall, the wave force is reduced on the floating bridge. As porosity increases, lower values in the reflection coefficient were observed. We also observed a connection between the reflection coefficient and hydrodynamic forces on the floating bridge, that is, higher value of reflection turned out to have caused less load on the bridge. It was noted that, as incident wave angle θ increases, the value of the reflection coefficient decreases, and after that, it increases again. We also studied the impact of the friction factor on reflection; as the friction factor increases, the value of the reflection coefficient decreases. All these observations lead to the selection of suitable values of various parameters so as to control the reflection and forces on the floating bridge as per requirement. We validated our result with that of Abul-Azm and Gesraha [2] by making some assumptions and we found very good agreement. This shows that the present model is reasonably accurate. This study was expected to help researchers and designers in mitigating wave forces so that the bridge or a similar structure gets a safer environment in its vicinity. It also depicts a clear scenario with respect to the wave scattering pattern.

CHAPTER 3

Impact of two vertical porous barriers in the reflection of water waves and mitigation of wave forces on a rigid floating structure with consideration of a uniform current over a porous sea-bed

This work takes up the boundary value problem for the oblique wave interaction with a rigid floating structure which is placed after two vertical porous barriers with different porous-effect parameters and of different heights, in the presence of current and also without current. The sea-bed is considered flat and permeable. The entire fluid region is split into five subdomains, and the boundary value problems are set up in each of them. Utilizing the linear potential theory, the velocity potentials in each fluid region are obtained by employing the eigenfunction expansion method. The study focuses on how different parameters, such as the distance between the barriers, the porous-effect parameters, the height of the barriers, the presence of the porous sea-bed and current, influence the reflection coefficient as well as the horizontal and vertical forces. The results of the present study are successfully validated against available results for verifying the effectiveness of this model which can be used for problems involving floating structures such as a floating bridge, floating airport, floating dock, or any other floating facility.

3.1 Mathematical formulation

An oblique water wave interacts with a rigid floating structure S placed after two submerged thin vertical permeable barriers B_1 and B_2, which are of different heights and not touching each other. Linear water wave theory in finite ocean depth is applied to the irrotational motion of an incompressible and non-viscous fluid. The sea-bed is considered

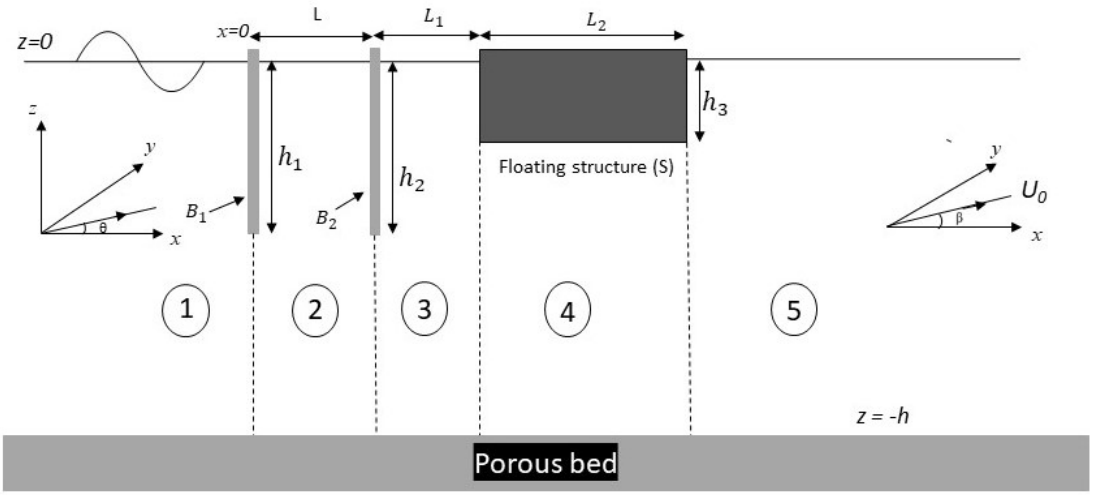

Figure 3.1: Definition sketch of the problem with the wave striking a rigid rectangular floating structure placed in front of two vertical porous barriers over a porous sea-bed.

flat and porous. We take up the work for two situations: (i) without current, (ii) with current. For case (ii), we consider a flowing current speed U_0 with components $U_0 \cos\beta$ and $U_0 \sin\beta$. The formulation is developed in the right-handed Cartesian coordinate system with the xy-plane representing the undisturbed free surface and the positive z-axis oriented in the upward direction. At $x = 0$ and $x = L$, the barriers B_1 and B_2 of heights h_1 and h_2, respectively, are erected. The rectangular rigid floating structure of finite length L_2 and with draft h_3 is considered with its distance from the second barrier as L_1 as shown in Figure 3.1. The location of the horizontal porous sea-bed is taken as $z = -h$. The whole fluid domain is split into five sub-regions as follows: Region 1 ($-\infty < x < 0$, $-h < z < 0$); Region 2 ($0 < x < L$, $-h < z < 0$); Region 3 ($L < x < L + L_1$, $-h < z < 0$); Region 4 ($L + L_1 < x < L + L_1 + L_2$, $-h < z < -h_3$) and Region 5 ($L + L_1 + L_2 < x < \infty$, $-h < z < 0$). An oblique water wave propagating from the negative x-direction is assumed to be incident at an angle θ to the x-axis. Figure 3.1 also shows a current of magnitude U_0 interacting with the wave at an angle β to the x-axis, which is relevant to problem (ii) to be taken up later.

3.1.1 Formulation for the case without current

It is assumed that all the motions are simple harmonic in time with an angular frequency ω and also along the y-direction. For an oblique water wave, for problem (i), the scattered velocity potential in each of the fluid regions can be written as $\Phi_j(x, y, z, t) = \mathrm{Re}[\phi_j(x, z)e^{\mathrm{i}(k_y y - \omega t)}]$, for $j = 1, 2, 3, 4, 5$, where $k_y = k_0 \sin\theta$, k_0 is the incident wavenumber. In each fluid region, the spatial two-dimensional velocity potential ϕ_j satisfies the

modified Helmholtz equation

$$\left(\frac{\partial^2}{\partial x^2}+\frac{\partial^2}{\partial z^2}-{k_y}^2\right)\phi_j=0. \tag{3.1}$$

The linearized free surface boundary condition in Regions 1, 2, 3 and 5 is as follows:

$$\frac{\partial \phi_j}{\partial z}-K\phi_j=0 \ \text{ at } \ z=0, \ \ j=1,2,3,5, \tag{3.2}$$

The boundary condition on the flat porous bottom has the form

$$\frac{\partial \phi_j}{\partial z}+G\phi_j=0 \ \text{ at } \ z=-h, \ \ j=1,2,3,4,5, \tag{3.3}$$

where $G=\mathrm{i}b\rho\omega/\mu$ is the porous-effect parameter of the sea-bed with b as the coefficient having dimension of length, ρ the fluid density and μ the coefficient of dynamic viscosity [16]. In general, the parameter G is a complex number that has both resistance and inertia effect as defined in [96] and is represented as $G=G_r+\mathrm{i}G_i$ where G_r and G_i, respectively, denote the real and imaginary parts. However, for convenience, we consider here the porous-effect parameter G to be a real number that implies that only the resistance effect of the sea-bed is taken into account. It may be mentioned that the works in [51], [52], and [19] also adopted such a consideration. Further, the porous sea-bed is considered only as a boundary and the fluid motion within it is not analyzed. Since the vertical and horizontal sides of the floating structure are rigid, therefore, vanishing of the vertical and horizontal velocities at the sides implies the following conditions:

$$\frac{\partial \phi_3}{\partial x}=0 \ \text{ at } \ x=L+L_1, \ \ -h_3<z<0, \tag{3.4}$$

$$\frac{\partial \phi_5}{\partial x}=0 \ \text{ at } \ x=L+L_1+L_2, \ \ -h_3<z<0, \tag{3.5}$$

$$\frac{\partial \phi_4}{\partial z}=0 \ \text{ at } \ z=-h_3, \ \ L+L_1<x<L+L_1+L_2. \tag{3.6}$$

The continuity of mass flux and pressure across the vertical boundaries $x=0$, $x=L$, $x=L+L_1$ and $x=L+L_1+L_2$ imply that the velocity potentials ϕ_j, $j=1,2,3,4,5$, satisfy the following matching conditions as applicable:

$$\frac{\partial \phi_1}{\partial x}=\frac{\partial \phi_2}{\partial x}=\mathrm{i}k_0G_1(\phi_1-\phi_2) \ \text{ at } \ x=0, \ \ -h_1<z<0, \tag{3.7}$$

$$\frac{\partial \phi_1}{\partial x}=\frac{\partial \phi_2}{\partial x} \ \text{ at } \ x=0, \ \ -h<z<-h_1, \tag{3.8}$$

$$\phi_1=\phi_2 \ \text{ at } \ x=0, \ \ -h<z<-h_1, \tag{3.9}$$

$$\frac{\partial \phi_2}{\partial x}=\frac{\partial \phi_3}{\partial x}=\mathrm{i}k_0G_2(\phi_2-\phi_3) \ \text{ at } \ x=L, \ \ -h_2<z<0, \tag{3.10}$$

$$\frac{\partial \phi_2}{\partial x} = \frac{\partial \phi_3}{\partial x} \text{ at } x = L, \ -h < z < -h_2, \tag{3.11}$$

$$\phi_2 = \phi_3 \text{ at } x = L, \ -h < z < -h_2, \tag{3.12}$$

$$\frac{\partial \phi_3}{\partial x} = \frac{\partial \phi_4}{\partial x} \text{ at } x = L + L_1, \ -h < z < -h_3, \tag{3.13}$$

$$\phi_3 = \phi_4 \text{ at } x = L + L_1, \ -h < z < -h_3, \tag{3.14}$$

$$\frac{\partial \phi_4}{\partial x} = \frac{\partial \phi_5}{\partial x} \text{ at } x = L + L_1 + L_2, \ -h < z < -h_3, \tag{3.15}$$

$$\phi_4 = \phi_5 \text{ at } x = L + L_1 + L_2, \ -h < z < -h_3, \tag{3.16}$$

where G_1 and G_2 are the dimensionless porous-effect parameters of the barriers B_1 and B_2, respectively.

The far-field conditions are given by

$$\phi_1 \to -\frac{\mathrm{i}g(k_0\cosh(k_0(z+h)) - G\sinh(k_0(z+h)))}{\omega(k_0\cosh(k_0h) - G\sinh(k_0h))}(e^{\mathrm{i}q_0x} + R_0e^{-\mathrm{i}q_0x}) \text{ as } x \to -\infty, \tag{3.17}$$

$$\phi_5 \to -\frac{\mathrm{i}g(k_0\cosh(k_0(z+h)) - G\sinh(k_0(z+h)))}{\omega(k_0\cosh(k_0h) - G\sinh(k_0h))}T_0e^{\mathrm{i}q_0x} \text{ as } x \to \infty, \tag{3.18}$$

where, R_0 and T_0, respectively, are the unknown reflection and transmission coefficients, $q_0 = \sqrt{k_0^2 - k_y^2}$, and k_0 is the positive real root of the dispersion relation [51]

$$K(k - G\tanh(kh)) - k(k\tanh(kh) - G) = 0. \tag{3.19}$$

3.1.2 Formulation for the case with current

Having completed the formulation for problem (i), we now proceed to formulate problem (ii). Let us define the velocity potential in this case as $\oplus(x, y, z, t) = U_0(x\cos\beta + y\sin\beta) + \tilde{\Phi}(x, y, z, t)$, where $\tilde{\Phi}(x, y, z, t) = \mathrm{Re}[\tilde{\phi}(x, z)e^{\mathrm{i}(\tilde{k}_y y - \omega t)}]$.

The kinematic boundary condition is given by

$$\frac{\partial \tilde{\phi}}{\partial z} = -\mathrm{i}(\omega - U_0\sin(\beta)k_y)\eta + U_0\cos(\beta)\frac{\partial \eta}{\partial x} \text{ at } z = 0, \tag{3.20}$$

and the dynamic boundary condition is given by

$$g\eta = -\mathrm{i}(\omega - U_0\sin(\beta)k_y)\phi + U_0\cos(\beta)\frac{\partial \tilde{\phi}}{\partial x} \text{ at } z = 0. \tag{3.21}$$

The upper free surface condition is the combination of the kinematic and the dynamic boundary conditions, and the linearized combined free surface condition is given by

$$\frac{\partial\tilde{\phi}}{\partial z} = \frac{1}{g}\left(-\mathrm{i}(\omega - U_0\sin(\beta)k_y) + U_0\cos(\beta)\frac{\partial}{\partial x}\right)^2\tilde{\phi} \ \text{ at } \ z = 0. \tag{3.22}$$

The expressions of conditions (3.3)-(3.16) remain similar with ϕ_j getting changed to $\tilde{\phi}_j$ and k to $\tilde{k}$ for problem (ii). The dispersion relation in this case takes the form

$$\begin{aligned}[\omega - U_0\tilde{k}\cos(\theta-\beta)]^2[\tilde{k} - G\tanh(\tilde{k}h)] &= (\hat{\omega})^2[\tilde{k} - G\tanh(\tilde{k}h)] \\ &= g\tilde{k}[\tilde{k}\tanh(\tilde{k}h) - G],\end{aligned} \tag{3.23}$$

where $\hat{\omega} = \omega - U_0\tilde{k}\cos(\theta-\beta)$ and $\tilde{k}$ is the root of the new dispersion relation (3.23).

The far-field conditions for this case are given by

$$\tilde{\phi}_1 \to -\frac{\mathrm{i}g(\tilde{k}\cosh(\tilde{k}(z+h)) - G\sinh(\tilde{k}(z+h)))}{\hat{\omega}(\tilde{k}\cosh(\tilde{k}h) - G\sinh(\tilde{k}h))}(e^{\mathrm{i}\tilde{q}x} + \tilde{R}_0 e^{-\mathrm{i}\tilde{q}x}) \ \text{ as } \ x \to -\infty, \tag{3.24}$$

$$\tilde{\phi}_5 \to -\frac{\mathrm{i}g(\tilde{k}\cosh(\tilde{k}(z+h)) - G\sinh(\tilde{k}(z+h)))}{\hat{\omega}(\tilde{k}\cosh(\tilde{k}h) - G\sinh(\tilde{k}h))}\tilde{T}_0 e^{\mathrm{i}\tilde{q}x} \ \text{ as } \ x \to \infty, \tag{3.25}$$

where, $\tilde{R}_0$ and $\tilde{T}_0$, respectively, are the unknown reflection and transmission coefficients and $\tilde{q} = \sqrt{\tilde{k}^2 - \tilde{k}_y^2}$.

3.2 Method of solution

For solving the boundary value problems formulated above, the separation of variables method is used to expand the eigenfunctions of the velocity potentials. Subsequently, the fact of vanishing horizontal and vertical velocities on the horizontal and vertical sides of the floating structure is utilized. The solutions are matched across the boundaries by using mass flux and pressure continuity. A set of linear algebraic equations is developed to find the unknown coefficients in the expressions of the velocity potentials. Standard matrix techniques are used for obtaining solution to this system of equations. After that, the reflection coefficient and wave forces can be calculated.

3.2.1 Full-wave solution

We first take up the problem for the case without current.

We now find the spatial velocity potentials $\phi_j(x,z),\ j = 1,2,3,4,5$ in all subregions.

The velocity potential $\phi_1(x,z)$ in Region 1 can be expressed as

$$\phi_1(x,z) = e^{\mathrm{i}q_0 x} Z_0(k_0,z) + \sum_{n=0}^{\infty} R_n e^{-\mathrm{i}q_n x} Z_n(k_n,z), \tag{3.26}$$

where R_n are the unknown complex reflection coefficients. The depth eigenfunction $Z_n(k_n,z)$ and q_n are, respectively, given by

$$Z_n(k_n,z) = -\frac{\mathrm{i}g(k_n\cosh(k_n(z+h)) - G\sinh(k_n(z+h)))}{\omega(k_n\cosh(k_nh) - G\sinh(k_nh))}, \quad n = 0,1,2,...,$$
$$q_n = \sqrt{k_n^2 - k_y^2},$$

where k_0 is the positive real root and $k_n,\ n = 1,2,3,...,$ are the purely imaginary roots of the dispersion relation (3.19).

The scattered velocity potential $\phi_2(x,z)$ in Region 2 can be obtained in the form

$$\phi_2(x,z) = \sum_{n=0}^{\infty} \left(A_n e^{\mathrm{i}q_n x} + B_n e^{-\mathrm{i}q_n x}\right) Z_n(k_n,z), \tag{3.27}$$

with the unknown coefficients A_n and B_n.

In Region 3, the velocity potential $\phi_3(x,z)$ has the following form:

$$\phi_3(x,z) = \sum_{n=0}^{\infty} \left(C_n e^{\mathrm{i}q_n x} + D_n e^{-\mathrm{i}q_n x}\right) Z_n(k_n,z), \tag{3.28}$$

with the unknown coefficients C_n and D_n.

The velocity potential $\phi_4(x,z)$ in Region 4 is as follows:

$$\phi_4(x,z) = \sum_{n=0}^{\infty} \left(E_n \frac{\cosh(s_n x)}{\cosh(s_n b)} + F_n \frac{\sinh(s_n x)}{\sinh(s_n b)}\right) Z_{4,n}(r_n,z), \tag{3.29}$$

where E_n, F_n are the unknown coefficients, $b = L_2/2$, and $Z_{4,n}(r_n,z)$ and s_n are, respectively, given by

$$Z_{4,n}(r_n,z) = -\frac{\mathrm{i}g}{\omega} r_n\cos(r_n(z+h)) - G\sin(r_n(z+h)),$$

where r_n's are the roots of the equation $r\tan(r(h-h_3)) + G = 0$ which are rapidly increasing. Therefore, we consider the smallest value of r_n, and $s_n = \sqrt{k_y^2 + r_n^2}$. In Region 5, the velocity potential $\phi_5(x,z)$ is obtained in the form

$$\phi_5(x,z) = \sum_{n=0}^{\infty} T_n e^{\mathrm{i}q_n x} Z_n(k_n,z), \tag{3.30}$$

where T_n are the unknown coefficients. Now, using the matching conditions (3.7)-(3.16), applying the orthogonality of $Z_n(k_n, z)$ and $Z_{4,n}(r_n, z)$, and after truncating the infinite series at $n = N$, we get the following system of equations:

$$\sum_{n=0}^{N} \mathrm{i}q_n\delta_{n,m}R_n + \sum_{n=0}^{N} \mathrm{i}q_n\delta_{n,m}A_n - \sum_{n=0}^{N} \mathrm{i}q_n\delta_{n,m}B_n = \mathrm{i}q_0\delta_{0,m}, \tag{3.31}$$

$$\sum_{n=0}^{N} \left(-\mathrm{i}k_0G_1A_{n,m} + B_{n,m}\right)R_n + \sum_{n=0}^{N} \left(\mathrm{i}\left(q_n + k_0G_1\right)A_{n,m} - B_{n,m}\right)A_n + \sum_{n=0}^{N} \left(\mathrm{i}\left(-q_n + k_0G_1\right)A_{n,m} - B_{n,m}\right)B_n = \mathrm{i}k_0G_1A_{0,m} - B_{0,m}, \tag{3.32}$$

$$\sum_{n=0}^{N} \left(\mathrm{i}q_ne^{\mathrm{i}q_nL}\delta_{n,m}\right)A_n - \sum_{n=0}^{N} \left(\mathrm{i}q_ne^{-\mathrm{i}q_nL}\delta_{n,m}\right)B_n - \sum_{n=0}^{N} \left(\mathrm{i}q_ne^{\mathrm{i}q_nL}\delta_{n,m}\right)C_n + \sum_{n=0}^{N} \left(\mathrm{i}q_ne^{-\mathrm{i}q_nL}\delta_{n,m}\right)D_n = 0, \tag{3.33}$$

$$\sum_{n=0}^{N} e^{\mathrm{i}q_nL}\left(\mathrm{i}\left(k_0G_2 - q_n\right)C_{n,m} + D_{n,m}\right)A_n + \sum_{n=0}^{N} e^{-\mathrm{i}q_nL}\left(\mathrm{i}\left(k_0G_2 + q_n\right)C_{n,m} + D_{n,m}\right)B_n - \sum_{n=0}^{N} e^{\mathrm{i}q_nL}\left(\mathrm{i}k_0G_2C_{n,m} + D_{n,m}\right)C_n - \sum_{n=0}^{N} e^{-\mathrm{i}q_nL}\left(\mathrm{i}k_0G_2C_{n,m} + D_{n,m}\right)D_n = 0, \tag{3.34}$$

$$\sum_{n=0}^{N} \left(e^{\mathrm{i}q_nd_1}\delta_{n,m}\right)C_n + \sum_{n=0}^{N} \left(e^{-\mathrm{i}q_nd_1}\delta_{n,m}\right)D_n - \sum_{n=0}^{N} \left(\frac{\cosh(s_nd_1)}{\cosh(s_nb)}E_{n,m}\right)E_n - \sum_{n=0}^{N} \left(\frac{\sinh(s_nd_1)}{\sinh(s_nb)}E_{n,m}\right)F_n = 0, \tag{3.35}$$

$$\sum_{n=0}^{N} \left(\mathrm{i}q_ne^{\mathrm{i}q_nd_1}\delta_{n,m}\right)C_n - \sum_{n=0}^{N} \left(\mathrm{i}q_ne^{-\mathrm{i}q_nd_1}\delta_{n,m}\right)D_n - \sum_{n=0}^{N} \left(s_n\frac{\sinh(s_nd_1)}{\cosh(s_nb)}E_{n,m}\right)E_n - \sum_{n=0}^{N} \left(s_n\frac{\cosh(s_nd_1)}{\sinh(s_nb)}E_{n,m}\right)F_n = 0, \tag{3.36}$$

$$\sum_{n=0}^{N} \left(\frac{\cosh(s_nd_2)}{\cosh(s_nb)}E_{n,m}\right)E_n + \sum_{n=0}^{N} \left(\frac{\sinh(s_nd_2)}{\sinh(s_nb)}E_{n,m}\right)F_n - \sum_{n=0}^{N} \left(e^{\mathrm{i}q_nd_2}\delta_{n,m}\right)T_n = 0, \tag{3.37}$$

$$\sum_{n=0}^{N} \left(s_n\frac{\sinh(s_nd_2)}{\cosh(s_nb)}E_{n,m}\right)E_n + \sum_{n=0}^{N} \left(s_n\frac{\cosh(s_nd_2)}{\sinh(s_nb)}E_{n,m}\right)F_n - \sum_{n=0}^{N} \left(\mathrm{i}q_ne^{\mathrm{i}q_nd_2}\delta_{n,m}\right)T_n = 0, \tag{3.38}$$

where $d_1 = L + L_1$, $d_2 = L + L_1 + L_2$ and

$$\delta_{n,m} = \begin{cases} N_n & n = m \\ 0 & n \neq m \end{cases},$$

$$N_n = \int_{z=-h}^{0} Z_n(k_n, z) Z_n(k_n, z) dz = \frac{1}{(k_n \cosh(k_n h) - G \sinh(k_n h))^2} \times$$
$$\left(\frac{k_n^2}{2} \Big(h + \frac{\sinh(2k_n h)}{2k_n} \Big) + \frac{G^2}{2} \Big(\frac{\sinh(2k_n h)}{2k_n} - h \Big) - \frac{G}{2} \Big(\cosh(2k_n h) - 1 \Big) \right),$$

$$A_{n,m} = \int_{z=-h_1}^{0} Z_n(k_n, z) Z_m(k_m, z) dz = \frac{G}{2} \Big(\cosh(k_n - k_m)h - \cosh(k_n + k_m)h$$
$$+ \cosh(k_n + k_m)(h - h_1) - \cosh(k_n - k_m)(h - h_1) \Big)$$
$$\frac{(k_n k_m + G^2)}{2(k_n + k_m)} \Big(\sinh(k_n + k_m)h - \sinh(k_n + k_m)(h - h_1) \Big)$$
$$+ \frac{(k_n k_m - G^2)}{2(k_n - k_m)} \Big(\sinh(k_n - k_m)h - \sinh(k_n - k_m)(h - h_1) \Big),$$

$$B_{n,m} = \int_{z=-h}^{-h_1} Z_n(k_n, z) Z_m(k_m, z) dz = \frac{\sinh(k_n + k_m)(h - h_1)}{2(k_n + k_m)} \Big(k_n k_m + G^2 \Big)$$
$$- \frac{G}{2} \Big(\cosh(k_n + k_m)(h - h_1) - \cosh(k_n - k_m)(h - h_1) \Big)$$
$$+ \frac{\sinh(k_n - k_m)(h - h_1)}{2(k_n - k_m)} \Big(k_n k_m - G^2 \Big),$$

$$C_{n,m} = \int_{z=-h_2}^{0} Z_n(k_n, z) Z_m(k_m, z) dz = \frac{G}{2} \Big(\cosh(k_n - k_m)h - \cosh(k_n + k_m)h$$
$$+ \cosh(k_n + k_m)(h - h_2) - \cosh(k_n - k_m)(h - h_2) \Big)$$
$$\frac{(k_n k_m + G^2)}{2(k_n + k_m)} \Big(\sinh(k_n + k_m)h - \sinh(k_n + k_m)(h - h_2) \Big)$$
$$+ \frac{(k_n k_m - G^2)}{2(k_n - k_m)} \Big(\sinh(k_n - k_m)h - \sinh(k_n - k_m)(h - h_2) \Big),$$

$$D_{n,m} = \int_{z=-h}^{-h_2} Z_n(k_n, z) Z_m(k_m, z) dz = \frac{\sinh(k_n + k_m)(h - h_2)}{2(k_n + k_m)} \Big(k_n k_m + G^2 \Big)$$
$$- \frac{G}{2} \Big(\cosh(k_n + k_m)(h - h_2) - \cosh(k_n - k_m)(h - h_2) \Big)$$
$$+ \frac{\sinh(k_n - k_m)(h - h_2)}{2(k_n - k_m)} \Big(k_n k_m - G^2 \Big),$$

$$E_{n,m} = \int_{z=-h}^{0} Z_{4,n}(r_n, z) Z_m(k_m, z) dz = \frac{1}{r_n^2 + k_m^2} \Big(r_n (k_m^2 - G^2) \cos(r_n h) \sinh(k_m h) + k_m (r_n^2 + G^2) \sin(r_n h) \cosh(k_m h) - G(r_n^2 + k_m^2) \sin(r_n h) \sinh(k_m h) \Big).$$

To calculate the reflection coefficient and the wave forces, it is essential to evaluate the coefficients $R_n, A_n, B_n, C_n, D_n, E_n, F_n$ and T_n. To achieve this, we construct a system of $8N + 8$ linear equations as follows:

$$\mathcal{A}\mathcal{X} = \mathcal{B}, \tag{3.39}$$

where $\mathcal{X} = \Big[R_0, R_1, ..., R_N, A_0, A_1, ..., A_N, B_0, B_1, ..., B_N, C_0, C_1, ..., C_N, D_0, D_1, ..., D_N, E_0, E_1, ..., E_N, F_0, F_1, ...F_N, T_0, T_1, ..., T_N\Big]^t$ is the unknown vector, $\mathcal{B}$ is the vector of size $(8N + 8) \times 1$ and $\mathcal{A}$ is the matrix of size $(8N + 8) \times (8N + 8)$.

For problem (ii), all the equations (3.26)-(3.39) remain the similar type with k_n, q_n, r_n and s_n getting changed to $\tilde{k}_n, \tilde{q}_n, \tilde{r}_n$ and $\tilde{s}_n$, respectively, since the dispersion relation gets changed because of the inclusion of the uniform current U_0 in the formulation.

3.2.2 Plane-wave approximations

From the full solution above, if we ignore all the infinite summations and consider only the terms corresponding to $n = 0$, then we get what is called a plane-wave approximation. In this problem, we proceed to calculate only the unknowns R_0, A_0, B_0, C_0, D_0, E_0, F_0 and T_0. The other values for $n \geq 1$ are not considered since they correspond to evanescent modes which are not accounted for. In the plane-wave assumption, only the most progressive mode, i.e., the least damped one, among all the modes in each region is taken into account for satisfying the matching conditions. For small f, the only wavenumbers used for this problem are $k = k_0$ and $k = \tilde{k}_0$ from the dispersion relations (3.19) and (3.23), respectively. This justification allows one to ignore the evanescent modes for such problems. It leads to a substantial simplification of the mathematics involved in solving the problem. For more information, one may refer to the work in [23].

Having obtained the expressions for the velocity potentials, we proceed to determine the wave-induced forces on the floating structure. For problem (i), to compute the complex-valued horizontal force X_{hf} and vertical force Y_{vf} on the floating structure, we use the formulas given, respectively, by

$$X_{hf} = \mathrm{i}\rho\omega \int_{-h_3}^{0} \left[\phi_5 \left(L + L_1 + L_2, z\right) - \phi_3 \left(L + L_1, z\right)\right] dz, \tag{3.40}$$

$$Y_{vf} = \mathrm{i}\rho\omega \int_{L+L_1}^{L+L_1+L_2} \phi_4(x,-h_3)\,dx. \tag{3.41}$$

The horizontal force X_{hf} acting on S is the integral of the pressure difference of both sides of S, which is obtained from the linearized Bernoulli's equation. In a similar manner, vertical force Y_{vf} is the integral of the pressure. The non-dimensional forms of the forces X_{hf} and Y_{vf} can be written as follows:

$$F_h = \frac{|X_{hf}|}{\rho g A b}, \quad F_v = \frac{|Y_{vf}|}{\rho g A b}, \tag{3.42}$$

with ρ as the water density, $b = L_2/2$ and $A = 1$ the incident wave amplitude.
For problem (ii), the horizontal and vertical forces can be computed by using the following formulas:

$$\tilde{X}_{hf} = \mathrm{i}\rho\hat{\omega} \int_{-h_3}^{0} \Big(\tilde{\phi}_5(L+L_1+L_2,z) - \tilde{\phi}_3(L+L_1,z)\Big)dz, \tag{3.43}$$

$$\tilde{Y}_{vf} = \rho \int_{L+L_1}^{L+L_1+L_2} \Big(\mathrm{i}\hat{\omega}\tilde{\phi}_4(x,-h_3) + \frac{U_0^2}{2}\Big)dx, \tag{3.44}$$

and the non-dimensional forms of the forces $\tilde{X}_{hf}$ and $\tilde{Y}_{vf}$ can be written as

$$\tilde{F}_h = \frac{|\tilde{X}_{hf}|}{\rho g A b}, \quad \tilde{F}_v = \frac{|\tilde{Y}_{vf}|}{\rho g A b}, \tag{3.45}$$

where $\hat{\omega} = \omega - U_0\tilde{k}\cos(\theta-\beta)$.

3.3 Energy identity relation

In water wave scattering problems, energy identity plays an essential role in establishing a relation that connects the amplitude of the incident wave with those of the reflected and transmitted waves. In the case of wave interaction with finite rigid barriers, the energy identity relation is given by $|R_0|^2 + |T_0|^2 = 1$, but when water waves interact with a rigid floating structure in the presence of two thin vertical porous barriers and a porous sea-bed, the system dissipates a significant amount of wave energy. By utilizing Green's second identity, we establish an energy identity relation for the present problem.

Green's identity for the function $\phi(x,z)$ and its complex conjugate $\phi^*(x,z)$, for finite

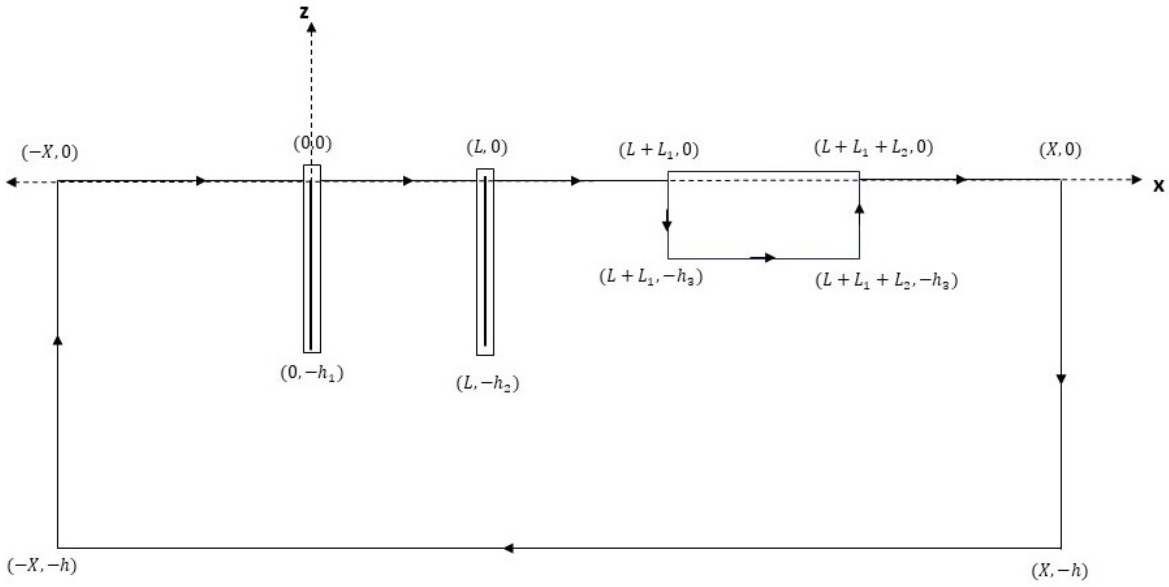

Figure 3.2: Contour in the plane

depth, is given by

$$\int_{\Gamma} \left(\phi^* \frac{\partial \phi}{\partial n} - \phi \frac{\partial \phi^*}{\partial n} \right) ds = 0, \tag{3.46}$$

where the closed contour Γ is $\{z = 0, -X \leq x \leq 0;\ z = 0, 0 \leq x \leq L;\ z = 0, L \leq x \leq L + L_1;\ z = 0, L + L_1 + L_2 \leq x \leq X;\ x = X, -h \leq z \leq 0;\ x = -X, -h \leq z \leq 0;\ z = -h, -X \leq x \leq X;\ x = 0, -h_1 \leq z \leq 0;\ x = L, -h_2 \leq z \leq 0;\ L + L_1 \leq x \leq L + L_1 + L_2, -h_3 \leq z \leq 0\}$ (Figure 3.2), and $\frac{\partial}{\partial n}$ denotes the derivative in the direction of the outward normal to the enclosed boundary Γ. Now, we take the limit as $X \to \infty$. There is no contribution from the lines $z = 0, -X \leq x \leq 0;\ z = 0, 0 \leq x \leq L;\ z = 0, L \leq x \leq L + L_1;\ z = 0, L + L_1 + L_2 \leq x \leq X$ because of the free surface condition. The contribution along $L + L_1 \leq x \leq L + L_1 + L_2, -h_3 \leq z \leq 0$ is zero due to the rigid boundary. The contribution from the line at $z = -h, -X \leq x \leq X$ is

$$\int \left(\phi^* \frac{\partial \phi}{\partial n} - \phi \frac{\partial \phi^*}{\partial n} \right) ds = 2\ \mathrm{Im}(G) \int_{-X}^{X} |\phi|^2 dx, \tag{3.47}$$

where Im(.) denotes the imaginary part.

The contribution from the line at $x = 0, -h_1 \leq z \leq 0$ is

$$\int \left(\phi^* \frac{\partial \phi}{\partial n} - \phi \frac{\partial \phi^*}{\partial n}\right) ds = -2\mathrm{i}k_0 \ \mathrm{Re}(G_1) \int_{-h_1}^{0} |\phi_1 - \phi_2|^2 dz. \tag{3.48}$$

The contribution from the line at $x = L, -h_2 \leq z \leq 0$ is

$$\int \left(\phi^* \frac{\partial \phi}{\partial n} - \phi \frac{\partial \phi^*}{\partial n}\right) ds = -2\mathrm{i}k_0 \ \mathrm{Re}(G_2) \int_{-h_2}^{0} |\phi_2 - \phi_3|^2 dz. \tag{3.49}$$

The contributions from the integral along $x = -X, -h \leq z \leq 0$ and $x = X, -h \leq z \leq 0$ are non-zero. Thus, the integral at $x = -X, -h \leq z \leq 0$ is

$$\int \left(\phi^* \frac{\partial \phi}{\partial n} - \phi \frac{\partial \phi^*}{\partial n}\right) ds = (1 - |R_0|^2)\xi, \tag{3.50}$$

and the integral at $x = X, -h \leq z \leq 0$ is

$$\int \left(\phi^* \frac{\partial \phi}{\partial n} - \phi \frac{\partial \phi^*}{\partial n}\right) ds = -|T_0|^2 \xi, \tag{3.51}$$

where $\xi = 2\mathrm{i}k_0 \cos(\theta) \int_{z=-h}^{0} Z_0(k_0, z) Z_0^*(k_0, z) dz.$

Finally, summing up the contributions from (3.47) - (3.51), we obtain the energy balance relation as

$$|R_0|^2 + |T_0|^2 + P_d = 1, \tag{3.52}$$

where

$$P_d = \frac{2\mathrm{i}k_0 \ \mathrm{Re}(G_1)}{\xi} \int_{-h_1}^{0} |\phi_1 - \phi_2|^2 dz + \frac{2\mathrm{i}k_0 \ \mathrm{Re}(G_2)}{\xi} \int_{-h_2}^{0} |\phi_2 - \phi_3|^2 dz - \frac{2 \ \mathrm{Im}(G)}{\xi} \int_{-X}^{X} |\phi|^2 dx \tag{3.53}$$

is the dissipation coefficient.

For our problem, since G is real, (3.53) reduces to

$$P_d = \frac{2\mathrm{i}k_0 \ \mathrm{Re}(G_1)}{\xi} \int_{-h_1}^{0} |\phi_1 - \phi_2|^2 dz + \frac{2\mathrm{i}k_0 \ \mathrm{Re}(G_2)}{\xi} \int_{-h_2}^{0} |\phi_2 - \phi_3|^2 dz. \tag{3.54}$$

3.4 Validation

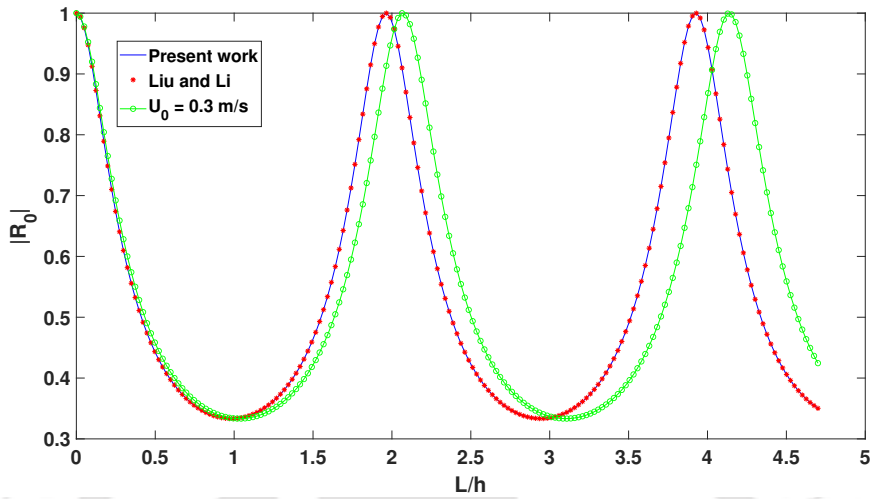

Figure 3.3: Validation of the present work with that of Liu and Li [45] without the floating structure.

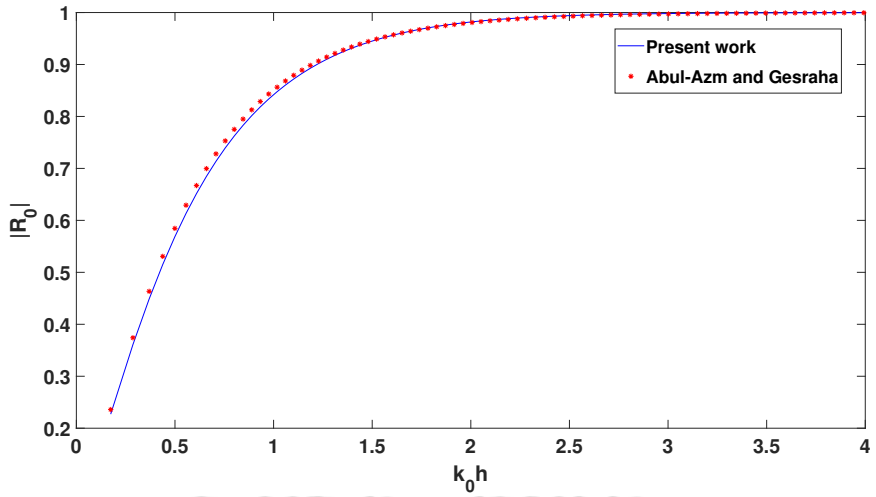

Figure 3.4: Validation of the present work with that of Abul-Azm and Gesraha [2] without the porous barriers.

In this section, we validate the present work against a couple of earlier works corresponding to a similar structure/situation. For this, the work of Liu and Li [45] in the absence of a floating structure, and that of Abul-Azm and Gesraha [2] without the consideration of porous barriers, for a flat and impermeable sea-bed, are considered.

For Figure 3.3, to resemble our work with that in [45], the length of the floating bridge is neglected. We plot the reflection coefficient against the non-dimensional distance between the porous barriers by considering $k_0h = 1.6$, $h_1 = h_2$, $h_1/h = 1$, $G_1 = 0.5$, $G_2 = 0$ and $\theta = 0°$, for both works in the absence of the floating structure. It presents

an excellent agreement of our result with that in [45]. Here, we also include current in the work in [45], and it is observed that the current significantly impacts the reflection coefficient.

For comparing our work with that in [2], we consider larger absolute values of the complex porous-effect parameters for both barriers so that the permeable barriers tend to impermeable ones which can be assumed to act as transparent barriers. As such, both models get converted to the same problem. For validating our result against that of [2], we consider $\theta = 0°$, $L_2/2h = 1$ and $h_3/h = 0.25$ to bring similarity to both problems. In Figure 3.4, the reflection coefficient is plotted against the dimensionless wavenumber for the present model and that of [2]. This figure shows that the reflection coefficient for the larger absolute value of the porous-effect parameters exhibits the same pattern as in [2]. With these successful validations, it is quite reasonable to consider that the present model can be appropriately utilized in problems related to the use of porous breakwaters for the safety of VLFS.

3.5 Results and discussion

The unknown coefficients are obtained by solving (3.39) with the help of MATLAB. For computing purpose, particular values of some parameters are considered as: the acceleration due to gravity $g = 9.81$ m/s^2; $h = 15$ m; the height of B_1 as $h_1 = 9$ m; the height of B_2 as $h_2 = 9$ m; the draft of the floating structure as $h_3 = 3$ m; the space between the second permeable barrier B_2 and the floating structure S as $L_1 = 7$ m; the length of the floating structure as $L_2 = 20$ m; the porous-effect parameter of the sea-bed $Gh = 0.75$, the porous-effect parameters of B_1 and B_2 as $G_1 = 0.5$; $G_2 = 0.5$, respectively; and the angle of wave incidence as $\theta = 30°$. For problem (ii), we additionally consider U_0 and β, respectively, as $U_0 = -0.4, -0.2, 0.2, 0.4$ m/sec; β is taken equal to the wave incident angle θ. Here, we consider the numerical values of the porous-effect parameter Gh of the sea-bed in the range of 0 to 1, which was also considered in the works of [51] and [16].

3.5.1 Case I: Without current

Effect of the vertical porous barriers on the reflection coefficient

Here, we study the effect of the vertical porous barriers as a combined breakwater on $|R_0|$ by considering different values of G_1 and G_2; and h_1 and h_2.

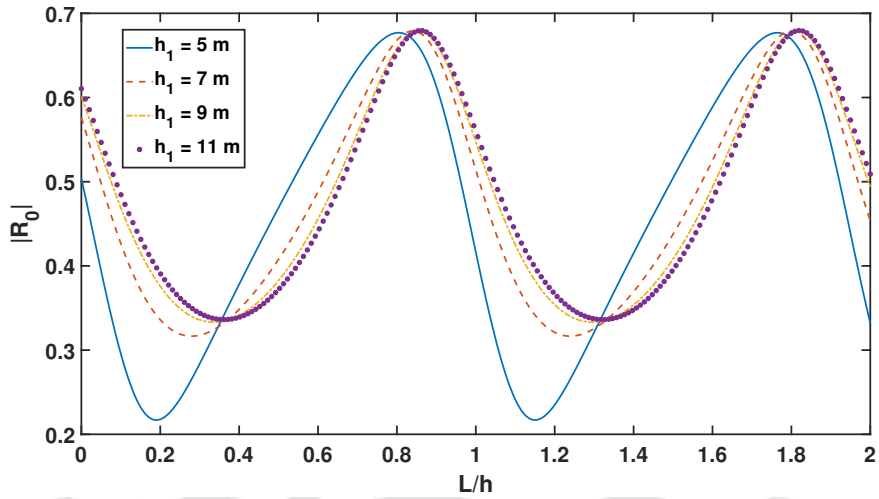

Figure 3.5: Variation of $|R_0|$ against non-dimensional distance (L/h) between two barriers for different values of height h_1 of the first porous barrier; $G_1 = 0.5$ and $G_2 = 0.5$

Figure 3.5 demonstrates reflection coefficient $|R_0|$ versus non-dimensional distance L/h corresponding to different values of non-dimensional height h_1/h for values of $h_1 = 5, 7, 9, 11$ m of the first porous barrier for real porous-effect parameters $G_1 = G_2 = 0.5$. Here, it can be observed that $|R_0|$ exhibits an oscillatory pattern corresponding to an increase in L/h for all h_1: as non-dimensional height h_1 of the first porous barrier increases, the reflection coefficient increases. It is also noticed that a greater barrier height corresponds to an increased reflection, while a lower height leads to a reduced reflection. This phenomenon can be explained by the fact that, as the barrier height increases, a significant portion of the incident wave energy is bounced back by the barrier, and a higher value of the height of the first porous barrier results in the maximum reflection.

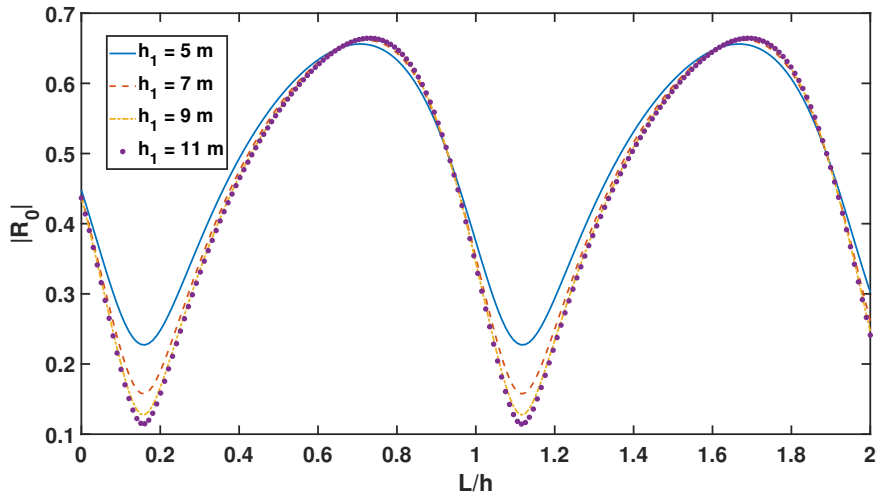

Figure 3.6: Variation of $|R_0|$ against non-dimensional distance (L/h) between two barriers for different values of height h_1 of the first porous barrier; $G_1 = 0.5 + \mathrm{i}$ and $G_2 = 0.5$

In Figure 3.6, we plot $|R_0|$ against non-dimensional distance L/h between two barriers for different values of h_1 with $G_1 = 0.5 + \mathrm{i}$ and $G_2 = 0.5$. From Figures 3.5 and 3.6, we observe that, as G_1 gets changed from 0.5 to $0.5 + \mathrm{i}$, the maxima of the reflection coefficient get reduced which indicates that the submerged porous barriers attenuate the reflected wave energy corresponding to the complex value of G_1, which causes the inertial effect. It is also observed that both maxima and minima occur for higher values of h_1.

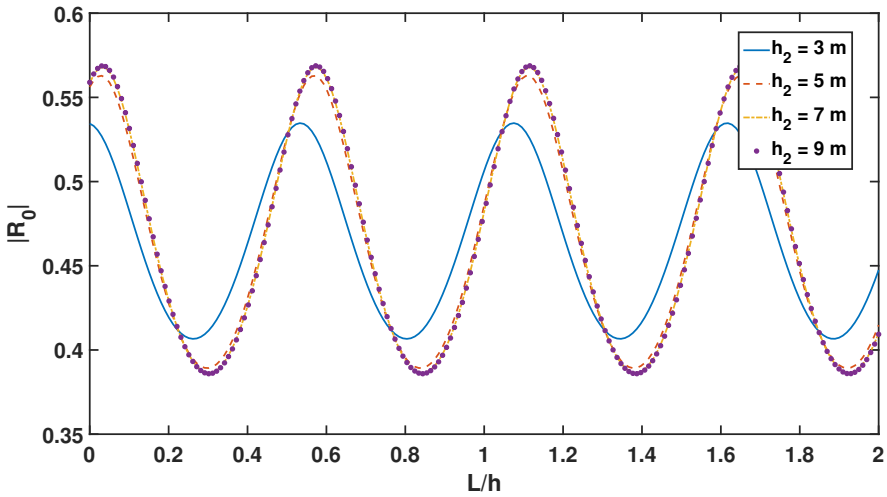

Figure 3.7: Variation of $|R_0|$ against non-dimensional distance (L/h) between two barriers for different values of height h_2 of the second porous barrier; $G_1 = 0.5$ and $G_2 = 0.5$

In Figure 3.7, we plot $|R_0|$ against L/h corresponding to different values of height h_2 of B_2. Here, we observe an oscillating pattern of the reflection coefficient as L/h increases. It is further noticed that the reflection coefficient increases with an increase in the height of B_2. This happens because, as the height of the second barrier increases, more amount of waves can get reflected. Therefore, for higher values of the height of the second barrier, the highest reflection coefficient is obtained. It is also seen that both maxima and minima occur for higher values of h_2.

Figure 3.8 also shows that the reflection coefficient decreases as G_1 gets changed from $G_1 = 0.5$ to $G_1 = 0.5+\mathrm{i}$ because of the imaginary part of G_1, which introduces the inertial effect.

Figure 3.9 shows the variation of reflection coefficient $|R_0|$ against non-dimensional distance L/h corresponding to different values of G_1. It is observed that, as the absolute value of G_1 increases, the maxima of reflection coefficient decrease corresponding to an increase in friction. However, as the porosity of the first porous barrier increases, the reflection shifts toward the right due to the fact that the barrier becomes transparent for larger porosity.

Figure 3.10 shows the variation of $|R_0|$ against L/h corresponding to different incident angles θ. The minima of the reflection coefficient get shifted towards the right correspond-

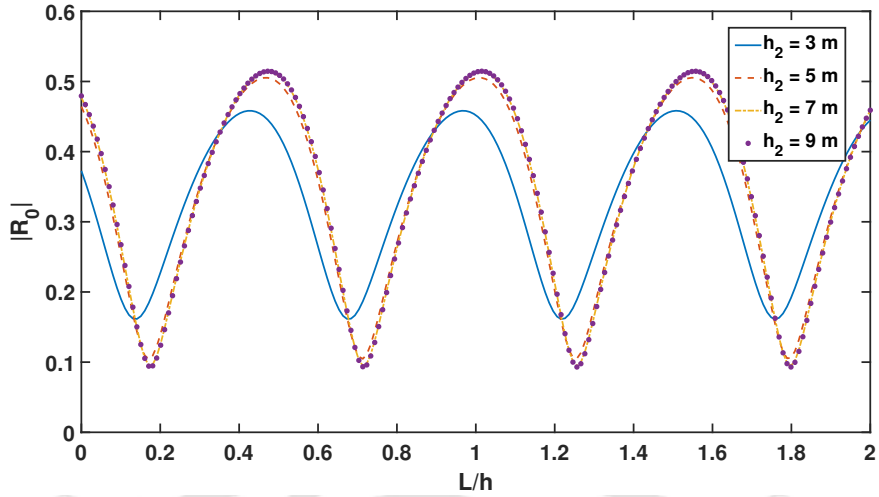

Figure 3.8: Variation of $|R_0|$ against non-dimensional distance (L/h) between two barriers for different values of height h_2 of the second porous barrier; $G_1 = 0.5 + \mathrm{i}$ and $G_2 = 0.5$

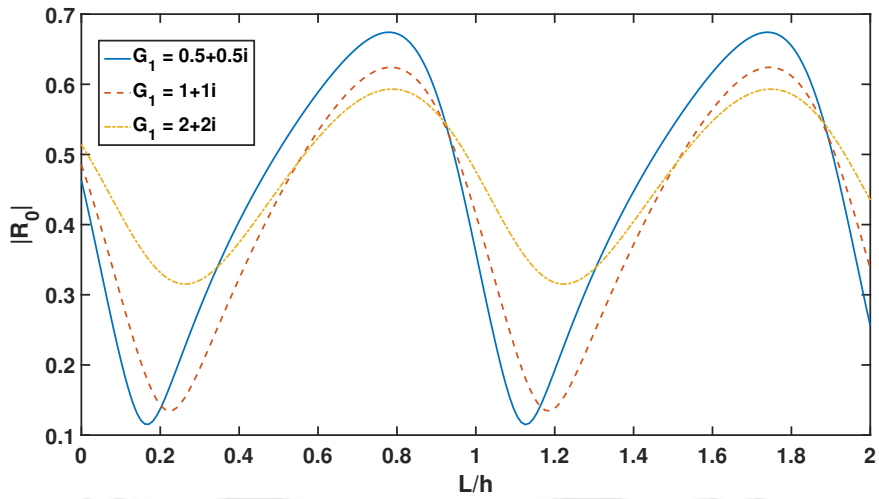

Figure 3.9: Variation of $|R_0|$ against non-dimensional distance (L/h) between two barriers corresponding to different values of G_1; $(G_2 = 0.5)$

ing to an increase in θ. There is a subsequent decrease in the number of occurrences of reflection minima. It is also noted that the maxima of $|R_0|$ decrease for the obliquely incident waves.

In Figure 3.11, the reflection coefficient is plotted against the non-dimensional distance between two barriers for different sea-bed porous-effect parameter values. $Gh = 0$ represents the case of an impermeable bed. As Gh increases, reflection coefficient $|R_0|$ also increases, which can be interpreted as: the porous sea-bed can dissipate a major portion of the incident wave energy. It may be noted that the same pattern was observed in [16].

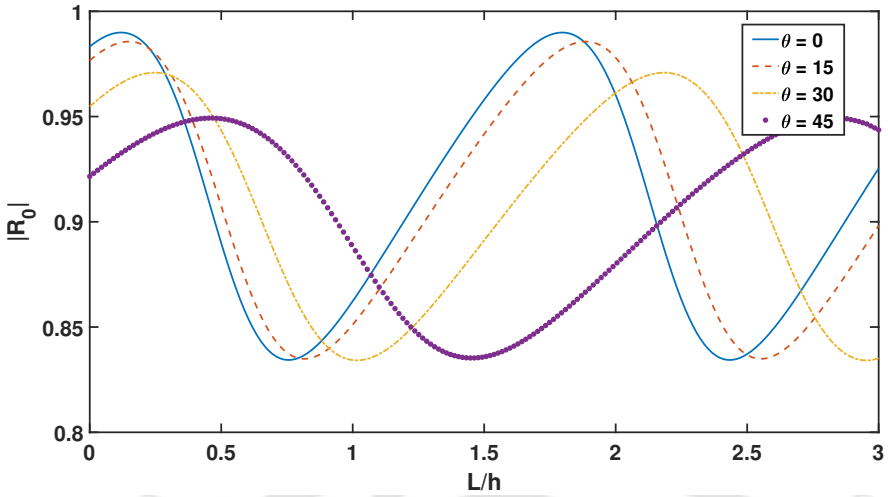

Figure 3.10: Variation of $|R_0|$ against non-dimensional distance (L/h) between two barriers for different values of angle of incidence θ

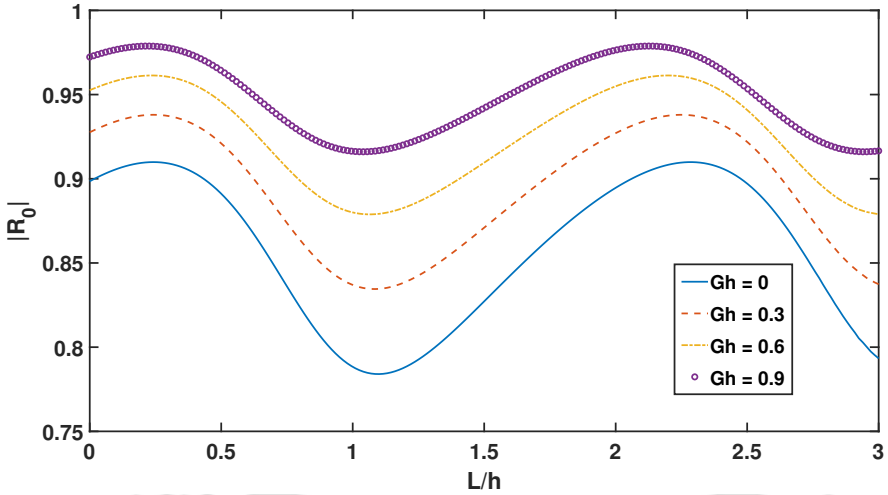

Figure 3.11: Variation of $|R_0|$ against non-dimensional distance (L/h) between two barriers for different values of porous-effect parameter (Gh) of the sea-bed

Table 3.1: Variation of reflection coefficient $|R_0|$ for different parameters

h_1	$\|R_0\|$
5	0.4163
7	0.5139
9	0.5474
11	0.5600

h_2	$\|R_0\|$
3	0.4909
5	0.5462
7	0.5514
9	0.5474

Gh	$\|R_0\|$
0	0.7883
0.3	0.8370
0.6	0.8800
0.9	0.9163

θ	$\|R_0\|$
0	0.9460
15	0.9297
30	0.8803
45	0.8354

We present Table 3.1 which gives an overall view of the results that are obtained. It shows the variation of reflection coefficient $|R_0|$ against various parameters such as depth h_1 of the first porous barrier, depth h_2 of the second porous barrier, porous-effect parameter Gh of the sea-bed and angle of wave incidence θ. This table sums up the main observations in a compact manner. All these can also be observed through various plots already displayed.

Impact of the vertical porous barriers in the reduction of forces

In this part, the role of B_1 and B_2 in the mitigation of wave forces acting on the floating structure is studied.

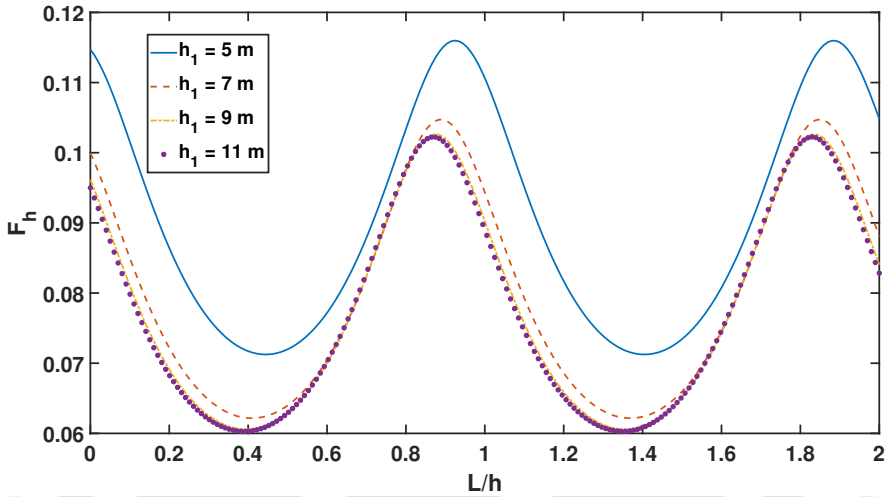

Figure 3.12: Variation of horizontal force F_h against non-dimensional distance (L/h) between two barriers corresponding to different values of height (h_1) of B_1

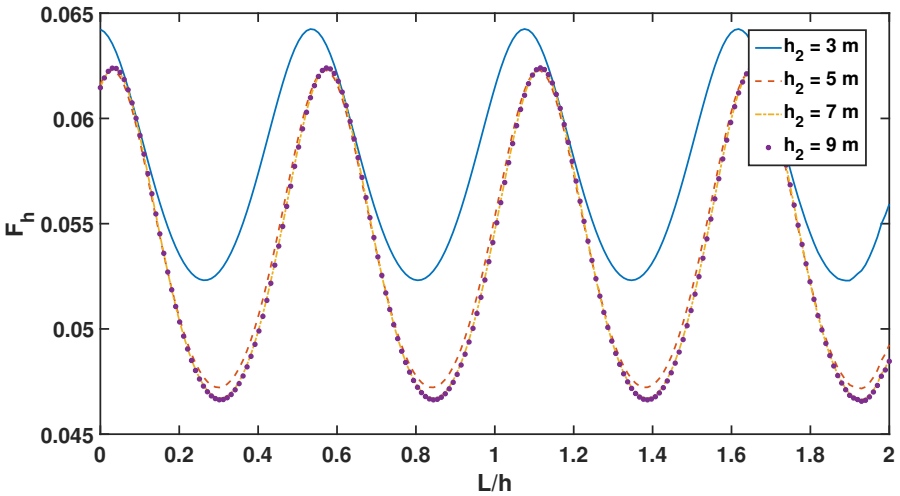

Figure 3.13: Variation of horizontal force F_h against non-dimensional distance (L/h) between two barriers corresponding to different values of height (h_2) of B_2

In Figures 3.12 and 3.13, we plot horizontal force F_h against non-dimensional distance L/h for different values of heights h_1 of the first porous barrier and h_2 of the second porous barrier, respectively. In both cases, it is clear that they show an opposite behaviour to the ones displayed in Figures 3.5 and 3.7. In Figure 3.12, for lower values of h_1 of B_1, the highest horizontal force is observed, which again appears in Figure 3.13 for lower height $h_2 = 3$ m of B_2. In both cases for this height, lower reflection is obtained as depicted in Figures 3.5 and 3.7, and for higher values of h_1 or h_2, the lowest horizontal force is observed because of higher reflection at this height of h_1 or h_2.

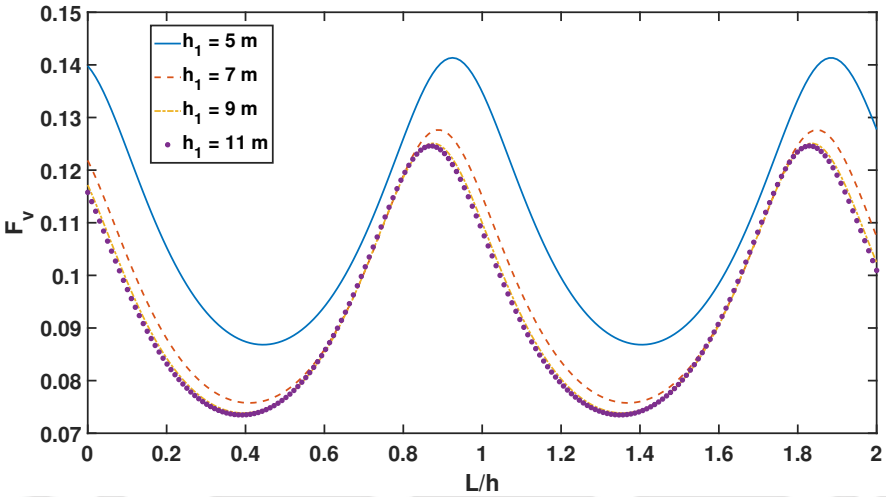

Figure 3.14: Variation of vertical force F_v against non-dimensional distance (L/h) between two barriers corresponding to different values of height (h_1) of B_1

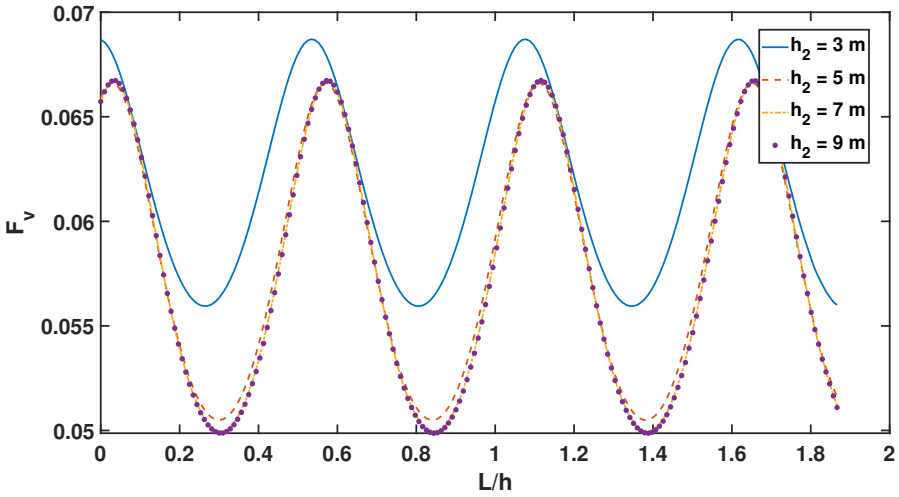

Figure 3.15: Variation of vertical force F_v against non-dimensional distance (L/h) between two barriers corresponding to different values of height (h_2) of B_2

Figures 3.14 and 3.15 show the variation of vertical force F_v against L/h corresponding to different values of height h_1 of B_1 and h_2 of B_2. In these cases also, we observe the

opposite trend of the reflection coefficient displayed in Figures 3.5 and 3.7. We also observe that vertical force F_v decreases as the height of the porous barriers increases. It is also noticed that the value of the vertical wave force is higher than the horizontal wave force.

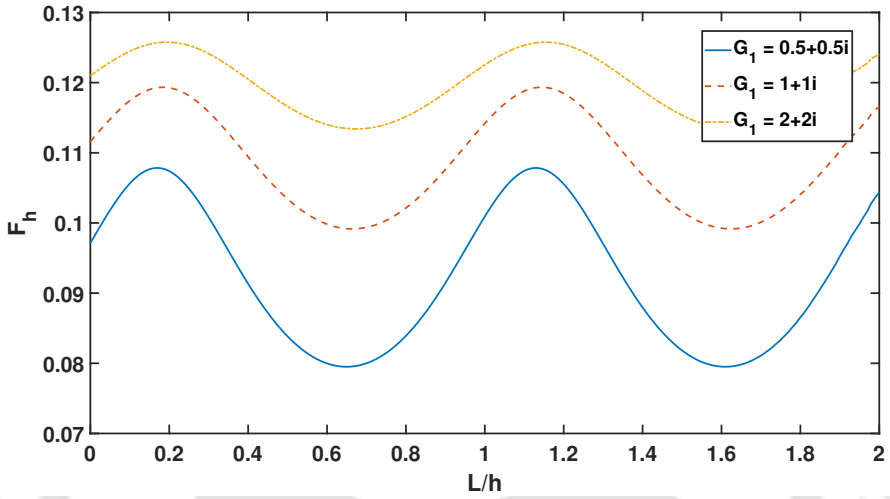

Figure 3.16: Variation of horizontal force F_h against non-dimensional distance (L/h) between two barriers corresponding to different values of porous-effect parameter G_1 of the first porous barrier

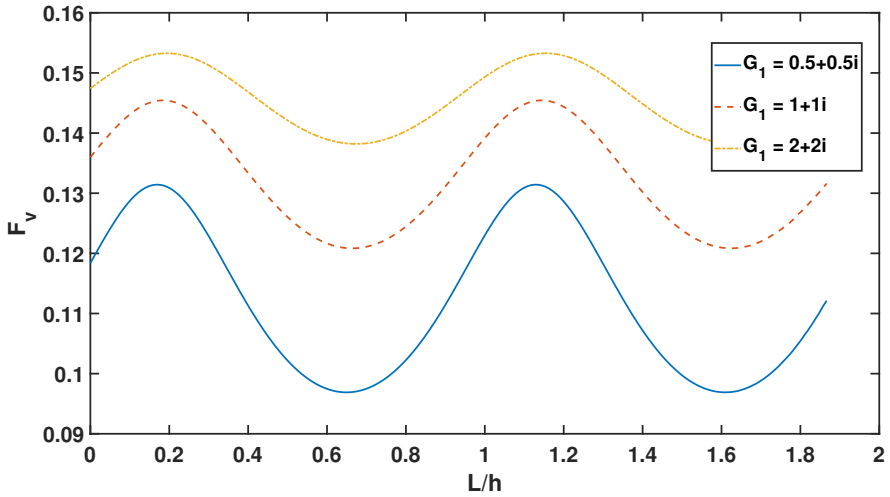

Figure 3.17: Variation of vertical force F_v against non-dimensional distance (L/h) between two barriers corresponding to different values of porous-effect parameter G_1 of the first porous barrier

In Figures 3.16 and 3.17, the variations of horizontal force F_h and vertical force F_v, respectively, are plotted against L/h corresponding to different values of porous-effect parameter G_1. It is observed that the horizontal force and the vertical force both increase corresponding to an increase in the absolute value of G_1. This occurs because, as the

absolute value of G_1 increases, the maximum of the reflection coefficient decreases, as already observed in Figure 3.9.

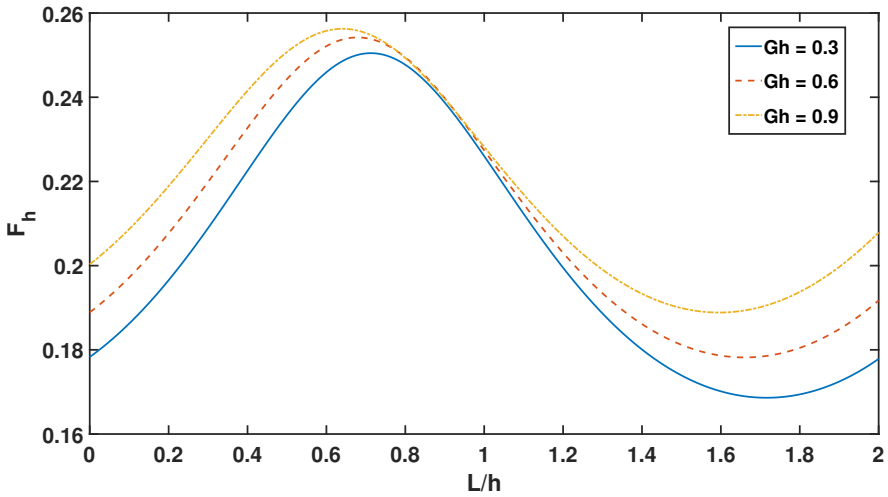

Figure 3.18: Variation of horizontal force F_h against non-dimensional distance (L/h) between two barriers corresponding to different values of porous-effect parameter Gh of the sea-bed

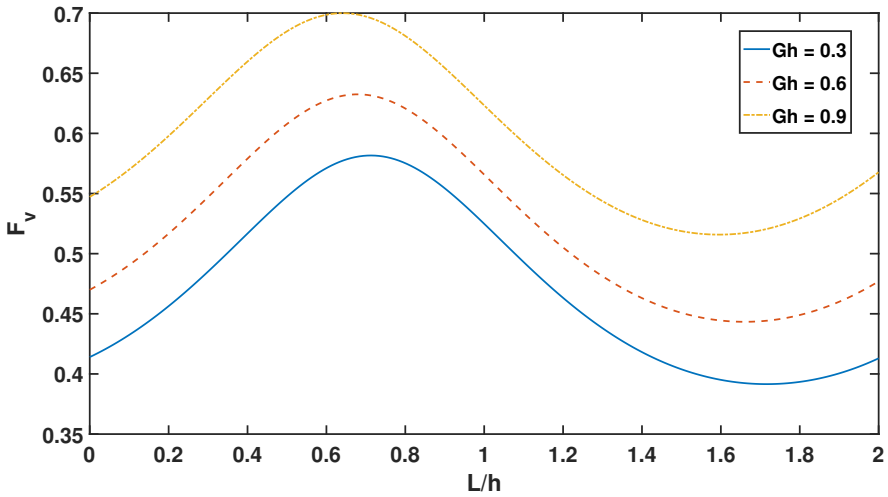

Figure 3.19: Variation of vertical force F_v against non-dimensional distance (L/h) between two barriers corresponding to different values of porous-effect parameter Gh of the sea-bed

Figures 3.18 and 3.19, respectively, represent the variation of the horizontal and vertical forces against the non-dimensional distance between two barriers corresponding to different values of porous-effect parameter Gh of the sea-bed. It is observed that, as Gh increases, the horizontal and vertical forces acting on the floating structure also increase. It implies that a porous sea-bed can dissipate a substantial portion of the energy of the incident wave.

3.5.2 Case II: With current

Water wave scattering by the floating structure in the presence of uniform current, which tends to be a more realistic problem, is now studied. Due to the presence of current, significant changes in the reflection coefficient and forces are observed. However, we present here only some results for this case in order to avoid repetition. The presented results are thought to be sufficient to depict the influence of the current on reflection and mitigation of force.

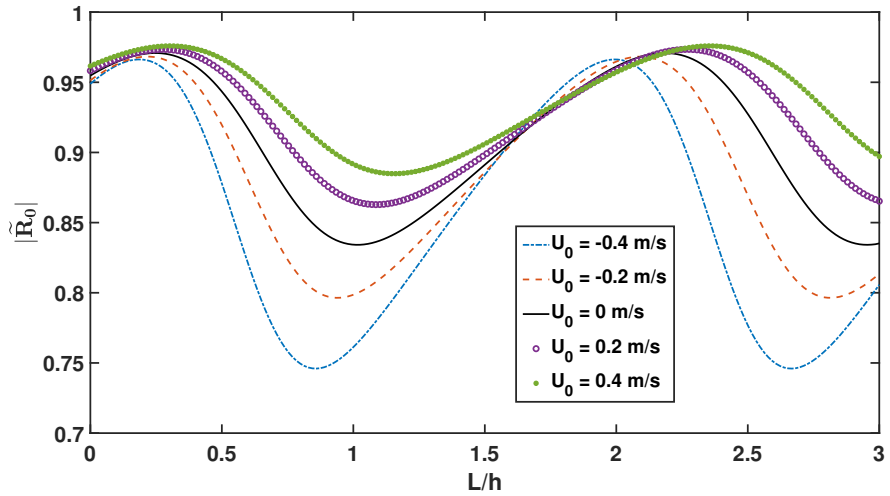

Figure 3.20: Variation of reflection coefficient $|\tilde{R}_0|$ against non-dimensional distance (L/h) between two barriers corresponding to different values of current U_0

The effect of current on the reflection coefficient is studied in Figure 3.20 in which reflection coefficient $|\tilde{R}_0|$ is plotted against the non-dimensional distance between two barriers for different values of the current. Here $U_0 = 0$ corresponds to the case of no current. When current is present in the direction of wave propagation, an enhancement in reflection coefficient $|\tilde{R}_0|$ is observed; and in the presence of an opposite current, the reflection coefficient decreases. Due to an increase in current, a shift in the phase is also noticed.

In Figure 3.21, horizontal force $\tilde{F}_h$ is plotted against non-dimensional distance L/h between the barriers for different values of the current. Here, it is observed that, in the presence of the current, horizontal force decreases with an increase in the value of the current because of the increase of the reflection coefficient, which can be clearly noticed from Figure 3.20.

We plot vertical force $\tilde{F}_v$ against the non-dimensional distance between the barriers for different values of the current in Figure 3.22. As the value of the current increases, the vertical force on the floating structure increases. Here, it is observed that the horizontal force is less than the vertical force for all the values of the current.

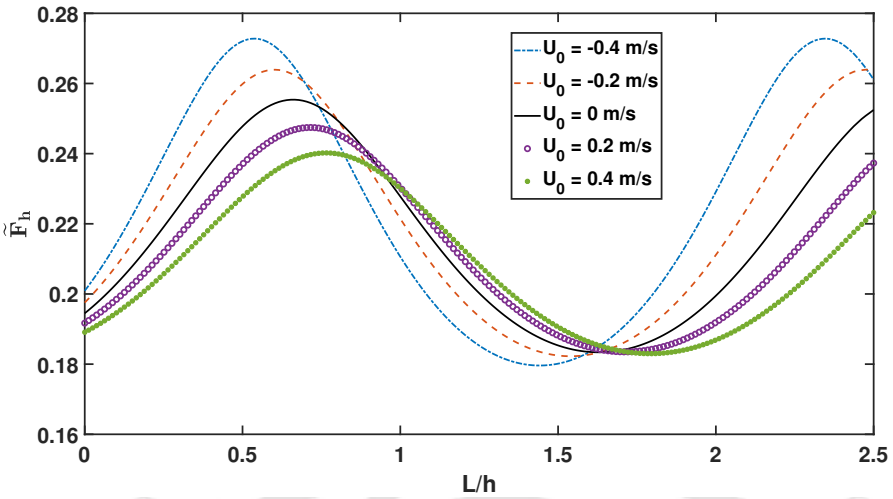

Figure 3.21: Variation of horizontal force $\tilde{F}_h$ against non-dimensional distance (L/h) between two barriers corresponding to different values of current U_0

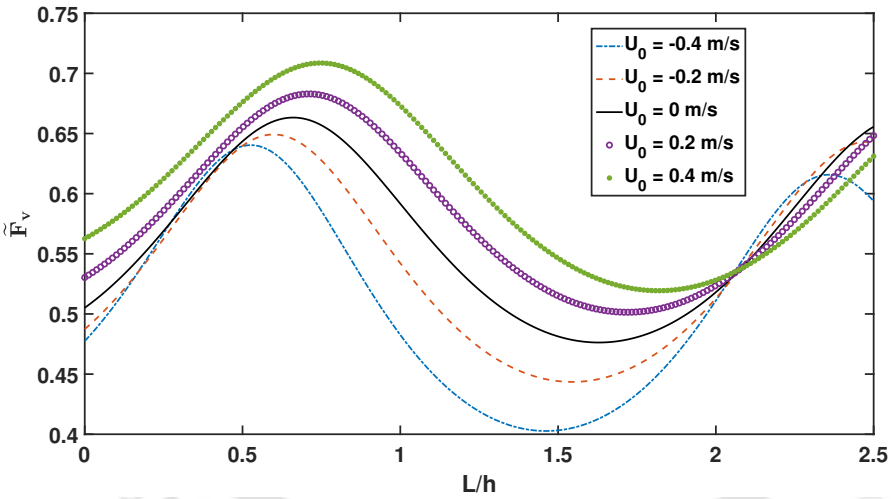

Figure 3.22: Variation of vertical force $\tilde{F}_v$ against non-dimensional distance (L/h) between two barriers corresponding to different values of current U_0

From the above demonstration, it can be concluded that the consideration of current in the formulation leads to changes in the values of the reflection coefficient and wave forces. It is intended to show that, in ocean engineering problems, it may be realistic to incorporate current in the formulation while solving practical problems.

3.6 Conclusions

An oblique water wave interaction with a floating structure placed in front of two submerged vertical porous barriers was studied in the presence of current and also for no current with the waves propagating over a porous sea-bed having real porous-effect pa-

rameter G. These porous barriers were placed at some distance from each other with different porous-effect parameters G_1 and G_2, and different heights h_1 and h_2, respectively. By splitting the fluid region into a number of sub-regions, the scattered velocity potentials in each fluid region were obtained by using variable separable and eigenfunction expansion methods. After deriving the velocity potentials in each fluid region, we used the matching conditions that occurred due to the continuity of the mass flux and pressure across each virtual vertical boundary. From this, we deduced a system of linear equations, which was solved by using MATLAB to determine the unknown coefficients in the velocity potentials. In this work, we also studied the hydrodynamic forces and reflection coefficient due to different parameter values.

The main observations, analysis and findings of this study can be summed up as follows:

1. As the height of the first porous barrier increases, an enhancement in the reflection coefficient was observed, and with an increase in the height of the second barrier, the reflection coefficient also increases.

2. It was also noted that, as the distance between these two barriers increases, the reflection coefficient exhibits an oscillatory nature.

3. The impact of the porous-effect parameters was also studied and analyzed comprehensively.

4. The behaviour of the hydrodynamic forces on the floating structure was also analyzed. We observed that certain values of those parameters, which showed higher reflection, cause less amount of force on the floating structure. Therefore, higher values of the height of the porous barriers, which showed higher reflection, reduce wave force on the rectangular floating structure, and the same was observed for the porous-effect parameters also.

5. The impact of the wave incident angle on the reflection coefficient was also studied.

6. While the above observations were for the case of without current, a significant change in the reflection coefficient was also observed when the current was included in the formulation. In this case, a right shift in the minima of the reflection coefficient was observed. This can be considered as a very important finding.

7. In the presence of current, horizontal force on the floating structure showed an opposite behaviour to the reflection coefficient.

8. As a consequence, these observations suggest the selection of vertical porous barriers with suitable parameters and configurations so as to mitigate horizontal and vertical forces on the floating structure to a reasonable extent.

The results of the present study were successfully validated against available results for verifying the effectiveness of this model which can be used for problems involving floating structures such as a floating bridge, floating airport, floating dock, or any other floating facility.

CHAPTER 4

Impact of a vertical porous barrier in the reflection of water waves and mitigation of wave forces on a rigid floating structure in the presence of an elevated bottom and a trench

In this work, we assume an oblique wave to interact with a floating structure placed after a porous barrier with the consideration of two types of bottom topography: (i) an elevated-type, and (ii) a trench-type, each as a separate case. The sea-bed is considered impermeable and the entire fluid region is split into five sub-regions in each of which relevant boundary value problems are set up. Utilizing the linear water wave theory, the velocity potentials in each sub-region are obtained by employing the eigenfunction expansion method. This study focuses on how different parameters, such as the distance between the barrier and the floating structure, the porous-effect parameter, and the height of the barrier, influence the reflection coefficient as well as the forces acting on the floating structure in the horizontal and vertical directions.

4.1 Mathematical formulation

We consider the interaction of oblique water waves with a thin vertical porous barrier and a floating structure in the presence of a specific uneven sea-bed in the form of an elevated-type or a trench. All geometrical and physical conditions remain the same for both types of the sea-bed, throughout except for the sea-bed condition. In the immediate following portion, we elaborately study the case when the sea-bed is considered as a step-type one. Later on, we study the problem for the trench-type sea-bed by referring to the initial formulation connected to the step-type sea-bed. This study attempts to

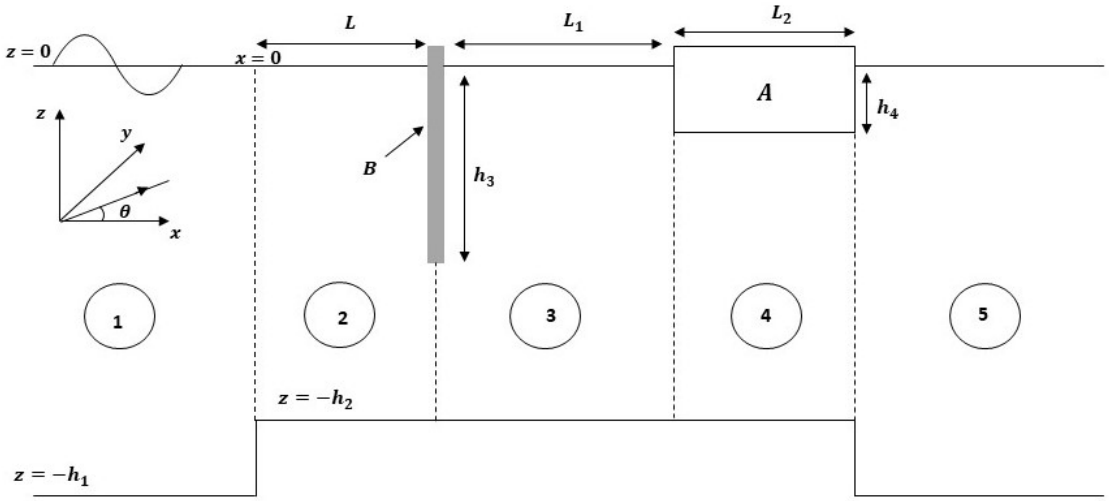

Figure 4.1: Definition sketch of the problem with the wave striking a rigid rectangular floating structure placed after a vertical porous barrier in the presence of an elevated bottom topography.

investigate the interaction of an oblique wave with a rigid rectangular floating structure (A), considering a thin vertical porous barrier (B) positioned in front of the structure, along with an elevated bottom topography. Upon employing linear water wave theory for a finite ocean depth for the irrotational motion of an incompressible and non-viscous fluid, the formulation of the associated problem is carried out within the framework of the right-handed Cartesian coordinate system, where the x-axis represents the horizontal direction and the z-axis represents the vertically upward direction. The porous barrier of draft h_3 with porous-effect parameter G_1 is placed at $x = L$, and the floating structure is located at a distance L_1 from the porous barrier between $L + L_1 < x < L + L_1 + L_2$ with draft h_4 as shown in Figure 4.1. The entire fluid domain is split into five sub-regions as follows: Region 1 ($-\infty < x < 0$, $-h_1 < z < 0$); Region 2 ($0 < x < L$, $-h_2 < z < 0$); Region 3 ($L < x < L+L_1$, $-h_2 < z < 0$); Region 4 ($L+L_1 < x < L+L_1+L_2$, $-h_2 < z < -h_4$) and Region 5 ($L + L_1 + L_2 < x < \infty$, $-h_1 < z < 0$). For Regions 1 and 5, the impermeable sea-bed is assumed at $z = -h_1$, while for Regions 2, 3 and 4, it is assumed at $z = -h_2$. It is further assumed that all the motions are simple harmonic in time with an angular frequency ω and also along the y-direction. For an oblique water wave, the spatial velocity potential in each of the fluid regions can be written as $\Phi_j(x, y, z, t) = \mathrm{Re}[\phi_j(x, z)e^{\mathrm{i}(k_y y - \omega t)}]$ for $j = 1, 2, 3, 4, 5$, where $k_y = k_0 \sin\theta$, k_0 is the incident wavenumber, θ is the incident wave angle to the x-axis.

In each fluid region, the scattered velocity potential ϕ_j satisfies the modified Helmholtz equation:

$$\Big(\frac{\partial^2}{\partial x^2} + \frac{\partial^2}{\partial z^2} - k_y^2\Big)\phi_j = 0. \tag{4.1}$$

The free-surface condition in Regions 1, 2, 3 and 5 at the mean free surface is as follows:

$$\frac{\partial \phi_j}{\partial z} - K\phi_j = 0 \ \text{ at } \ z = 0, \ \ j = 1, 2, 3, 5. \tag{4.2}$$

The boundary conditions on the impermeable bottom are expressed through

$$\frac{\partial \phi_j}{\partial z} = 0 \ \text{ at } \ z = -h_1, \ \ j = 1, 5, \tag{4.3}$$

$$\frac{\partial \phi_j}{\partial z} = 0 \ \text{ at } \ z = -h_2, \ \ j = 2, 3, 4. \tag{4.4}$$

Since the vertical and horizontal sides of the floating structure are rigid, therefore, the vertical and horizontal velocities vanish at the sides implying the following conditions:

$$\frac{\partial \phi_3}{\partial x} = 0 \ \text{ at } \ x = L + L_1, \ \ -h_4 < z < 0, \tag{4.5}$$

$$\frac{\partial \phi_5}{\partial x} = 0 \ \text{ at } \ x = L + L_1 + L_2, \ \ -h_4 < z < 0, \tag{4.6}$$

$$\frac{\partial \phi_4}{\partial z} = 0 \ \text{ at } \ z = -h_4, \ \ L + L_1 < x < L + L_1 + L_2. \tag{4.7}$$

The wall conditions of the elevated bottom have the forms

$$\frac{\partial \phi_1}{\partial x} = 0 \ \text{ at } \ x = 0, \ \ -h_1 < z < -h_2, \tag{4.8}$$

$$\frac{\partial \phi_5}{\partial x} = 0 \ \text{ at } \ x = L + L_1 + L_2, \ \ -h_1 < z < -h_2. \tag{4.9}$$

Further, the continuity of mass flux and pressure across the vertical boundaries $x = 0$, $x = L$, $x = L + L_1$ and $x = L + L_1 + L_2$ imply that ϕ_j, $j = 1, 2, 3, 4, 5$, satisfy the matching conditions as applicable as follows:

$$\phi_1 = \phi_2 \ \text{ at } \ x = 0, \ \ -h_2 < z < 0, \tag{4.10}$$

$$\frac{\partial \phi_1}{\partial x} = \frac{\partial \phi_2}{\partial x} \ \text{ at } \ x = 0, \ \ -h_2 < z < 0, \tag{4.11}$$

$$\phi_2 = \phi_3 \ \text{ at } \ x = L, \ \ -h_2 < z < -h_3, \tag{4.12}$$

$$\frac{\partial \phi_2}{\partial x} = \frac{\partial \phi_3}{\partial x} = \mathrm{i}k_0 G_1(\phi_2 - \phi_3) \ \text{ at } \ x = L, \ \ -h_3 < z < 0, \tag{4.13}$$

$$\frac{\partial \phi_2}{\partial x} = \frac{\partial \phi_3}{\partial x} \ \text{ at } \ x = L, \ \ -h_2 < z < -h_3, \tag{4.14}$$

$$\phi_3 = \phi_4 \ \text{ at } \ x = L + L_1, \ \ -h_2 < z < -h_4, \tag{4.15}$$

$$\frac{\partial \phi_3}{\partial x} = \frac{\partial \phi_4}{\partial x} \ \text{ at } \ x = L + L_1, \ \ -h_2 < z < -h_4, \tag{4.16}$$

$$\phi_4 = \phi_5 \ \text{ at } \ x = L + L_1 + L_2, \ \ -h_2 < z < -h_4, \tag{4.17}$$

$$\frac{\partial \phi_4}{\partial x} = \frac{\partial \phi_5}{\partial x} \ \text{ at } \ x = L + L_1 + L_2, \ \ -h_2 < z < -h_4. \tag{4.18}$$

Since we assume that the porous barrier is composed of material with very fine pores, therefore, condition (4.13) is applied as was used in [95], and the other equations are due to the geometry of the structure. Consequently, the present model caters to low Reynolds numbers. Since the flow is assumed to be laminar, for the validity of Darcy's law, the values of Reynolds number need to be between 1 and 10. Furthermore, the condition given by (4.13) is associated with linear pressure drop only. The assumption of ignoring quadratic pressure drop is valid since the vertical porous barrier is considered thin and is at rest.

4.2 Method of solution

To solve the aforementioned boundary value problems, the variable separation method is employed to expand the eigenfunctions of the velocity potentials. Subsequently, the fact of vanishing horizontal and vertical velocities on the vertical and horizontal sides of the floating structure is utilized. The solutions are matched across the boundaries by using mass flux and pressure continuity. A set of linear algebraic equations is developed to find the unknown coefficients appearing in the expressions of the velocity potentials. Standard matrix techniques are used for obtaining the solution to this system of equations. After that, it becomes possible to calculate the reflection coefficient and the wave forces.

We first go ahead to find the velocity potentials ϕ_j for $j = 1, 2, 3, 4, 5$ in all regions.

Region 1**:**

$$\phi_1(x,z) = e^{\mathrm{i}p_0 x} Z_{0,1}(k_{0,1}, z) + \sum_{n=0}^{\infty} R_n e^{-\mathrm{i}p_n x} Z_{n,1}(k_{n,1}, z), \tag{4.19}$$

where R_0 represents the complex reflection coefficient, while all other R_n denote the decaying modes of reflection. Here, $Z_{n,1}(k_{n,1}, z)$ and p_n are, respectively, as follows:

$$Z_{n,1}(k_{n,1}, z) = -\Big(\frac{\mathrm{i}g}{\omega}\Big)\frac{\cosh(k_{n,1}(z+h_1))}{\cosh(k_{n,1}h_1)}, \quad n = 0, 1, 2, ...,$$
$$p_n = \sqrt{k_{n,1}^2 - k_y^2},$$

where $k_{0,1}$ denotes a positive real root, while $k_{n,1}$'s, for $n \geq 1$, correspond to the purely imaginary roots of the dispersion relation $k\tanh(kh_1) - K = 0$.

Region 2**:**

$$\phi_2(x,z) = \sum_{n=0}^{\infty} \Big(A_n e^{\mathrm{i}q_n x} + B_n e^{-\mathrm{i}q_n x} \Big) Z_{n,2}(k_{n,2}, z), \tag{4.20}$$

with A_n and B_n as the unknown coefficients. Here, $Z_{n,2}(k_{n,2}, z)$ and q_n are, respectively, given by

$$Z_{n,2}(k_{n,2}, z) = -\Big(\frac{\mathrm{i}g}{\omega}\Big) \frac{\cosh(k_{n,2}(z+h_2))}{\cosh(k_{n,2}h_2)}, \quad n = 0, 1, 2, ...,$$
$$q_n = \sqrt{k_{n,2}^2 - k_y^2},$$

where $k_{n,2}$'s are the roots of the dispersion relation $k\tanh(kh_2) - K = 0$.

Region 3**:**

$$\phi_3(x,z) = \sum_{n=0}^{\infty} \Big(C_n e^{\mathrm{i}q_n x} + D_n e^{-\mathrm{i}q_n x} \Big) Z_{n,2}(k_{n,2}, z), \tag{4.21}$$

with the unknown coefficients C_n and D_n.

Region 4**:**

$$\phi_4(x,z) = \sum_{n=0}^{\infty} \Big(E_n \frac{\cosh(s_n x)}{\cosh(s_n b)} + F_n \frac{\sinh(s_n x)}{\sinh(s_n b)} \Big) Z_{n,4}(r_n, z), \tag{4.22}$$

where E_n, F_n are the unknown coefficients, $b = L_2/2$, and $Z_{n,4}(r_n, z)$ and s_n are, respectively, as follows:

$$Z_{n,4}(r_n, z) = -\Big(\frac{\mathrm{i}g}{\omega}\Big) \cos(r_n(z+h_2)), \quad n = 0, 1, 2, ...,$$
$$r_n = \frac{n\pi}{h_2 - h_4} \quad \text{and} \quad s_n = \sqrt{r_n^2 + k_y^2}. \tag{4.23}$$

Region 5**:**

$$\phi_5(x,z) = \sum_{n=0}^{\infty} T_n e^{\mathrm{i}p_n x} Z_{n,1}(k_{n,1}, z), \tag{4.24}$$

where T_n are the unknown coefficients.

By using matching conditions (4.10)-(4.18), and after truncating the infinite series at

$n = N$, we get the following system of equations:

$$\sum_{n=0}^{N} \mathscr{A}_{n,m} R_n - \sum_{n=0}^{N} \gamma_{n,m} A_n - \sum_{n=0}^{N} \gamma_{n,m} B_n = -\mathscr{A}_{0,m}, \tag{4.25}$$

$$\sum_{n=0}^{N} \mathrm{i}p_n \delta_{n,m} R_n + \sum_{n=0}^{N} \mathrm{i}q_n \mathscr{B}_{n,m} A_n - \sum_{n=0}^{N} \mathrm{i}q_n \mathscr{B}_{n,m} B_n = \mathrm{i}p_0 \delta_{0,m}, \tag{4.26}$$

$$\begin{aligned}
&\sum_{n=0}^{N} \Big(\mathrm{i}k_0 G_1 \mathscr{C}_{n,m} - \mathscr{D}_{n,m}\Big) e^{\mathrm{i}q_n L} A_n + \sum_{n=0}^{N} \Big(\mathrm{i}k_0 G_1 \mathscr{C}_{n,m} - \mathscr{D}_{n,m}\Big) e^{-\mathrm{i}q_n L} B_n \\
&\quad - \sum_{n=0}^{N} \Big[\Big(\mathrm{i}k_0 G_1 + \mathrm{i}q_n\Big) \mathscr{C}_{n,m} - \mathscr{D}_{n,m}\Big] e^{\mathrm{i}q_n L} C_n \\
&\quad - \sum_{n=0}^{N} \Big[\Big(\mathrm{i}k_0 G_1 - \mathrm{i}q_n\Big) \mathscr{C}_{n,m} - \mathscr{D}_{n,m}\Big] e^{-\mathrm{i}q_n L} D_n = 0,
\end{aligned} \tag{4.27}$$

$$\begin{aligned}
&\sum_{n=0}^{N} \mathrm{i}q_n e^{\mathrm{i}q_n L} \gamma_{n,m} A_n - \sum_{n=0}^{N} \mathrm{i}q_n e^{-\mathrm{i}q_n L} \gamma_{n,m} B_n - \sum_{n=0}^{N} \mathrm{i}q_n e^{\mathrm{i}q_n L} \gamma_{n,m} C_n \\
&\qquad + \sum_{n=0}^{N} \mathrm{i}q_n e^{-\mathrm{i}q_n L} \gamma_{n,m} D_n = 0,
\end{aligned} \tag{4.28}$$

$$\begin{aligned}
&\sum_{n=0}^{N} e^{\mathrm{i}q_n d_1} \mathscr{E}_{n,m} C_n + \sum_{n=0}^{N} e^{-\mathrm{i}q_n d_1} \mathscr{E}_{n,m} D_n - \sum_{n=0}^{N} \Big(\frac{\cosh(s_n d_1)}{\cosh(s_n b)} \mathscr{F}_{n,m}\Big) E_n \\
&\qquad - \sum_{n=0}^{N} \Big(\frac{\sinh(s_n d_1)}{\sinh(s_n b)} \mathscr{F}_{n,m}\Big) F_n = 0,
\end{aligned} \tag{4.29}$$

$$\begin{aligned}
&\sum_{n=0}^{N} \mathrm{i}q_n e^{\mathrm{i}q_n d_1} \gamma_{n,m} C_n - \sum_{n=0}^{N} \mathrm{i}q_n e^{-\mathrm{i}q_n d_1} \gamma_{n,m} D_n - \sum_{n=0}^{N} s_n \Big(\frac{\sinh(s_n d_1)}{\cosh(s_n b)}\Big) \mathscr{G}_{n,m} E_n \\
&\qquad - \sum_{n=0}^{N} s_n \Big(\frac{\cosh(s_n d_1)}{\sinh(s_n b)}\Big) \mathscr{G}_{n,m} F_n = 0,
\end{aligned} \tag{4.30}$$

$$\begin{aligned}
&\sum_{n=0}^{N} \Big(\frac{\cosh(s_n d_2)}{\cosh(s_n b)} \mathscr{F}_{n,m}\Big) E_n + \sum_{n=0}^{N} \Big(\frac{\sinh(s_n d_2)}{\sinh(s_n b)} \mathscr{F}_{n,m}\Big) F_n \\
&\qquad - \sum_{n=0}^{N} e^{\mathrm{i}p_n d_2} \mathscr{H}_{n,m} T_n = 0,
\end{aligned} \tag{4.31}$$

$$\begin{aligned}
&\sum_{n=0}^{N} \Big(s_n \frac{\sinh(s_n d_2)}{\cosh(s_n b)} \mathscr{I}_{n,m}\Big) E_n + \sum_{n=0}^{N} \Big(s_n \frac{\cosh(s_n d_2)}{\sinh(s_n b)} \mathscr{I}_{n,m}\Big) F_n \\
&\qquad - \sum_{n=0}^{N} \mathrm{i}p_n e^{\mathrm{i}p_n d_2} \delta_{n,m} T_n = 0,
\end{aligned} \tag{4.32}$$

with $d_1 = L + L_1$, $d_2 = L + L_1 + L_2$ and

$$\mathscr{A}_{n,m} = \int_{z=-h_2}^{0} Z_{n,1}(k_{n,1}, z) Z_{m,2}(k_{m,2}, z) dz, \quad \mathscr{B}_{n,m} = \int_{z=-h_2}^{0} Z_{n,2}(k_{n,2}, z) Z_{m,1}(k_{m,1}, z) dz,$$

$$\gamma_{n,m} = \begin{cases} \beta_m & n = m \\ 0 & n \neq m \end{cases}, \quad \beta_m = \int_{z=-h_2}^{0} Z_{m,2}(k_{m,2}, z) Z_{m,2}(k_{m,2}, z) dz,$$

$$\delta_{n,m} = \begin{cases} \alpha_m & n = m \\ 0 & n \neq m \end{cases}, \quad \alpha_m = \int_{z=-h_1}^{0} Z_{m,1}(k_{m,1}, z) Z_{m,1}(k_{m,1}, z) dz,$$

$$\mathscr{C}_{n,m} = \int_{z=-h_3}^{0} Z_{n,2}(k_{n,2}, z) Z_{m,2}(k_{m,2}, z) dz, \quad \mathscr{D}_{n,m} = \int_{z=-h_2}^{-h_3} Z_{n,2}(k_{n,2}, z) Z_{m,2}(k_{m,2}, z) dz,$$

$$\mathscr{E}_{n,m} = \int_{z=-h_2}^{-h_4} Z_{n,2}(k_{n,2}, z) Z_{m,4}(r_m, z) dz, \quad \mathscr{F}_{n,m} = \int_{z=-h_2}^{-h_4} Z_{n,4}(r_n, z) Z_{m,4}(r_m, z) dz,$$

$$\mathscr{G}_{n,m} = \int_{z=-h_2}^{-h_4} Z_{n,4}(r_n, z) Z_{m,2}(k_{m,2}, z) dz, \quad \mathscr{H}_{n,m} = \int_{z=-h_2}^{-h_4} Z_{n,1}(k_{n,1}, z) Z_{m,4}(r_m, z) dz,$$

$$\mathscr{I}_{n,m} = \int_{z=-h_2}^{-h_4} Z_{n,4}(r_n, z) Z_{m,1}(k_{m,1}, z) dz.$$

To calculate the reflection coefficient as well as the wave forces acting on the floating structure, it becomes essential to evaluate the coefficients R_n, A_n, B_n, C_n, D_n, E_n, F_n and T_n. To achieve this, we construct a system of $8N + 8$ linear equations as follows:

$$\mathscr{A}\mathscr{X} = \mathscr{B}, \tag{4.33}$$

where $\mathscr{X} = [R_0, R_1, ..., R_n, A_0, A_1, ..., A_n, B_0, B_1, ..., B_n, C_0, C_1, ..., C_n, D_0, D_1, ..., D_n, E_0, E_1, ..., E_n, F_0, F_1, ..., F_n, T_0, T_1, ..., T_n]^t$ is the vector containing the unknown coefficients, $\mathscr{A}$ is the coefficient matrix of size $(8N + 8) \times (8N + 8)$ and $\mathscr{B}$ is a vector of size $(8N + 8) \times 1$. This gives us the coeffcients required for a full-wave solution. In other words, we mathematically develop the full-wave solution for the considered problem. However, for focusing on the plane-wave solution which corresponds to the propagating mode, we ignore all the infinite summations and consider only the terms corresponding to $n = 0$, that is, the plane wave approximation as in [23] and also our earlier problems. Once the unknown coefficients are determined, we can proceed to evaluate the necessary quantities, namely, the reflection coefficient $|R_0|$ and the wave forces.

To compute the complex-valued horizontal force X_{hf} and vertical force Y_{vf} acting on

the floating structure, we use the formulas given, respectively, by

$$X_{hf} = \mathrm{i}\rho\omega \int_{-h_4}^{0} \left[\phi_5\left(L+L_1+L_2, z\right) - \phi_3\left(L+L_1, z\right)\right] dz, \tag{4.34}$$

$$Y_{vf} = \mathrm{i}\rho\omega \int_{L+L_1}^{L+L_1+L_2} \phi_4\left(x, -h_4\right) dx, \tag{4.35}$$

where X_{hf} is the integral of the pressure difference of both sides of the floating structure, which is easily obtainable from the linearized Bernoulli's equation.

Since the porous barrier is considered as a thin structure, therefore, the horizontal force acting on the porous barrier is given by

$$X_{B_{hf}} = \mathrm{i}\rho\omega \int_{-h_3}^{0} \left[\phi_3\left(L, z\right) - \phi_2\left(L, z\right)\right] dz. \tag{4.36}$$

The non-dimensional forms of the forces X_{hf}, Y_{vf} and $X_{B_{hf}}$ can, respectively, be written as follows:

$$F_h = \frac{|X_{hf}|}{\rho g A b}, \quad F_v = \frac{|Y_{vf}|}{\rho g A b}, \quad B_{hf} = \frac{|X_{B_{hf}}|}{\rho g A b}, \tag{4.37}$$

with ρ as the water density, $b = (L_2/2)$ m and $A = 1$ m the incident wave amplitude.

4.3 Validation

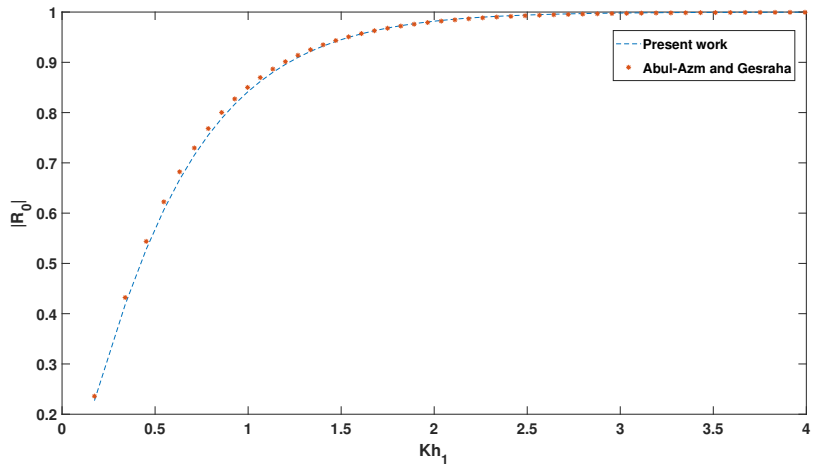

Figure 4.2: Validation of the present work against that of Abul-Azm and Gesraha [2] in the absence of the porous barrier for a flat and impermeable bottom.

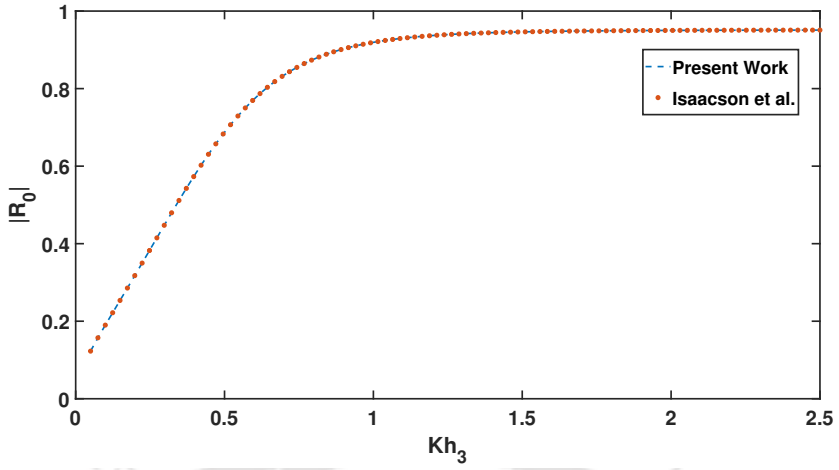

Figure 4.3: Validation of the present work against that of Isaacson et al. [37] in the absence of the floating structure for a flat and impermeable bottom.

In this section, the present work is validated against a couple of earlier works which were carried out for a similar structure. To achieve this, we first consider the work of Abul-Azm and Gesraha [2] with larger absolute value of the complex porous-effect parameter of the thin vertical porous barrier so that the porous barrier acts as a transparent structure. In Figure 4.2, we consider $\theta = 0°$, $L_2/2h_1 = 1$, $h_2/h_1 = 1$ and $h_4/h_1 = 0.25$ for validating our work against that of Abul-Azm and Gesraha [2]. The reflection coefficient is plotted against the dimensionless wavenumber for both models. Figure 4.2 shows that the reflection coefficient for larger absolute value of the porous-effect parameter gives the same pattern as in [2].

For comparing our work with that of Isaacson et al. [37], we neglect the length of the floating structure. In Figure 4.3, for the validation purpose, we consider $\theta = 0$, $h_3/h_1 = 0.5$ and $h_2/h_1 = 1$. Here, the reflection coefficient is plotted against the non-dimensional wavenumber for the present work and that of Isaacson et al. It shows a good agreement between our result and that in [37]. It reveals that the present model can be appropriately used in problems related to the utilization of porous breakwaters to enhance the safety of the VLFS.

4.4 Results and discussion

In this section, we examine the impact of various structural parameters on the reflection coefficient and the forces exerted on the floating structure by developing a numerical code in MATLAB. It may be noted that, the calculation of different quantities involves the use of only a single-mode approximation to the velocity potential associated with the propagating wave as in [23]. For the numerical computation, some physical parameters are considered as follows: acceleration due to gravity $g = 9.81$ m/s^2; $h_1 = 50$ m, $h_2 = 47$

m, $h_3 = 9$ m, $h_4 = 3$ m, $G_1 = 0.5$, $L + L_1 = 100$ m, $L_2 = 30$ m and the angle of wave incidence as $\theta = 30°$.

4.4.1 Effect of the elevated bottom in wave reflection and mitigation of wave forces

Role of the vertical porous barrier on the reflection coefficient

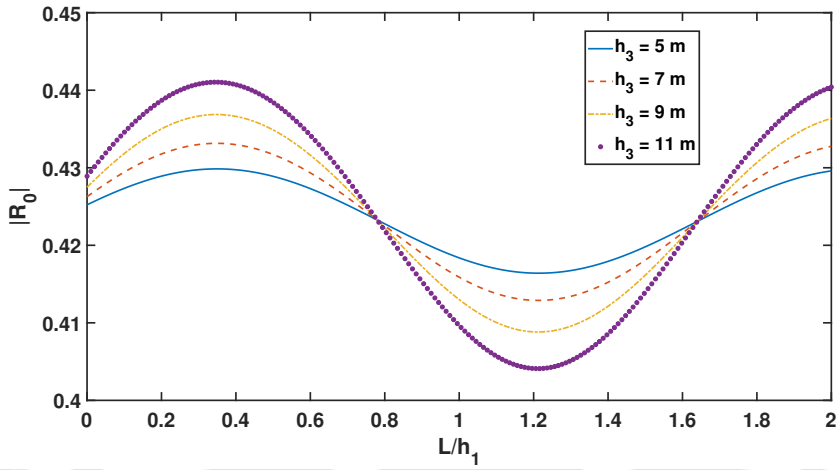

Figure 4.4: $|R_0|$ against L/h_1 for different barrier height h_3 with $h_1 = 50$ m, $h_2 = 47$ m, $h_4 = 3$ m, $G_1 = 0.5$, $L_1 = 100 - L$, $L_2 = 30$ m and $\theta = 30°$

Figure 4.4 illustrates the reflection coefficient plotted against the non-dimensional distance for the different barrier height. As L/h_1 increases, $|R_0|$ demonstrates an oscillatory pattern. It is observed that both maximum and minimum values of $|R_0|$ are obtained at some specific values of L/h_1 corresponding to all values of h_3. However, higher oscillation corresponds to higher values of h_3. Moreover, when the value of h_3 increases, the reflection coefficient also increases. It happens because, with the consideration of higher values of h_3, the porous barrier takes a position closer to the bottom, causing a significant portion of wave energy concentrated near the sea-bed to be reflected by the porous barrier which also dissipates some amount of the wave energy.

Figure 4.5 depicts the variation of the reflection coefficient against the non-dimensional distance corresponding to different values of porous-effect parameter G_1. The reflection coefficient shows a reduction when the absolute value of G_1 increases. This occurrence surfaces since, for larger values of $|G_1|$, the porous barrier becomes almost transparent and hence, more waves can pass through the barrier making $|R_0|$ decrease.

Figure 4.6 illustrates the behaviour of the reflection coefficient against the non-dimensional distance for various values of elevated bottom height h_2. As h_2 increases, that is, when the

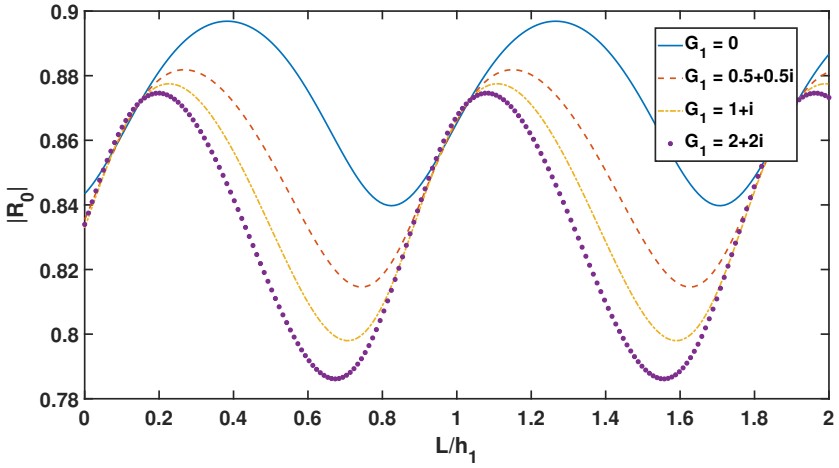

Figure 4.5: Variation of $|R_0|$ against L/h_1 corresponding to various values of porous-effect parameter G_1 with $h_1 = 50$ m, $h_2 = 47$ m, $h_3 = 9$ m, $h_4 = 3$ m, $L_1 = 100 - L$, $L_2 = 30$ m and $\theta = 30°$

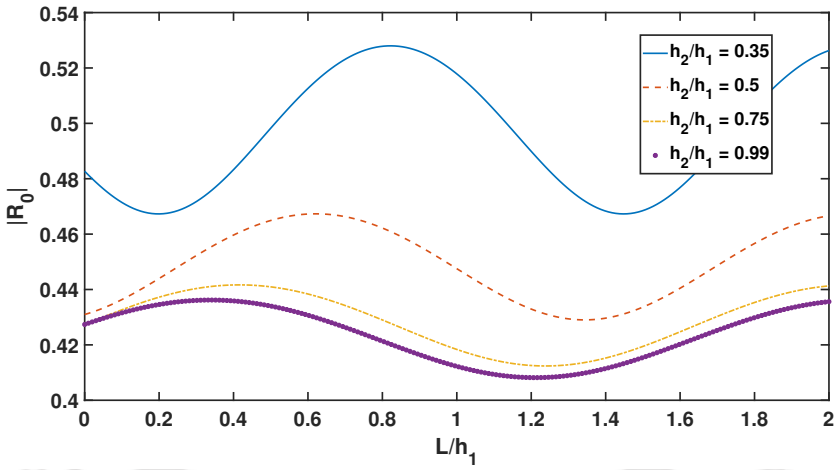

Figure 4.6: Variation of $|R_0|$ against L/h_1 for different elevated bottom height h_2 with $h_1 = 50$ m, $h_3 = 9$ m, $h_4 = 3$ m, $G_1 = 0.5$, $L_1 = 100 - L$, $L_2 = 30$ m and $\theta = 30°$

height of the elevated bottom decreases, the reflection coefficient also reduces. This happens since, for the smallest value of h_2 (i.e., the greatest height of the elevated bottom), the elevated bottom can reflect more waves which results in higher reflection.

Figure 4.7 shows the variation of the reflection coefficient against the wave incident angle across various values of normalized distance L_1 between the barrier and floating structure. The reflection coefficient increases in an oscillatory trend corresponding to an increase in the incident angle. This happens because of the wave energy trapped between the porous barrier and the floating structure as the space between them increases. Additionally, a higher frequency of oscillations occurs with an increase in this distance. At $\theta = 90°$, full reflection is obtained.

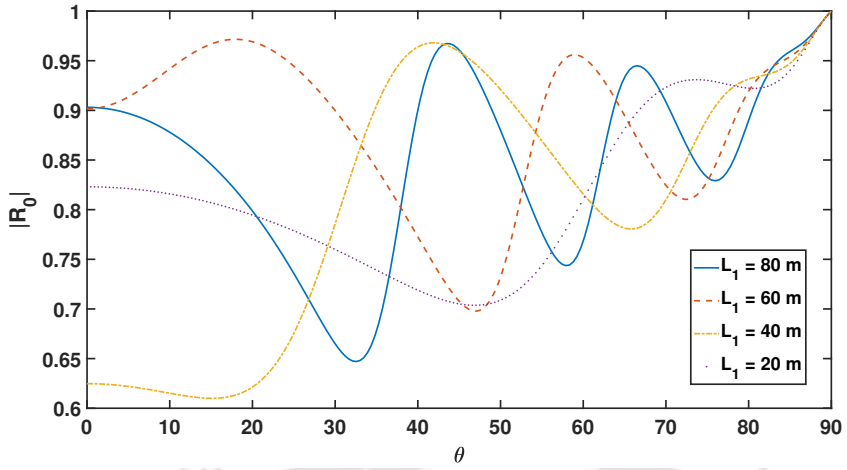

Figure 4.7: $|R_0|$ against θ for different values of L_1 with $h_1 = 50$ m, $h_2 = 47$ m, $h_3 = 9$ m, $h_4 = 3$ m, $G_1 = 0.5$, $L = 100 - L_1$ and $L_2 = 30$ m

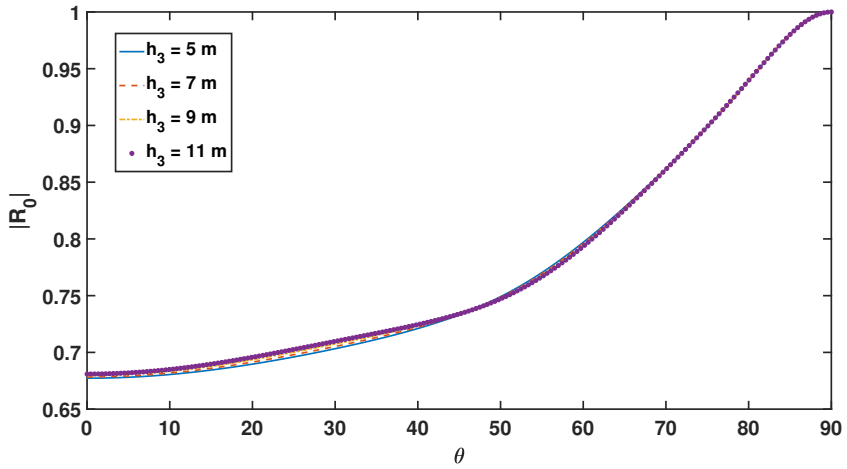

Figure 4.8: $|R_0|$ against θ for different values of height h_3 of the porous barrier with $h_1 = 50$ m, $h_2 = 47$ m, $h_4 = 3$ m, $G_1 = 0.5$, $L + L_1 = 100$ m and $L_2 = 30$ m

Figures 4.8, 4.9 and 4.10 depict the variation in wave reflection against incident wave angle θ for various values of height h_3 of the porous barrier, porous-effect parameter G_1 of the porous barrier and height h_2 of elevated bottom, respectively. Here also, the same pattern concerning h_3, G_1 and h_2 is observed as in Figures 4.4, 4.5 and 4.6. At $\theta = 90°$, full reflection is obtained since the waves are tangential to the structure.

Figure 4.11 depicts the variation of the reflection coefficient against the non-dimensional distance between the porous barrier and the floating structure for different values of h_3. It shows the same pattern of the reflection coefficient as observed in Figure 4.4. Furthermore, we observe a right shift in the oscillation of the reflection coefficient.

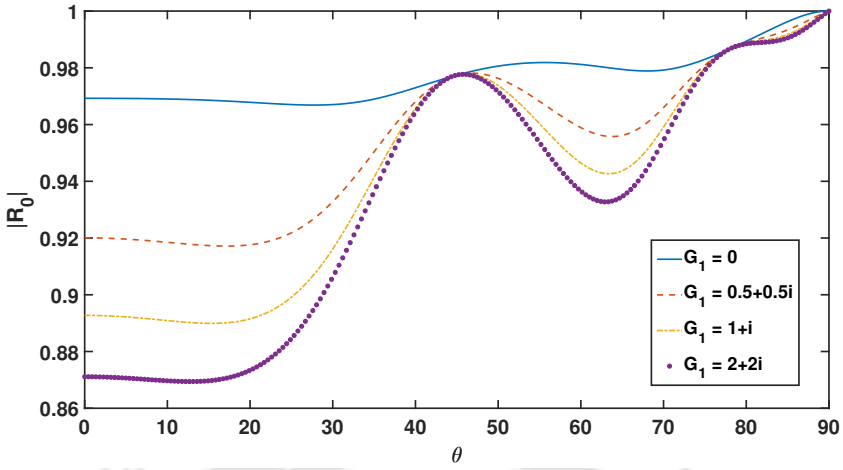

Figure 4.9: $|R_0|$ against θ for different values of porous-effect parameter G_1 of the porous barrier with $h_1 = 50$ m, $h_2 = 47$ m, $h_3 = 9$ m, $h_4 = 3$ m, $L + L_1 = 100$ m, and $L_2 = 30$ m

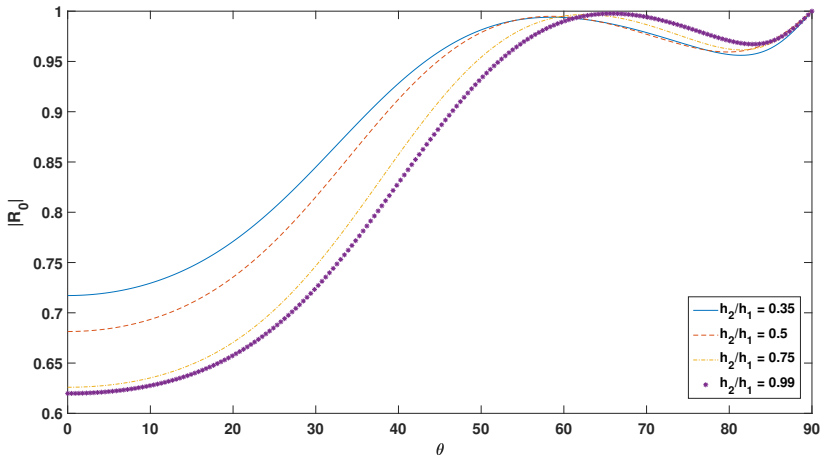

Figure 4.10: $|R_0|$ against θ for different values of height h_2 of the elevated bottom with $h_1 = 50$ m, $h_3 = 9$ m, $h_4 = 3$ m, $G_1 = 0.5$, $L + L_1 = 100$ m and $L_2 = 30$ m

Impact of the vertical porous barrier in the mitigation of wave forces

Here, the impact of the porous barrier in mitigating the wave forces acting on the floating structure in the presence of the elevated bottom topography is studied.

In Figure 4.12, the horizontal force acting on the porous barrier is plotted against L/h_1 for different values of height h_3 of the barrier. An oscillatory pattern is observed with an increase in L/h_1. Figure 4.12 shows that the waveload on the porous barrier increases with an increase in height h_3.

In Figures 4.13 and 4.14, horizontal force F_h and vertical force F_v exerted on the floating structure are depicted against L/h_1 for various values of h_3. These figures exhibit an oscillatory trend as L/h_1 increases. They both show the opposite behaviour of the reflection coefficient as observed in Figure 4.4. From Figure 4.12, the values of h_3 which

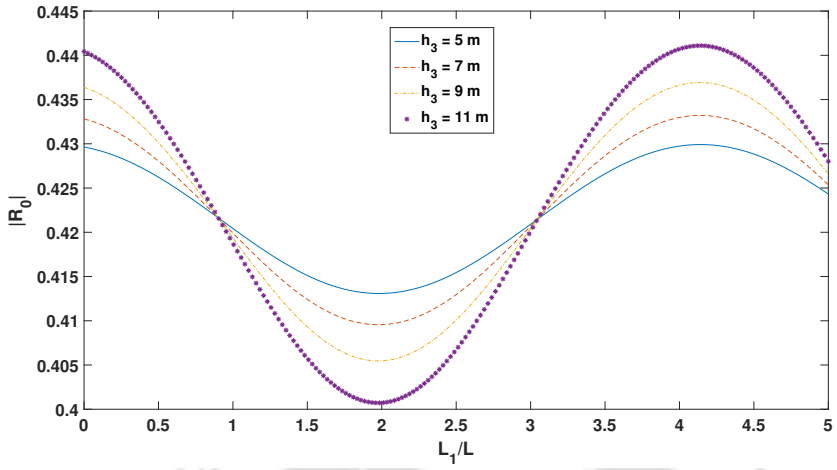

Figure 4.11: $|R_0|$ against non-dimensional distance (L_1/L) between porous barrier and floating structure for different porous barrier height h_3 with $h_1 = 50$ m, $h_2 = 47$ m, $h_4 = 3$ m, $G_1 = 0.5$, $L = 20$ m, $L_2 = 30$ m and $\theta = 30°$

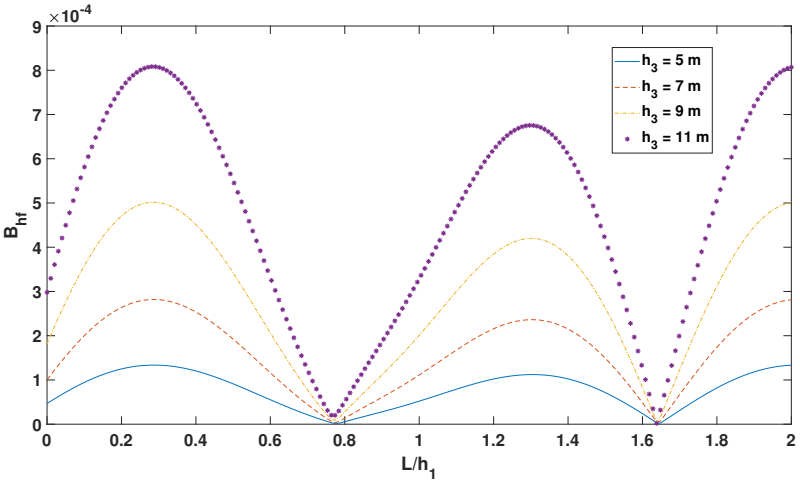

Figure 4.12: Variation of horizontal force B_{hf} acting on the porous barrier against L/h_1 for different values of height h_3 of the porous barrier with $h_1 = 50$ m, $h_2 = 47$ m, $h_4 = 3$ m, $G_1 = 0.5$, $L_1 = 100 - L$, $L_2 = 30$ m and $\theta = 30°$

showed higher waveloads on the vertical porous barrier turn out to cause less amount of forces acting on the floating structure.

Figures 4.15 and 4.16 illustrate the variation of horizontal force F_h and vertical force F_v, respectively, against L/h_1 for different values of the porous-effect parameter. From both figures, it is observed that, as $|G_1|$ increases, the horizontal and vertical forces on the floating structure decrease. This phenomenon can be explained as follows: when $|G_1|$ increases, the waveload on the porous barrier increases. Therefore, it results in the reduction of the wave forces acting on the floating structure.

Figure 4.17 shows the variation of horizontal force F_h against L/h_1 for different values

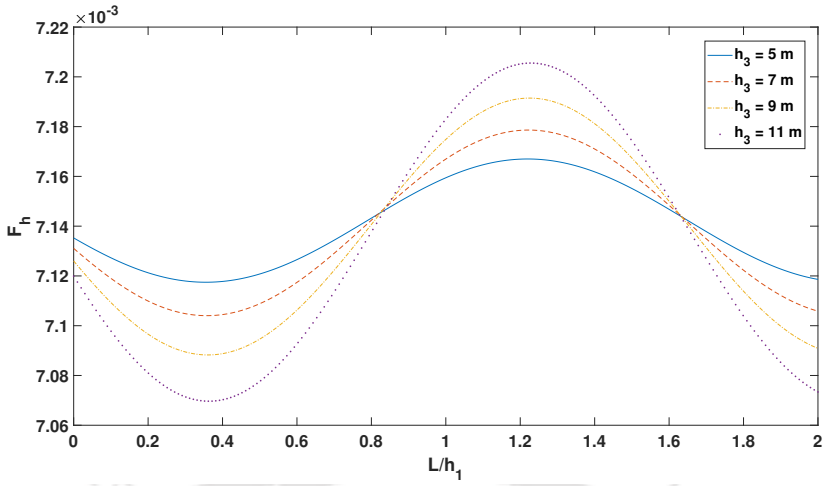

Figure 4.13: Variation of horizontal force F_h acting on the floating structure against L/h_1 for different values of height h_3 of the porous barrier with $h_1 = 50$ m, $h_2 = 47$ m, $h_4 = 3$ m, $G_1 = 0.5$, $L_1 = 100 - L$, $L_2 = 30$ m and $\theta = 30°$

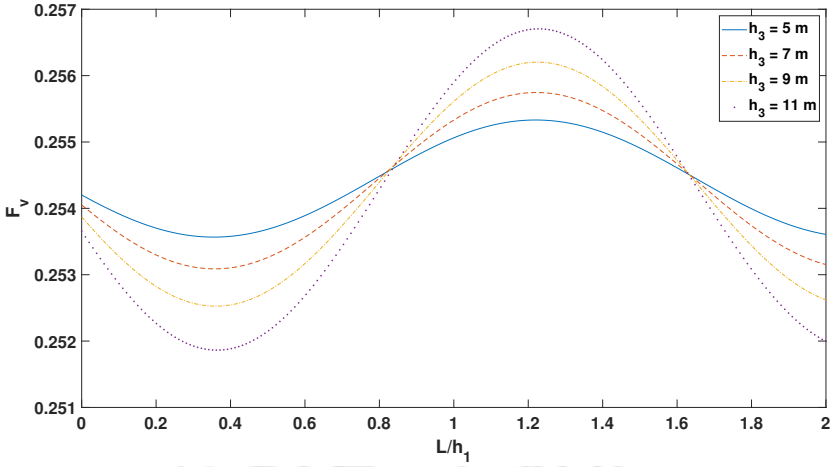

Figure 4.14: Variation of vertical force F_v acting on the floating structure against L/h_1 for different values of height h_3 of the porous barrier with $h_1 = 50$ m, $h_2 = 47$ m, $h_4 = 3$ m, $G_1 = 0.5$, $L_1 = 100 - L$, $L_2 = 30$ m and $\theta = 30°$

of h_2. When the normalized distance between the porous barrier and the floating structure increases, the horizontal force shows an oscillatory pattern. The graph depicted in Figure 4.17 exhibits an opposite nature concerning the reflection coefficient as shown in Figure 4.6.

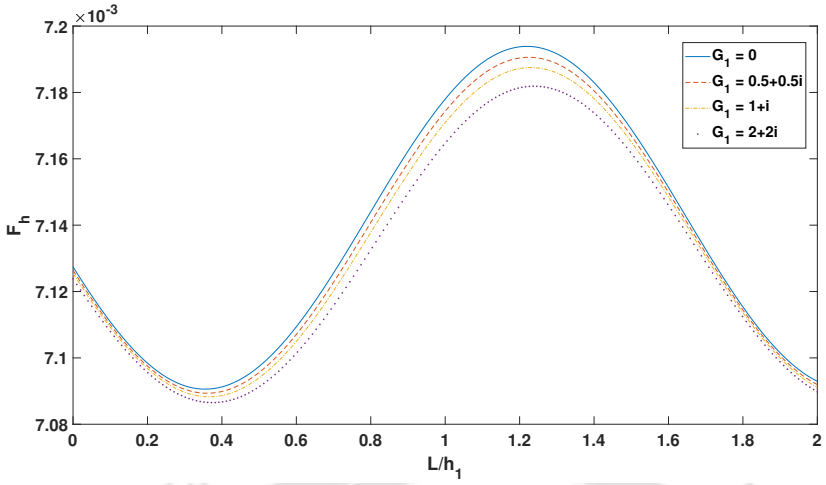

Figure 4.15: Variation of horizontal force F_h acting on the floating structure against L/h_1 for different values of porous-effect parameter G_1 of the porous barrier with $h_1 = 50$ m, $h_2 = 47$ m, $h_3 = 9$ m, $h_4 = 3$ m, $L_1 = 100 - L$, $L_2 = 30$ m and $\theta = 30°$

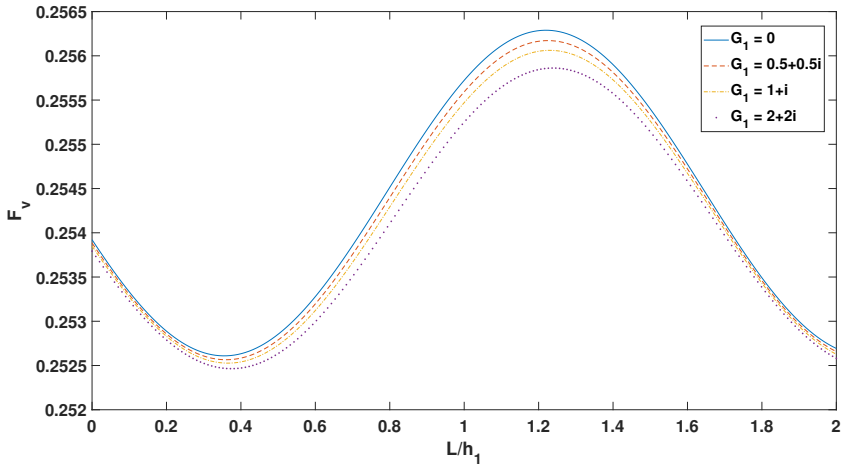

Figure 4.16: Variation of vertical force F_v acting on the floating structure against L/h_1 for different values of porous-effect parameter G_1 of the porous barrier with $h_1 = 50$ m, $h_2 = 47$ m, $h_3 = 9$ m, $h_4 = 3$ m, $L_1 = 100 - L$, $L_2 = 30$ m and $\theta = 30°$

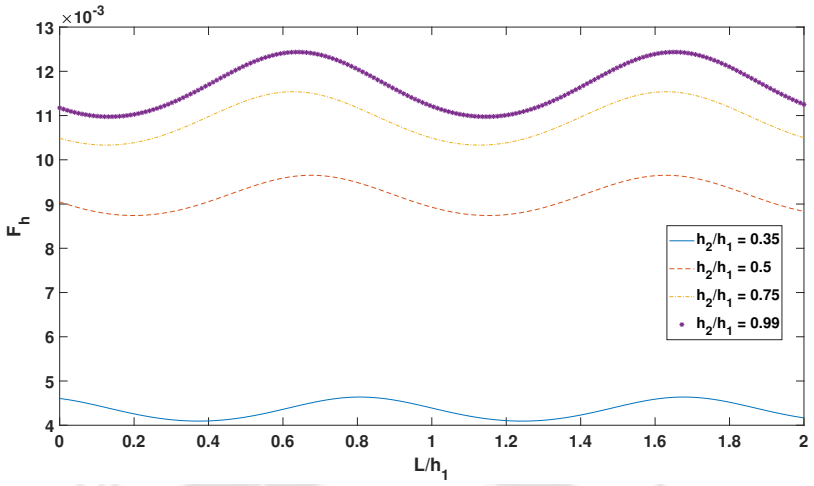

Figure 4.17: Variation of horizontal force F_h acting on the floating structure against L/h_1 for different values of h_2 with $h_1 = 50$ m, $h_3 = 9$ m, $h_4 = 3$ m, $G_1 = 0.5$, $L_1 = 100 - L$, $L_2 = 30$ m and $\theta = 30^\circ$

4.5 Problem extended for a trench-type sea-bed

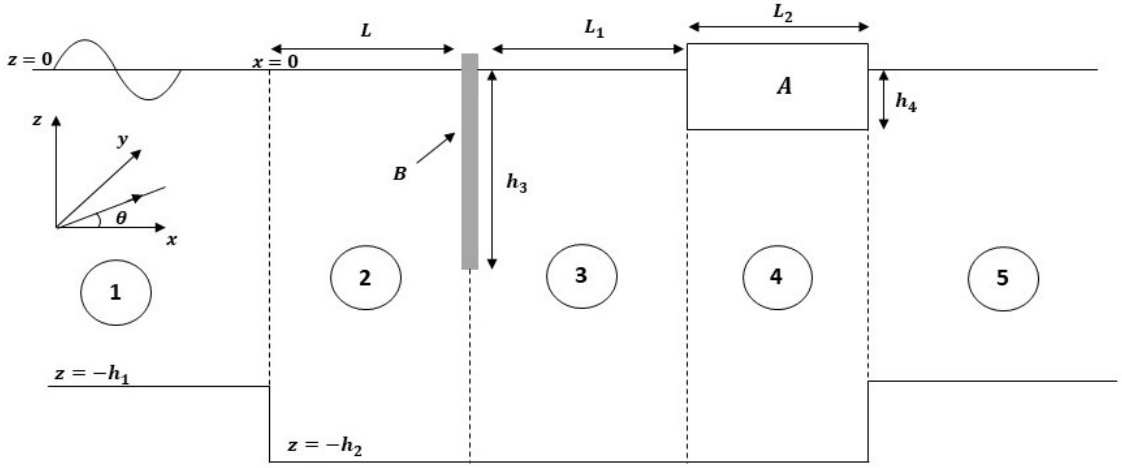

Figure 4.18: Definition sketch of the problem with wave striking a rigid rectangular floating structure placed after a vertical porous barrier in the presence of a trench-type bottom.

In this section, the scattering of water waves by the floating structure in the presence of a vertical porous barrier and a trench is studied. Here, the trench is considered in $0 < x < L + L_1 + L_2$ as shown in Figure 4.18. The expression of the boundary conditions remain unchanged as in the case of the elevated bottom. However, the wall conditions of the trench bottom (which replaces the step-type bottom of problem (i)) are as follows:

$$\frac{\partial \phi_2}{\partial x} = 0 \text{ at } x = 0, \quad -h_2 < z < -h_1, \tag{4.38}$$

$$\frac{\partial \phi_4}{\partial x} = 0 \text{ at } x = L + L_1 + L_2, \quad -h_2 < z < -h_1. \tag{4.39}$$

Now, we go ahead to study the effect of the trench on the wave reflection and the mitigation of the wave forces acting on the floating structure.

4.5.1 Role of the vertical porous barrier on the reflection coefficient

Here, we study how the trench and the porous barrier affect the reflection of the waves.

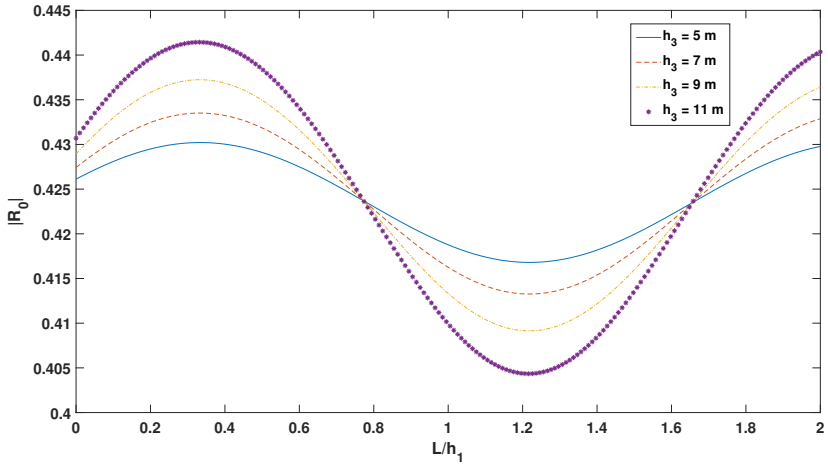

Figure 4.19: Variation of $|R_0|$ against L/h_1 for different porous barrier height h_3 with $h_1 = 50$ m, $h_2 = 55$ m, $h_4 = 3$ m, $G_1 = 0.5$, $L_1 = 100 - L$, $L_2 = 30$ m and $\theta = 30°$

Figure 4.19 illustrates the behaviour of reflection coefficient $|R_0|$ against non-dimensional distance L/h_1 across various values of h_3. The reflection coefficient demonstrates an oscillatory trend as L/h_1 increases. It is observed that both maximum and minimum values of $|R_0|$ are obtained at some specific values of L/h_1 for all the values of h_3. However, as h_3 increases, the reflection coefficient also increases because a higher value of h_3 can reflect more waves.

Figure 4.20 depicts the variation of the reflection coefficient against non-dimensional distance L/h_1 for various values of porous-effect parameter G_1. The reflection coefficient decreases as the absolute value of G_1 increases since, for larger values of $|G_1|$, the porous barrier becomes almost transparent whereby more waves can pass through the barrier, and consequently, $|R_0|$ decreases.

Figure 4.21 displays the effect of the trench on the reflection coefficient when plotted against L/h_1. Here, $h_2 = h_1$ represents the flat bottom, and $h_2 > h_1$ indicates the presence of a trench. The reflection coefficient demonstrates an oscillatory trend as L/h_1 increases. We obtain the maxima and minima of the reflection coefficient at some specific values of L/h_1 for all h_3. It is noted that, with an increase in h_2, there also occurs an increase in

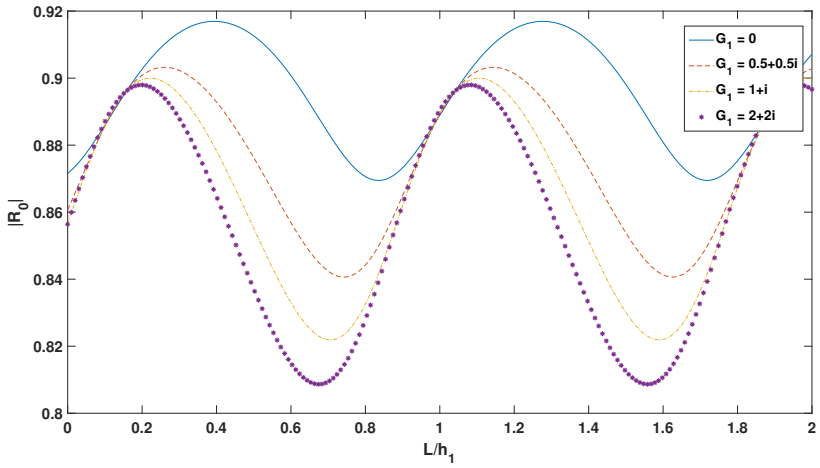

Figure 4.20: Variation of $|R_0|$ against L/h_1 for different values of porous-effect parameter G_1 with $h_1 = 50$ m, $h_2 = 55$ m, $h_3 = 9$ m, $h_4 = 3$ m, $L_1 = 100 - L$, $L_2 = 30$ m and $\theta = 30°$

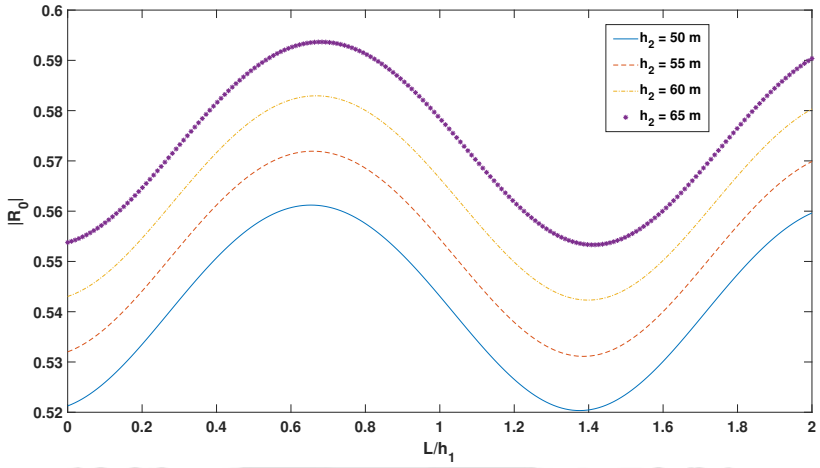

Figure 4.21: Variation of $|R_0|$ against L/h_1 for different values of h_2 with $h_1 = 50$ m, $h_3 = 9$ m, $h_4 = 3$ m, $G_1 = 0.5$, $L_1 = 100 - L$, $L_2 = 30$ m and $\theta = 30°$

the reflection coefficient. Corresponding to higher values of h_2, the reflection coefficient too attains higher values.

In Figure 4.22, the reflection coefficient is plotted against non-dimensional distance L_1/L between the porous barrier and floating structure for the different values of h_3. In the presence of the trench, the same behaviour of the reflection coefficient is observed, as noted in the case of an elevated bottom, i.e., in Figure 4.11.

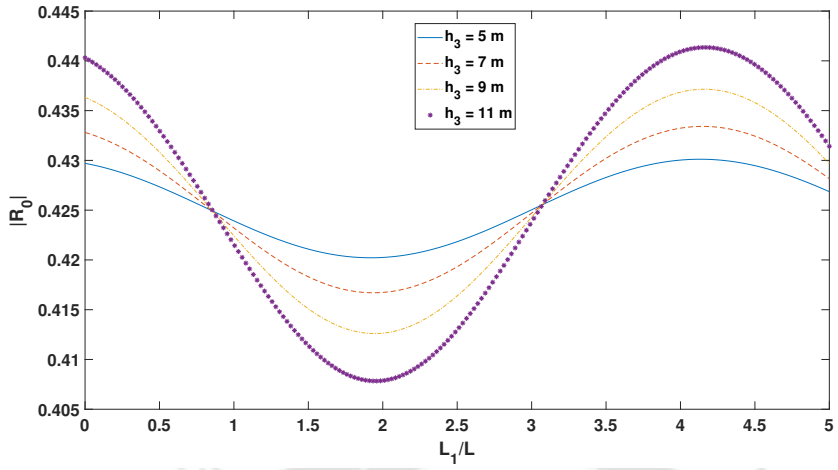

Figure 4.22: $|R_0|$ against non-dimensional distance (L_1/L) between porous barrier and floating structure for different porous barrier height h_3 with $h_1 = 50$ m, $h_2 = 55$ m, $h_4 = 3$ m, $G_1 = 0.5$, $L = 20$ m, $L_2 = 30$ m and $\theta = 30°$

4.5.2 Impact of the vertical porous barrier in the reduction of forces

The effect of the thin vertical porous barrier in mitigating waveload on the floating structure in the presence of the trench-type bottom is studied.

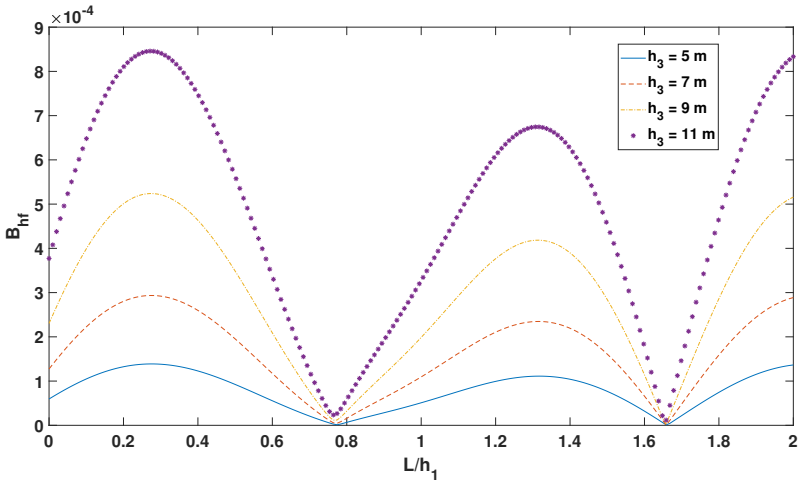

Figure 4.23: Variation of horizontal force B_{hf} acting on the porous barrier against L/h_1 for different values of the height h_3 of the porous barrier with $h_1 = 50$ m, $h_2 = 55$ m, $h_4 = 3$ m, $G_1 = 0.5$, $L_1 = 100 - L$, $L_2 = 30$ m and $\theta = 30°$

In Figure 4.23, the horizontal force acting on the porous barrier is plotted against L/h_1 for different values of height h_3 of the barrier. Here also, the same pattern is observed as in Figure 4.12. It shows that the waveload on the porous barrier increases with an increase in height h_3.

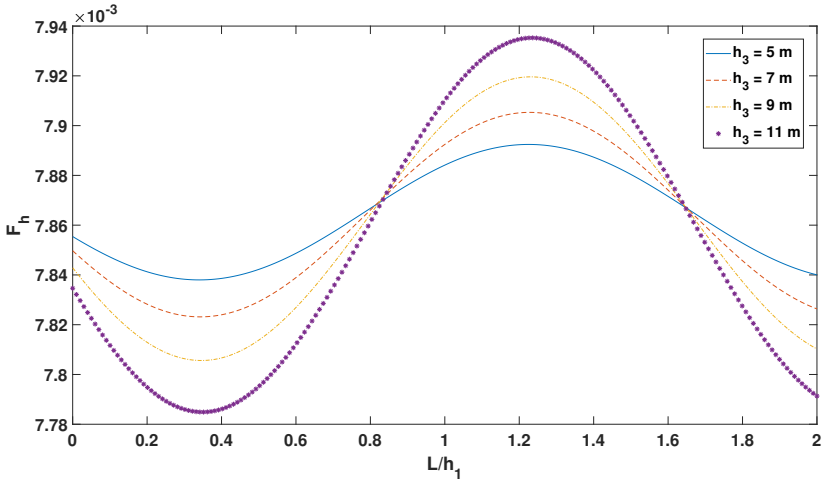

Figure 4.24: Variation of horizontal force F_h acting on the floating structure against L/h_1 for different values of porous barrier height h_3 with $h_1 = 50$ m, $h_2 = 55$ m, $h_4 = 3$ m, $G_1 = 0.5$, $L_1 = 100 - L$, $L_2 = 30$ m and $\theta = 30°$

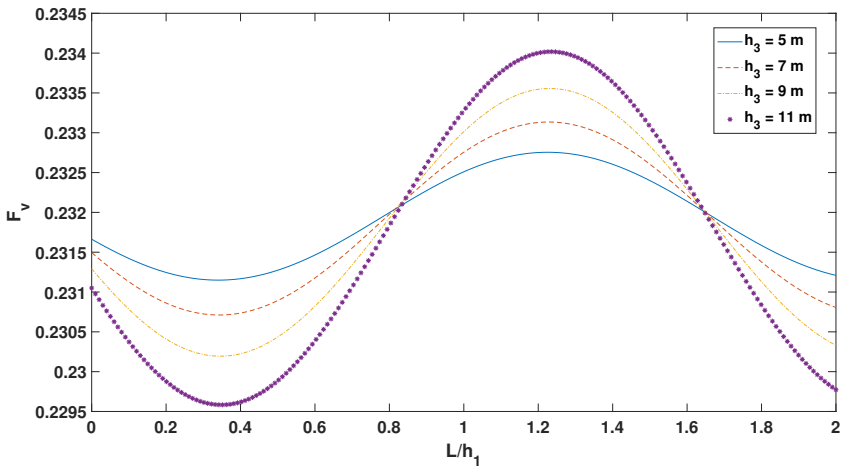

Figure 4.25: Variation of vertical force F_v acting on the floating structure against L/h_1 for different values of porous barrier height h_3 with $h_1 = 50$ m, $h_2 = 55$ m, $h_4 = 3$ m, $G_1 = 0.5$, $L_1 = 100 - L$, $L_2 = 30$ m and $\theta = 30°$

In Figures 4.24 and 4.25, we plot the horizontal and vertical forces, respectively, against L/h_1 for various values of height h_3 of the vertical porous barrier. It is noticeable that, with an increase in height h_3 of the porous barrier, both the horizontal and vertical forces acting on the floating structure exhibit a reduction. In this case, we get an opposite trend of the forces as compared with the reflection coefficient as observed in Figure 4.19.

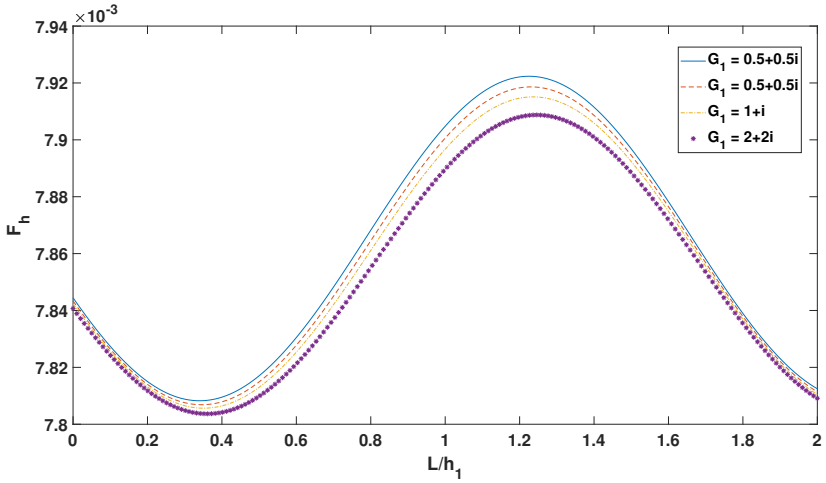

Figure 4.26: Variation of horizontal force F_h acting on the floating structure against L/h_1 corresponding to various values of G_1 with $h_1 = 50$ m, $h_2 = 55$ m, $h_3 = 9$ m, $h_4 = 3$ m, $L_1 = 100 - L$, $L_2 = 30$ m and $\theta = 30°$

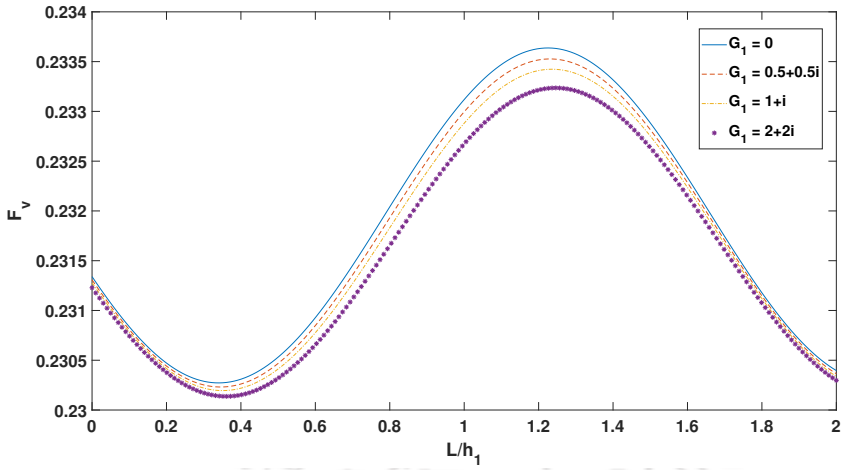

Figure 4.27: Variation of vertical force F_v acting on the floating structure against L/h_1 corresponding to various values of G_1 with $h_1 = 50$ m, $h_2 = 55$ m, $h_3 = 9$ m, $h_4 = 3$ m, $L_1 = 100 - L$, $L_2 = 30$ m and $\theta = 30°$

Figures 4.26 and 4.27, respectively, show the variation of the horizontal force and the vertical force against L/h_1 corresponding to various values of porous-effect parameter G_1. It is observed from both figures that, as the absolute value of the porous-effect parameter increases, the horizontal and vertical forces exerted on the floating structure decrease. It can be explained as follows: when the value of $|G_1|$ increases, the waveload on the porous barrier also increases. This brings a reduction in the horizontal and vertical forces.

4.6 Conclusions

In this work, the effect of the porous barrier as well as that of an uneven sea-bed in a specific form was examined for their role in mitigating wave force on a rectangular rigid floating structure. Two types of bottom configuration were considered: (i) an elevated-type, and (ii) a trench-type. The porous barrier was placed at some distance in front of the floating structure. The fluid domain was divided into five sub-regions in each of which the separation of variables and eigenfunction expansion methods were used to obtain the scattered velocity potential in each sub-region. The mathematical development was carried out for the full-wave solution. For computational purpose, the plane-wave solution was analyzed through the results with the help of MATLAB. Once the unknown coefficients were known, the reflection coefficient and the hydrodynamic forces acting on the porous barrier and the floating structure were evaluated.

To understand the role of different bottom topography and the porous barrier, we plotted the reflection coefficient and wave forces against the dimensionless distance between the porous barrier and floating structure, and wave incident angle. It was noted that, when the distance between the porous barrier and the floating structure increased, the reflection coefficient and the hydrodynamic forces on the porous barrier and the floating structure showed an oscillatory pattern. The effect of both bottom topographies on the reflection coefficient and wave forces was thoroughly studied. As the height of the elevated bottom or trench-bottom increased, the reflection coefficient also increased – the reflection in the presence of a trench was observed to be higher than the one due to the elevated bottom. We also studied various parameters of the porous barrier to clearly understand their impact. As the height of the porous barrier increased, the wave reflection and the horizontal force on the barrier also increased, and as a result, the horizontal and vertical forces on the floating structure reduced. The influence of the porous-effect parameter on the reflection coefficient, and the horizontal and vertical forces acting on the floating structure was also investigated. Further, the study revealed that the reflection coefficient increased with an oscillatory trend as the wave incident angle increased corresponding to different values of the normalized distance between the porous barrier and the floating structure. The results of the present study were successfully validated against available results for verifying the effectiveness of this model. The ideas and methods explained in this work may be utilized in addressing similar type of issues in ocean engineering and allied subjects. Furthermore, the present modeling is expected to be valuable in reducing the wave action on large floating structures.

Although the present model is expected to serve a reasonable number of problems in ocean engineering involving breakwater, the future for such investigations can be envisaged as per the following trajectory:

1. The quadratic pressure drop, ignored in this work, may be considered which will

present the exact situation regarding pressure drop across the thin vertical porous barrier.

2. For lower values of the porous effect-parameter, the possibility of sloshing may be accounted for.

3. The sea-bed may be considered to comprise a number of steps or trenches.

CHAPTER 5

Scattering of oblique incident waves by a rigid floating structure in the presence of two surface-piercing thick porous breakwaters

In this work, the water wave interaction with a floating structure in the presence of two surface-piercing rectangular porous structures is studied to ascertain the attenuation of the wave-induced forces on the floating structure. The porous structures are assumed to have different heights and porosity. The water depth is considered finite, and the sea-bed flat and impermeable. The laterally unbounded fluid domain is divided into nine regions and the boundary value problems are formulated in each of them in a three-dimensional Cartesian coordinate system under the assumption of linearized water wave theory. For solving the boundary value problems, an eigenfunction expansion method is used. The effect of various parameters on the reflection coefficient, transmission coefficient, dissipation coefficient, and horizontal and vertical wave forces is studied. This work intends to determine the appropriate porosity of the porous structures (breakwaters) in order to mitigate the hydrodynamic responses on the floating structure. For reducing the wave-induced forces on the floating structure, the thickness of the porous structure is also analyzed. Moreover, the impact of the height of the porous structures is also studied. In order to match our model with some practical application, the rigid floating structure can be viewed as a floating bridge or a floating airport or any other such facility.

5.1 Mathematical Formulation

The interaction of oblique water waves with a floating structure, in the presence of two surface-piercing porous breakwaters, is studied using linearized water wave theory. A

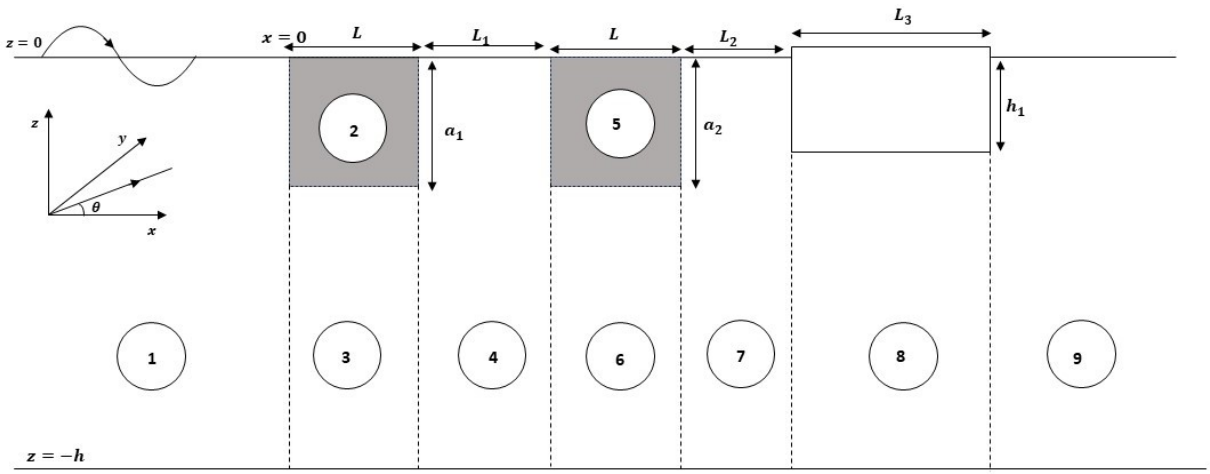

Figure 5.1: Definition sketch of the problem

right-handed Cartesian system is considered with the x-axis in the horizontal direction and the z-axis in the upward vertical direction, as shown in Figure 5.1. Each of the porous structures is considered to be of width L and heights a_1 and a_2, and they are placed between $0 \leq x \leq L$ and $L + L_1 \leq x \leq 2L + L_1$ with L_1 the distance between these porous structures. The second porous structure is placed at a distance L_2 before the floating structure, which is assumed to be a rigid rectangular structure of length L_3 and draft h_1. The sea-bed, considered flat and impermeable, is located at $z = -h$. The whole fluid domain is divided into nine regions: Region 1 $(-\infty < x < 0, -h < z < 0)$; Region 2, a porous region $(0 \leq x \leq L, -a_1 < z < 0)$; Region 3 $(0 \leq x \leq L, -h < z < -a_1)$; Region 4 $(L \leq x \leq L+L_1, -h < z < 0)$; Region 5, a porous region $(L+L_1 \leq x \leq 2L+L_1, -a_2 < z < 0)$; Region 6 $(L + L_1 \leq x \leq 2L + L_1, -h < z < -a_2)$; Region 7 $(2L + L_1 \leq x \leq 2L+L_1+L_2, -h < z < 0)$; Region 8 $(2L+L_1+L_2 \leq x \leq 2L+L_1+L_2+L_3, -h < z < -h_1)$; Region 9 $(2L + L_1 + L_2 + L_3 < x < \infty, -h < z < 0)$. Additionally, the motion is considered simple harmonic along the y-direction as well as with respect to time with an angular wave frequency of ω. The scattered potential for an oblique incident water wave in each fluid region is expressed as follows: $\Phi_j(x, y, z, t) = \mathrm{Re}[\phi_j(x, z)e^{\mathrm{i}(k_y y - \omega t)}]$ for $j = 1, 2, 3, 5, 6, 7, 8, 9$, where $k_y = k_0 \sin(\theta)$, θ is the incident wave angle to the x-axis, and k_0 is the incident wavenumber.

Each of the spatial velocity potential satisfies the modified Helmholtz equation as follows:

$$\left(\frac{\partial^2}{\partial x^2} + \frac{\partial^2}{\partial z^2} - k_y^2\right)\phi_j = 0 \quad \text{for} \quad j = 1, 2, 3, 4, 5, 6, 7, 8, 9. \tag{5.1}$$

The linearized free surface condition for Regions 1, 4, 7 and 9 is the following:

$$\frac{\partial \phi_j}{\partial z} - K\phi_j = 0 \quad \text{for} \quad j = 1, 4, 7, 9 \quad \text{at} \quad z = 0, \tag{5.2}$$

while the mean free surface condition in Region 2 is

$$\frac{\partial \phi_2}{\partial z} - K\gamma_1\phi_2 = 0 \ \text{ at } \ z = 0, \tag{5.3}$$

and that in Region 5 is given by

$$\frac{\partial \phi_5}{\partial z} - K\gamma_2\phi_5 = 0 \ \text{ at } \ z = 0, \tag{5.4}$$

where $\gamma_1 = m_1 + \mathrm{i}f_1$ and $\gamma_2 = m_2 + \mathrm{i}f_2$, respectively, are the dimensionless porous impedance parameters of the first and second porous structures with m_1 and m_2 representing the corresponding the inertial coefficients, and f_1 and f_2 representing the corresponding linearized friction factors, as in [83].

The boundary condition on the flat and impermeable sea-bed is

$$\frac{\partial \phi_j}{\partial z} = 0 \ \text{ for } \ j = 1, 3, 4, 6, 7, 8, 9 \ \text{ at } \ z = -h. \tag{5.5}$$

The floating structure being rigid, the horizontal and vertical velocities vanish on its sides. This leads to the following boundary conditions on the vertical and horizontal sides:

$$\frac{\partial \phi_7}{\partial x} = 0 \ \text{ at } \ x = 2L + L_1 + L_2, \ \ -h_1 < z < 0, \tag{5.6}$$

$$\frac{\partial \phi_9}{\partial x} = 0 \ \text{ at } \ x = 2L + L_1 + L_2 + L_3, \ \ -h_1 < z < 0, \tag{5.7}$$

$$\frac{\partial \phi_8}{\partial z} = 0 \ \text{ at } \ z = -h_1, \ \ 2L + L_1 + L_2 < x < 2L + L_1 + L_2 + L_3. \tag{5.8}$$

When fluid passes through the virtual boundaries, the continuity of mass flux and pressure gives rise to the following matching conditions across the vertical boundaries $x = 0$, $x = L$, $x = L + L_1$, $x = 2L + L_1$, $x = 2L + L_1 + L_2$, and $x = 2L + L_1 + L_2 + L_3$, and the horizontal boundaries $z = -a_1$ and $z = -a_2$, as applicable:

$$\phi_1 = \gamma_1\phi_2 \ \text{ at } \ x = 0, \ \ -a_1 < z < 0, \tag{5.9}$$

$$\frac{\partial \phi_1}{\partial x} = \epsilon_1 \frac{\partial \phi_2}{\partial x} \ \text{ at } \ x = 0, \ \ -a_1 < z < 0, \tag{5.10}$$

$$\phi_1 = \phi_3 \ \text{ at } \ x = 0, \ \ -h < z < -a_1, \tag{5.11}$$

$$\frac{\partial \phi_1}{\partial x} = \frac{\partial \phi_3}{\partial x} \ \text{ at } \ x = 0, \ \ -h < z < -a_1, \tag{5.12}$$

$$\gamma_1\phi_2 = \phi_3 \ \text{ at } \ z = -a_1, \ \ 0 < x < L, \tag{5.13}$$

$$\epsilon_1 \frac{\partial \phi_2}{\partial z} = \frac{\partial \phi_3}{\partial z} \ \text{ at } \ z = -a_1, \ \ 0 < x < L, \tag{5.14}$$

$$\gamma_1\phi_2 = \phi_4 \ \text{ at } \ x = L, \ \ -a_1 < z < 0, \tag{5.15}$$

$$\epsilon_1 \frac{\partial \phi_2}{\partial x} = \frac{\partial \phi_4}{\partial x} \ \text{ at } \ x = L, \ \ -a_1 < z < 0, \tag{5.16}$$

$$\phi_3 = \phi_4 \text{ at } x = L, \ -h < z < -a_1, \tag{5.17}$$
$$\frac{\partial \phi_3}{\partial x} = \frac{\partial \phi_4}{\partial x} \text{ at } x = L, \ -h < z < -a_1, \tag{5.18}$$
$$\phi_4 = \gamma_2 \phi_5 \text{ at } x = L + L_1, \ -a_2 < z < 0, \tag{5.19}$$
$$\frac{\partial \phi_4}{\partial x} = \epsilon_2 \frac{\partial \phi_5}{\partial x} \text{ at } x = L + L_1, \ -a_2 < z < 0, \tag{5.20}$$
$$\phi_4 = \phi_6 \text{ at } x = L + L_1, \ -h < z < -a_2, \tag{5.21}$$
$$\frac{\partial \phi_4}{\partial x} = \frac{\partial \phi_6}{\partial x} \text{ at } x = L + L_1, \ -h < z < -a_2, \tag{5.22}$$
$$\gamma_2 \phi_5 = \phi_6 \text{ at } z = -a_2, \ L + L_1 < x < 2L + L_1, \tag{5.23}$$
$$\epsilon_2 \frac{\partial \phi_5}{\partial z} = \frac{\partial \phi_6}{\partial z} \text{ at } z = -a_2, \ L + L_1 < x < 2L + L_1, \tag{5.24}$$
$$\gamma_2 \phi_5 = \phi_7 \text{ at } x = 2L + L_1, \ -a_2 < z < 0, \tag{5.25}$$
$$\epsilon_2 \frac{\partial \phi_5}{\partial x} = \frac{\partial \phi_7}{\partial x} \text{ at } x = 2L + L_1, \ -a_2 < z < 0, \tag{5.26}$$
$$\phi_6 = \phi_7 \text{ at } x = 2L + L_1, \ -h < z < -a_2, \tag{5.27}$$
$$\frac{\partial \phi_6}{\partial x} = \frac{\partial \phi_7}{\partial x} \text{ at } x = 2L + L_1, \ -h < z < -a_2, \tag{5.28}$$
$$\phi_7 = \phi_8 \text{ at } x = 2L + L_1 + L_2, \ -h < z < -h_1, \tag{5.29}$$
$$\frac{\partial \phi_7}{\partial x} = \frac{\partial \phi_8}{\partial x} \text{ at } x = 2L + L_1 + L_2, \ -h < z < -h_1, \tag{5.30}$$
$$\phi_8 = \phi_9 \text{ at } x = 2L + L_1 + L_2 + L_3, \ -h < z < -h_1, \tag{5.31}$$
$$\frac{\partial \phi_8}{\partial x} = \frac{\partial \phi_9}{\partial x} \text{ at } x = 2L + L_1 + L_2 + L_3, \ -h < z < -h_1, \tag{5.32}$$

where ϵ_1 and ϵ_2 are the porosity of the first and second porous structures, respectively.

In addition to the above conditions, appropriate edge conditions are to be satisfied by some of the velocity potentials for such problems as in [24]. In the present context, we require the satisfaction of the condition given by

$$r^{\frac{1}{3}} \nabla \phi \text{ is bounded as } r \to 0, \tag{5.33}$$

where r is the distance from a submerged edge of the thick porous structures or floating structure.

For our case, we require the following:

The left and right edge conditions for the first thick porous structure:

$$\begin{aligned} &r_1^{\frac{1}{3}} \nabla \phi_1 \text{ is bounded as } r_1 \to 0 \text{ where } r_1^2 = x^2 + (z + a_1)^2, \\ &r_2^{\frac{1}{3}} \nabla \phi_4 \text{ is bounded as } r_2 \to 0 \text{ where } r_2^2 = (x - L)^2 + (z + a_1)^2. \end{aligned} \tag{5.34}$$

The left and right edge conditions for the second thick porous structure:

$$r_3^{\frac{1}{3}} \nabla \phi_4 \text{ is bounded as } r_3 \to 0 \text{ where } r_3^2 = (x - L - L_1)^2 + (z + a_2)^2,$$

$$r_4^{\frac{1}{3}}\nabla\phi_7 \text{ is bounded as } r_4 \to 0 \text{ where } r_4^2 = (x-2L-L_1)^2 + (z+a_2)^2. \quad (5.35)$$

The left and right edge conditions for the floating structure:

$$\begin{aligned} r_5^{\frac{1}{3}}\nabla\phi_7 &\text{ is bounded as } r_5 \to 0 \text{ where } r_5^2 = (x-2L-L_1-L_2)^2 + (z+h_1)^2, \\ r_6^{\frac{1}{3}}\nabla\phi_9 &\text{ is bounded as } r_6 \to 0 \text{ where } r_6^2 = (x-2L-L_1-L_2-L_3)^2 \\ &\qquad +(z+h_1)^2. \end{aligned} \quad (5.36)$$

The above conditions are found to be satisfied at the corners of each structure.
The far-field conditions are given by

$$\phi_1(x,z) = -\frac{\mathrm{i}g}{\omega}(e^{\mathrm{i}p_0 x} + R_0 e^{-\mathrm{i}p_0 x})\frac{\cosh(k_0(z+h))}{\cosh(k_0 h)} \text{ as } x \to -\infty, \quad (5.37)$$

$$\phi_9(x,z) = -\frac{\mathrm{i}g}{\omega}T_0 e^{\mathrm{i}p_0 x}\frac{\cosh(k_0(z+h))}{\cosh(k_0 h)} \text{ as } x \to \infty, \quad (5.38)$$

where R_0 and T_0, respectively, are the unknown reflection and transmission coefficients, k_0 is the root of the dispersion relation $k\tanh(kh) - K = 0$ and $p_0 = \sqrt{k_0^2 - k_y^2}$.

Remark

It may be observed that, due to the presence of the porous breakwaters, some of the matching conditions across the vertical boundaries are different from the usual ones. These also lead to dispersion relations which are not like the standard ones. Such dispersion relations can be found in the next section. In this context, we refer to some works, such as Barman and Bora [3], Boral et al. [11], Behera et al. [6], Chanda and Bora [17], Yang et al. [93] etc.

5.2 Solution procedure

The above-mentioned boundary value problems are solved by applying the separation of variables method to equation (5.1), with eigenfunction expansion of the velocity potentials adopted in each region. Then, the boundary conditions on the horizontal and vertical sides of the floating structure are applied. Following that, the matching conditions across the virtual boundaries are employed to generate a system of linear equations. This set of linear equations is then solved using MATLAB in order to determine the values of the unknown coefficients appearing in the expressions of the velocity potentials. From this evaluation, we can calculate the necessary quantities, such as the reflection coefficient, transmission coefficient, dissipation coefficient and the wave-induced forces acting on the floating structure.

We first find the velocity potentials $\phi_j(x,z)$ for $j = 1,2,3,4,5,6,7,8,9$ in each region.

The velocity potential $\phi_1(x,z)$ in Region 1 can be expressed as

$$\phi_1(x,z) = \big(e^{\mathrm{i}p_0 x}Z_{0,1}(k_0,z) + \sum_{n=0}^{\infty} R_n e^{-\mathrm{i}p_n x}Z_{n,1}(k_n,z)\big), \tag{5.39}$$

with the depth eigenfunction $Z_{n,1}(k_n,z)$ and p_n given, respectively, by

$$Z_{n,1}(k_n,z) = -\Big(\frac{\mathrm{i}g}{\omega}\Big)\frac{\cosh(k_n(z+h))}{\cosh(k_n h)}, \quad n = 0,1,2,...,$$
$$p_n = \sqrt{k_n^2 - k_y^2}.$$

In above, k_n's are the roots of the dispersion relation

$$k\tanh(kh) - K = 0, \tag{5.40}$$

and R_n's are the unknown complex reflection coefficients.

In Region 2, the scattered potential $\phi_2(x,z)$ has the following form:

$$\phi_2(x,z) = \sum_{n=0}^{\infty}\big(A_n e^{\mathrm{i}q_{n,1}x} + B_n e^{-\mathrm{i}q_{n,1}x}\big)Z_{n,2}(t_{n,1},z), \tag{5.41}$$

with the depth eigenfunction $Z_{n,2}(t_{n,1},z)$, $S_{n,1}$ and $q_{n,1}$, respectively, given by

$$Z_{n,2}(t_{n,1},z) = -\Big(\frac{\mathrm{i}g}{\omega}\Big)\frac{\cosh(t_{n,1}(z+h)) - S_{n,1}\sinh(t_{n,1}(z+h))}{\cosh(t_{n,1}h) - S_{n,1}\sinh(t_{n,1}h)}, \quad n = 0,1,2,...,$$
$$q_{n,1} = \sqrt{t_{n,1}^2 - k_y^2},$$

where

$$S_{n,1} = \Big(1 - \frac{\epsilon_1}{\gamma_1}\Big)\frac{\tanh(t_{n,1}(h-a_1))}{\tanh^2(t_{n,1}(h-a_1)) - \frac{\epsilon_1}{\gamma_1}}.$$

In above, $t_{n,1}$'s are the roots of the dispersion relation

$$K\gamma_1 - t_{n,1}\tanh(t_{n,1}h) - S_{n,1}\big(K\gamma_1\tanh(t_{n,1}h) - t_{n,1}\big) = 0, \tag{5.42}$$

and A_n's and B_n's are the unknown coefficients.

The velocity potential $\phi_3(x,z)$ in Region 3 is found as follows:

$$\phi_3(x,z) = \sum_{n=0}^{\infty}\big(A_n e^{\mathrm{i}q_{n,1}x} + B_n e^{-\mathrm{i}q_{n,1}x}\big)Z_{n,3}(t_{n,1},z), \tag{5.43}$$

with the depth eigenfunction $Z_{n,3}(t_{n,1}, z)$ given by

$$Z_{n,3}(t_{n,1}, z) = -\Big(\frac{ig}{\omega}\Big)\frac{\gamma_1(1 - S_{n,1}\tanh(t_{n,1}(h - a_1)))}{(\cosh(t_{n,1}h) - S_{n,1}\sinh(t_{n,1}h))}\cosh(t_{n,1}(z + h)),$$

where A_n's and B_n's are the unknown coefficients - the same as the ones for ϕ_2.

In Region 4, the velocity potential $\phi_4(x, z)$ is expressed as

$$\phi_4(x, z) = \sum_{n=0}^{\infty}\big(C_n e^{ip_n x} + D_n e^{-ip_n x}\big)Z_{n,1}(k_n, z), \tag{5.44}$$

where C_n's and D_n's are the unknown coefficients.

The velocity potential $\phi_5(x, z)$ in Region 5 can be written as

$$\phi_5(x, z) = \sum_{n=0}^{\infty}\big(E_n e^{iq_{n,2}x} + F_n e^{-iq_{n,2}x}\big)Z_{n,5}(t_{n,2}, z), \tag{5.45}$$

with the depth eigenfunction $Z_{n,5}(t_{n,2}, z)$, $S_{n,2}$ and $q_{n,2}$, respectively, as

$$Z_{n,5}(t_{n,2}, z) = -\Big(\frac{ig}{\omega}\Big)\frac{\cosh(t_{n,2}(z + h)) - S_{n,2}\sinh(t_{n,2}(z + h))}{\cosh(t_{n,2}h) - S_{n,2}\sinh(t_{n,2}h)}, \quad n = 0, 1, 2, ...,$$
$$S_{n,2} = \Big(1 - \frac{\epsilon_2}{\gamma_2}\Big)\frac{\tanh(t_{n,2}(h - a_2))}{\tanh^2(t_{n,2}(h - a_2)) - \frac{\epsilon_2}{\gamma_2}},$$
$$q_{n,2} = \sqrt{t_{n,2}^2 - k_y^2}.$$

In above, $t_{n,2}$'s represent the roots of the dispersion relation

$$K\gamma_2 - t_{n,2}\tanh(t_{n,2}h) - S_{n,2}\big(K\gamma_2\tanh(t_{n,2}h) - t_{n,2}\big) = 0, \tag{5.46}$$

and E_n's and F_n's are the unknown coefficients.

The velocity potential $\phi_6(x, z)$ in Region 6 is as follows:

$$\phi_6(x, z) = \sum_{n=0}^{\infty}\big(E_n e^{iq_{n,2}x} + F_n e^{-iq_{n,2}x}\big)Z_{n,6}(t_{n,2}, z), \tag{5.47}$$

with the depth eigenfunction $Z_{n,6}(t_{n,2}, z)$ given by

$$Z_{n,6}(t_{n,2}, z) = -\Big(\frac{ig}{\omega}\Big)\frac{\gamma_2(1 - S_{n,2}\tanh(t_{n,2}(h - a_2)))}{(\cosh(t_{n,2}h) - S_{n,2}\sinh(t_{n,2}h))}\cosh(t_{n,2}(z + h)),$$

where E_n's and F_n's are the unknown coefficients - the same as the ones for ϕ_5.

In Region 7, the velocity potential $\phi_7(x,z)$ is the following:

$$\phi_7(x,z) = \sum_{n=0}^{\infty} \left(G_n e^{\mathrm{i}p_n x} + H_n e^{-\mathrm{i}p_n x}\right) Z_{n,1}(k_n, z), \tag{5.48}$$

where G_n's and H_n's are the unknown coefficients.

In Region 8, the velocity potential $\phi_8(x,z)$ is expressed as

$$\phi_8(x,z) = \sum_{n=0}^{\infty} \left(I_n \frac{\cosh(s_n x)}{\cosh(s_n b)} + J_n \frac{\sinh(s_n x)}{\sinh(s_n b)}\right) Z_{n,8}(r_n, z), \tag{5.49}$$

with the depth eigenfunction $Z_{n,8}(r_n,z)$, r_n and s_n, respectively, as

$$\begin{aligned} Z_{n,8}(r_n,z) &= -\left(\frac{\mathrm{i}g}{\omega}\right)\cos(r_n(z+h_1)), \quad n = 0,1,2,..., \\ r_n &= \frac{n\pi}{h-h_1}, \qquad s_n = \sqrt{r_n^2 + k_y^2}, \end{aligned} \tag{5.50}$$

where I_n's and J_n's are the unknown coefficients.

The velocity potential $\phi_9(x,z)$ in Region 9 is as follows:

$$\phi_9(x,z) = \sum_{n=0}^{\infty} T_n e^{\mathrm{i}p_n x} Z_{n,1}(k_n, z), \tag{5.51}$$

where T_n's are the unknown transmission coefficients.

In the above expressions of the velocity potentials, it is required to be careful in analyzing the roots so that the expressions are valid. In this direction, a complete analysis of mode swapping is provided in the next section.

Now, applying the matching conditions (5.9) - (5.32) and using the orthogonality of the depth eigenfunctions $Z_{n,1}(k_n,z)$ and $Z_{n,8}(r_n,z)$, and truncating all the infinite series at N, we obtain the following system of equations:

$$-\sum_{n=0}^{N} \delta_{n,m} R_n + \sum_{n=0}^{N} \left(\gamma_1 \mathscr{A}_{n,m} + \mathscr{B}_{n,m}\right) A_n + \sum_{n=0}^{N} \left(\gamma_1 \mathscr{A}_{n,m} + \mathscr{B}_{n,m}\right) B_n = \delta_{0,m}, \tag{5.52}$$

$$\begin{aligned} \sum_{n=0}^{N} \mathrm{i}p_n \delta_{n,m} R_n + \sum_{n=0}^{N} \mathrm{i}q_{n,1}\left(\epsilon_1 \mathscr{A}_{n,m} + \mathscr{B}_{n,m}\right) A_n - \sum_{n=0}^{N} \mathrm{i}q_{n,1}\left(\epsilon_1 \mathscr{A}_{n,m} + \mathscr{B}_{n,m}\right) B_n \\ = \mathrm{i}p_0 \delta_{0,m}, \end{aligned} \tag{5.53}$$

$$\sum_{n=0}^{N} \left(\gamma_1 \mathscr{A}_{n,m} + \mathscr{B}_{n,m}\right) e^{\mathrm{i}q_{n,1}L} A_n + \sum_{n=0}^{N} \left(\gamma_1 \mathscr{A}_{n,m} + \mathscr{B}_{n,m}\right) e^{-\mathrm{i}q_{n,1}L} B_n$$

$$-\sum_{n=0}^{N}\delta_{n,m}e^{\mathrm{i}p_nL}C_n-\sum_{n=0}^{N}\delta_{n,m}e^{-\mathrm{i}p_nL}D_n=0, \tag{5.54}$$

$$\sum_{n=0}^{N}\mathrm{i}q_{n,1}\big(\epsilon_1\mathscr{A}_{n,m}+\mathscr{B}_{n,m}\big)e^{\mathrm{i}q_{n,1}L}A_n-\sum_{n=0}^{N}\mathrm{i}q_{n,1}\big(\epsilon_1\mathscr{A}_{n,m}+\mathscr{B}_{n,m}\big)e^{-\mathrm{i}q_{n,1}L}B_n$$
$$-\sum_{n=0}^{N}\mathrm{i}p_n\delta_{n,m}e^{\mathrm{i}p_nL}C_n+\sum_{n=0}^{N}\mathrm{i}p_n\delta_{n,m}e^{-\mathrm{i}p_nL}D_n=0, \tag{5.55}$$

$$\sum_{n=0}^{N}\delta_{n,m}e^{\mathrm{i}p_nd_1}C_n+\sum_{n=0}^{N}\delta_{n,m}e^{-\mathrm{i}p_nd_1}D_n-\sum_{n=0}^{\infty}(\gamma_2\mathscr{C}_{n,m}+\mathscr{D}_{n,m})e^{\mathrm{i}q_{n,2}d_1}E_n$$
$$-\sum_{n=0}^{\infty}(\gamma_2\mathscr{C}_{n,m}+\mathscr{D}_{n,m})e^{-\mathrm{i}q_{n,2}d_1}F_n=0, \tag{5.56}$$

$$\sum_{n=0}^{\infty}\mathrm{i}p_n\delta_{n,m}e^{\mathrm{i}p_nd_1}C_n-\sum_{n=0}^{\infty}\mathrm{i}p_n\delta_{n,m}e^{-\mathrm{i}p_nd_1}D_n-\sum_{n=0}^{\infty}\mathrm{i}q_{n,2}\big(\epsilon_2\mathscr{C}_{n,m}+\mathscr{D}_{n,m}\big)e^{\mathrm{i}q_{n,2}d_1}E_n$$
$$+\sum_{n=0}^{\infty}\mathrm{i}q_{n,2}\big(\epsilon_2\mathscr{C}_{n,m}+\mathscr{D}_{n,m}\big)e^{-\mathrm{i}q_{n,2}d_1}F_n=0, \tag{5.57}$$

$$\sum_{n=0}^{\infty}\big(\gamma_2\mathscr{C}_{n,m}+\mathscr{D}_{n,m}\big)e^{\mathrm{i}q_{n,2}d_2}E_n+\sum_{n=0}^{\infty}\big(\gamma_2\mathscr{C}_{n,m}+\mathscr{D}_{n,m}\big)e^{-\mathrm{i}q_{n,2}d_2}F_n$$
$$-\sum_{n=0}^{\infty}\delta_{n,m}e^{\mathrm{i}p_nd_2}G_n-\sum_{n=0}^{\infty}\delta_{n,m}e^{-\mathrm{i}p_nd_2}H_n=0, \tag{5.58}$$

$$\sum_{n=0}^{\infty}\mathrm{i}q_{n,2}\big(\epsilon_2\mathscr{C}_{n,m}+\mathscr{D}_{n,m}\big)e^{\mathrm{i}q_{n,2}d_2}E_n-\sum_{n=0}^{\infty}\mathrm{i}q_{n,2}\big(\epsilon_2\mathscr{C}_{n,m}+\mathscr{D}_{n,m}\big)e^{-\mathrm{i}q_{n,2}d_2}F_n$$
$$-\sum_{n=0}^{\infty}\mathrm{i}p_n\delta_{n,m}e^{\mathrm{i}p_nd_2}G_n+\sum_{n=0}^{N}\mathrm{i}p_n\delta_{n,m}e^{-\mathrm{i}p_nd_2}H_n=0, \tag{5.59}$$

$$\sum_{n=0}^{N}e^{\mathrm{i}p_nd_3}\mathscr{E}_{n,m}G_n+\sum_{n=0}^{N}e^{-\mathrm{i}p_nd_3}\mathscr{E}_{n,m}H_n-\sum_{n=0}^{N}\Big(\frac{\cosh(s_nd_3)}{\cosh(s_nb)}\mathscr{F}_{n,m}\Big)I_n$$
$$-\sum_{n=0}^{N}\Big(\frac{\sinh(s_nd_3)}{\sinh(s_nb)}\mathscr{F}_{n,m}\Big)J_n=0, \tag{5.60}$$

$$\sum_{n=0}^{N}\mathrm{i}p_ne^{\mathrm{i}p_nd_3}\delta_{n,m}G_n-\sum_{n=0}^{N}\mathrm{i}p_ne^{-\mathrm{i}p_nd_3}\delta_{n,m}H_n-\sum_{n=0}^{N}\Big(s_n\frac{\sinh(s_nd_3)}{\cosh(s_nb)}\mathscr{G}_{n,m}\Big)I_n$$
$$-\sum_{n=0}^{N}\Big(s_n\frac{\cosh(s_nd_3)}{\sinh(s_nb)}\mathscr{G}_{n,m}\Big)J_n=0, \tag{5.61}$$

$$\sum_{n=0}^{N}\Big(\frac{\cosh(s_nd_4)}{\cosh(s_nb)}\mathscr{F}_{n,m}\Big)I_n+\sum_{n=0}^{N}\Big(\frac{\sinh(s_nd_4)}{\sinh(s_nb)}\mathscr{F}_{n,m}\Big)J_n-\sum_{n=0}^{N}e^{\mathrm{i}p_nd_4}\mathscr{E}_{n,m}T_n$$
$$=0, \tag{5.62}$$

$$\sum_{n=0}^{N}\left(s_n\frac{\sinh(s_nd_4)}{\cosh(s_nb)}\mathscr{G}_{n,m}\right)I_n+\sum_{n=0}^{N}\left(s_n\frac{\cosh(s_nd_4)}{\sinh(s_nb)}\mathscr{G}_{n,m}\right)J_n$$
$$-\sum_{n=0}^{N}\mathrm{i}p_ne^{\mathrm{i}p_nd_4}\delta_{n,m}T_n=0, \tag{5.63}$$

where $d_1=L+L_1$, $d_2=2L+L_1$, $d_3=2L+L_1+L_2$, $d_4=2L+L_1+L_2+L_3$ and

$$\delta_{n,m}=\begin{cases}\alpha_m & n=m\\ 0 & n\neq m\end{cases},\quad \alpha_m=\int_{z=-h}^{0}Z_{m,1}(k_{m,1},z)Z_{m,1}(k_{m,1},z)dz,$$

$$\mathscr{A}_{n,m}=\int_{z=-a}^{0}Z_{n,2}(t_{n,1},z)Z_{m,1}(k_m,z)dz,\quad \mathscr{B}_{n,m}=\int_{z=-h}^{-a}Z_{n,3}(t_{n,1},z)Z_{m,1}(k_m,z)dz,$$

$$\mathscr{C}_{n,m}=\int_{z=-a_2}^{0}Z_{n,5}(t_{n,2},z)Z_{m,1}(k_m,z)dz,\quad \mathscr{D}_{n,m}=\int_{z=-h}^{-a_2}Z_{n,6}(t_{n,2},z)Z_{m,1}(k_m,z)dz,$$

$$\mathscr{E}_{n,m}=\int_{z=-h}^{-h_1}Z_{n,1}(k_n,z)Z_{m,8}(r_m,z)dz,\quad \mathscr{F}_{n,m}=\int_{z=-h}^{-h_1}Z_{n,8}(r_n,z)Z_{m,8}(r_m,z)dz,$$

$$\mathscr{G}_{n,m}=\int_{z=-h}^{-h_1}Z_{n,8}(r_n,z)Z_{m,1}(k_m,z)dz.$$

To understand the role of the thick porous structures, it is essential to obtain the unknown coefficients R_n, A_n, B_n, C_n, D_n, E_n, F_n, G_n, H_n, I_n, J_n and T_n appearing in the system of equations (5.52)−(5.63). For this, the above system of equations can be compactly written as

$$\mathscr{A}\mathscr{X}=\mathscr{B}, \tag{5.64}$$

where $\mathscr{A}$ is the coefficient matrix of the above system of order $(12N+12)\times(12N+12)$, $\mathscr{B}$ is the column vector of size $(12N+12)\times1$ and $\mathscr{X}=[R_0,R_1,...,R_n,A_0,A_1,...,A_n,B_0,B_1,...,B_n,C_0,C_1,...,C_n,D_0,D_1,...,D_n,E_0,E_1,...,E_n,F_0,F_1,...,F_n,G_0,G_1,...,G_n,H_0,H_1,...,H_n,I_0,I_1,...,I_n,J_0,J_1,...,J_n,T_0,T_1,...,T_n]^t$ is the unknown vector. This will allow us to obtain the complete solution of the problem under consideration. After obtaining all the unknowns, we can proceed further to evaluate the reflection, transmission, and dissipation coefficients, and the hydrodynamic forces acting on the floating structure.

The complex-valued horizontal force X_{hf} and vertical force Y_{vf} acting on the floating structure are calculated using linearized Bernoulli's equation. To obtain the forces, we

use the formulas given by

$$X_{hf} = \mathrm{i}\rho\omega \int_{z=-h_1}^{0} \left[\phi_9\left(d_4, z\right) - \phi_7\left(d_3, z\right)\right] dz, \tag{5.65}$$

$$Y_{vf} = \mathrm{i}\rho\omega \int_{d_3}^{d_4} \phi_8\left(x, -h_1\right) dx. \tag{5.66}$$

Subsequently, the non-dimensional forms of the horizontal force X_{hf} and vertical force Y_{vf} can be written, respectively, as follows:

$$F_h = \frac{|X_{hf}|}{\rho g A b}, \quad F_v = \frac{|Y_{vf}|}{\rho g A b}, \tag{5.67}$$

where ρ represents the water density, $b = (L_3/2)$ m, and $A = 1$ m the unit amplitude of the incident wave.

5.3 Analysis of the dispersion relation

A complete analysis of the dispersion relations (5.40), (5.42), (5.46) and (5.50), which arise due to various considerations, is provided here.

5.3.1 The root analysis

The dispersion relation (5.40) can be written as

$$Kh - \mathcal{K}\tanh(\mathcal{K}) = 0 \text{ where } \mathcal{K} = kh. \tag{5.68}$$

The only positive real root of (5.68) is $\mathcal{K}_0$ and other infinite number of imaginary roots are $\mathrm{i}\mathcal{K}_\mathrm{n}$ $(n = 1, 2, \cdots)$ with the property $(n - \frac{1}{2})\pi < \mathcal{K}_n < n\pi$, where $\mathcal{K}_n$ are the real positive roots of

$$Kh + \mathcal{K}\tan(\mathcal{K}) = 0. \tag{5.69}$$

An approximate value of $\mathcal{K}_0$ is given by Chamberlain and Porter [15] as

$$\mathcal{K}_0 = \mathcal{M}\left(1 - \frac{4(1 - (1 + \mathcal{M})e^{-2\mathcal{M}})}{2\mathcal{M} + \sinh(2\mathcal{M})}\right)^{-1/4}, \text{ where } \mathcal{M} = Kh. \tag{5.70}$$

To approximate $\mathcal{K}_n$ $(n = 1, 2, \cdots)$, we again use an iterative method suggested by Chamberlain and Porter [15]:

$$\mathcal{K}_{n,m+1} = u_n(\mathcal{K}_{n,m}), \quad m = 0, 1, 2, \cdots,$$

where

$$u_n(a_n) = a_n \Big/ \sqrt{1 - \frac{2(a_n \tan(a_n) + \mathcal{M})\sin(2a_n)}{\mathcal{M}(\sin(2a_n) + 2a_n)}},$$
$$\mathcal{K}_{n,0} = \beta_n = n\pi - \frac{\pi}{2}\tanh\left(\frac{2\mathcal{M}}{n\pi^2}\right).$$

Once we obtain the values of $\mathcal{K}_n$ $(n = 0, 1, 2, \cdots)$, k_n can be calculated by using the relation $\mathcal{K}_n = k_n h$.
The corresponding errors are defined by

$$Error^{\pm} = \Big|K - k_n \tanh(k_n h)\Big|. \tag{5.71}$$

The dispersion relation (5.42) can be written as

$$Kh = \frac{\mu}{\gamma_1}\left(\frac{\tanh(\alpha_1\mu) + \frac{\epsilon_1}{\gamma_1}\tanh(\beta_1\mu)}{\frac{\epsilon_1}{\gamma_1} + \tanh(\alpha_1\mu)\tanh(\beta_1\mu)}\right), \tag{5.72}$$

where, $\mu = t_{n,1}h$, $\alpha_1 = 1 - \frac{a_1}{h}$ and $\beta_1 = 1 - \alpha_1$.
If $\gamma_1 = 1$, then (5.72) can be written as

$$g_r(\mu) \equiv \frac{\mu\epsilon_1\tanh(\beta_1\mu) - \mathcal{M}\epsilon_1}{\mathcal{M}\tanh(\beta_1\mu) - \mu} = \tanh(\alpha_1\mu). \tag{5.73}$$

Now, we can easily obtain the real roots of (5.73) graphically if we plot $f(x) = \tanh(\alpha_1 x)$ and $f(x) = g_r(x)$ from where we can show that (5.73) has two real roots (one positive and one negative) since (5.73) remains unchanged if $t_{n,1}$ is replaced by $-t_{n,1}$. Now, replacing $t_{n,1}$ by $it_{n,1}$ in (5.73) gives us

$$g_i(\mu) \equiv \frac{\mu\epsilon_1\tan(\beta_1\mu) + \mathcal{M}\epsilon_1}{\mathcal{M}\tan(\beta_1\mu) - \mu} = \tan(\alpha_1\mu). \tag{5.74}$$

Similarly, using graphical method, the purely imaginary roots of (5.73) can also be obtained by plotting $f(x) = \tan(\alpha_1 x)$ and $f(x) = g_i(x)$, from which we can show that there exist infinite number of purely imaginary roots of (5.73) given by $\pm t_{n,1}$ $(n = 1, 2, \cdots)$.
Further, Mendez and Losada [54] demonstrated in their algorithm that, as the dissipation factor (here γ_1, which is real for plain water region) changes from real to complex in

the porous region, the corresponding dispersive roots of the pure water region also gets converted to the roots of dispersion equation in the porous region. Moreover, the form of K (equation (5.72)) clearly shows that the associated wavenumber within porous medium is complex in nature due to the effect of the complex porous impedance parameter γ_1. After evaluating the roots numerically in the porous region, the absolute error can be determined as

$$Error^{\pm} = \left| K\gamma_1 - t_{n,1}\left(\frac{\tanh(\alpha_1\mu) + \frac{\epsilon_1}{\gamma_1}\tanh(\beta_1\mu)}{\frac{\epsilon_1}{\gamma_1} + \tanh(\alpha_1\mu)\tanh(\beta_1\mu)}\right)\right|. \tag{5.75}$$

Similarly, the roots of equation (5.46) can also be obtained.
For the values of r_n, we can use equation (5.50).

5.3.2 Asymptotic analysis of roots

The dispersion relation (5.40) can be written as

$$\mathcal{K}\tanh(\mathcal{K}) - G = 0 \text{ where } \mathcal{K} = kh \text{ and } G = Kh. \tag{5.76}$$

1. **Analysis of real roots**

   (a) Behavior for small $\mathcal{K}$ (near zero):
   For small $\mathcal{K}$, the Taylor series expansion of $\tanh(\mathcal{K})$ is

   $$\tanh(\mathcal{K}) \approx \mathcal{K} - \frac{\mathcal{K}^3}{3} + \frac{2\mathcal{K}^5}{15} + \cdots.$$

   Substituting this into equation (5.76), we get

   $$\mathcal{K}^2 - \frac{\mathcal{K}^4}{3} + \frac{2\mathcal{K}^6}{15} + \cdots - G = 0. \tag{5.77}$$

   For small $\mathcal{K}$, the leading term is $\mathcal{K}^2$, and so the above equation approximately becomes

   $$\mathcal{K}^2 \approx G \implies \mathcal{K} \approx \pm\sqrt{G}.$$

   This implies that for small $\mathcal{K}$, two real roots exist near $\mathcal{K} = \sqrt{G}$ and $\mathcal{K} = -\sqrt{G}$.

   (b) Behavior for large $\mathcal{K}$:
   We have

   $$\tanh(\mathcal{K}) \approx 1 - 2e^{-2\mathcal{K}}.$$

Substituting this expression in equation (5.76) yields

$$\mathcal{K} - 2\mathcal{K}e^{-2\mathcal{K}} - G = 0. \tag{5.78}$$

For large $\mathcal{K}$, $e^{-2\mathcal{K}}$ is negligible, and hence equation (5.78) simplifies to

$$\mathcal{K} \approx G.$$

This confirms that there is a real root near $x = G$.

2. **Analysis of imaginary roots**

For purely imaginary roots, let $\mathcal{K} = iy$, where y is real. Upon this substitution, equation (5.76) becomes

$$y\tan(y) = -G. \tag{5.79}$$

We now analyze the roots of equation (5.79).

(a) Behavior for small y:
For small y, the Taylor series expansion of $\tan(y)$ is

$$\tan(y) \approx y + \frac{y^3}{3} + \cdots.$$

Consequently, equation (5.79) becomes

$$y\left(y + \frac{y^3}{3} + \cdots\right) = -G,$$

where the dominant term is y^2, and hence,

$$y^2 \approx -G.$$

This implies the absence of real roots for small y, which is consistent with the fact that the roots are purely imaginary.

(b) Behavior for large y:
For large y, $\tan(y)$ oscillates between $-\infty$ and $+\infty$. The equation $y\tan(y) = -G$ has infinitely many solutions, corresponding to the intersections of $\tan(y)$ with $\left(-\frac{G}{y}\right)$. These roots occur near the poles of $\tan(y)$, i.e., near $y = \frac{(2n+1)}{2}\pi$ for integer n.

3. **Asymptotic behavior of imaginary roots**

For large y, let $y = \frac{(2n+1)}{2}\pi + \delta$, where δ is a small correction term. Substituting this in equation (5.79) yields

$$\left(\frac{(2n+1)}{2}\pi + \delta\right)\tan\left(\frac{(2n+1)}{2}\pi + \delta\right) = -G. \tag{5.80}$$

Using the approximation $\tan\left(\frac{(2n+1)}{2}\pi + \delta\right) \approx -\frac{1}{\delta}$, equation (5.80) becomes

$$\begin{aligned} &\left(\frac{(2n+1)}{2}\pi + \delta\right)\left(-\frac{1}{\delta}\right) = -G \\ \implies \quad &\delta = \frac{(2n+1)\pi}{2(G-1)}. \end{aligned} \tag{5.81}$$

Therefore, the approximate imaginary roots are

$$y \approx \frac{(2n+1)\pi}{2} + \frac{(2n+1)\pi}{2(G-1)}. \tag{5.82}$$

This shows that the imaginary roots grow linearly with n.

Let us rewrite the dispersion relation (5.42) as

$$K\gamma_1 - t_{n,1}\tanh(t_{n,1}h) - S_{n,1}\big(K\gamma_1\tanh(t_{n,1}h) - t_{n,1}\big) = 0, \tag{5.83}$$

where

$$S_{n,1} = \left(1 - \frac{\epsilon_1}{\gamma_1}\right)\frac{\tanh(t_{n,1}(h-a_1))}{\tanh^2(t_{n,1}(h-a_1)) - \frac{\epsilon_1}{\gamma_1}}. \tag{5.84}$$

Asymptotic behavior for large $|t_{n,1}|$:

For large $|z|$, the hyperbolic tangent function $\tanh(z)$ behaves as follows:

$$\tanh(z) \approx \begin{cases} 1 & \text{if } \mathrm{Re}(z) > 0, \\ -1 & \text{if } \mathrm{Re}(z) < 0. \end{cases}$$

From this, we can make the following approximations:

1. $\tanh(t_{n,1}h) \approx \mathrm{sign}(\mathrm{Re}(t_{n,1}))$,
2. $\tanh(t_{n,1}(h-a_1)) \approx \mathrm{sign}(\mathrm{Re}(t_{n,1}))$.

Substituting these approximations in equations (5.83) and (5.84), we get

$$K\gamma_1 - t_{n,1}\text{sign}(\text{Re}(t_{n,1})) - S_{n,1}(K\gamma_1\text{sign}(\text{Re}(t_{n,1})) - t_{n,1}) \approx 0, \tag{5.85}$$

$$S_{n,1} \approx \left(1 - \frac{\epsilon_1}{\gamma_1}\right)\frac{\text{sign}(\text{Re}(t_{n,1}))}{\left(1 - \frac{\epsilon_1}{\gamma_1}\right)} = \text{sign}(\text{Re}(t_{n,1})). \tag{5.86}$$

Now, equations (5.85) and (5.86) together give

$$K\gamma_1 - t_{n,1}\text{sign}(\text{Re}(t_{n,1})) - \text{sign}(\text{Re}(t_{n,1}))(K\gamma_1\text{sign}(\text{Re}(t_{n,1})) - t_{n,1}) \approx 0,$$

which implies

$$K\gamma_1 - t_{n,1}\text{sign}(\text{Re}(t_{n,1})) - K\gamma_1 + t_{n,1}\text{sign}(\text{Re}(t_{n,1})) \approx 0. \tag{5.87}$$

This suggests that, for large $|t_{n,1}|$, equation (5.83) is approximately satisfied for any value, implying that the roots become asymptotically independent of the parameter of the equation.

5.3.3 Observation of mode swapping

The interaction of the two modes implies that another new mode must be present. This phenomenon is called mode swapping. In such situations, eigenfunction expansion in the porous medium fails, and a new solution procedure is required for these cases.

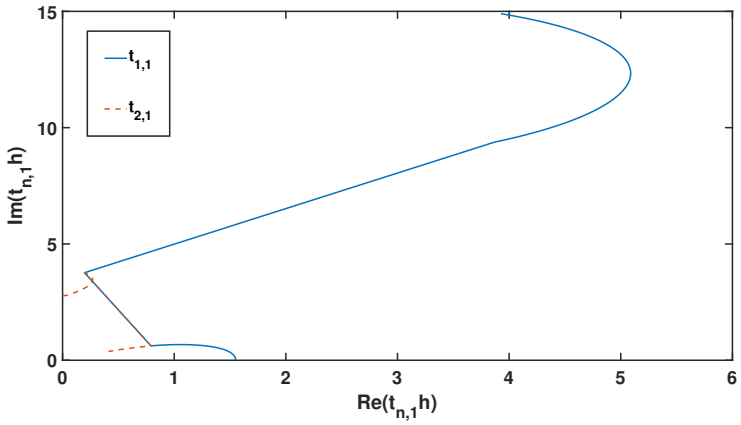

Figure 5.2: Roots of dispersion relation (5.42) corresponding to varying f_1 in [0,12] corresponding to $Kh = 1.8623$

Figures 5.2 - 5.6 illustrate the behaviour of the roots of the dispersion relation (5.42) with dimensionless depth to determine if there are situations where the eigenfunction solution fails. Here, $\text{Re}(t_{n,1}h)$ and $\text{Im}(t_{n,1}h)$, respectively, denote the real and imaginary

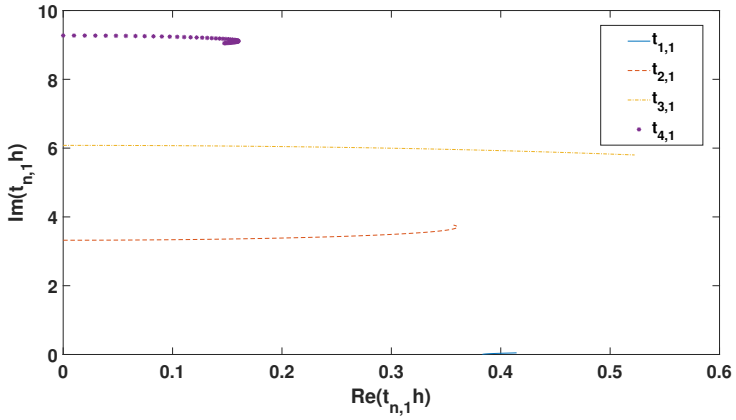

Figure 5.3: Roots of dispersion relation (5.42) corresponding to varying f_1 in [0,2] corresponding to $Kh = 0.2012$

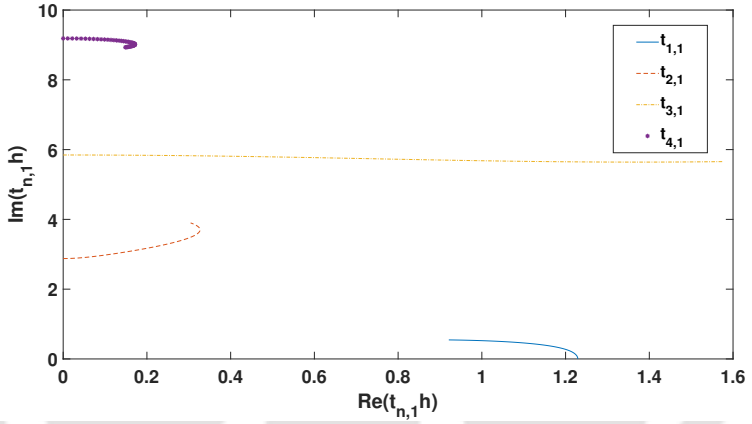

Figure 5.4: Roots of dispersion relation (5.42) corresponding to varying f_1 in [0,2] corresponding to $Kh = 1.32$

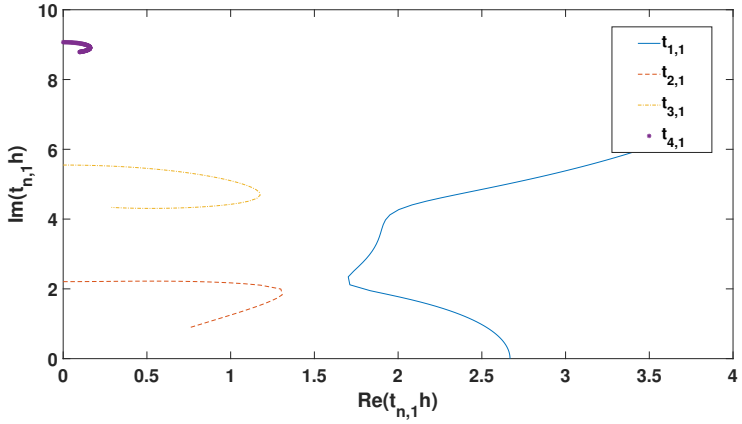

Figure 5.5: Roots of dispersion relation (5.42) corresponding to varying f_1 in [0,2] corresponding to $Kh = 2.925$

parts of the non-dimensional roots.

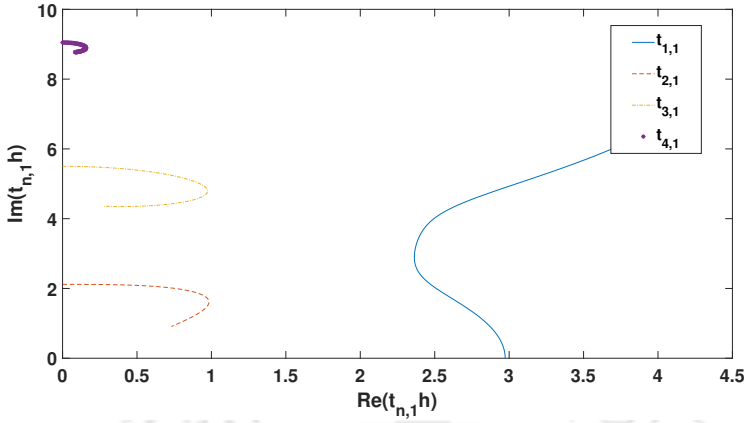

Figure 5.6: Roots of dispersion relation (5.42) corresponding to varying f_1 in [0,2] corresponding to $Kh = 3.2182$

For the value of $Kh = 1.8623$, the curves of $t_{1,1}$ and $t_{2,1}$ are plotted for different values of f_1 with $s_1 = 1$, as shown in Figure 5.2 in which the curve corresponding to $t_{1,1}$ intersects the curve corresponding to $t_{2,1}$ once at $f_1 = 3.5645$ and again at $f_1 = 3.612$. This is referred to as mode swapping. The coalescence of the two modes implies that another new mode must be present in a similar way when double roots are obtained in the characteristic equation while solving an ordinary differential equation with constant coefficients ([21]). As defined by Dalrymple et al. [23], the Green's function technique may probably be used to overcome this situation.

The figures 5.3, 5.4, 5.5 and 5.6 depict the complex wavenumbers corresponding to the first four non-dimensional modes $t_{n,1}$ for $n = 1, 2, 3, 4$, with $s_1 = 1$, f_1 in the range $[0, 2]$, and different values of Kh.

Figure 5.3 shows the dimensionless wavenumbers resulting from f_1 for $Kh = 0.2012$. In this case, the real part of $t_{1,1}$ first increases, then decreases as f_1 increases, while the real parts of the evanescent modes increase with an increase in f_1. The real part of the evanescent mode $t_{3,1}$ crosses the value of the real part of $t_{1,1}$ for higher values of f_1, specifically for $f_1 > 1.28$. This implies that the plane-wave approximation is not valid for $f_1 > 1.28$. Further, no mode swapping appears in this case.

For $Kh = 1.32$, Figure 5.4 depicts that the real part of $t_{1,1}$ decreases as f_1 increases, while the real part of the evanescent modes increases: the real part of $t_{3,1}$ surpasses the real part of $t_{1,1}$ for higher values of f_1 (specifically, for $f_1 > 1.41$). In this case also, the plane-wave approximation is not valid for large values of f_1. Furthermore, no mode swapping occurs for this value of Kh.

Figures 5.5 and 5.6, corresponding to $Kh = 2.925$ and $Kh = 3.2182$, respectively,

demonstrate that, as f_1 increases, the real part of $t_{1,1}$ shows an increasing nature, while the evanescent modes initially increase and then begin to decrease with increasing f_1.

For the shallow depth, the curve representing propagating modes falls below the dimensionless evanescent curves. However, for higher Kh, this curve maintains a significant distance from the non-dimensional evanescent curves. Figures 5.5 and 5.6 depict that the possibility of intersection of two curves disappears. If two roots appear to overlap, the Green's function method may be preferred for addressing the issue, as suggested by [23]. In this study, with the selected parameter values, including γ_1 and γ_2, no mode swapping is observed.

5.4 Energy Identity Relation

In the problems related to wave scattering, the energy identity plays an important role in relating the incident wave amplitude to the reflected and transmitted wave amplitudes of the system. For wave scattering by rigid breakwaters, energy identity relation is given by a relation connecting the reflection coefficient and the transmission coefficient as $|R_0|^2 + |T_0|^2 = 1$. In the case of wave scattering by a rigid floating structure, but in the presence of two surface-piercing thick porous structures, the system dissipates a significant amount of wave energy. We now establish an energy identity relation for the present problem through the utilization of Green's second identity.

The Green's identity involving a complex velocity potential $\phi(x, z)$ and its complex conjugate $\phi^*(x, z)$ over a curve Γ is given by

$$\int_{\Gamma} \left(\phi^* \frac{\partial \phi}{\partial n} - \phi \frac{\partial \phi^*}{\partial n} \right) ds = 0, \tag{5.88}$$

where $\frac{\partial}{\partial n}$ is the outward normal derivative to $\Gamma = C_1 \cup C_2 \cup C_3$, with $C_1 = \{x = -X, -h \leq z \leq 0;\ z = -h, -X \leq x \leq X;\ x = X, -h \leq 0;\ z = 0, 2L + L_1 + L_2 + L_3 \leq x \leq X;\ z = 0, 2L + L_1 \leq x \leq 2L + L_1 + L_2;\ z = 0, L \leq x \leq L + L_1;\ z = 0, X \leq x \leq 0;\ 2L + L_1 + L_2 \leq x \leq 2L + L_1 + L_2 + L_3, -h_1 \leq z \leq 0\}$, $C_2 = \{x = 0, -a_1 \leq z \leq 0;\ z = -a_1, 0 \leq x \leq L;\ x = L, -a_1 \leq z \leq 0;\ z = 0, 0 \leq x \leq L\}$, $C_3 = \{x = L + L_1, -a_2 \leq z \leq 0;\ z = -a_2, L + L_1 \leq x \leq 2L + L_1;\ x = 2L + L_1, -a_2 \leq z \leq 0;\ z = 0, L + L_1 \leq x \leq 2L + L_1\}$, which is the closed contour. Now, due to the free surface, there is no contribution for the integral from the boundaries $z = 0, -X \leq x \leq 0;\ z = 0, L \leq x \leq L + L_1;\ z = 0, 2L + L_1 \leq x \leq 2L + L_1 + L_2$ and $z = 0, 2L + L_1 + L_2 + L_3 \leq x \leq X$. The contribution along the boundary $z = -h, -X \leq x \leq X$ is zero because of the no-slip condition. The contribution along the boundary of the floating structure $2L + L_1 + L_2 \leq x \leq 2L + L_1 + L_2 + L_3, -h_1 \leq z \leq 0$ is zero due to the rigid boundary.

The contribution from the other boundaries are as follows:

(A) Along the boundary $x = -X,\ -h \le z \le 0$:

$$\int_{-h}^{0} \left(\phi \frac{\partial \phi^\star}{\partial n} - \phi^\star \frac{\partial \phi}{\partial n}\right) ds = (1 - |R_0|^2) \frac{\mathrm{i}p_0}{\cosh^2(k_0 h)} \left(\frac{\sinh(2k_0 h) + 2k_0 h}{2k_0}\right). \tag{5.89}$$

(B) Along the boundary $x = X,\ -h \le z \le 0$:

$$\int_{-h}^{0} \left(\phi \frac{\partial \phi^\star}{\partial n} - \phi^\star \frac{\partial \phi}{\partial n}\right) ds = -|T_0|^2 \frac{\mathrm{i}p_0}{\cosh^2(k_0 h)} \left(\frac{\sinh(2k_0 h) + 2k_0 h}{2k_0}\right). \tag{5.90}$$

(C) Along the boundary $x = 0,\ -a_1 \le z \le 0$:

$$\int_{-a_1}^{0} \left(\phi \frac{\partial \phi^\star}{\partial n} - \phi^\star \frac{\partial \phi}{\partial n}\right) ds = \int_{-a_1}^{0} \left([\epsilon_1(m_1 + \mathrm{i}f_1) - 1]\phi_2 \phi_{2x}^\star - [\epsilon_1(m_1 - \mathrm{i}f_1) - 1]\phi_2^\star \phi_{2x}\right) dz. \tag{5.91}$$

(D) Along the boundary $z = -a_1,\ 0 \le x \le L$:

$$\int_{0}^{L} \left(\phi \frac{\partial \phi^\star}{\partial n} - \phi^\star \frac{\partial \phi}{\partial n}\right) ds = \int_{0}^{L} \left([\epsilon_1(m_1 + \mathrm{i}f_1) - 1]\phi_2 \phi_{2z}^\star - [\epsilon_1(m_1 - \mathrm{i}f_1) - 1]\phi_2^\star \phi_{2z}\right) dx. \tag{5.92}$$

(E) Along the boundary $x = L,\ -a_1 \le z \le 0$:

$$\int_{-a_1}^{0} \left(\phi \frac{\partial \phi^\star}{\partial n} - \phi^\star \frac{\partial \phi}{\partial n}\right) ds = \int_{-a_1}^{0} \left([\epsilon_1(m_1 - \mathrm{i}f_1) - 1]\phi_2^\star \phi_{2x} - [\epsilon_1(m_1 + \mathrm{i}f_1) - 1]\phi_2 \phi_{2x}^\star\right) dz. \tag{5.93}$$

(F) Along the boundary $z = 0,\ 0 \le x \le L$:

$$\int_{0}^{L} \left(\phi \frac{\partial \phi^\star}{\partial n} - \phi^\star \frac{\partial \phi}{\partial n}\right) ds = \int_{0}^{L} \left(-2\mathrm{i}K f_1 |\phi_2|^2\right) dx. \tag{5.94}$$

(G) Along the boundary $x = L + L_1,\ -a_2 \le z \le 0$:

$$\int_{-a_2}^{0} \left(\phi \frac{\partial \phi^\star}{\partial n} - \phi^\star \frac{\partial \phi}{\partial n}\right) ds = \int_{-a_2}^{0} \left([\epsilon_2(m_2 + \mathrm{i}f_2) - 1]\phi_5 \phi_{5x}^\star - [\epsilon_2(m_2 - \mathrm{i}f_2) - 1]\phi_5^\star \phi_{5x}\right) dz. \tag{5.95}$$

(H) Along the boundary $z = -a_2,\ L + L_1 \leq x \leq 2L + L_1$:

$$\int_{L+L_1}^{2L+L_1} \left(\phi \frac{\partial \phi^\star}{\partial n} - \phi^\star \frac{\partial \phi}{\partial n}\right) ds = \int_{L+L_1}^{2L+L_1} \Big([\epsilon_2(m_2 + \mathrm{i}f_2) - 1]\phi_5 \phi_{5z}^\star - [\epsilon_2(m_2 - \mathrm{i}f_2) - 1]\phi_5^\star \phi_{5z} \Big) dx. \tag{5.96}$$

(I) Along the boundary $x = 2L + L_1,\ -a_2 \leq z \leq 0$:

$$\int_{-a_2}^{0} \left(\phi \frac{\partial \phi^\star}{\partial n} - \phi^\star \frac{\partial \phi}{\partial n}\right) ds = \int_{-a_2}^{0} \Big([\epsilon_2(m_2 - \mathrm{i}f_2) - 1]\phi_5^\star \phi_{5x} - [\epsilon_2(m_2 + \mathrm{i}f_2) - 1]\phi_5 \phi_{5x}^\star \Big) dz. \tag{5.97}$$

(J) Along the boundary $z = 0,\ L + L_1 \leq x \leq 2L + L_1$:

$$\int_{L+L_1}^{2L+L_1} \left(\phi \frac{\partial \phi^\star}{\partial n} - \phi^\star \frac{\partial \phi}{\partial n}\right) ds = \int_{L+L_1}^{2L+L_1} \Big(- 2\mathrm{i}K f_2 |\phi_5|^2 \Big) dx. \tag{5.98}$$

Finally, summing up all the contributions from C_1, C_2 and C_3, the energy identity relation is obtained as

$$|R_0|^2 + |T_0|^2 + k_d = 1, \tag{5.99}$$

where

$$\begin{aligned} k_d = \frac{2k_0 \cosh^2(k_0 h)}{\mathrm{i}p_0(\sinh(2k_0 h) + 2k_0 h)} \Bigg[& \int_0^L \Big(- 2\mathrm{i}K f_1 |\phi_2|^2 \Big)_{z=0} dx + \int_{-a_1}^{0} \Big([\epsilon_1(m_1 + \mathrm{i}f_1) - 1]\phi_2 \phi_{2x}^\star \\ & - [\epsilon_1(m_1 - \mathrm{i}f_1) - 1]\phi_2^\star \phi_{2x} \Big)_{x=0} dz + \int_{-a_1}^{0} \Big([\epsilon_1(m_1 - \mathrm{i}f_1) - 1]\phi_2^\star \phi_{2x} \\ & - [\epsilon_1(m_1 + \mathrm{i}f_1) - 1]\phi_2 \phi_{2x}^\star \Big)_{x=L} dz + \int_0^L \Big([\epsilon_1(m_1 + \mathrm{i}f_1) - 1]\phi_2 \phi_{2z}^\star \\ & - [\epsilon_1(m_1 - \mathrm{i}f_1) - 1]\phi_2^\star \phi_{2z} \Big)_{z=-a_1} dx + \int_{L+L_1}^{2L+L_1} \Big(- 2\mathrm{i}K f_2 |\phi_5|^2 \Big)_{z=0} dx \\ & + \int_{-a_2}^{0} \Big([\epsilon_2(m_2 + \mathrm{i}f_2) - 1]\phi_5 \phi_{5x}^\star - [\epsilon_2(m_2 - \mathrm{i}f_2) - 1]\phi_5^\star \phi_{5x} \Big)_{x=L+L_1} dz \\ & + \int_{-a_2}^{0} \Big([\epsilon_2(m_2 - \mathrm{i}f_2) - 1]\phi_5^\star \phi_{5x} - [\epsilon_2(m_2 + \mathrm{i}f_2) - 1]\phi_5 \phi_{5x}^\star \Big)_{x=2L+L_1} dz \\ & + \int_{L+L_1}^{2L+L_1} \Big([\epsilon_2(m_2 + \mathrm{i}f_2) - 1]\phi_5 \phi_{5z}^\star - [\epsilon_2(m_2 - \mathrm{i}f_2) - 1]\phi_5^\star \phi_{5z} \Big)_{z=-a_2} dx \Bigg] \end{aligned} \tag{5.100}$$

is the dissipation coefficient.

5.5 Results and discussion

After having obtained the analytical solution, we are first going to validate our model and then proceed to study the effect of different parameters on various quantities such as the reflection coefficient, transmission coefficient, dissipation coefficient and wave forces acting on the floating structure. For this purpose, a numerical code in MATLAB is developed. For the purpose of computation, the specific values of different parameters considered are $g = 9.81$ m/s^2, $T = 6$ s, $h = 15$ m, $h_1 = 3$ m, $a_1 = 3$ m, $a_2 = 3$ m, $\epsilon_1 = 0.6$, $\epsilon_2 = 0.6$, $s_1 = 1, f_1 = 1, s_2 = 1, f_2 = 1$, $L = 3$ m, $L_2 = 3$ m, $L_3 = 10$ m and $\theta = 30°$.

5.5.1 Convergence study for N

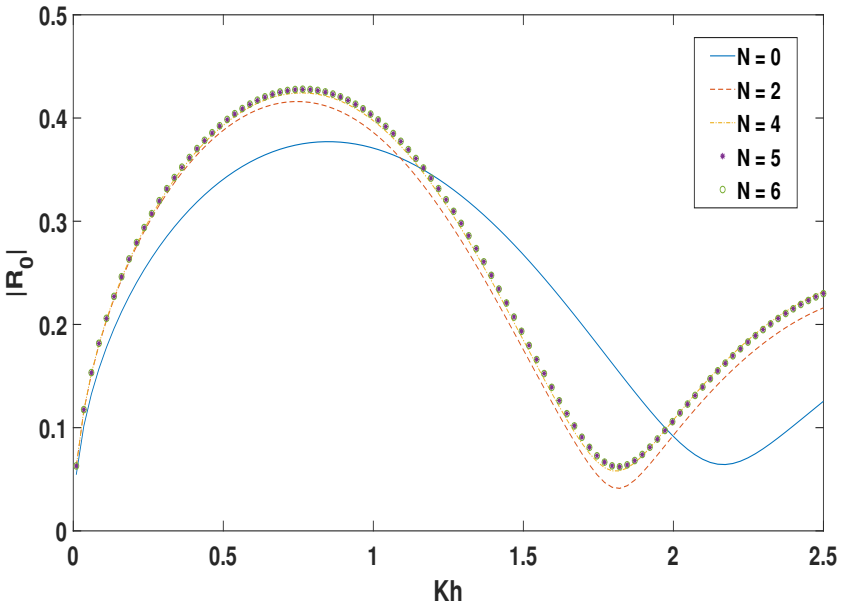

Figure 5.7: Reflection coefficient $|R_0|$ against Kh for different numbers of evanescent modes (N)

First, we investigate the effect of the evanescent modes so as to select the most appropriate value of N. In Figures 5.7 and 5.8, we plot reflection coefficient $|R_0|$ against Kh and L_1/h, respectively, for different values of the number of evanescent modes. Here, we consider $N = 0, 2, 4, 5, 6$ for this purpose, and observe that $|R_0|$ converges from $N = 6$ onward. Therefore, it is considered appropriately to use $N = 6$ for our study since the convergence is achieved for this value.

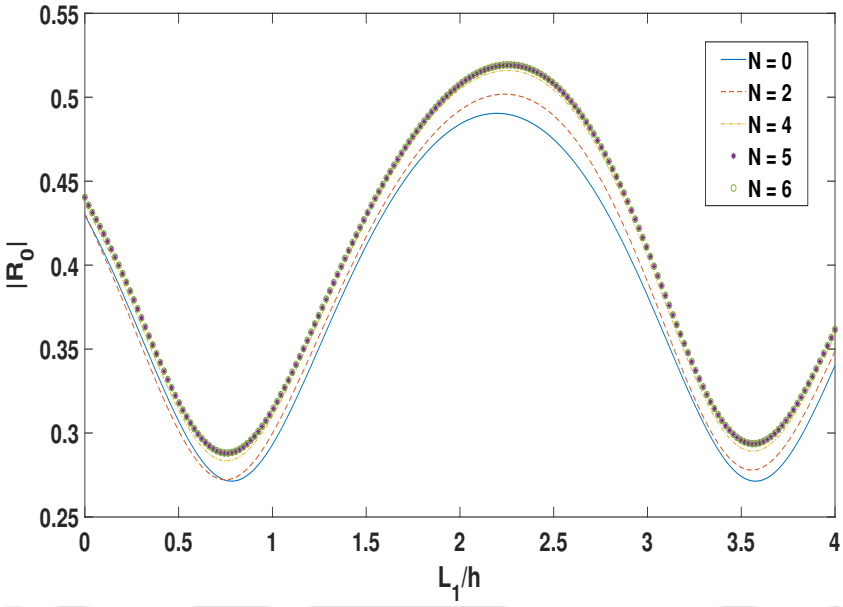

Figure 5.8: Reflection coefficient $|R_0|$ against L_1/h for different numbers of evanescent modes (N)

5.5.2 Validation

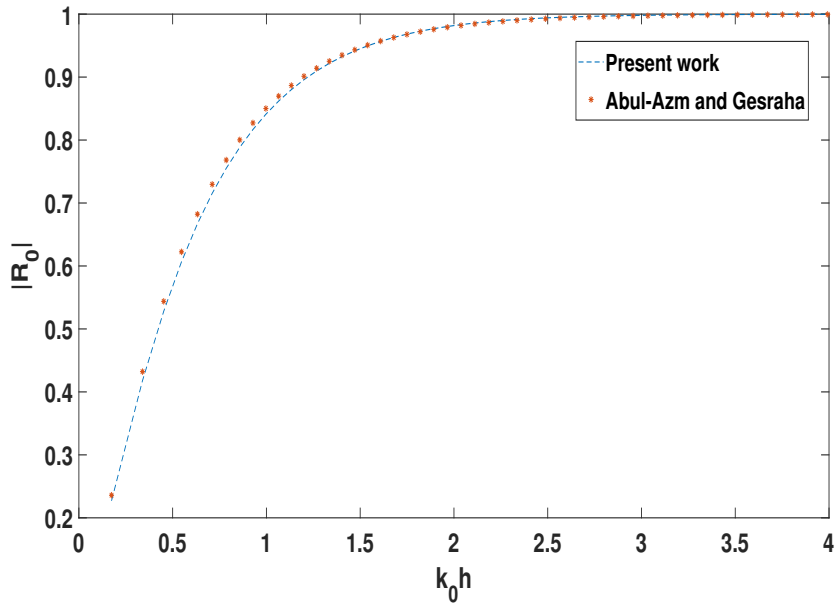

Figure 5.9: Reflection coefficient $|R_0|$ against non-dimensional wavenumber k_0h for the current work and Abul-Azm and Gesraha [2]

To validate the present results, a couple of earlier works on similar structures are considered. It may be noted that, in the absence of the porous breakwaters, the present model gets converted to that of Abul-Azm and Gesraha [2]. Abul-Azm and Gesraha [2]

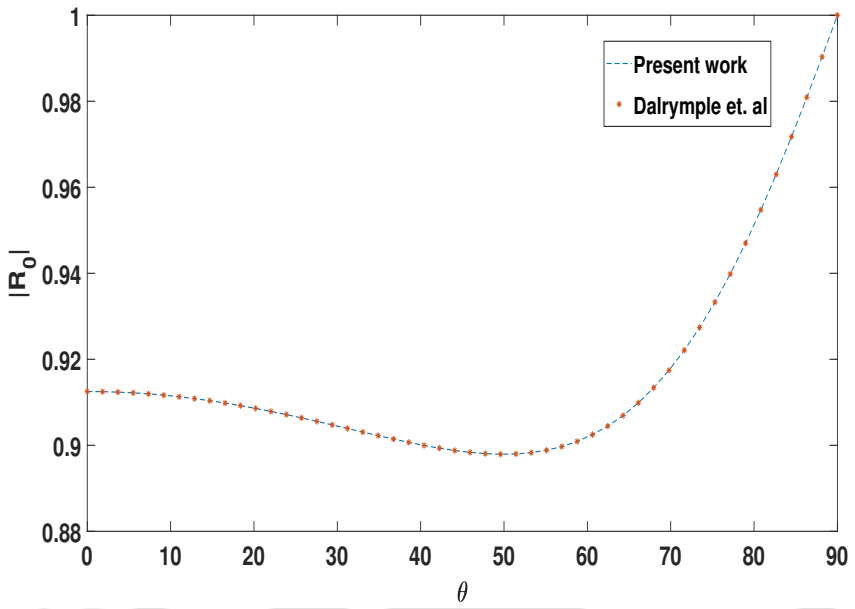

Figure 5.10: Reflection coefficient $|R_0|$ against incident wave angle θ for the current work and Dalrymple et al. [23]

studied an oblique wave interaction with the long rigid floating pontoon. For validating our model with that, we assume very high porosity of the breakwaters, effectively making them transparent. Thus, both models reduce to the same problem. To validate our model against that of Abul-Azm and Gesraha [2], we consider $\theta = 0°$, $L_3/2h = 1$ and $h_1/h = 0.25$. The variation of reflection coefficient $|R_0|$ against non-dimensional wavenumber k_0h for both models is displayed in Figure 5.9. The pattern for the reflection coefficient is the same for both models, as depicted by this figure.

Furthermore, when the floating structure is absent, we compare our results in this scenario with those of Dalrymple et al. [23], who investigated an oblique wave interaction with a vertically sided porous structure. For validating our model against that, we neglect the second porous structure and use the following parameter values: $\theta = 30°$, $L/h = 1$, $a_1/h = 1$, $Kh = 0.2012, \epsilon_1 = 0.4$, $f_1 = 1$. In Figure 5.10, the reflection coefficient is plotted against wave incident angle θ for the present model and that of Dalrymple et al. [23]. This figure illustrates an excellent match between both models. As a consequence, we observe that Figures 5.9 and 5.10 show a good agreement of our model with two earlier works as stated, and it allows us to apply our model to analyze problems concerning the suitability of porous breakwaters in securing the safety of various VLFS.

Furthermore, the energy identity is derived and validated numerically, as shown in Table 5.1, where the dissipation coefficients for various values of k_0h are presented. The results confirm that the derived energy identity relation (5.99) holds true.

Table 5.1: Validation of the energy identity relation derived in equation (5.99)

k_0h	$\lvert R_0\rvert$	$\lvert T_0\rvert$	$1-\lvert R_0\rvert^2-\lvert T_0\rvert^2$	k_d
0.1	0.054794855600173	0.996723099378091	0.003540586965888	0.003536407721000
0.2	0.109005624996737	0.990297321196439	0.007428989350227	0.007399059832109
0.4	0.213623067614419	0.967682239605370	0.017956268135341	0.017771661292919
0.6	0.309179494093334	0.932004475083321	0.035775698856853	0.035449466094065
0.8	0.390698780881194	0.883990147002278	0.065915882620840	0.066127035064018

5.5.3 Effect of the surface-piercing porous structures on the reflection coefficient, transmission coefficient and dissipation coefficient

In this subsection, we examine the impact of the porosity, height, width, and friction factor of the porous structures on the reflection, transmission and dissipation coefficients.

In Figure 5.11, we plot reflection coefficient $|R_0|$, transmission coefficient $|T_0|$, and dissipation coefficient k_d against dimensionless distance L_1/h between the two porous structures for various values of porosity ϵ_1 of the first porous structure. As ϵ_1 increases, dissipation coefficient k_d increases, while the reflection and transmission coefficients are found to decrease.

Figure 5.12 illustrates the behaviour of $|R_0|$, $|T_0|$ and k_d against L_1/h corresponding to various values of porosity ϵ_2 of the second porous structure. A left shift in the maxima of the reflection coefficient is noted with an increase in ϵ_2. Similarly, the dissipation coefficient exhibits the same pattern as in Figure 5.11: as the porosity of the second porous structure increases, the dissipation coefficient increases, while the reflection and transmission coefficients decrease.

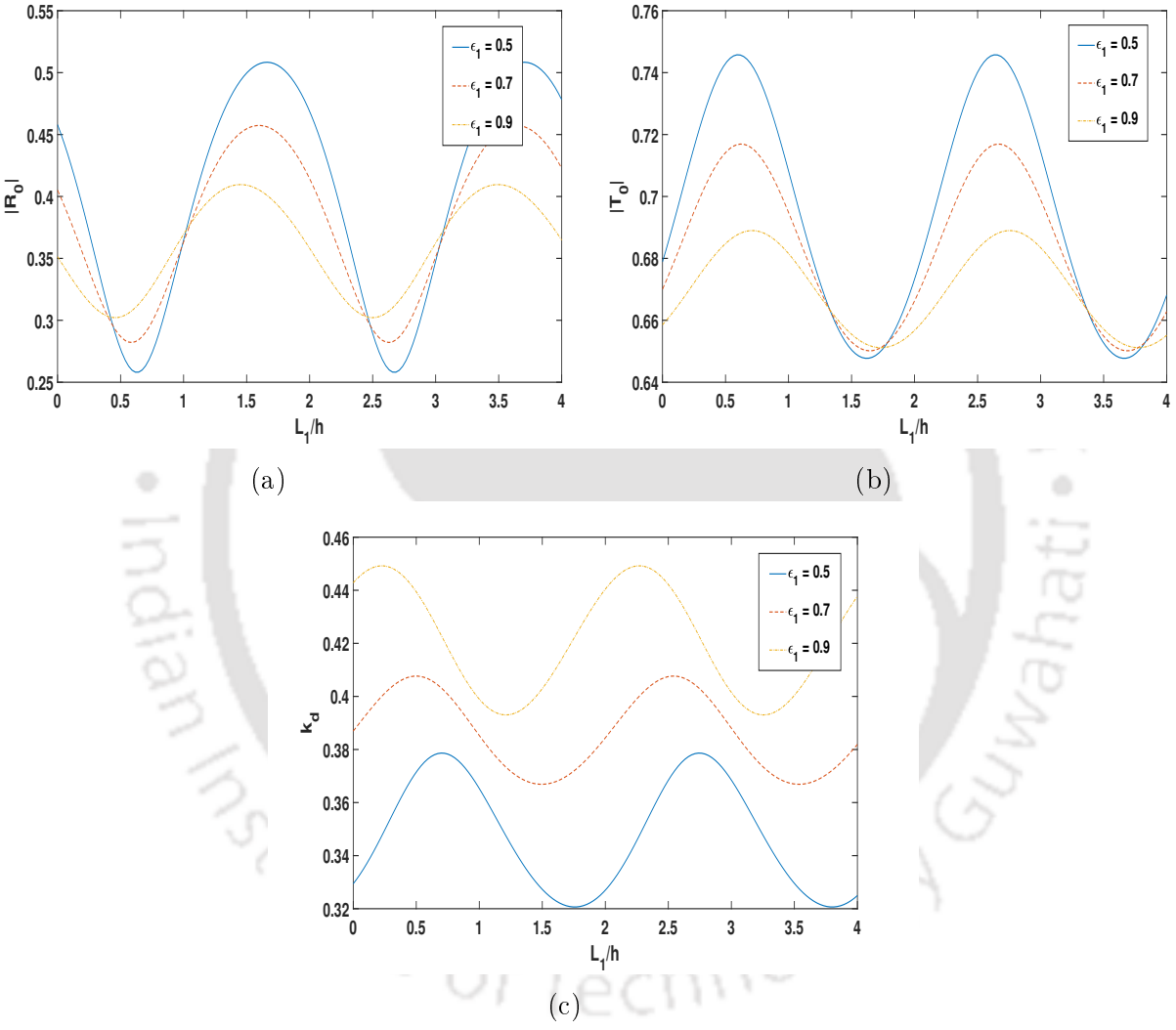

Figure 5.11: (a) $|R_0|$, (b) $|T_0|$, and (c) k_d against L_1/h for different values of porosity ϵ_1 with $h = 15$ m, $h_1 = 3$ m, $a_1 = 3$ m, $a_2 = 3$ m, $\epsilon_2 = 0.6$, $s_1 = 1$, $f_1 = 1$, $s_2 = 1$, $f_2 = 1$, $L = 3$ m, $L_2 = 3$ m, $L_3 = 10$ m, $N = 6$ and $\theta = 30°$

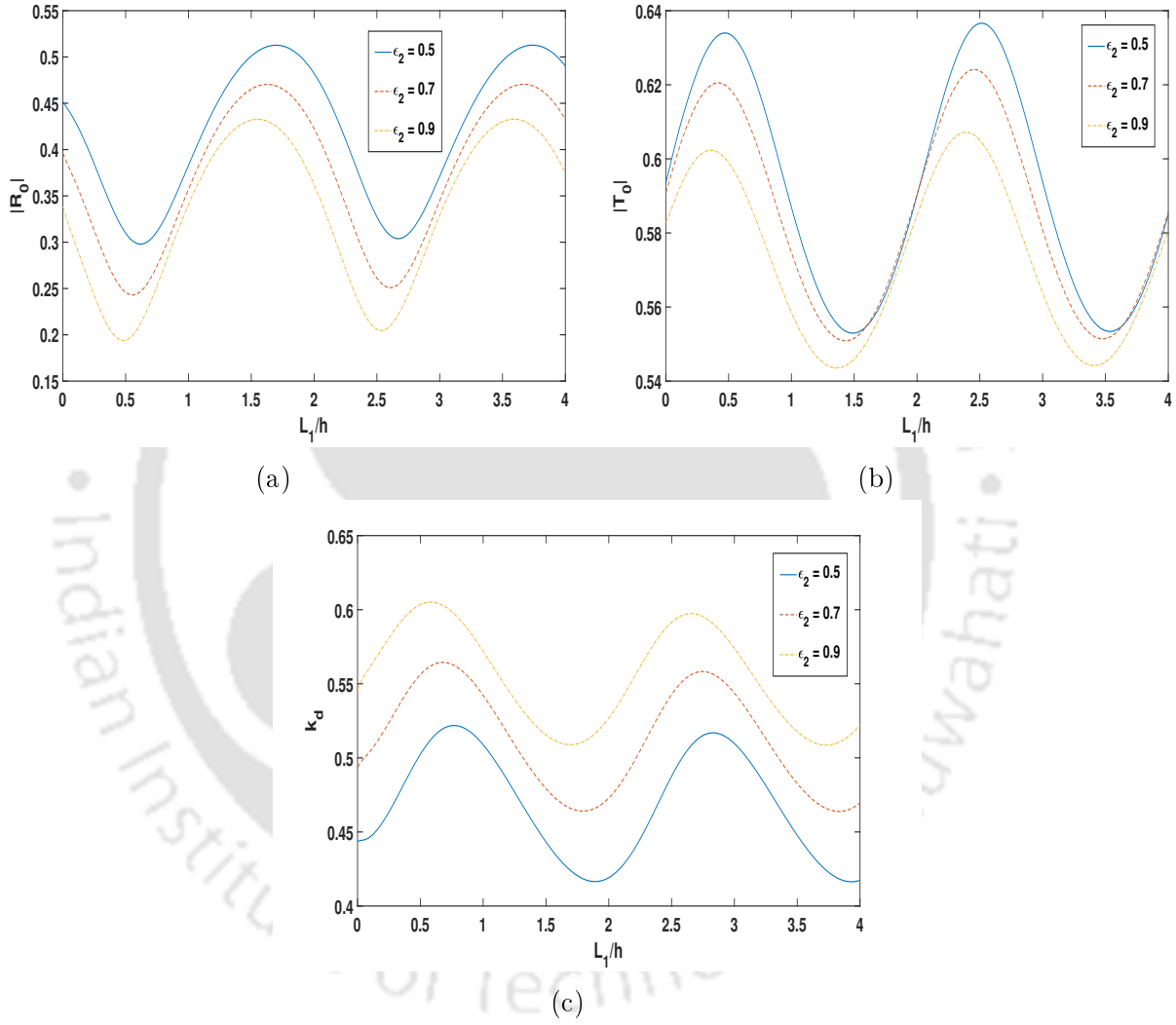

Figure 5.12: (a) $|R_0|$, (b) $|T_0|$, and (c) k_d against L_1/h for different values of porosity ϵ_2 with $h = 15$ m, $h_1 = 3$ m, $a_1 = 3$ m, $a_2 = 3$ m, $\epsilon_1 = 0.6$, $s_1 = 1$, $f_1 = 1$, $s_2 = 1$, $f_2 = 1$, $L = 3$ m, $L_2 = 3$ m, $L_3 = 10$ m, $N = 6$ and $\theta = 30°$

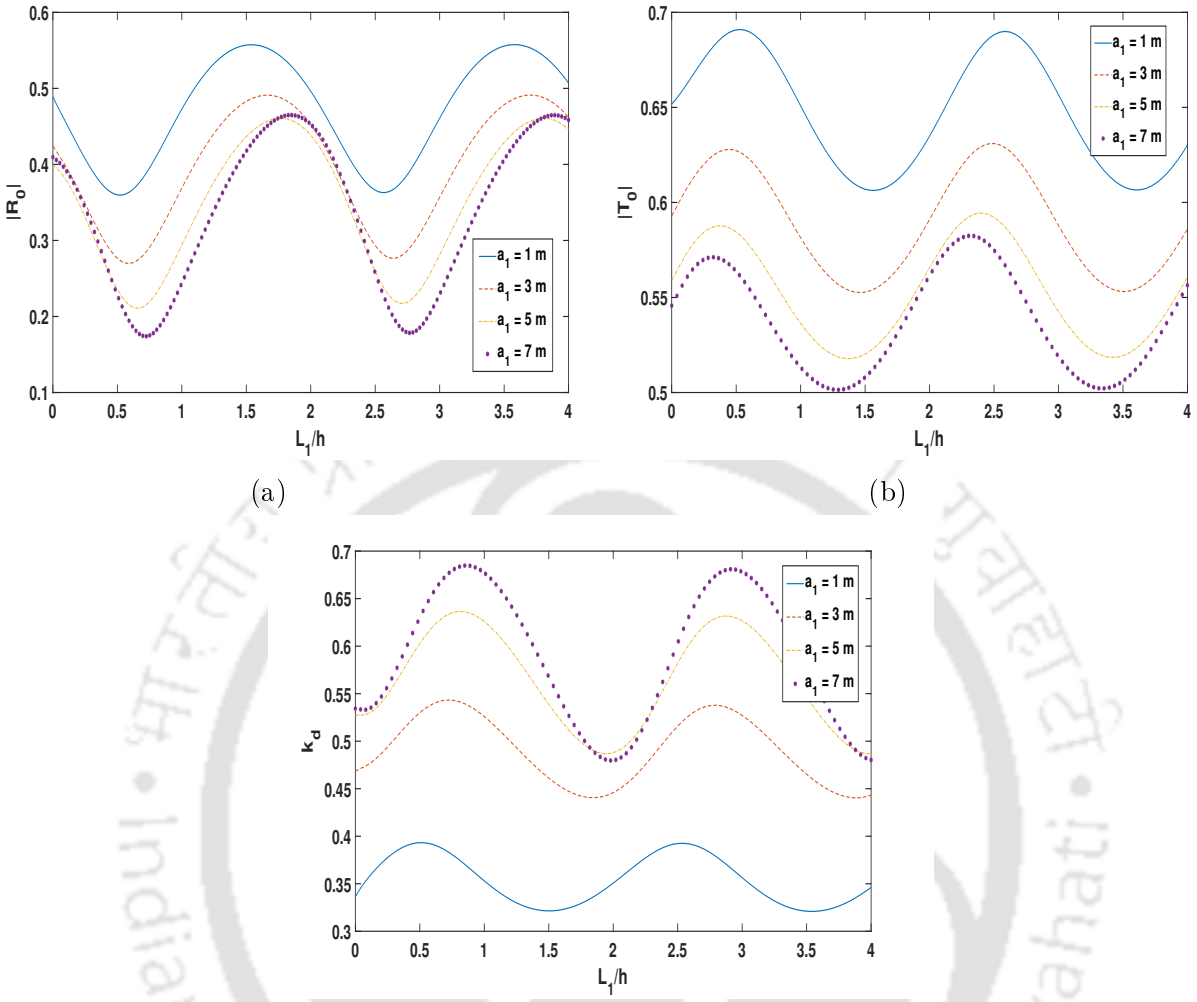

Figure 5.13: (a) $|R_0|$, (b) $|T_0|$, and (c) k_d against L_1/h for different values of the height a_1 with $h = 15$ m, $h_1 = 3$ m, $\epsilon_1 = 0.6$, $\epsilon_2 = 0.6$, $a_2 = 3$ m, $s_1 = 1$, $f_1 = 1$, $s_2 = 1$, $f_2 = 1$, $L = 3$ m, $L_2 = 3$ m, $L_3 = 10$ m, $N = 6$ and $\theta = 30^\circ$

Figure 5.13 depicts the behaviour of $|R_0|$, $|T_0|$ and k_d against L_1/h corresponding to different values of height a_1 of the first porous structure. It shows that, with an increase in a_1, the dissipation coefficient increases which causes a reduction in $|R_0|$ and $|T_0|$. Here, for $a_1 = 7$ m, the values of the dissipation coefficient are higher than those for $a_1 = 1$ m, and the values of the reflection and transmission coefficients are minimum for $a_1 = 7$ m.

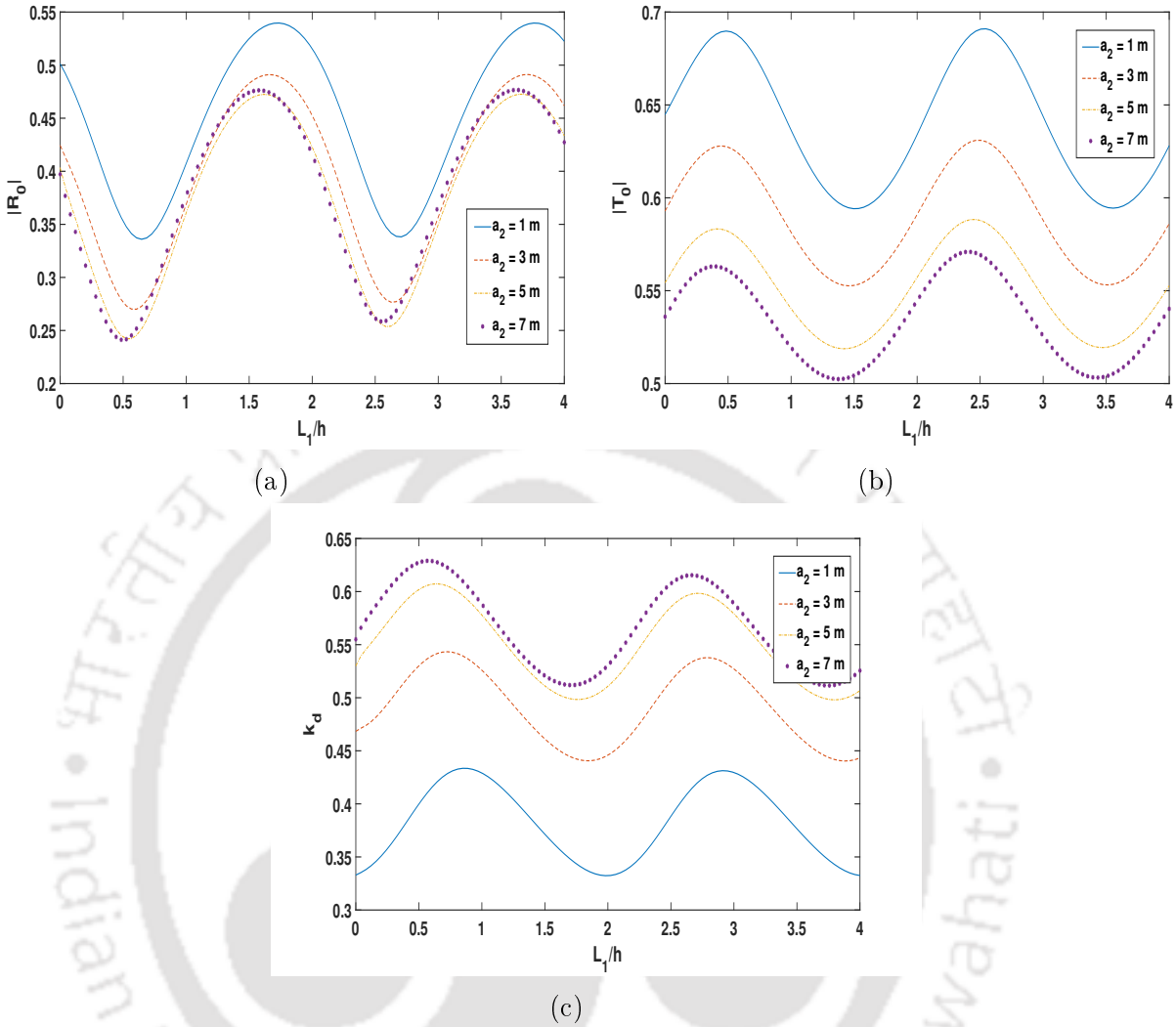

Figure 5.14: (a) $|R_0|$, (b) $|T_0|$, and (c) k_d against L_1/h for different values of height a_2 with $h = 15$ m, $h_1 = 3$ m, $\epsilon_1 = 0.6$, $\epsilon_2 = 0.6$, $a_1 = 3$ m, $s_1 = 1$, $f_1 = 1$, $s_2 = 1$, $f_2 = 1$, $L = 3$ m, $L_2 = 3$ m, $L_3 = 10$ m, $N = 6$ and $\theta = 30°$

Figure 5.14 illustrates the behaviour of $|R_0|$, $|T_0|$ and k_d against L_1/h corresponding to different values of height a_2 of the second porous structure. As a_2 increases, k_d increases, and the reflection and transmission coefficients decrease, as is observed in Figure 5.13. Here, for $a_2 = 1$ m, the values of the dissipation coefficient are lower than those for $a_2 = 7$ m. Figures 5.13 and 5.14 establish that the first porous structure with a greater height can dissipate more wave energy with a greater height than the second porous structure.

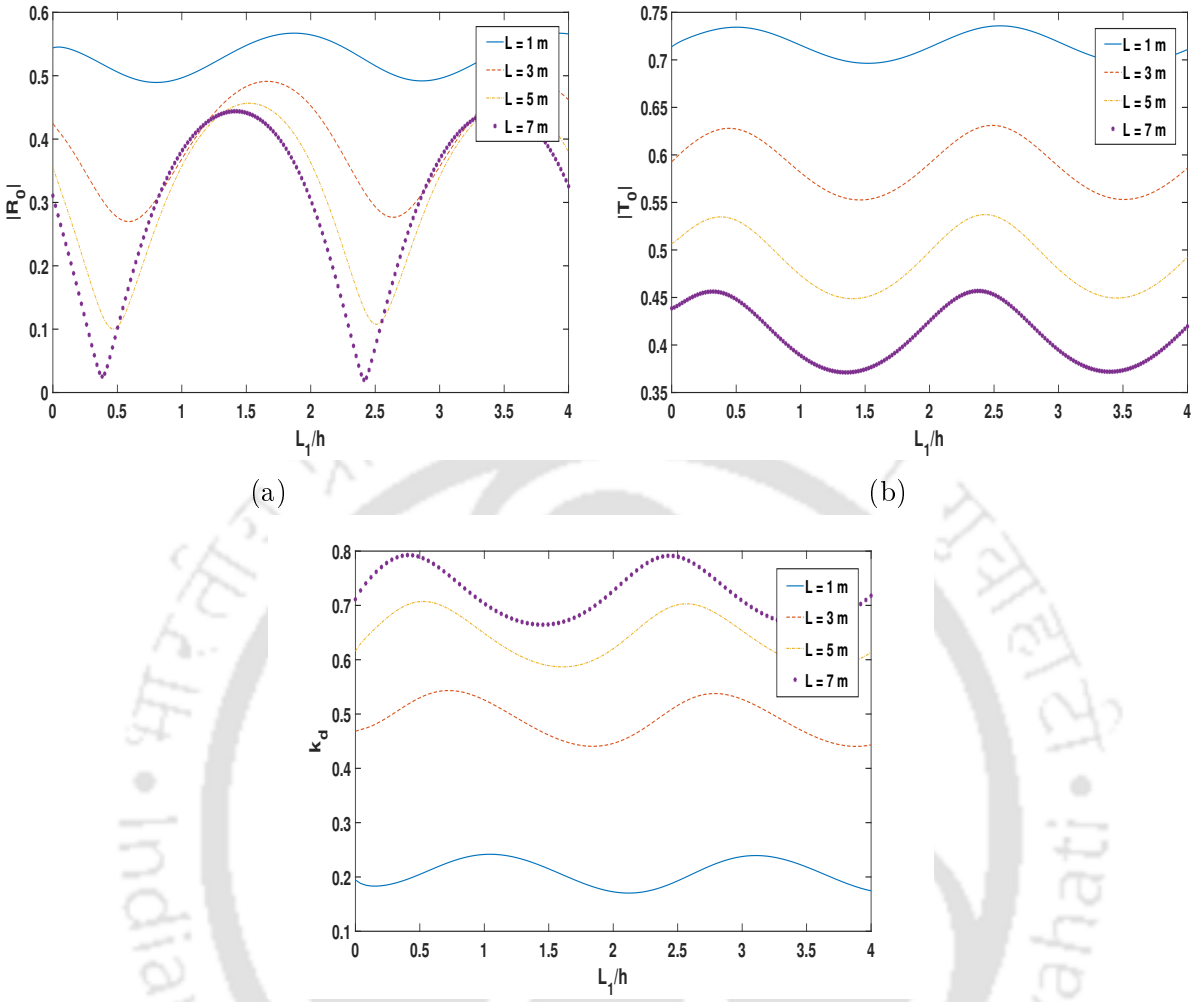

Figure 5.15: (a) $|R_0|$, (b) $|T_0|$, and (c) k_d against L_1/h for different values of width L of both the porous structures with $h = 15$ m, $h_1 = 3$ m, $\epsilon_1 = 0.6$, $\epsilon_2 = 0.6$, $a_1 = 3$ m, $a_2 = 3$ m, $s_1 = 1$, $f_1 = 1$, $s_2 = 1$, $f_2 = 1$, $L_2 = 3$ m, $L_3 = 10$ m, $N = 6$ and $\theta = 30°$

Figure 5.15 shows the variation of $|R_0|$, $|T_0|$ and k_d against L_1/h corresponding to different values of width L of both the porous structures. We observe that, with an increase in the width of the porous structures, the dissipation coefficient increases, which causes a decrease in both reflection and transmission coefficients.

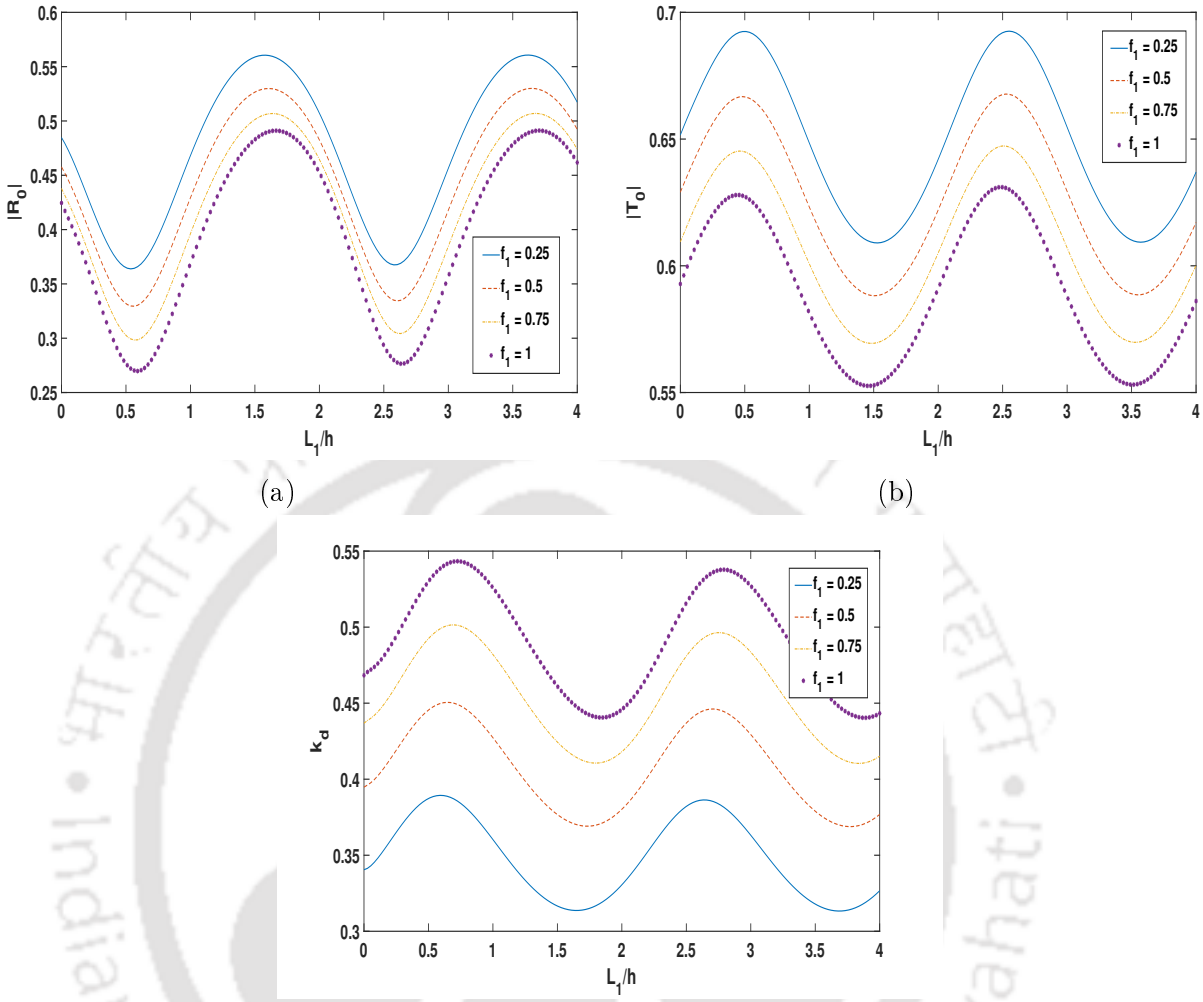

Figure 5.16: (a) $|R_0|$, (b) $|T_0|$, and (c) k_d against L_1/h for different values of friction factor f_1 with $h = 15$ m, $h_1 = 3$ m, $\epsilon_1 = 0.6$, $\epsilon_2 = 0.6$, $a_1 = 3$ m, $a_2 = 3$ m, $s_1 = 1$, $s_2 = 1$, $f_2 = 1$, $L = 3$ m, $L_2 = 3$ m, $L_3 = 10$ m, $N = 6$ and $\theta = 30°$

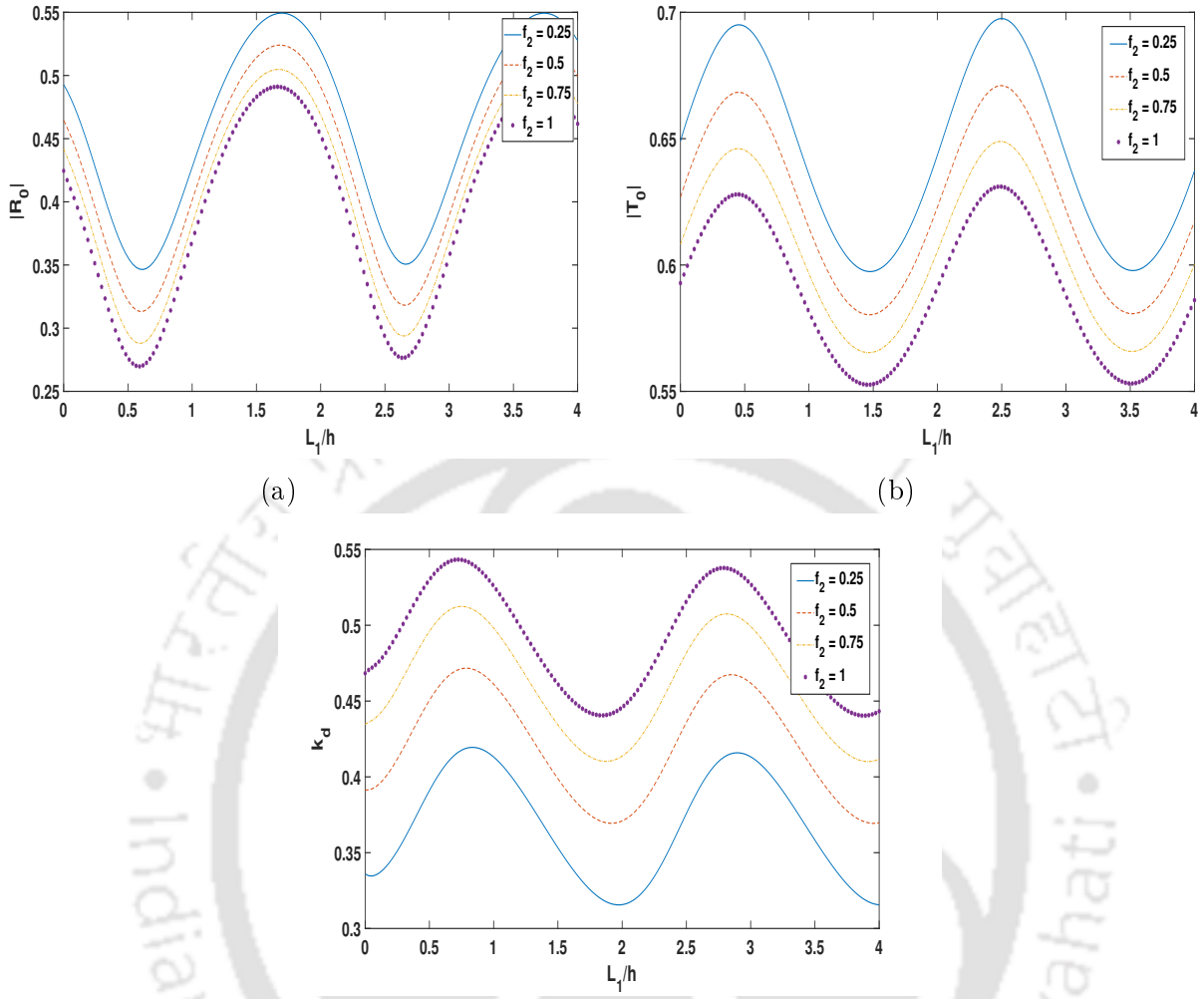

Figure 5.17: (a) $|R_0|$, (b) $|T_0|$, and (c) k_d against L_1/h for different values of friction factor f_2 with $h = 15$ m, $h_1 = 3$ m, $\epsilon_1 = 0.6$, $\epsilon_2 = 0.6$, $a_1 = 3$ m, $a_2 = 3$ m, $s_1 = 1$, $f_1 = 1$, $s_2 = 1$, $L = 3$ m, $L_2 = 3$ m, $L_3 = 10$ m, $N = 6$ and $\theta = 30°$

Figures 5.16 and 5.17 depict the behaviour of $|R_0|$, $|T_0|$ and k_d against L_1/h corresponding to different values of friction factors f_1 and f_2 of the first and second porous structures, respectively. As the values of both f_1 and f_2 increase, the reflection coefficient decreases. This outcome is anticipated since friction always introduces damping, and as a result, the wave energy dissipation increases.

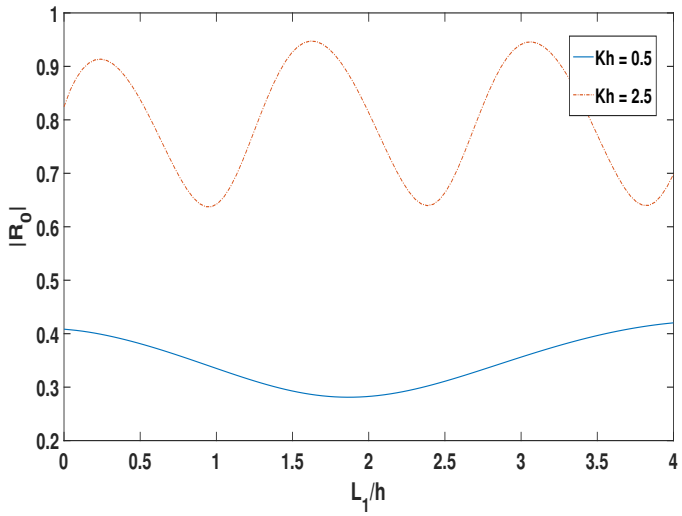

Figure 5.18: $|R_0|$ against L_1/h for different values of Kh

In Figure 5.18, we plot $|R_0|$ against L_1/h for $Kh = 0.5, 2.5$. In other words, we consider these values of Kh to represent the deep water regime and shallow water regime. This figure clearly shows that the reflection coefficient is higher in the deep water regime than in the shallow water regime.

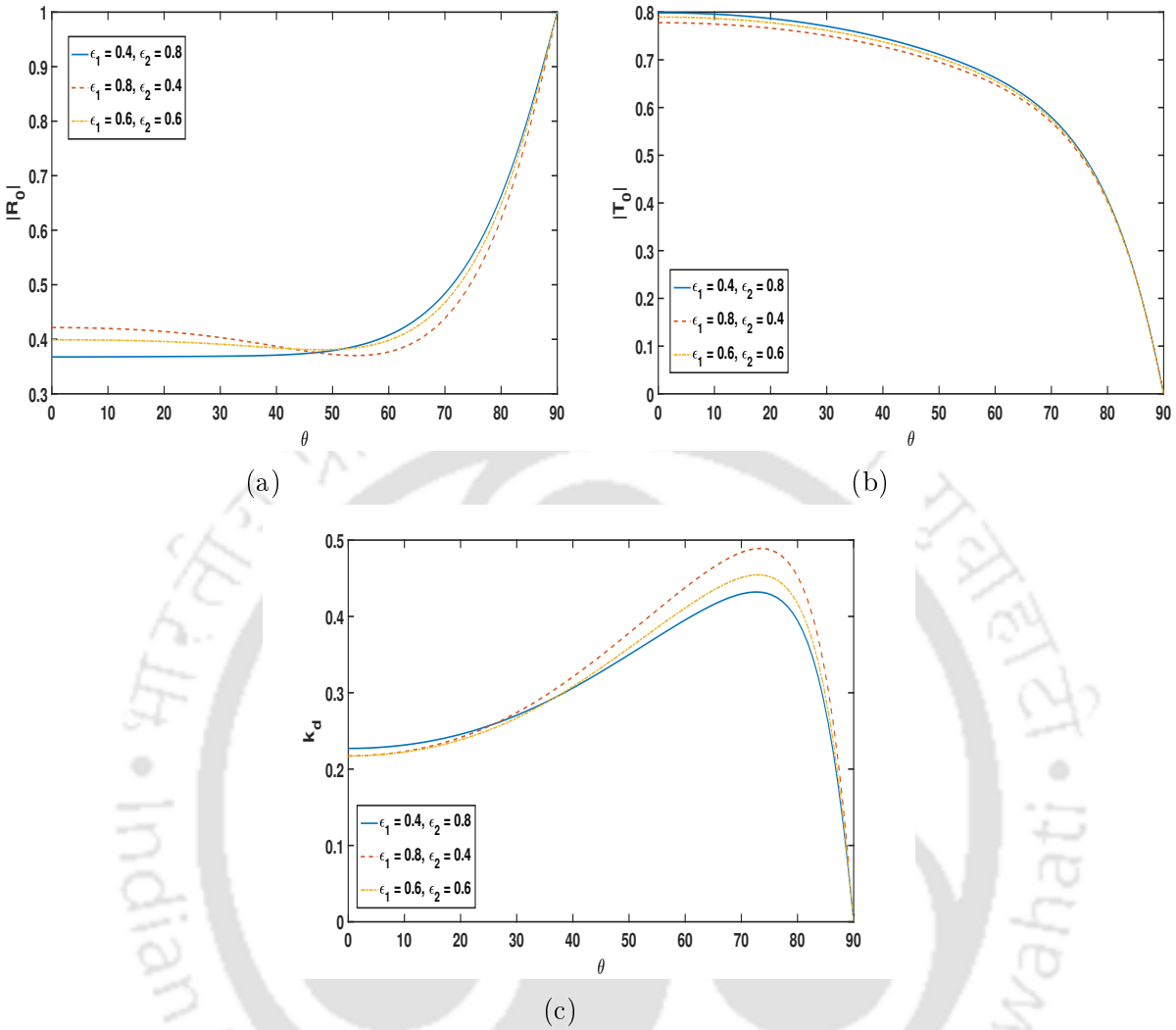

Figure 5.19: (a) $|R_0|$, (b) $|T_0|$, and (c) k_d against incident wave angle θ for different values of the porosity of the first and second porous structures with $h = 15$ m, $h_1 = 3$ m, $a_1 = 3$ m, $a_2 = 3$ m, $s_1 = 1$, $f_1 = 1$, $s_2 = 1$, $f_2 = 1$, $L = 3$ m, $L_1 = 2$ m, $L_2 = 3$ m and $L_3 = 10$ m

Figure 5.19 looks at the behaviour of $|R_0|$, $|T_0|$ and k_d against incident wave angle θ corresponding to various values of porosity ϵ_1 of the first and ϵ_2 of the second thick porous structures. It depicts that, when ϵ_2 is less than ϵ_1, higher wave energy dissipation is observed. From Figure 5.19, it can also be observed that, as θ increases, the reflection coefficient initially decreases, reaches a minimum value, then begins to increase, and at $\theta = 90°$, complete reflection ($|R_0| = 1$) is noted. This phenomenon can be explained as: at $\theta = 90°$, waves are tangential to the breakwaters, and therefore, there is no penetration inside them, and the full reflection is attained.

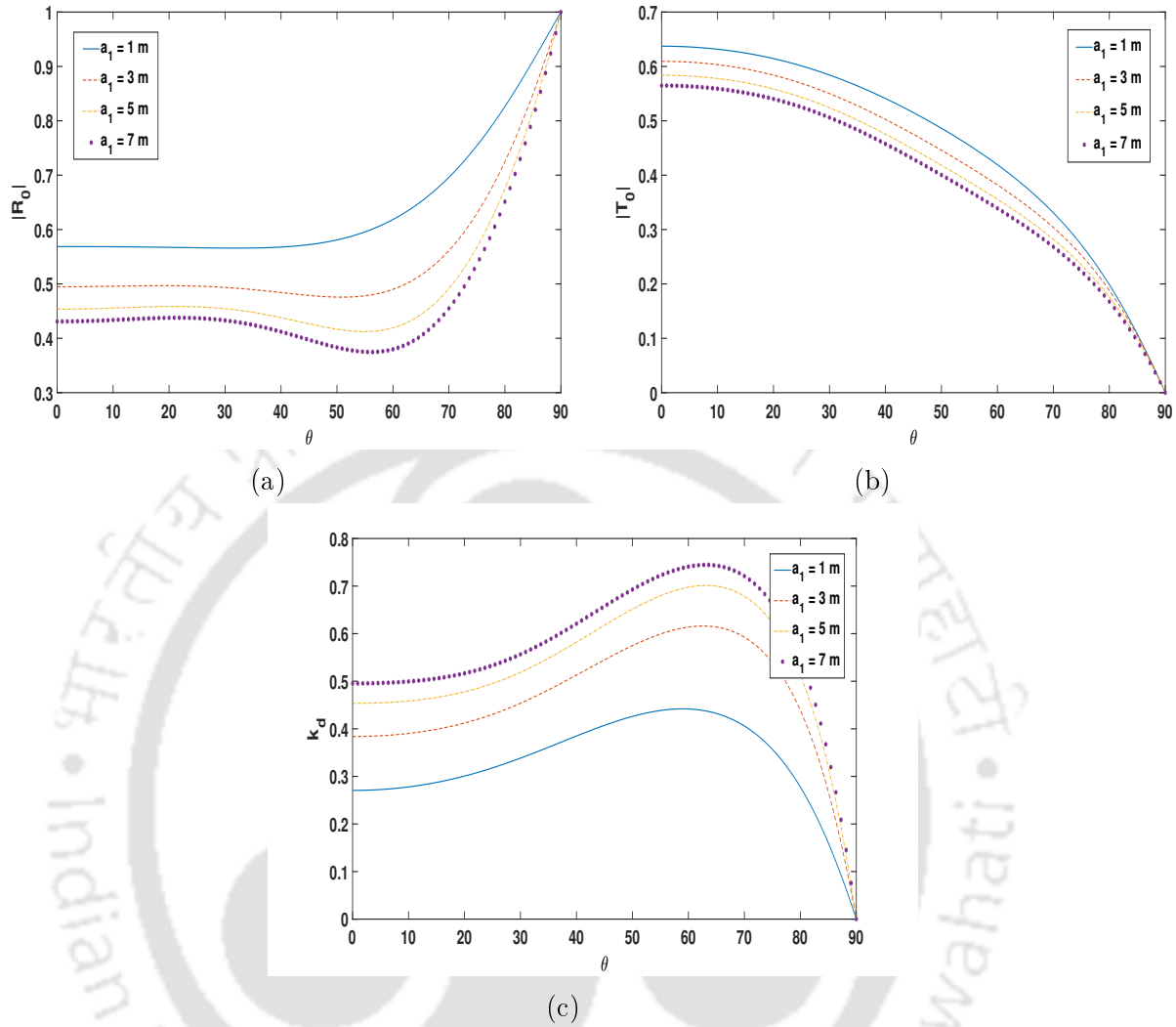

Figure 5.20: (a) $|R_0|$, (b) $|T_0|$, and (c) k_d against incident wave angle θ for different values of height a_1 with $h = 15$ m, $h_1 = 3$ m, $\epsilon_1 = 0.6$, $\epsilon_2 = 0.6$, $a_2 = 3$ m, $s_1 = 1$, $f_1 = 1$, $s_2 = 1$, $f_2 = 1$, $L = 3$ m, $L_1 = 2$ m, $L_2 = 3$ m and $L_3 = 10$ m

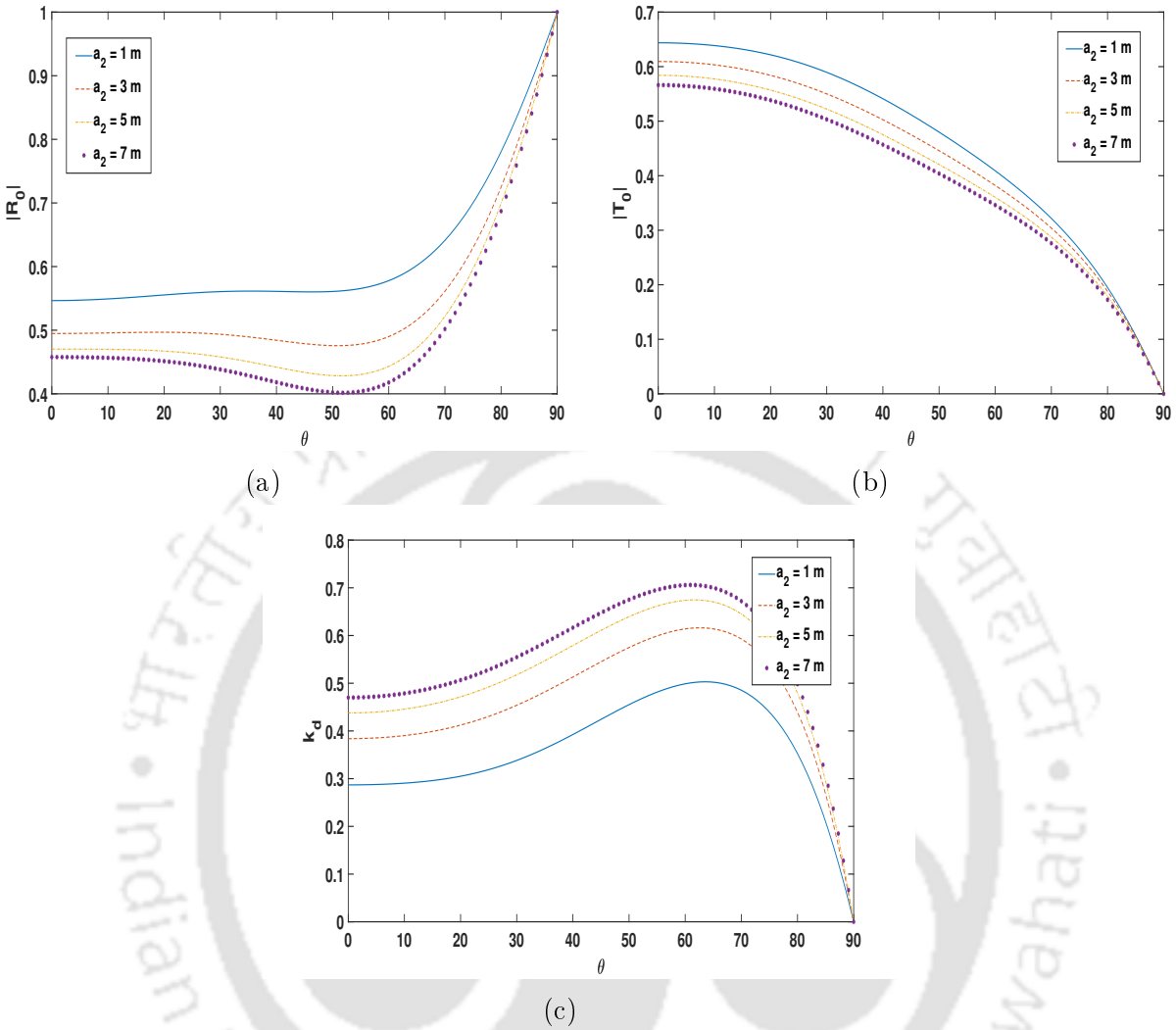

Figure 5.21: (a) $|R_0|$, (b) $|T_0|$, and (c) k_d against incident wave angle θ for different values of height a_2 with $h = 15$ m, $h_1 = 3$ m, $\epsilon_1 = 0.6$, $\epsilon_2 = 0.6$, $a_1 = 3$ m, $s_1 = 1$, $f_1 = 1$, $s_2 = 1$, $f_2 = 1$, $L = 3$ m, $L_1 = 2$ m, $L_2 = 3$ m and $L_3 = 10$ m

Figures 5.20 and 5.21 illustrate the variation of $|R_0|$, $|T_0|$ and k_d against θ corresponding to different values of height a_1 of the first porous structure and a_2 of the second porous structure, respectively. We note that, with an increase in a_1 and a_2, the dissipation coefficient increases as observed in Figures 5.13 and 5.14. As earlier, the full reflection is observed at $\theta = 90°$.

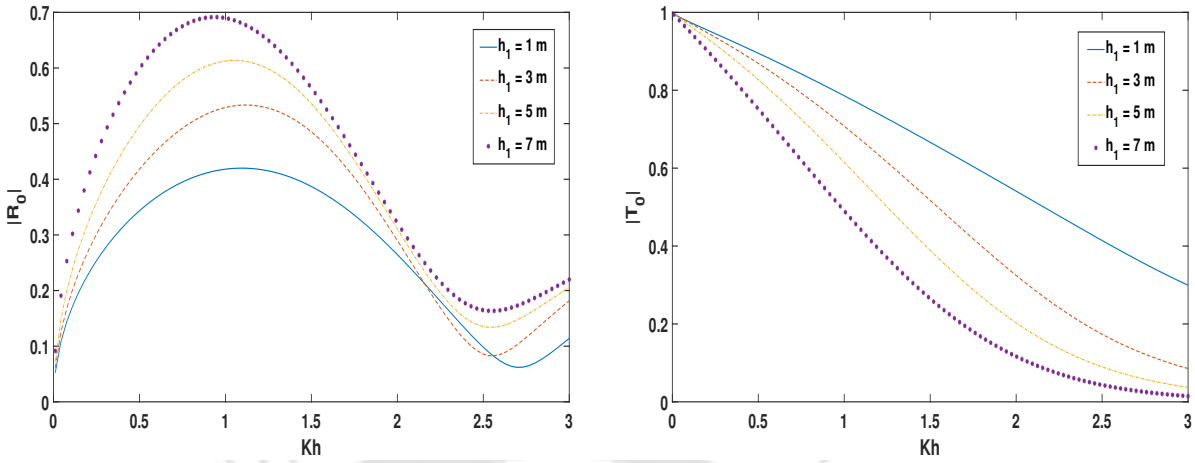

(a) (b)

Figure 5.22: (a) $|R_0|$, and (b) $|T_0|$ against Kh for different values of draft h_1 with $h = 15$ m, $\epsilon_1 = 0.6$, $\epsilon_2 = 0.6$, $a_1 = 3$ m, $a_2 = 3$ m, $s_1 = 1$, $f_1 = 1$, $s_2 = 1$, $f_2 = 1$, $L = 3$ m, $L_1 = 2$ m, $L_2 = 3$ m, $L_3 = 10$ m, $N = 6$ and $\theta = 30°$

Figure 5.22 shows the variation of reflection coefficient $|R_0|$ and transmission coefficient $|T_0|$ against Kh for different values of draft h_1 of the floating structure. It can be observed that, as h_1 increases, $|R_0|$ also increases since a greater draft height reflects more waves. Therefore, in this case, the transmission coefficient is less for higher values of h_1.

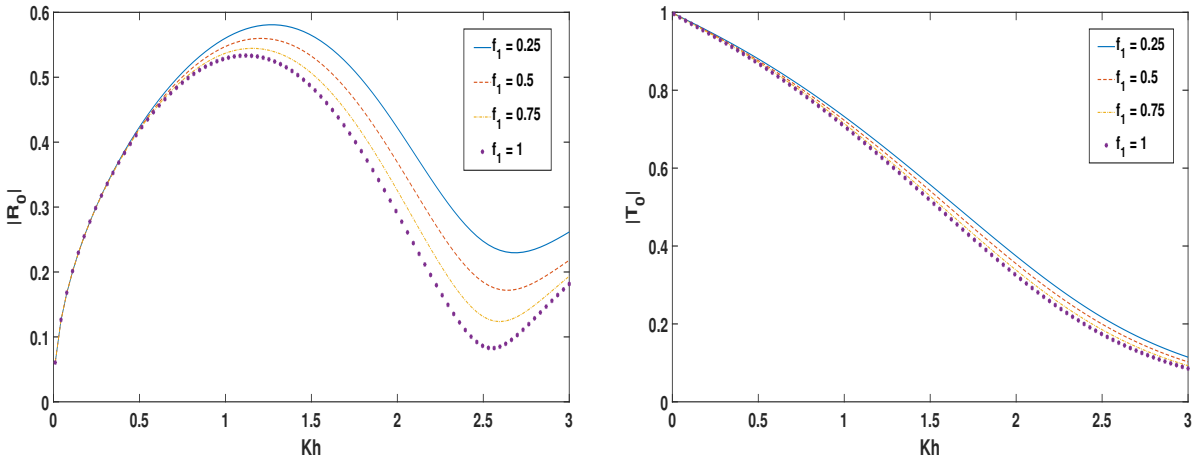

(a) (b)

Figure 5.23: (a) $|R_0|$, and (b) $|T_0|$ against Kh for different values of friction factor f_1 of the first porous structure with $h = 15$ m, $\epsilon_1 = 0.6$, $\epsilon_2 = 0.6$, $a_1 = 3$ m, $a_2 = 3$ m, $s_1 = 1$, $s_2 = 1$, $f_2 = 1$, $h_1 = 3$ m, $L = 3$ m, $L_1 = 2$ m, $L_2 = 3$ m, $L_3 = 10$ m, $N = 6$ and $\theta = 30°$

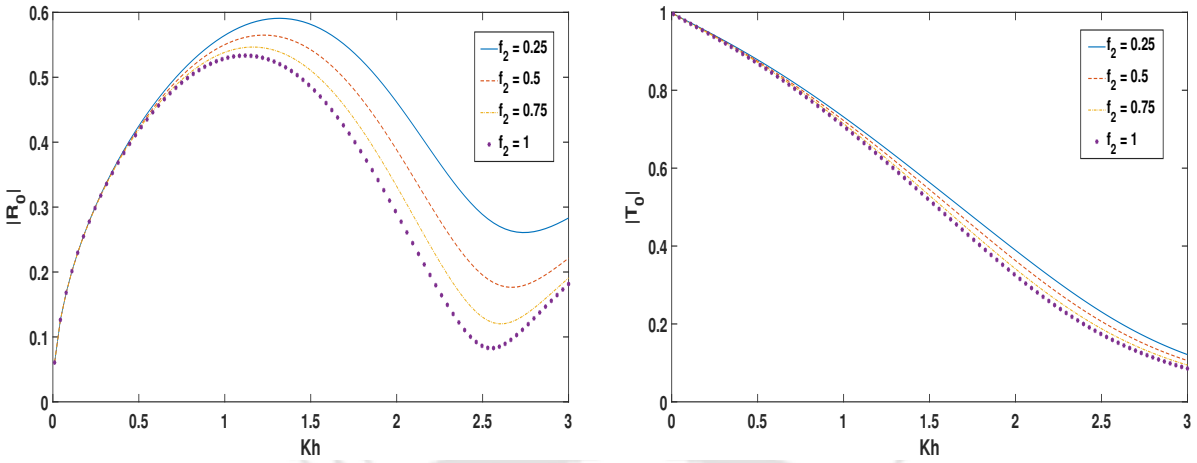

(a) (b)

Figure 5.24: (a) $|R_0|$, and (b) $|T_0|$ against Kh for different values of friction factor f_2 of the second porous structure with $h = 15$ m, $\epsilon_1 = 0.6$, $\epsilon_2 = 0.6$, $a_1 = 3$ m, $a_2 = 3$ m, $s_1 = 1$, $f_1 = 1$, $s_2 = 1$, $h_1 = 3$ m, $L = 3$ m, $L_1 = 2$ m, $L_2 = 3$ m, $L_3 = 10$ m, $N = 6$ and $\theta = 30°$

Figures 5.23 and 5.24 both show that, as friction factor f_1 or f_2 increases, the reflection and transmission coefficients both decrease as already observed in Figures 5.16 and 5.17.

5.5.4 Effect of the surface-piercing porous structures in mitigating wave forces

Here, the effect of various parameters of the porous structures is studied in order to suggest means to reduce the wave forces on the floating structure.

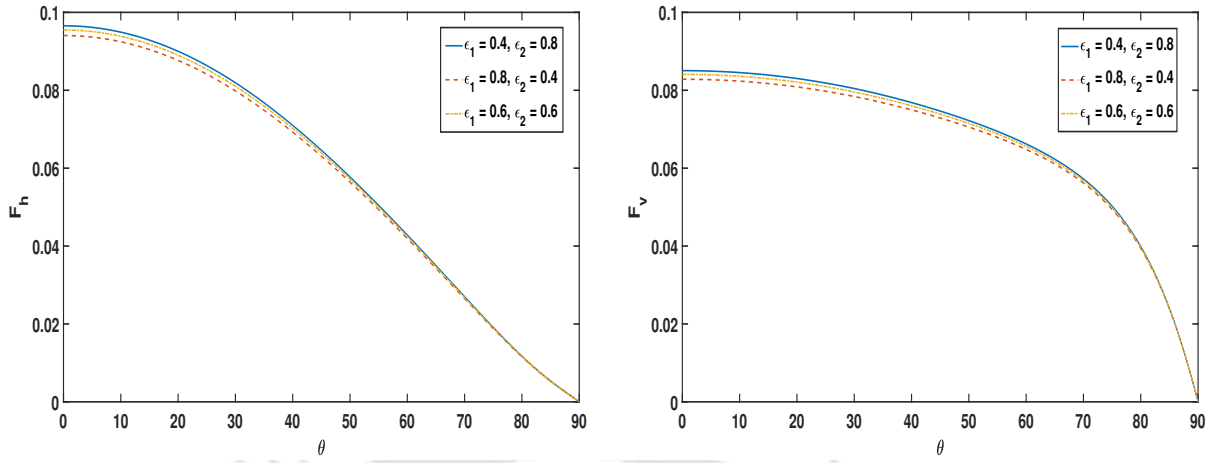

(a) (b)

Figure 5.25: (a) F_h (b) F_v against incident wave angle θ for the different values of the porosity of the first and second porous structures with $h = 15$ m, $h_1 = 3$ m, $a_1 = 3$ m, $a_2 = 3$ m, $s_1 = 1$, $f_1 = 1$, $s_2 = 1$, $f_2 = 1$, $L = 3$ m, $L_1 = 2$ m, $L_2 = 3$ m and $L_3 = 10$ m

Figure 5.25 shows the variation of horizontal force F_h and vertical force F_v on the floating structure against incident wave angle θ for various values of the porosity of the first and second porous structures. In Figure 5.19, we observed that, when porosity ϵ_1 is greater than porosity ϵ_2, the wave energy dissipation was high. In this case, Figure 5.25 shows that both horizontal and vertical forces acting on the floating structure are low. Figure 5.25 also demonstrates that, when θ approaches 90°, F_h and F_v approach zero. This occurs because reflection coefficient $|R_0|$ tends to 1, as already indicated in Figure 5.19.

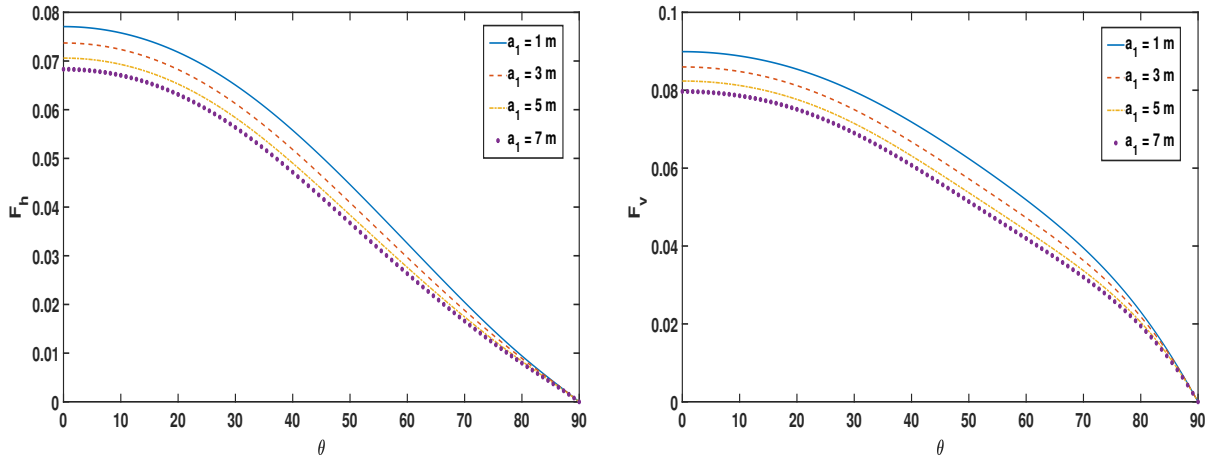

(a) (b)

Figure 5.26: (a) F_h (b) F_v against incident wave angle θ for the different values of height a_1 with $h = 15$ m, $h_1 = 3$ m, $\epsilon_1 = 0.6$, $\epsilon_2 = 0.6$, $a_2 = 3$ m, $s_1 = 1$, $f_1 = 1$, $s_2 = 1$, $f_2 = 1$, $L = 3$ m, $L_1 = 2$ m, $L_2 = 3$ m and $L_3 = 10$ m

Figures 5.26 shows the variation of F_h and F_v against θ for different values of height a_1 of the first porous structure. As a_1 increases, both F_h and F_v decrease. This phenomenon happens because the porous structure with greater height can dissipate more wave energy (as in Figures 5.13 and 5.20) and reduce both forces. Here, the lowest horizontal and vertical forces are obtained for $a_1 = 7$ m. Further, as θ approaches 90°, both horizontal and vertical forces approach zero because the reflection coefficient tends to 1 (Figure 5.20).

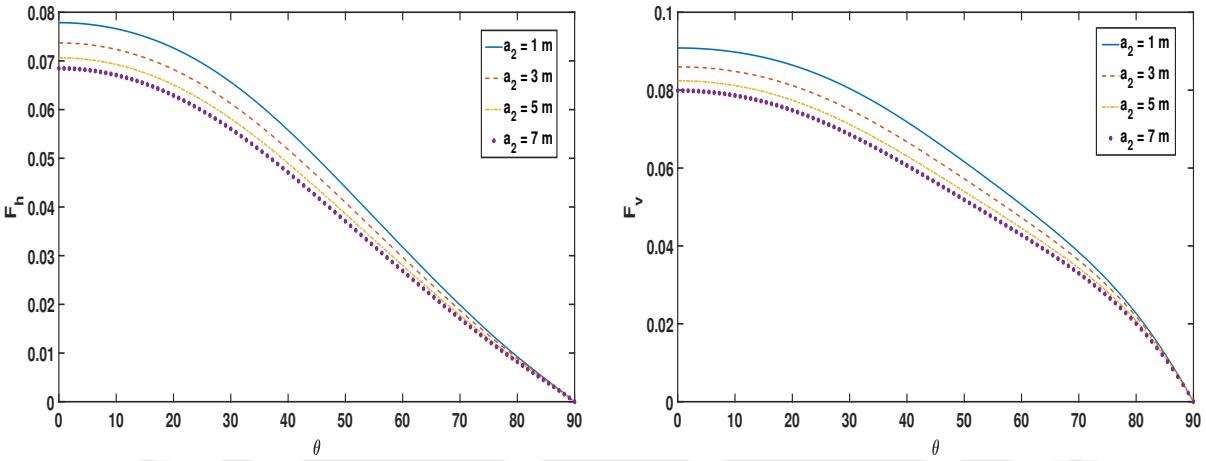

(a) (b)

Figure 5.27: (a) F_h (b) F_v against incident wave angle θ for the different values of height a_2 with $h = 15$ m, $h_1 = 3$ m, $\epsilon_1 = 0.6$, $\epsilon_2 = 0.6$, $a_1 = 3$ m, $s_1 = 1$, $f_1 = 1$, $s_2 = 1$, $f_2 = 1$, $L = 3$ m, $L_1 = 2$ m, $L_2 = 3$ m and $L_3 = 10$ m

In Figure 5.27, F_h and F_v are plotted against θ for different values of height a_2 of the second porous structure. This figure shows the same phenomenon as in Figure 5.26, i.e., as a_2 increases, both F_h and F_v decrease. For $a_2 = 7$ m, the lowest values of horizontal force and vertical force are obtained since the wave energy dissipation is higher for this value of a_2. Next, for $a_2 = 1$ m, the highest values for F_h and F_v are obtained since the wave energy dissipation is lower for this case. Additionally, both F_h and F_v tend to zero when θ tends to 90° because, in this case, the reflection coefficient approaches 1 (Figure 5.21).

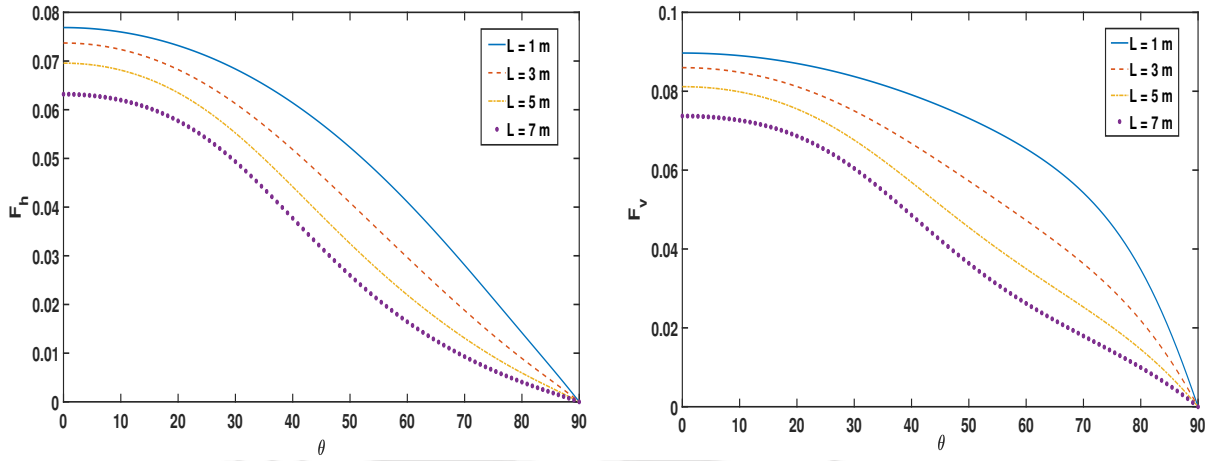

(a) (b)

Figure 5.28: (a) F_h (b) F_v against incident wave angle θ for the different values of width L of the both porous structures with $h = 15$ m, $h_1 = 3$ m, $\epsilon_1 = 0.6$, $\epsilon_2 = 0.6$, $a_1 = 3$ m, $a_2 = 3$ m, $s_1 = 1$, $f_1 = 1$, $s_2 = 1$, $f_2 = 1$, $L_1 = 2$ m, $L_2 = 3$ m and $L_3 = 10$ m

Figure 5.28 shows the variation of F_h and F_v against θ for various values of width L of both the porous structures. This figure shows that, as L increases, F_h and F_v decrease. This phenomenon can be explained as: when the width of the porous structures increases, they can dissipate more wave energy (as in Figure 5.15) and mitigate the wave forces appreciably. Here, for $L = 7$ m, both F_h and F_v attain the minimum values. Both forces tend to zeros as θ approaches 90°.

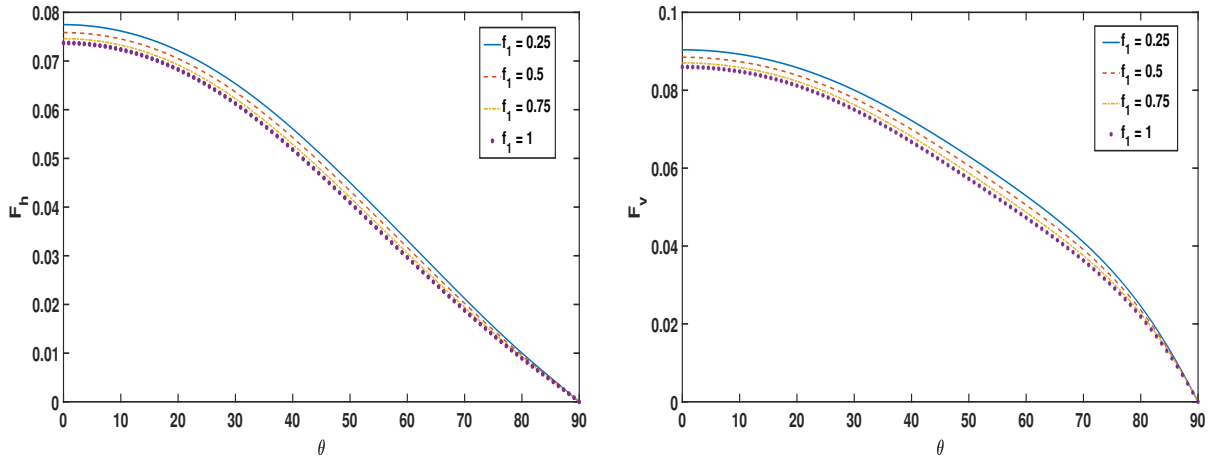

(a) (b)

Figure 5.29: (a) F_h (b) F_v against incident wave angle θ for the different values of friction factor f_1 with $h = 15$ m, $h_1 = 3$ m, $\epsilon_1 = 0.6$, $\epsilon_2 = 0.6$, $a_1 = 3$ m, $a_2 = 3$ m, $s_1 = 1$, $s_2 = 1$, $f_2 = 1$, $L = 3$ m, $L_1 = 2$ m, $L_2 = 3$ m and $L_3 = 10$ m

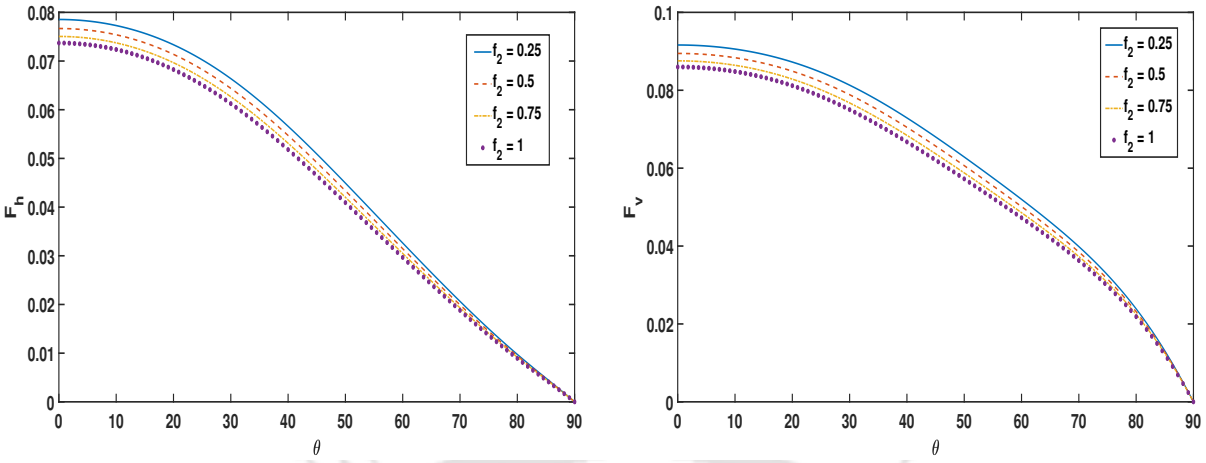

(a) (b)

Figure 5.30: (a) F_h (b) F_v against incident wave angle θ for the different values of friction factor f_2 with $h = 15$ m, $h_1 = 3$ m, $\epsilon_1 = 0.6$, $\epsilon_2 = 0.6$, $a_1 = 3$ m, $a_2 = 3$ m, $s_1 = 1$, $f_1 = 1$, $s_2 = 1$, $L = 3$ m, $L_1 = 2$ m, $L_2 = 3$ m and $L_3 = 10$ m

Figures 5.29 and 5.30 show the variation of F_h and F_v against θ corresponding to various values of friction factors f_1 and f_2 of the porous structures. Both figures depict that, as f_1 or f_2 increases, both F_h and F_v decrease. For $f_1 = 1$ or $f_2 = 1$, the lowest horizontal and vertical forces are observed since the wave energy dissipation is higher in this case (Figures 5.16 and 5.17).

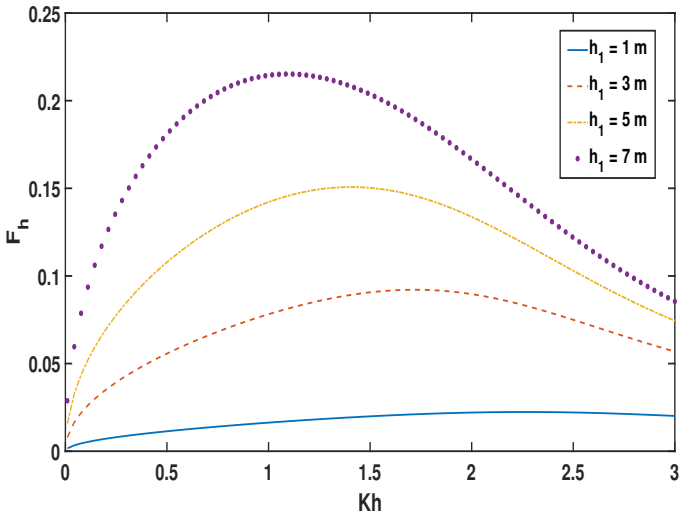

Figure 5.31: F_h against Kh for different values of height h_1 with $h = 15$ m, $\epsilon_1 = 0.6$, $\epsilon_2 = 0.6$, $a_1 = 3$ m, $a_2 = 3$ m, $s_1 = 1$, $f_1 = 1$, $s_2 = 1$, $f_2 = 1$, $L = 3$ m, $L_1 = 2$ m, $L_2 = 3$ m, $L_3 = 10$ m, $N = 6$ and $\theta = 30°$

Figure 5.31 illustrates the behaviour of horizontal force F_h against Kh for different values of draft h_1 of the floating structure. It shows that, as h_1 increases, F_h also increases

because, in this situation, more wave is reflected by the floating structure of larger draft as observed in Figure 5.22.

5.6 Conclusion

We examined the impact of two surface-piercing thick porous structures in mitigating wave-induced forces on a floating structure over a flat and impermeable sea-bed. The porous structures were considered to have different porosity, heights, and widths. The boundary value problems associated with each region were solved using the eigenfunction expansion method. These solutions were matched by applying the usual condition of continuity of mass flux and pressure, which gave rise to a system of linear equations. These equations were solved to determine the unknown coefficients. Subsequently, the reflection coefficient, transmission coefficient, dissipation coefficient and hydrodynamic forces acting on the floating structure were computed. A complete study on the root analysis of the dispersion relations was done, and also the behaviour of the roots of the dispersion relation was carried out to observe the mode swapping. To understand the role of the porous breakwaters, a number of graphs were produced corresponding to various parameters.

The main observations, analysis and findings of this work can be summed up as follows:

1. With an increase in the distance between the breakwaters, the reflection coefficient showed an oscillatory pattern.

2. It was observed that, as the porosity, width, height, and friction factor of the porous structures increased, the reflection coefficient and transmission coefficient decreased, and therefore, the wave energy dissipation by the porous breakwaters increased. This, in turn, reduced the wave forces acting on the floating structure.

3. Here, for $\epsilon_1 = 0.9$, $\epsilon_2 = 0.9$, $a_1 = 7$ m, $a_2 = 7$ m, $L = 7$ m, $f_1 = 1$ and $f_2 = 1$, we observed higher wave energy dissipation, and for these values, we obtained minimum wave-induced forces on the floating structure.

4. It was also noted that, as the incident wave angle increased, the reflection coefficient started decreasing. After reaching its minimum value, it started increasing, and as θ tended to 90°, the reflection coefficient approached 1. Consequently, the horizontal and vertical forces on the floating structure approached zero.

5. It was found that, if the porosity of the first breakwater was less than that of the second one, then reflection and transmission were high, and wave energy dissipation was low. Conversely, if the porosity of the second breakwater was less than that

of the first one, the reflection and transmission were lower and the wave energy dissipation was higher.

6. Here, for $\epsilon_1 = 0.8$ and $\epsilon_2 = 0.4$, we observed higher energy dissipation.

7. Therefore, as an appropriate combination to protect the floating structure, the porosity of the second porous breakwater should be less than that of the first one.

The present study concluded that a suitable arrangement of thick porous structures could efficiently mitigate the wave-induced forces acting on the floating structure. It presents a complete study of the associated reflection, dissipation and wave forces for the floating structure in the presence of two porous breakwaters.

CHAPTER 6

Scattering of oblique incident waves by a floating structure with a porous wall fitted on its vertical sides in the presence of a varying bottom topography

In the present work, the oblique wave scattering by a floating structure with a porous wall fitted on its vertical sides is analyzed with the consideration of a varying bottom topography. The sea-bed is impermeable and features varying topography. The entire fluid domain is divided into nine regions, in which two regions are porous regions, while the others are water regions. The relevant boundary value problems are set up in each region. Linearized water wave theory is utilized to obtain the solution of the corresponding boundary value problems in each region within a three-dimensional Cartesian coordinate system. The velocity potentials in each region are obtained using the eigenfunction expansion method. The unknown coefficients of the velocity potentials are computed by implementing a standard matrix technique. The use of modified mild slope equation (MMSE) helps in tackling the condition on the varying bottom. This work aims to calculate appropriate values of different parameters to reduce wave-induced forces on the floating structure. To achieve this, the effects of varying bottom, porosity, thickness, and draft of the porous wall on the reflection and transmission coefficients, as well as on the horizontal and vertical forces, are studied.

6.1 Mathematical formulation

The problem of oblique water wave interaction with a floating structure in the presence of a varying bottom topography is analyzed. The vertical sides of the structure have porous

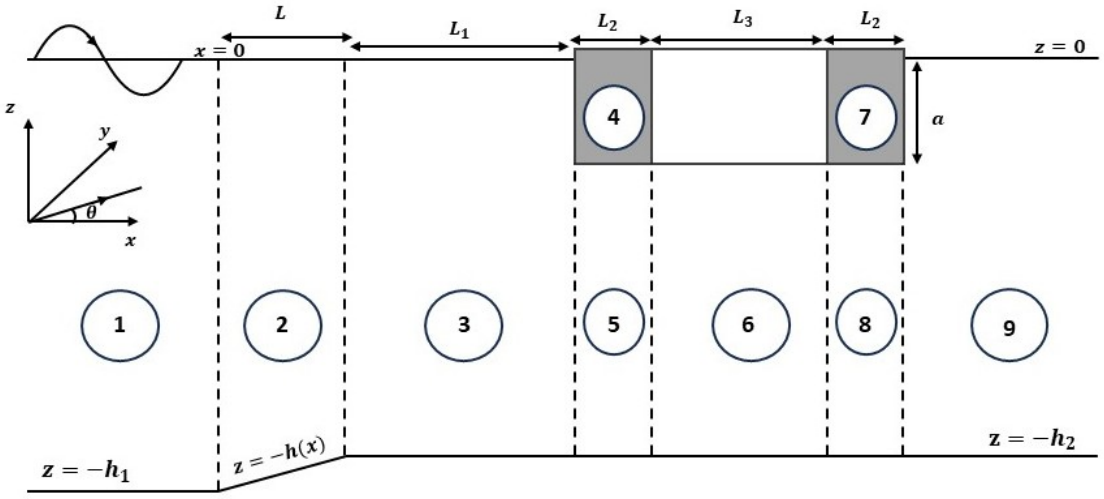

Figure 6.1: Definition sketch of a rigid floating structure fitted with a porous wall on its vertical sides, and a varying bottom

wall fitted. A three-dimensional Cartesian coordinate system (x, y, z) is considered with the xy-plane as the horizontal plane, the positive z-axis in the upward direction, and $z = 0$ as the undisturbed free surface as depicted in Figure 6.1. The sea-bed ($z = -h_1,\ -\infty < x < 0;\ z = -h(x),\ 0 < x < L;\ z = -h_2,\ L < x < \infty$) is considered impermeable. The floating structure is considered as a rigid rectangular structure of finite width L_3 and draft a. The porous wall of thickness L_2 and draft a is fitted on the vertical sides of the floating structure between $x = L + L_1$ and $x = L + L_1 + L_2$, and between $x = L + L_1 + L_2 + L_3$ and $x = L + L_1 + 2L_2 + L_3$. The whole fluid domain is divided into nine sub-regions as follows: Region 1 (water region): $-\infty < x < 0,\ -h_1 < z < 0$; Region 2 (water region): $0 < x < L,\ -h(x) < z < 0$; Region 3 (water region) $L < x < L + L_1,\ -h_2 < z < 0$; Region 4 (porous region): $L + L_1 < x < L + L_1 + L_2,\ -a < z < 0$; Region 5 (water region): $L + L_1 < x < L + L_1 + L_2,\ -h_2 < z < -a$; Region 6 (water region): $L + L_1 + L2 < x < L + L_1 + L_2 + L_3,\ -h_2 < z < -a$; Region 7 (porous region): $L + L_1 + L_2 + L_3 < x < L + L_1 + 2L_2 + L_3,\ -a < z < 0$; Region 8 (water region): $L + L_1 + L_2 + L_3 < x < L + L_1 + 2L_2 + L_3,\ -h_2 < z < -a$; and Region 9 (water region): $L + L_1 + 2L_2 + L_3 < x < \infty,\ -h_2 < z < 0$.

We consider that the motions are simple harmonic along the y-direction and also time harmonic with angular frequency ω. Additionally, We assume that the waves propagate from the positive x-direction. The scattered potential for oblique water wave in each region can be considered as $\Phi_j(x, y, z, t) = \mathrm{Re}[\phi_j(x, z)e^{\mathrm{i}(k_y y - \omega t)}]$ for $j = 1, 2, 3, 4, 5, 6, 7, 8, 9$, where $k_y = k_0 \sin(\theta)$, θ is the incident wave angle inclined to the x-axis, and k_0 is the incident wavenumber.

Each velocity potential ϕ_j satisfies the modified Helmholtz equation

$$\left(\frac{\partial^2}{\partial x^2}+\frac{\partial^2}{\partial z^2}-k_y^2\right)\phi_j=0 \quad \text{for} \quad j=1,2,3,4,5,6,7,8,9. \tag{6.1}$$

The linearized free surface condition for Regions 1, 2, 3 and 9 is the following:

$$\frac{\partial \phi_j}{\partial z}-K\phi_j=0 \quad \text{at} \quad z=0 \quad \text{for} \quad j=1,2,3,9, \tag{6.2}$$

while the mean free surface condition for Regions 4 and 7 is

$$\frac{\partial \phi_j}{\partial z}-K\gamma\phi_j=0 \quad \text{at} \quad z=0 \quad \text{for} \quad j=4,7, \tag{6.3}$$

where $\gamma = m+\mathrm{i}f$ is the dimensionless porous impedance parameter of the porous wall with m representing the corresponding inertial coefficient and f representing the corresponding linearized friction factor.
The boundary condition on the uniform depth parts of the sea-bed are as follows:

$$\frac{\partial \phi_1}{\partial z}=0 \quad \text{at} \quad z=-h_1, \tag{6.4}$$

$$\frac{\partial \phi_j}{\partial z}=0 \quad \text{at} \quad z=-h_2 \quad \text{for} \quad j=3,5,6,8,9. \tag{6.5}$$

The boundary condition on the varying part of the bottom is given by

$$\frac{\partial \phi_2}{\partial z}+\frac{dh}{dx}\frac{\partial \phi_2}{\partial x}=0 \quad \text{at} \quad z=-h(x), \quad 0<x<L. \tag{6.6}$$

The floating structure being rigid, the horizontal and vertical velocities vanish on its sides. This leads to the following boundary conditions on the vertical and horizontal sides:

$$\frac{\partial \phi_4}{\partial x}=0 \quad \text{at} \quad x=L+L_1+L_2, \quad -a<z<0, \tag{6.7}$$

$$\frac{\partial \phi_7}{\partial x}=0 \quad \text{at} \quad x=L+L_1+L_2+L_3, \quad -a<z<0, \tag{6.8}$$

$$\frac{\partial \phi_6}{\partial z}=0 \quad \text{at} \quad z=-a, \quad L+L_1+L_2<x<L+L_1+L_2+L_3. \tag{6.9}$$

When the fluid passes through the virtual boundaries, the continuity of mass flux and pressure gives rise to the following matching conditions across the vertical boundaries $x=0$, $x=L$, $x=L+L_1$, $x=L+L_1+L_2$, $x=L+L1+L_2+L_3$, and $x=L+L_1+2L_2+L_3$, and the horizontal boundary $z=-a$:

$$\phi_1=\phi_2 \quad \text{at} \quad x=0, \quad -h_1<z<0, \tag{6.10}$$

$$\frac{\partial \phi_1}{\partial x} = \frac{\partial \phi_2}{\partial x} \text{ at } x = 0, \ -h_1 < z < 0, \tag{6.11}$$

$$\phi_2 = \phi_3 \text{ at } x = L, \ -h_2 < z < 0, \tag{6.12}$$

$$\frac{\partial \phi_2}{\partial x} = \frac{\partial \phi_3}{\partial x} \text{ at } x = L, \ -h_2 < z < 0, \tag{6.13}$$

$$\phi_3 = \gamma \phi_4 \text{ at } x = L + L_1, \ -a < z < 0, \tag{6.14}$$

$$\frac{\partial \phi_3}{\partial x} = \epsilon \frac{\partial \phi_4}{\partial x} \text{ at } x = L + L_1, \ -a < z < 0, \tag{6.15}$$

$$\phi_3 = \phi_5 \text{ at } x = L + L_1, \ -h_2 < z < -a, \tag{6.16}$$

$$\frac{\partial \phi_3}{\partial x} = \frac{\partial \phi_5}{\partial x} \text{ at } x = L + L_1, \ -h_2 < z < -a, \tag{6.17}$$

$$\gamma \phi_4 = \phi_5 \text{ at } z = -a, \ L + L_1 < x < L + L_1 + L_2, \tag{6.18}$$

$$\epsilon \frac{\partial \phi_4}{\partial z} = \frac{\partial \phi_5}{\partial z} \text{ at } z = -a, \ L + L_1 < x < L + L_1 + L_2, \tag{6.19}$$

$$\phi_5 = \phi_6 \text{ at } x = L + L_1 + L_2, \ -h_2 < z < -a, \tag{6.20}$$

$$\frac{\partial \phi_5}{\partial x} = \frac{\partial \phi_6}{\partial x} \text{ at } x = L + L_1 + L_2, \ -h_2 < z < -a, \tag{6.21}$$

$$\phi_6 = \phi_8 \text{ at } x = L + L_1 + L_2 + L_3, \ -h_2 < z < -a, \tag{6.22}$$

$$\frac{\partial \phi_6}{\partial x} = \frac{\partial \phi_8}{\partial x} \text{ at } x = L + L_1 + L_2 + L_3, \ -h_2 < z < -a, \tag{6.23}$$

$$\gamma \phi_7 = \phi_8 \text{ at } z = -a, \ L + L_1 + L_2 + L_3 < x < L + L_1 + 2L_2 + L_3, \tag{6.24}$$

$$\epsilon \frac{\partial \phi_7}{\partial z} = \frac{\partial \phi_8}{\partial z} \text{ at } z = -a, \ L + L_1 + L_2 + L_3 < x < L + L_1 + 2L_2 + L_3, \tag{6.25}$$

$$\gamma \phi_7 = \phi_9 \text{ at } x = L + L_1 + 2L_2 + L_3, \ -a < z < 0, \tag{6.26}$$

$$\epsilon \frac{\partial \phi_7}{\partial x} = \frac{\partial \phi_9}{\partial x} \text{ at } x = L + L_1 + 2L_2 + L_3, \ -a < z < 0, \tag{6.27}$$

$$\phi_8 = \phi_9 \text{ at } x = L + L_1 + 2L_2 + L_3, \ -h_2 < z < -a, \tag{6.28}$$

$$\frac{\partial \phi_8}{\partial x} = \frac{\partial \phi_9}{\partial x} \text{ at } x = L + L_1 + 2L_2 + L_3, \ -h_2 < z < -a, \tag{6.29}$$

where ϵ is the porosity of the porous wall.
The far-field conditions are given by

$$\phi_1(x,z) = -\left(\frac{\mathrm{i}g}{\omega}\right)(e^{\mathrm{i}p_0 x} + R_0 e^{-\mathrm{i}p_0 x})\frac{\cosh(k_0(z+h_1))}{\cosh(k_0 h_1)} \text{ as } x \to -\infty, \tag{6.30}$$

$$\phi_9(x,z) = -\left(\frac{\mathrm{i}g}{\omega}\right)T_0 e^{\mathrm{i}q_0 x}\frac{\cosh(d_0(z+h_2))}{\cosh(d_0 h_2)} \text{ as } x \to \infty, \tag{6.31}$$

where R_0 and T_0, respectively, are the reflected and transmitted coefficients, k_0 and d_0 are the roots of the dispersion relations $k\tanh(kh_1) - K = 0$ and $d\tanh(dh_2) - K = 0$, respectively, $p_0 = \sqrt{k_0^2 - k_y^2}$ and $q_0 = \sqrt{d_0^2 - k_y^2}$.

6.2 Solution procedure

The aforementioned boundary value problems are solved by employing the separation of variables method to equation (6.1) to expand the eigenfunctions of the velocity potentials in each region. Afterward, the boundary conditions of vanishing horizontal and vertical velocities on the sides of the rigid floating structure are applied. Subsequently, the matching conditions (continuity of the mass flux and pressure) are used across each vertical and horizontal virtual boundary to obtain a system of linear equations, which is solved by using MATLAB to evaluate the unknown coefficients appearing in the expressions of the velocity potentials. From these solutions, the necessary quantities, such as the reflection coefficient, transmission coefficient, and the vertical and horizontal forces acting on the floating structure, can be calculated.

In order to achieve our objective, we first go ahead to find the velocity potentials ϕ_j in all regions.

In Region 1, the scattered potential $\phi_1(x,z)$ can be expressed as

$$\phi_1(x,z) = \big(e^{\mathrm{i}p_0 x} Z_{0,1}(k_0,z) + \sum_{n=0}^{\infty} R_n e^{-\mathrm{i}p_n x} Z_{n,1}(k_n,z)\big), \tag{6.32}$$

where the depth function $Z_{n,1}(k_n,z)$ and p_n are, respectively, given by

$$Z_{n,1}(k_n,z) = -\left(\frac{\mathrm{i}g}{\omega}\right)\frac{\cosh(k_n(z+h_1))}{\cosh(k_n h_1)}, \quad n = 0,1,2,\cdots,$$
$$p_n = \sqrt{k_n^2 - k_y^2},$$

with k_n's as the roots of the dispersion relation

$$k\tanh(kh_1) - K = 0. \tag{6.33}$$

Here, R_n are the unknowns where R_0 is the reflection coefficient.

The velocity potential $\phi_2(x,z)$ in Region 2 can be written as

$$\phi_2(x,z) = \sum_{n=0}^{\infty} \psi_n(x) Z_{n,2}(h,z), \tag{6.34}$$

where $\psi_n(x)$ are the unknown functions and

$$Z_{n,2}(h,z) = -\left(\frac{\mathrm{i}g}{\omega}\right)\frac{\cosh(\beta_n(z+h))}{\cosh(\beta_n h)}, \quad n = 0,1,2,\cdots,$$

with β_n's as the roots of the dispersion relation

$$\beta\tanh(\beta h) - K = 0. \tag{6.35}$$

Here, β_0, β_1, β_2, $\cdots$ are functions of x, since they depend on the varying bottom $h(x)$ locally.

In Region 3, the velocity potential $\phi_3(x,z)$ has the following form:

$$\phi_3(x,z) = \sum_{n=0}^{\infty} \left(A_n e^{\mathrm{i}q_n x} + B_n e^{-\mathrm{i}q_n x}\right) Z_{n,3}(d_n, z), \tag{6.36}$$

where the depth function $Z_{n,3}(d_n,z)$ and q_n are, respectively, given by

$$Z_{n,3}(d_n,z) = -\left(\frac{\mathrm{i}g}{\omega}\right)\frac{\cosh(d_n(z+h_2))}{\cosh(d_n h_2)}, \quad n = 0,1,2,\cdots,$$
$$q_n = \sqrt{d_n^2 - k_y^2},$$

with d_n's as the roots of the dispersion relation

$$d\tanh(dh_2) - K = 0, \tag{6.37}$$

and A_n's and B_n's the unknown coefficients.

The velocity potentials $\phi_4(x,z)$ and $\phi_5(x,z)$ in Regions 4 and 5 are obtained, respectively, as

$$\phi_4(x,z) = \sum_{n=0}^{\infty} \left(C_n e^{\mathrm{i}\alpha_n x} + D_n e^{-\mathrm{i}\alpha_n x}\right) Z_{n,4}(t_n, z), \tag{6.38}$$

$$\phi_5(x,z) = \sum_{n=0}^{\infty} \left(C_n e^{\mathrm{i}\alpha_n x} + D_n e^{-\mathrm{i}\alpha_n x}\right) Z_{n,5}(t_n, z), \tag{6.39}$$

where C_n's and D_n's are the unknown coefficients, and the depth functions $Z_{n,4}(t_n,z)$ and $Z_{n,5}(t_n,z)$ and α_n are as follows:

$$Z_{n,4}(t_n,z) = -\left(\frac{\mathrm{i}g}{\omega}\right)\frac{\cosh(t_n(z+h_2)) - S_n\sinh(t_n(z+h_2))}{\cosh(t_n h_2) - S_n\sinh(t_n h_2)}, \quad n = 0,1,2,\cdots,$$
$$Z_{n,5}(t_n,z) = -\left(\frac{\mathrm{i}g}{\omega}\right)\frac{\gamma(1 - S_n\tanh(t_n(h_2-a)))}{(\cosh(t_n h_2) - S_n\sinh(t_n h_2))}\cosh(t_n(z+h_2)), \quad n = 0,1,2,\cdots,$$
$$\alpha_n = \sqrt{t_n^2 - k_y^2},$$

where S_n's are defined as

$$S_n = \left(1 - \frac{\epsilon}{\gamma}\right)\frac{\tanh(t_n(h_2-a))}{\tanh^2(t_n(h_2-a)) - \frac{\epsilon}{\gamma}}.$$

In above, t_n's are the roots of the dispersion relation

$$K\gamma - t_n \tanh(t_n h_2) - S_n(K\gamma \tanh(t_n h_2) - t_n) = 0. \tag{6.40}$$

In Region 6, the scattered potential can be expressed as

$$\phi_6(x,z) = \sum_{n=0}^{\infty} \Big(E_n \frac{\cosh(s_n x)}{\cosh(s_n b)} + F_n \frac{\sinh(s_n x)}{\sinh(s_n b)} \Big) Z_{n,6}(r_n, z), \tag{6.41}$$

with the depth function $Z_{n,6}(r_n, z)$, r_n and s_n written, respectively, as

$$\begin{aligned} Z_{n,6}(r_n,z) &= -\left(\frac{\mathrm{i}g}{\omega}\right)\cos(r_n(z+a)), \quad n = 0,1,2,..., \\ r_n &= \frac{n\pi}{h_2 - a}, \\ s_n &= \sqrt{r_n^2 + k_y^2}. \end{aligned}$$

In Regions 7 and 8, the velocity potentials $\phi_7(x,z)$ and $\phi_8(x,z)$ are obtained as

$$\phi_7(x,z) = \sum_{n=0}^{\infty} \big(G_n e^{\mathrm{i}\alpha_n x} + H_n e^{-\mathrm{i}\alpha_n x} \big) Z_{n,4}(t_n, z), \tag{6.42}$$

$$\phi_8(x,z) = \sum_{n=0}^{\infty} \big(G_n e^{\mathrm{i}\alpha_n x} + H_n e^{-\mathrm{i}\alpha_n x} \big) Z_{n,5}(t_n, z), \tag{6.43}$$

where G_n's and H_n's are the unknown coefficients.
The velocity potential $\phi_9(x,z)$ in Region 9 can be expressed as

$$\phi_9(x,z) = \sum_{n=0}^{\infty} T_n e^{\mathrm{i}q_n x} Z_{n,3}(d_n, z), \tag{6.44}$$

where T_n's are the unknown transmission coefficients.
For oblique waves, the function $\psi_n(x)$ in equation (6.34) can be obtained by solving the modified mild-slope equation

$$\begin{aligned} \frac{d}{dx}\Big(a_n \frac{d\psi_n}{dx}\Big) + \sum_{m=0}^{N} \Big[\Big(b_{mn} - b_{nm}\Big) \frac{dh}{dx}\frac{d\psi_m}{dx} + \Big\{ b_{mn}\frac{d^2h}{dx^2} + c_{mn}\Big(\frac{dh}{dx}\Big)^2 \\ + d_{mn} - k_y^2 a_n \Big\} \psi_m \Big] = 0, \end{aligned} \tag{6.45}$$

where

$$a_n(h) = \int_{-h}^{0} Z_{n,2}^2 dz, \quad b_{mn}(h) = \int_{-h}^{0} Z_{n,2} \frac{\partial Z_{m,2}}{\partial h} dz,$$

$$c_{mn}(h) = \frac{db_{mn}}{dh} - \int_{-h}^{0} \frac{\partial Z_{m,2}}{\partial h} \frac{\partial Z_{n,2}}{\partial h} dz,$$

$$d_{mn}(h) = \int_{-h}^{0} Z_{n,2} \frac{\partial^2 Z_{m,2}}{\partial z^2} dz \quad \text{for} \quad n = 0, 1, 2, ..., N.$$

Equation (6.45) will be solved numerically for functions $\psi_n(x)$ for $n = 0,\ 1,\ 2, ..., N$. The method used to solve equation (6.45) differs from the approach employed to obtain the velocity potentials in the other regions. This equation is solved numerically by using RK4 method after splitting it into two first-order equations.

Now, applying the matching conditions (6.10)-(6.29), using the depth functions and truncating all the infinite series at N, we obtain the following system of equations:

$$\left.\begin{aligned} \psi_0(0) &= 1 + R_0 \\ \psi_n(0) &= R_n \end{aligned}\right\} \text{ for } n = 1, 2, ..., N, \tag{6.46}$$

$$\left.\begin{aligned} \psi_0(L) &= A_0 e^{\mathrm{i}q_0 L} + B_0 e^{-\mathrm{i}q_0 L} \\ \psi_n(L) &= A_n e^{\mathrm{i}q_n L} + B_n e^{-\mathrm{i}q_n L} \end{aligned}\right\} \text{ for } n = 1, 2, ..., N, \tag{6.47}$$

$$\left.\begin{aligned} a_0 \tfrac{d\psi_0}{dx}\big|_{x=0} + \mathrm{i}p_0 a_0 \psi_0(0) + h' \textstyle\sum_{m=0}^{N} b_{m,0}\psi_m(0) &= 2\mathrm{i}p_0 a_0 \\ a_n \tfrac{d\psi_n}{dx}\big|_{x=0} + \mathrm{i}p_n a_n \psi_n(0) + h' \textstyle\sum_{m=0}^{N} b_{m,n}\psi_m(0) &= 0 \end{aligned}\right\} n = 1, 2, ..., N, \tag{6.48}$$

$$\left.\begin{aligned} a_0 \tfrac{d\psi_0}{dx}\big|_{x=L} - \mathrm{i}q_0 a_0 \psi_0(L) + h' \textstyle\sum_{m=0}^{N} b_{m,0}\psi_m(L) &= -2\mathrm{i}q_0 a_0 e^{-\mathrm{i}q_0 L} B_0 \\ a_n \tfrac{d\psi_n}{dx}\big|_{x=L} - \mathrm{i}q_n a_n \psi_n(L) + h' \textstyle\sum_{m=0}^{N} b_{m,n}\psi_m(L) &= -2\mathrm{i}q_n a_n e^{-\mathrm{i}q_n L} B_n \end{aligned}\right\}$$
$$n = 1, 2, ..., N, \tag{6.49}$$

$$\sum_{n=0}^{N} \delta_{n,m} e^{\mathrm{i}q_n b_1} A_n + \sum_{n=0}^{N} \delta_{n,m} e^{-\mathrm{i}q_n b_1} B_n - \sum_{n=0}^{N} \left(\gamma A_{n,m} + B_{n,m}\right) e^{\mathrm{i}\alpha_n b_1} C_n$$
$$- \sum_{n=0}^{N} \left(\gamma A_{n,m} + B_{n,m}\right) e^{-\mathrm{i}\alpha_n b_1} D_n = 0, \tag{6.50}$$

$$\sum_{n=0}^{N} \mathrm{i}q_n \delta_{n,m} e^{\mathrm{i}q_n b_1} A_n - \sum_{n=0}^{N} \mathrm{i}q_n \delta_{n,m} e^{-\mathrm{i}q_n b_1} B_n - \sum_{n=0}^{N} \mathrm{i}\alpha_n \left(\epsilon A_{n,m} + B_{n,m}\right) e^{\mathrm{i}\alpha_n b_1} C_n$$
$$+ \sum_{n=0}^{N} \mathrm{i}\alpha_n \left(\epsilon A_{n,m} + B_{n,m}\right) e^{-\mathrm{i}\alpha_n b_1} D_n = 0, \tag{6.51}$$

$$\sum_{n=0}^{N}\left(C_{n,m}e^{\mathrm{i}\alpha_n b_2}\right)C_n+\sum_{n=0}^{N}\left(C_{n,m}e^{-\mathrm{i}\alpha_n b_2}\right)D_n-\sum_{n=0}^{N}\left(\frac{\cosh(s_n b_2)}{\cosh(s_n b)}D_{n,m}\right)E_n$$
$$-\sum_{n=0}^{N}\left(\frac{\sinh(s_n b_2)}{\sinh(s_n b)}D_{n,m}\right)F_n=0, \tag{6.52}$$

$$\sum_{n=0}^{N}\mathrm{i}\alpha_n\big(E_{n,m}+F_{n,m}\big)e^{\mathrm{i}\alpha_n b_2}C_n-\sum_{n=0}^{N}\mathrm{i}\alpha_n\big(E_{n,m}+F_{n,m}\big)e^{-\mathrm{i}\alpha_n b_2}D_n$$
$$-\sum_{n=0}^{N}s_n\left(\frac{\sinh(s_n b_2)}{\cosh(s_n b)}G_{n,m}\right)E_n-\sum_{n=0}^{N}s_n\left(\frac{\cosh(s_n b_2)}{\sinh(s_n b)}G_{n,m}\right)F_n=0, \tag{6.53}$$

$$\sum_{n=0}^{N}\big(\frac{\cosh(s_n b_3)}{\cosh(s_n b)}D_{n,m}\big)E_n+\sum_{n=0}^{N}\big(\frac{\sinh(s_n b_3)}{\sinh(s_n b)}D_{n,m}\big)F_n-\sum_{n=0}^{N}\left(C_{n,m}e^{\mathrm{i}\alpha_n b_3}\right)G_n$$
$$-\sum_{n=0}^{N}\left(C_{n,m}e^{-\mathrm{i}\alpha_n b_3}\right)H_n=0, \tag{6.54}$$

$$\sum_{n=0}^{N}s_n\left(\frac{\sinh(s_n b_3)}{\cosh(s_n b)}G_{n,m}\right)E_n+\sum_{n=0}^{N}s_n\left(\frac{\cosh(s_n b_3)}{\sinh(s_n b)}G_{n,m}\right)F_n$$
$$-\sum_{n=0}^{N}\mathrm{i}\alpha_n\big(E_{n,m}+F_{n,m}\big)e^{\mathrm{i}\alpha_n b_3}G_n+\sum_{n=0}^{N}\mathrm{i}\alpha_n\big(E_{n,m}+F_{n,m}\big)e^{-\mathrm{i}\alpha_n b_3}H_n=0, \tag{6.55}$$

$$\sum_{n=0}^{N}\big(\gamma A_{n,m}+B_{n,m}\big)e^{\mathrm{i}\alpha_n b_4}G_n+\sum_{n=0}^{N}\big(\gamma A_{n,m}+B_{n,m}\big)e^{-\mathrm{i}\alpha_n b_4}H_n$$
$$-\sum_{n=0}^{N}\left(\delta_{n,m}e^{\mathrm{i}q_n b_4}\right)T_n=0, \tag{6.56}$$

$$\sum_{n=0}^{N}\mathrm{i}\alpha_n\big(\epsilon A_{n,m}+B_{n,m}\big)e^{\mathrm{i}\alpha_n b_4}G_n-\sum_{n=0}^{N}\mathrm{i}\alpha_n\big(\epsilon A_{n,m}+B_{n,m}\big)e^{-\mathrm{i}\alpha_n b_4}H_n$$
$$-\sum_{n=0}^{N}\left(\mathrm{i}q_n\delta_{n,m}e^{\mathrm{i}q_n b_4}\right)T_n=0, \tag{6.57}$$

with $b_1=L+L_1$, $b_2=L+L_1+L_2$, $b_3=L+L_1+L_2+L_3$, $b_4=L+L_1+2L_2+L_3$ and

$$\delta_{n,m}=\int_{z=-h_2}^{0}Z_{n,3}(d_n,z)Z_{m,3}(d_m,z)dz,\quad A_{n,m}=\int_{z=-a}^{0}Z_{n,4}(t_n,z)Z_{m,3}(d_m,z)dz,$$
$$B_{n,m}=\int_{z=-h_2}^{-a}Z_{n,5}(t_n,z)Z_{m,3}(d_m,z)dz,\quad C_{n,m}=\int_{z=-h_2}^{-a}Z_{n,5}(t_n,z)Z_{m,6}(r_m,z)dz,$$
$$D_{n,m}=\int_{z=-h_2}^{-a}Z_{n,6}(r_n,z)Z_{m,6}(r_m,z)dz,\quad E_{n,m}=\int_{z=-a}^{0}Z_{n,4}(t_n,z)Z_{m,4}(t_m,z)dz,$$

$$F_{n,m} = \int_{z=-h_2}^{-a} Z_{n,5}(t_n, z) Z_{m,5}(t_m, z) dz, \quad G_{n,m} = \int_{z=-h_2}^{-a} Z_{n,6}(r_n, z) Z_{m,5}(t_m, z) dz.$$

To understand the role of the porous wall and a varying bottom, it is essential to determine the unknown coefficients R_n, A_n, B_n, C_n, D_n, E_n, F_n, G_n, H_n and T_n, which appear in the system of equations (6.46)–(6.57), along with the unknowns $K_{1,n}$ and $K_{2,n}$ that arise while solving equation (6.45). For this, the above system of equations can be compactly written as

$$\mathcal{A}\mathcal{X} = \mathcal{B}, \tag{6.58}$$

where $\mathcal{A}$ is the coefficient matrix of the above system of order $(12N+12)\times(12N+12)$, $\mathcal{B}$ is the column vector of size $(12N+12)\times 1$ and $\mathcal{X}$ is the unknown vector. This will allow us to obtain the full-wave solution of the problem under consideration. However, we focus only on the plane-wave solution, considering only $n = 0$ associated with the propagating mode and ignoring all infinite summations for $n \geq 1$ ([23]). After obtaining all the unknowns, we proceed further to evaluate the reflection and transmission coefficients, and horizontal and vertical forces on the floating structure.

Having obtained the expressions for the velocity potentials, the complex-valued horizontal force X_{hf} and vertical force Y_{vf} acting on the floating structure are calculated using the linearized Bernoulli's equation. To obtain the forces, we use the formulas given by

$$X_{hf} = \mathrm{i}\rho\omega \int_{-a}^{0} \left[\phi_7(L + L_1 + L_2 + L_3, z) - \phi_4(L + L_1 + L_2, z)\right] dz, \tag{6.59}$$

$$Y_{vf} = \mathrm{i}\rho\omega \int_{b_2}^{b_3} \phi_6(x, -a) dx. \tag{6.60}$$

Subsequently, the non-dimensional forms of the horizontal force X_{hf} and vertical force Y_{vf} can be written, respectively, as follows:

$$F_h = \frac{|X_{hf}|}{\rho g A b}, \quad F_v = \frac{|Y_{vf}|}{\rho g A b}, \tag{6.61}$$

where ρ represents the water density, $b = (L_3/2)$ m, and $A = 1$ m the unit amplitude of the incident wave.

6.3 Validation

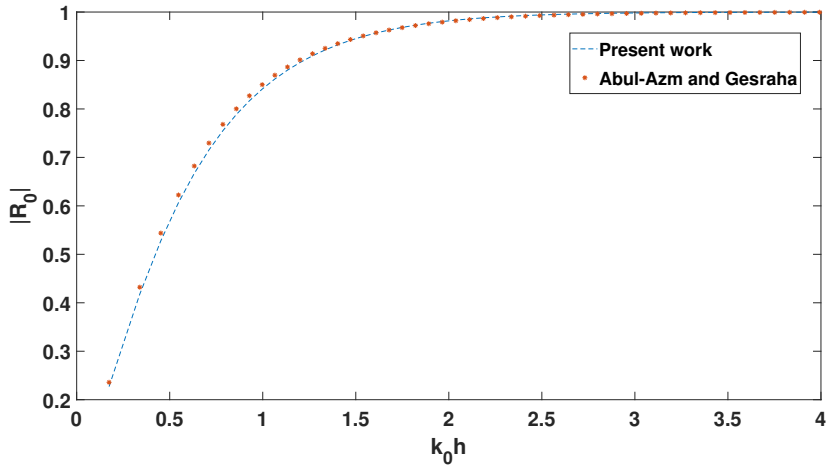

Figure 6.2: Reflection coefficient $|R_0|$ against non-dimensional wavenumber k_0h for the current work and Abul-Azm and Gesraha [2]

To validate the present results, a couple of earlier works on similar structures are considered. It may be noted that, in the absence of the porous wall and considering the sea-bed as a flat bottom, the present model converts to that of Abul-Azm and Gesraha [2]. For this, we assume very high porosity of the breakwaters, effectively making them transparent. Thus, both models reduce to the same problem. To validate our model against that of Abul-Azm and Gesraha [2], we consider $h_1 = h_2 = h$, $\theta = 0°$, $L_3/2h = 1$ and $a/h = 0.25$. The variation of reflection coefficient $|R_0|$ against non-dimensional wavenumber k_0h for both models is displayed in Figure 6.2. The pattern for this variation is the same for both models, as depicted by Figure 6.2. As a consequence, we observe that Figure 6.2 shows a good agreement of our model with that in [2] and this supports the employments of our model to analyze problems concerning the suitability of porous breakwaters in securing the safety of various VLFS.

6.4 Results and discussion

After having obtained the analytical solution and performed the validation, we proceed to study the effect of different parameters on various quantities such as the reflection coefficient, transmission coefficient and wave forces acting on the floating structure. For this purpose, a numerical code in MATLAB is developed. For the purpose of computation, specific values of different parameters are considered: $g = 9.81$ m/s^2, $T = 6$ s, $h_1 = 15$ m, $h_2 = 12$ m, $L = 12$ m, $L_2 = 2$ m, $L_3 = 10$ m, $a = 3$ m, $\epsilon = 0.6$, $s = 1$, $f = 1$ and $\theta = 30°$.

6.4.1 Effect of the porous wall and the varying bottom on the reflection coefficient and transmission coefficient

In this subsection, we examine the effect of the porosity, draft, thickness, and friction factor of the porous wall and the varying bottom on the reflection and transmission coefficients. The impact of the sea-bed slope is also analyzed.

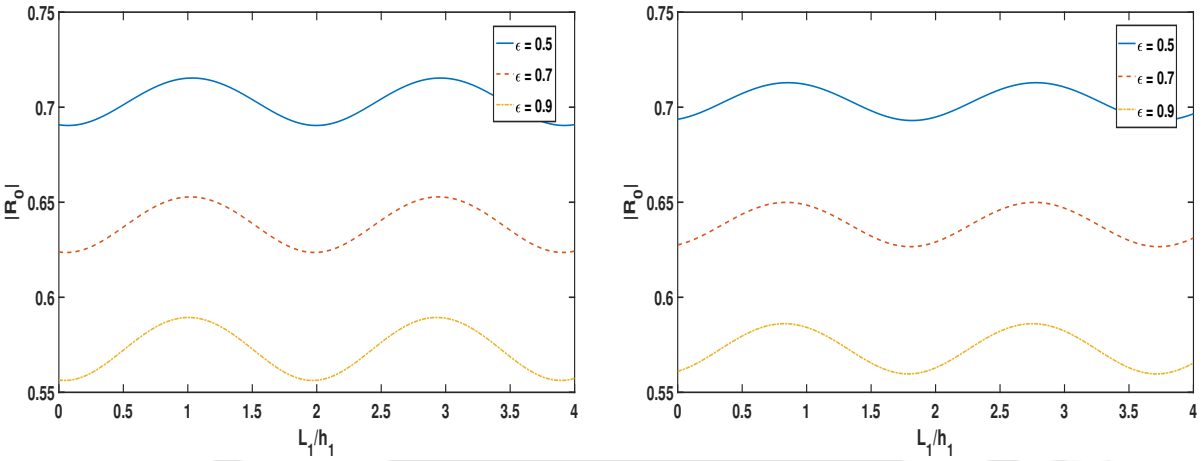

(a) (b)

Figure 6.3: $|R_0|$ against L_1/h_1 for different values of porosity ϵ with $h_1 = 15$ m, $h_2 = 12$ m, $a = 3$ m, $L_2 = 2$ m, $L_3 = 10$ m, $s = 1$, $f = 1$, $\theta = 30^\circ$ (a) $L = 3$ m, (b) $L = 9$ m

In Figure 6.3, reflection coefficient $|R_0|$ is plotted against L_1/h_1 for different values of porosity ϵ. Figure 6.3(a) corresponds to the reflection coefficient for a higher sea-bed slope, while Figure 6.3(b) corresponds to the same for a lower sea-bed slope. The figure exhibits an oscillatory pattern in the graphs as L_1/h_1 increases. It shows that, as porosity increases, we encounter lower reflection coefficient. In other words, for lower value of porosity ($\epsilon = 0.5$), $|R_0|$ is the highest. From both figures, it is observed that although the reflection is higher when the slope is steeper, the difference in the reflection coefficients is not significant.

In Figure 6.4, transmission coefficient $|T_0|$ is plotted against L_1/h_1 for different values of porosity ϵ. Figure 6.4(a) corresponds to the transmission coefficient for a higher sea-bed slope, while Figure 6.4(b) corresponds to the same for a lower sea-bed slope. This figure exhibits an oscillatory pattern in the graphs as L_1/h_1 increases. Figure 6.4 presents an opposite pattern to that in Figure 6.3, i.e., we obtain higher $|T_0|$ for higher value of porosity (here, $\epsilon = 0.9$). Both figures show that transmission is higher with a steeper slope, although differences in the transmission coefficients are minimal.

Figure 6.5 illustrates the variation of reflection coefficient $|R_0|$ against L_1/h_1 for different values of draft a of the structure. Figure 6.5(a) represents the reflection coefficient for a steeper sea-bed slope, while Figure 6.5(b) represents the same for a gentler sea-bed

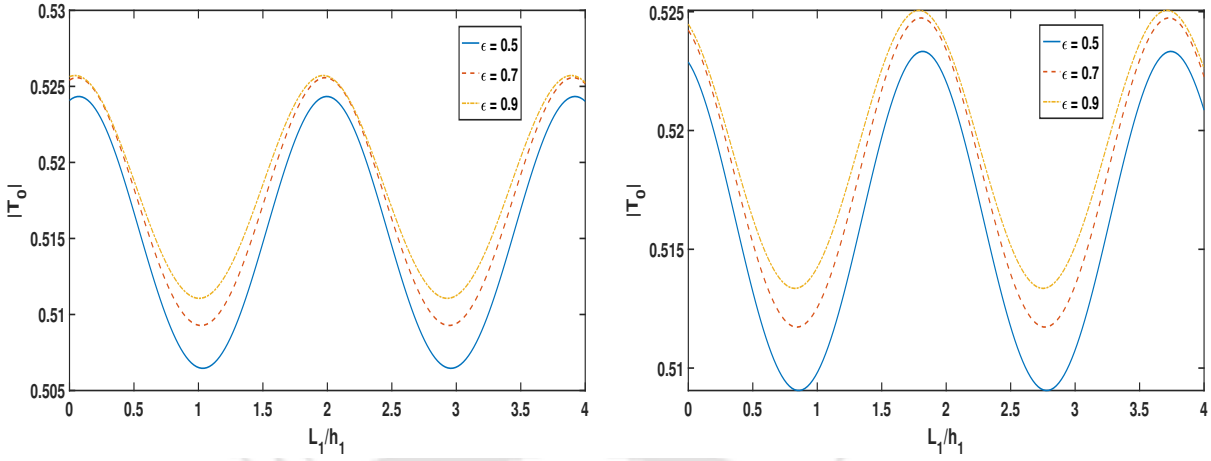

(a) (b)

Figure 6.4: $|T_0|$ against L_1/h_1 for different values of porosity ϵ with $h_1 = 15$ m, $h_2 = 12$ m, $a = 3$ m, $L_2 = 2$ m, $L_3 = 10$ m, $s = 1$, $f = 1$, $\theta = 30°$ (a) $L = 3$ m, (b) $L = 9$ m

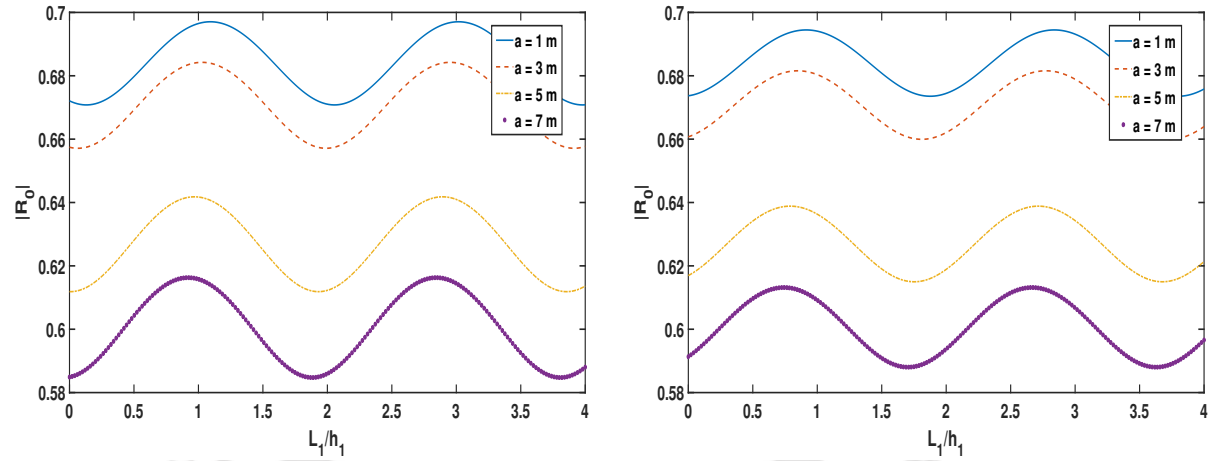

(a) (b)

Figure 6.5: $|R_0|$ against L_1/h_1 for different values of draft a of the porous wall with $h_1 = 15$ m, $h_2 = 12$ m, $L_2 = 2$ m, $L_3 = 10$ m, $\epsilon = 0.6$, $s = 1$, $f = 1$, $\theta = 30°$ (a) $L = 3$ m, (b) $L = 9$ m

slope. Since porous wall can absorb wave energy, Figures 6.5 demonstrates that the reflection coefficient decreases as a increases. Here, for $a = 7$ m, we encounter the lowest reflection coefficient. Figure 6.5 also presents an oscillatory pattern with an increase in L_1/h_1. It shows that the reflection coefficient increases with a steeper sea-bed slope.

Figure 6.6 demonstrates the variation of transmission coefficient $|T_0|$ against L_1/h_1 for different values of draft a of the structure. Figure 6.6(a) represents the transmission coefficient for a steeper sea-bed slope, while Figure 6.6(b) represents the same for a gentler sea-bed slope. Figure 6.6 shows that the transmission coefficient decreases as a increases

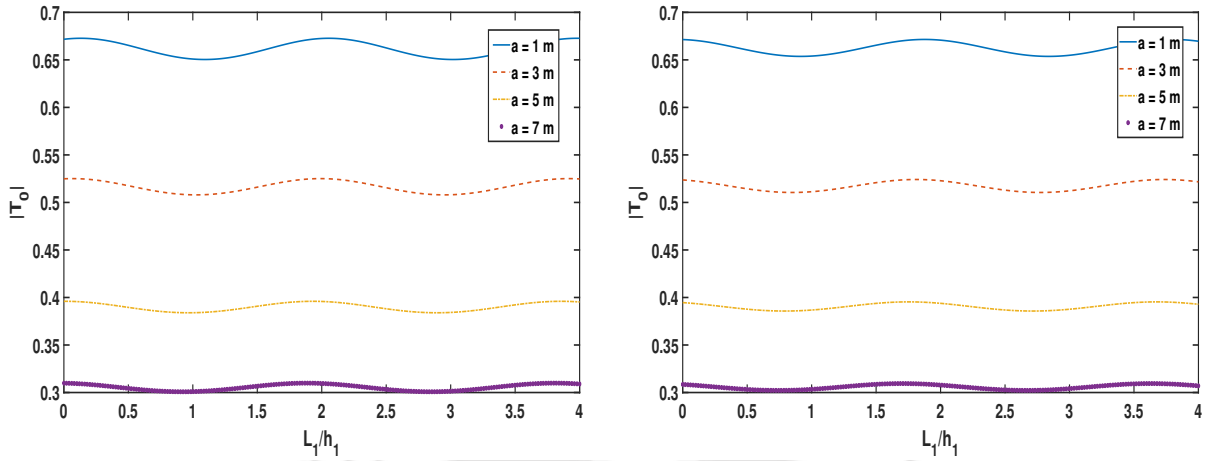

(a) (b)

Figure 6.6: $|T_0|$ against L_1/h_1 for different values of draft a of the porous wall with $h_1 = 15$ m, $h_2 = 12$ m, $L_2 = 2$ m, $L_3 = 10$ m, $\epsilon = 0.6$, $s = 1$, $f = 1$, $\theta = 30°$ (a) $L = 3$ m, (b) $L = 9$ m

because porous wall can absorb major portion of the wave energy. Here, for $a = 7$ m, we obtain the lowest transmission coefficient. We also observe that the transmission coefficient increases with a steeper sea-bed slope. Figure 6.6 also shows an oscillatory pattern.

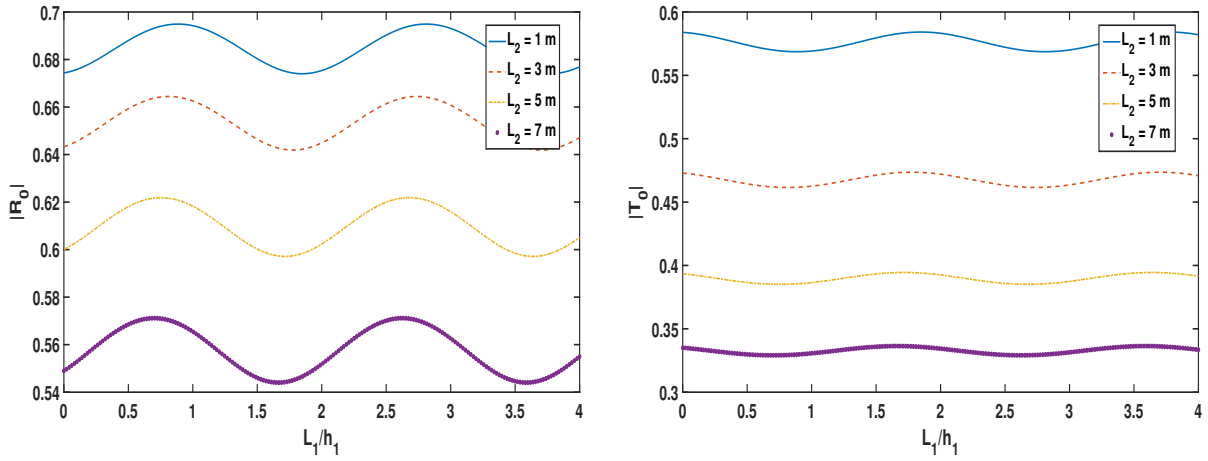

(a) (b)

Figure 6.7: (a) $|R_0|$ and (b) $|T_0|$ against L_1/h_1 for different values of thickness L_2 of porous wall with $h_1 = 15$ m, $h_2 = 12$ m, $a = 3$ m, $L = 9$ m, $L_3 = 10$ m, $\epsilon = 0.6$, $s = 1$, $f = 1$ and $\theta = 30°$

Figure 6.7 depicts the behaviour of the reflection and transmission coefficients against L_1/h_1 for different values of thickness L_2 of the porous wall. It is observed that both the reflection and transmission coefficients decrease with an increase in the thickness of the

porous wall since it can absorb major part of the wave energy. For $L_2 = 7$ m, the lowest reflection and transmission coefficients are observed, while for $L_2 = 1$ m, higher reflection and transmission coefficients are noted.

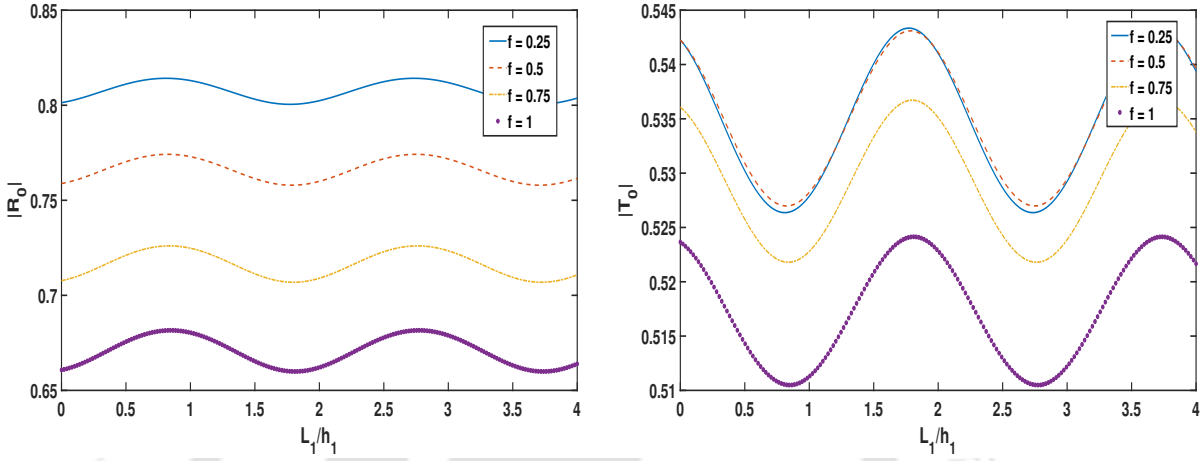

(a) (b)

Figure 6.8: (a) $|R_0|$ and (b) $|T_0|$ against L_1/h_1 for different values of friction factor f of porous wall with $h_1 = 15$ m, $h_2 = 12$ m, $a = 3$ m, $L = 9$ m, $L_2 = 2$ m, $L_3 = 10$ m, $\epsilon = 0.6$, $s = 1$, and $\theta = 30°$

Figure 6.8 shows the variation of reflection coefficient $|R_0|$ and transmission coefficient $|T_0|$ against L_1/h_1 for different values of friction factor f of the porous wall. The reflection and transmission coefficients decrease with an increase in f. This outcome is expected since friction introduces damping. Further, both Figures 6.8(a) and 6.8(b) present periodic and oscillatory pattern of graphs for the reflection and transmission coefficients.

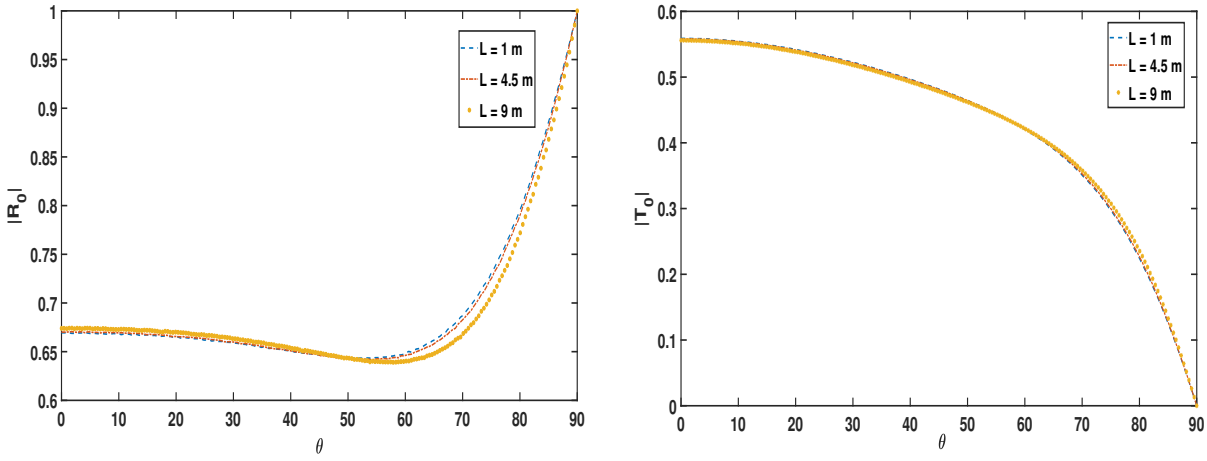

(a) (b)

Figure 6.9: (a) $|R_0|$ and (b) $|T_0|$ against θ for different values of L with $h_1 = 15$ m, $h_2 = 12$ m, $a = 3$ m, $L_1 = 2$ m, $L_2 = 2$ m, $L_3 = 10$ m, $\epsilon = 0.6$, $s = 1$, and $f = 1$

In Figure 6.9, we plot reflection coefficient $|R_0|$ and transmission coefficient $|T_0|$ against incident wave angle θ for various values of horizontal length L of the varying bottom. We observe that, as L increases, the reflection and transmission coefficients decrease. From Figure 6.9(a), we note that, as the incident angle increases, the reflection coefficient begins to decrease. After reaching its minimum, the reflection coefficient starts to increase. At $\theta = 90°$, full reflection ($|R_0| = 1$) occurs. At this angle, the waves are tangential to the structure, and there is no spike inside the structure, causing full reflection. Consequently, transmission tends to zero at $\theta = 90°$ (Figure 6.9(b)).

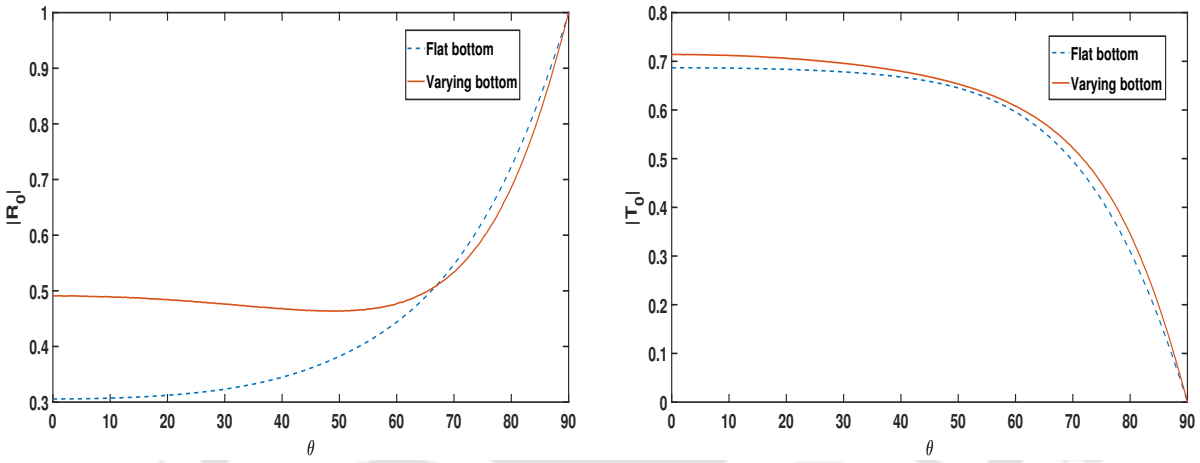

(a) (b)

Figure 6.10: (a) $|R_0|$ and (b) $|T_0|$ against θ for different bottom with $h_1 = 15$ m, $h_2 = 12$ m, $a = 3$ m, $L = 3$ m, $L_1 = 2$ m, $L_2 = 2$ m, $L_3 = 10$ m, $\epsilon = 0.6$, $f = 1$ and $s = 1$

Figure 6.10 depicts the variation of the reflection and transmission coefficients against incident wave angle θ for two cases: (a) a flat bottom and (b) a varying bottom. The reflection and transmission coefficients are observed to be higher in the case of the varying bottom. The difference between the reflection coefficients for the flat and varying bottoms is greater than the difference between the transmission coefficients.

6.4.2 Effect of the porous wall and sea-bed slope in mitigating wave forces

Here, the effect of various parameters of the porous structures and sea-bed slope is studied in order to suggest means to reduce the wave forces on the floating structure.

In Figure 6.11, horizontal force F_h is plotted against incident wave angle θ for different values of porosity ϵ. Figure 6.11(a) corresponds to the force for a higher sea-bed slope, while Figure 6.11(b) corresponds to the same for a lower sea-bed slope. Figure 6.11 shows that, as the porosity increases, we encounter higher horizontal force on the floating structure. This phenomenon can be explained using Figures 6.3 and 6.4: it was observed

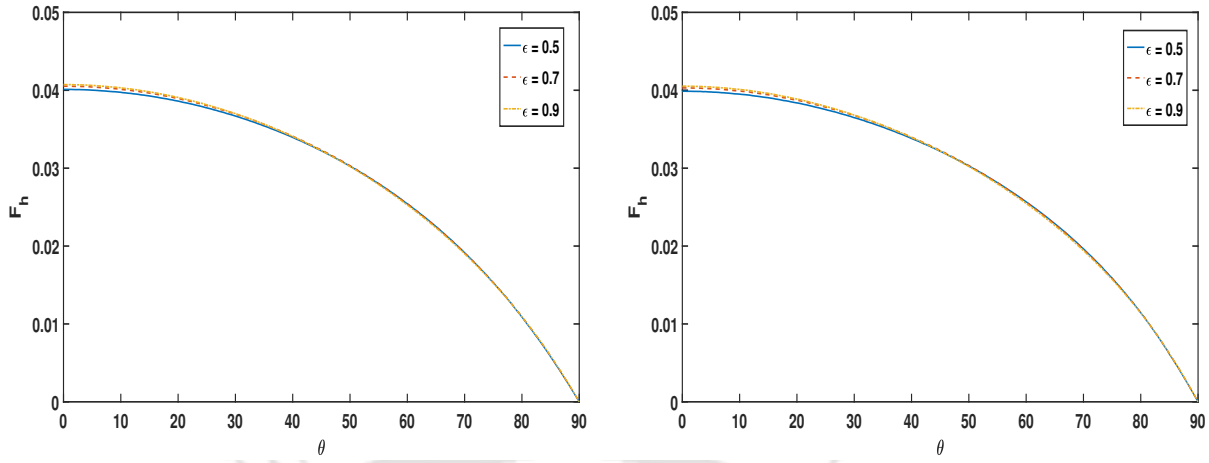

(a) (b)

Figure 6.11: F_h against θ for different values of porosity ϵ of porous wall with $h_1 = 15$ m, $h_2 = 12$ m, $a = 3$ m, $L_1 = 2$ m, $L_2 = 2$ m, $L_3 = 10$ m, $f = 1$ and $s = 1$ (a) $L = 3$ m, (b) $L = 9$ m

that, for higher value of the porosity, lower reflection and higher transmission occurred; consequently, a higher horizontal force is exerted on the floating structure. In other words, for a lower value of porosity ($\epsilon = 0.5$), F_h is the lowest. From both figures, it is observed that the horizontal force is higher when the slope is steeper; in other words, a lower horizontal force is obtained when the sea-bed slope is milder.

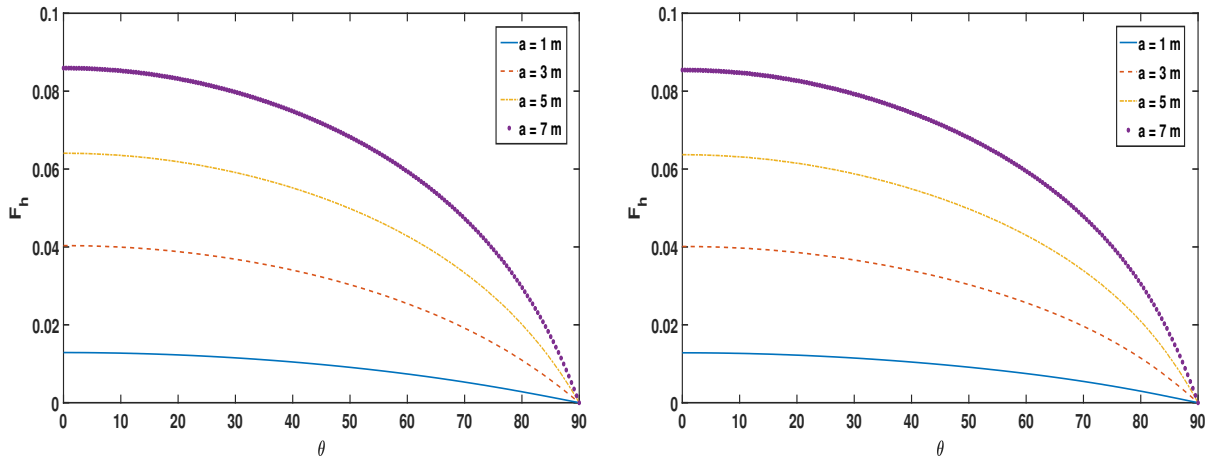

(a) (b)

Figure 6.12: F_h against θ for different values of draft a of the porous wall with $h_1 = 15$ m, $h_2 = 12$ m, $L_1 = 2$ m, $L_2 = 2$ m, $L_3 = 10$ m, $\epsilon = 0.6$, $f = 1$ and $s = 1$ (a) $L = 3$ m, (b) $L = 9$ m

Figure 6.12 depicts the variation of horizontal force F_h against incident angle θ for different values of draft a of the structure. Figure 6.12(a) represents the force for a steeper

sea-bed slope, while Figure 6.12(b) represents the same for a gentler sea-bed slope. It is observed that, as the draft of the structure increases, an enhancement in the horizontal force is encountered. This occurs because waves interact more with the floating structure when the porous wall has a greater draft, thereby increasing the force on the structure. Figures 6.12(a) and 6.12(b) depict that horizontal force is lower when the sea-bed slope is milder.

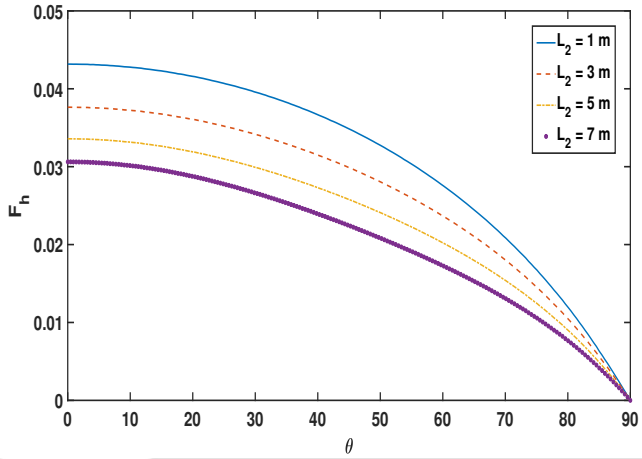

Figure 6.13: F_h against θ for different values of thickness L_2 of the porous wall with $h_1 = 15$ m, $h_2 = 12$ m, $a = 3$ m, $L = 9$ m, $L_1 = 2$ m, $L_3 = 10$ m, $\epsilon = 0.6$, $f = 1$ and $s = 1$

Figure 6.13 illustrates the variation of horizontal force F_h against incident angle θ for different values of thickness L_2 of the porous wall. It shows that as the thickness of the porous wall increases, the horizontal force on the floating structure decreases. This can be explained by the fact that a porous wall with greater thickness can absorb a significant portion of the wave energy, thereby reducing the wave-induced horizontal force on the floating structure.

Figure 6.14 shows the variation of horizontal force F_h against incident wave angle θ corresponding to various values of friction factor f of the porous wall. It depicts that, as f increases, F_h decreases. For $f = 1$, the lowest horizontal force on the floating structure is observed.

Figure 6.15 depicts the variation of the horizontal and vertical forces against the incident wave angle for two cases: (a) a flat bottom and (b) a varying bottom. Both the horizontal and vertical forces are reduced in the presence of a varying bottom as compared to a flat bottom. The horizontal force is observed to be less than the vertical force.

In Figure 6.16, horizontal force F_h and vertical force F_v are plotted against incident wave angle θ for different values of horizontal length L of the varying bottom. We observe that, as L increases, both horizontal and vertical forces acting on the floating structure decrease. This indicates that, for a milder slope of the sea-bed, the wave-induced horizontal and vertical forces acting on the floating structure are reduced. From Figures 6.16(a)

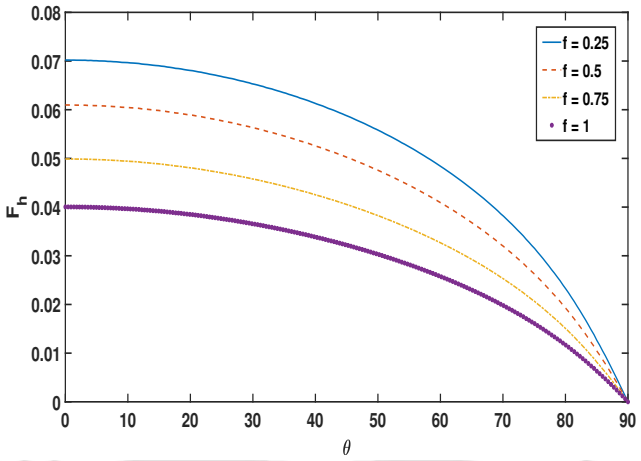

Figure 6.14: F_h against θ for different values of friction factor f of the porous wall with $h_1 = 15$ m, $h_2 = 12$ m, $a = 3$ m, $L = 9$ m, $L_1 = 2$ m, $L_2 = 2$ m, $L_3 = 10$ m, $\epsilon = 0.6$ and $s = 1$

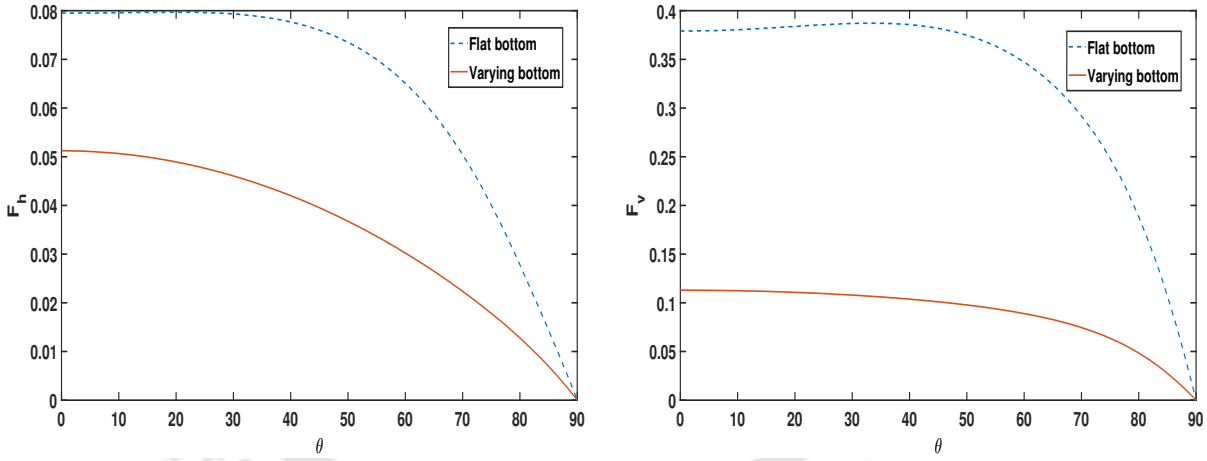

(a) (b)

Figure 6.15: (a) F_h and (b) F_v against θ for different bottom with $h_1 = 15$ m, $h_2 = 12$ m, $a = 3$ m, $L = 3$ m, $L_1 = 2$ m, $L_2 = 2$ m, $L_3 = 10$ m, $\epsilon = 0.6$, $f = 1$ and $s = 1$

and 6.16(b), we note that at $\theta = 90°$, the horizontal and vertical forces tend to zero. This is so because, at $\theta = 90°$, we get full reflection as depicted in Figure 6.9(a).

In Figure 6.17, horizontal force F_h and vertical force F_v are plotted against incident wave angle θ for the different values of h_2. It is observed that, as h_2 increases, the horizontal and vertical forces acting on the floating structure decrease. This suggests that, for a milder sea-bed slope, i.e., for the higher values of h_2, the wave-induced horizontal and vertical forces on the floating structure are reduced. From Figures 6.17(a) and 6.17(b), it is noted that, at $\theta = 90°$, the horizontal and vertical forces both approach zero.

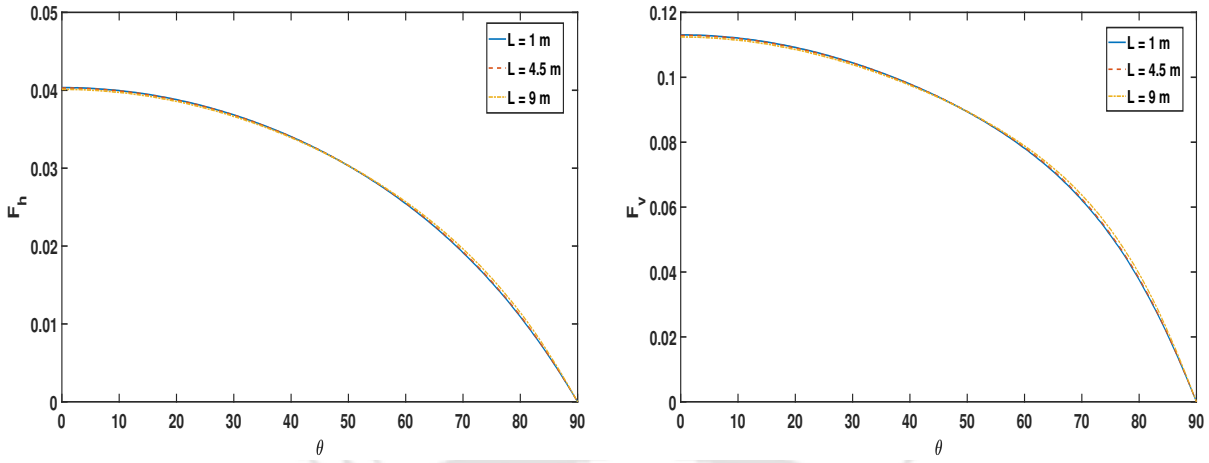

(a) (b)

Figure 6.16: (a) F_h and (b) F_v against θ for different values of L with $h_1 = 15$ m, $h_2 = 12$ m, $a = 3$ m, $L_1 = 2$ m, $L_2 = 2$ m, $L_3 = 10$ m, $\epsilon = 0.6$, $f = 1$ and $s = 1$

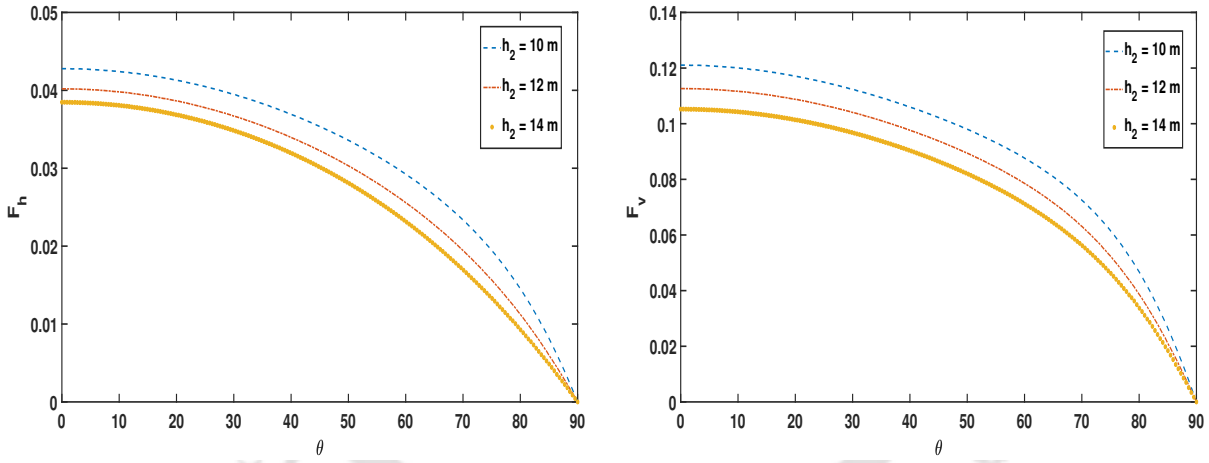

(a) (b)

Figure 6.17: (a) F_h and (b) F_v against θ for different values of h_2 with $h_1 = 15$ m, $a = 3$ m, $L = 9$ m, $L_1 = 2$ m, $L_2 = 2$ m, $L_3 = 10$ m, $\epsilon = 0.6$, $f = 1$ and $s = 1$

6.5 Conclusion

We analyzed the effect of the porous wall fitted to a floating structure in reducing the horizontal and vertical forces on the structure with the consideration of a varying sea-bed. The boundary value problems associated with each region were solved using the eigenfunction expansion method. It may be noted that tackling a varying sea-bed for coastal and ocean engineering problems is quite a challenging task. In our work, the utilization of modified mild slope equation (MMSE), which was solved numerically by RK4 method, is a significantly important step. These solutions were matched by applying

the usual condition of continuity of mass flux and pressure, which gave rise to a system of linear equations. Subsequently, the reflection coefficient, transmission coefficient and wave-induced forces acting on the floating structure were computed. To understand the role of the porous wall, a number of graphs were produced corresponding to various parameters. It was demonstrated that the presence of a varying bottom reduced both the horizontal and vertical forces acting on the floating structure compared to a flat bottom. It was observed that, as the thickness, draft, and friction factor of the porous wall and horizontal length of the varying bottom increased, the reflection coefficient and transmission coefficient decreased. With an increase in the distance between the porous wall and the varying bottom, the reflection coefficient and transmission coefficient showed an oscillatory pattern. It was also noted that, as the incident wave angle increased, the reflection coefficient started decreasing. After reaching its minimum value, it started increasing, and as θ tended to 90°, the reflection coefficient approached 1. Consequently, the horizontal and vertical forces on the floating structure approached zero. It was noted that, in the presence of a varying bottom, the horizontal and vertical forces on the floating structure got reduced. This study suggests that, for a milder sea-bed slope, the horizontal and vertical forces acting on the structure got reduced. It presents a complete study of the associated reflection, transmission and wave forces for the floating structure fitted with porous wall in the presence of a varying sea-bed.

Although we used MMSE for describing the uneven sea-bed, MMSE has some limitations as follows:

1. The MMSE may still struggle with rapidly varying small-amplitude topography, such as ripple beds.

2. It is derived from linear wave theory, meaning that it does not fully capture nonlinear wave effects such as wave breaking, wave-wave interactions, and strong turbulence.

3. The modified version is computationally more expensive than the original MSE due to additional correction terms, which can make it less efficient for large-scale simulations.

CHAPTER 7

Summary and future directions

This chapter presents a brief summary of the findings and contributions of this thesis. It also provides an outline for future research work and extensions of the current study.

7.1 Summary

In this thesis, the interaction of oblique water waves with a floating structure is studied in the presence of various types of porous breakwaters and different bottom topographies, using linearized water wave theory.

Chapter 2 deals with the oblique wave interaction with a floating bridge with porous layer fitted on its vertical sides. The eigenfunction expansion method has been employed to determine velocity potential in each region with the help of the variable-separable method for the modified Helmholtz equation. The hydrodynamic coefficients have been evaluated for various parameter values. The effect of the porosity of the porous layer on reflection and wave forces has been extensively analyzed. It has been observed that the presence of the porous wall reduces wave forces on the floating bridge. This study suggests appropriate parameter values to reduce wave forces, which will enhance the safety of the floating bridge.

In **Chapter 3**, the study examines the interaction of oblique water waves with a floating structure positioned in front of two submerged vertical porous barriers, in the presence of current and no current with the waves propagating over a porous sea-bed. These permeable barriers are placed at some distance from each other with different porous-effect parameters and different heights. The hydrodynamic coefficients are evaluated using the similar matched eigenfunction expansion method as described in **Chapter 2**. Various pa-

rameters are considered in this chapter that are physically relevant in practical scenarios. It is observed that significant wave energy is dissipated due to the porosity of the sea-bed. A significant change in the reflection coefficient is also observed when the current was included in the formulation.

Chapter 4 is concerned with the investigation of the effect of the porous barrier as well as that of an uneven sea-bed for their role in mitigating wave force on a rectangular rigid floating structure. Two types of bottom configurations are examined: (i) an elevated type and (ii) a trench type. The porous barrier is positioned at a certain distance in front of the floating structure. Using the same method as in **Chapters 2** and **3**, the boundary value problems are solved to obtain the velocity potential in corresponding domains. The corresponding reflection and transmission coefficients are determined by solving the system of equations numerically. To analyze the impact of different bottom topographies and the porous barrier, the reflection coefficient and wave forces are plotted for various parameters. Furthermore, the reflection in the presence of a trench is observed to be higher than the one due to the elevated bottom.

Chapter 5 is concerned with the investigation of the problem of scattering of oblique incident waves by two surface-piercing thick porous structures in mitigating wave-induced forces on a floating structure over a flat and impermeable sea-bed. The porous structures are considered to have different porosity, heights, and widths. The boundary value problems associated with each region are solved using the eigenfunction expansion method. A complete study on the root analysis of the dispersion relations is carried out, and the behavior of the roots of the dispersion relation is also analyzed to observe the mode swapping. Subsequently, the reflection coefficient, transmission coefficient, dissipation coefficient and hydrodynamic forces acting on the floating structure are computed. To understand the role of the porous structures, a number of graphs are produced corresponding to various parameters. This work concludes that a suitable arrangement of thick porous structures is required to mitigate the wave-induced forces on the floating structure.

Chapter 6 deals with the investigation of the oblique wave scattering by a floating structure with the porous walls fitted on the vertical sides of the structure over a varying sea-bed. Here, the porous walls are considered as a thick porous breakwater with some finite thickness and draft. The utilization of modified mild slope equation, which was numerically solved by RK4 method, is a significant step for dealing with a varying sea-bed. The complete solution of the boundary value problem is acquired by employing eigenfunction expansion under the assumption of linearized water wave theory. Computation for the reflection and transmission coefficients and horizontal and vertical wave forces on the floating structure is carried out. The effect of the porosity, thickness and draft of the porous wall and a varying bottom of the sea-bed is analyzed. This study suggests that, for a milder slope of the sea-bed, the horizontal and vertical forces on the floating structure are reduced.

7.2 Future directions

We now present some informal insights on how our current findings could be applied to other investigations. Additionally, we briefly discuss a few interesting topics that could be addressed in future research. In the works of **Chapter 2, 4, 5** and **6**, permeable sea-bed may be considered.

Shear stress, strain, and pressure are commonly observed on almost all coastal sea-beds due to their porous and elastic nature. A viscoelastic or poroelastic sea-bed could be utilized to revisit the works discussed in the thesis. This presents both a challenging mathematical problem and a more realistic physical scenario.

It has been observed that ocean water may not always exhibit homogeneity due to various reasons. In that case, consideration of the fluid as a multi-layer one will lead to more realistic problems. In this context, it may be important to investigate the scattering problems in a multi-layer fluid context (very likely a two-layer one). Such problems occur naturally in offshore engineering.

In all of the works, we have considered a rigid floating structure. The floating structure may be considered as a porous or poroelastic structure. In addition, shear current may be applied to the problems in **Chapters 2, 4, 5** and **6**.

In this thesis, we consider only eigenfunction expansion method to solve the boundary value problems. It is also possible that we can solve all the problems numerically using the multi-domain boundary element method (MBEM).

Although we consider only the scattering phenomenon in all the problems, it may be important to consider some aspects of radiation of waves too. In other words, however small it may be, the structure is likely to undergo different motions, i.e., oscillations, at least in the z-direction (heave) and may be in the x-direction (surge). The associated important quantities such as added mass and the damping coefficients are likely to play an important role that has the potency to alter the amount of energy. The associated radiation problem, along with the scattering problem already undertaken, will throw more light in this direction.

As per some studies, it has been suggested that the identification of trapped waves may be of importance for a complete knowledge of wave propagation. In this context, in addition to scattering, investigation of trapped waves may also be taken up.

Considering the above points and further, we may think of some problems which may be quite challenging.

1. Water wave scattering with N cylinders arranged in two rows with $N/2$ cylinders in each row with the consideration of nonlinear water wave theory. This arrangement may act as an appropriate system of breakwaters. We may also include time-dependent forcing which will give more insight into the phenomena as time progresses.

2. The first problem of the thesis can be extended by considering a viscoelastic sea-bed, which may correspond to a more realistic scenario. Further, depending on the success, this problem may also be considered in a multi-layer fluid, preferably a three-layer fluid with layer-wise distinct density.

3. Consideration of an array of poroelastic barriers may pose an interesting and challenging problem. Furthermore, assuming nonlinear water wave theory, water wave scattering by such an array can be studied. To make it more challenging, the sea-bed may be considered poroelastic too.

In other words, there is sufficient scope for further investigation of such type of problems. Idealizing problems with lesser restrictions will bring them much closer to the realistic scenarios. It is obvious that solving such problems will bring into fore various types of challenges. A need may arise to adopt alternative tools/techniques to tackle them.

Bibliography

[1] A. G. Abul-Azm. Wave diffraction through submerged breakwaters. *Journal of Waterway, Port, Coastal, and Ocean Engineering*, 119(6):587–605, 1993.

[2] A. G. Abul-Azm and M. R. Gesraha. Approximation to the hydrodynamics of floating pontoons under oblique waves. *Ocean Engineering*, 27(4):365–384, 2000.

[3] K. K. Barman and S. N. Bora. Scattering and trapping of water waves by a composite breakwater placed on an elevated bottom in a two-layer fluid flowing over a porous sea-bed. *Applied Ocean Research*, 113:102544, 2021.

[4] J. Bear. *Dynamics of Fluids in Porous Media*. Courier Corporation, 2013.

[5] H. Behera and S. Ghosh. Oblique wave trapping by a surface-piercing flexible porous barrier in the presence of step-type bottoms. *Journal of Marine Science and Application*, 18:433–443, 2019.

[6] H. Behera, S. Koley, and T. Sahoo. Wave transmission by partial porous structures in two-layer fluid. *Engineering Analysis with Boundary Elements*, 58:58–78, 2015.

[7] J. C. W. Berkhoff. Computation of combined refraction—diffraction. In *Coastal Engineering 1972*, pages 471–490. 1973.

[8] J. C. W. Berkhoff. Mathematical models for simple harmonic linear water waves: wave diffraction and refraction. *Ph. D. Thesis*, 1976.

[9] J. Bhattacharjee and C. G. Soares. Oblique wave interaction with a floating structure near a wall with stepped bottom. *Ocean Engineering*, 38(13):1528–1544, 2011.

[10] N. Booij. A note on the accuracy of the mild-slope equation. *Coastal Engineering*, 7(3):191–203, 1983.

[11] S. Boral, M. H. Meylan, T. Sahoo, and B.-Y. Ni. Time-dependent flexural gravity wave scattering due to uneven bottom in the paradigm of blocking dynamics. *Physics of Fluids*, 35(11), 2023.

[12] B. H. Buck and R. Langan. Aquaculture perspective of multi-use sites in the open ocean: The untapped potential for marine resources in the anthropocene. *Springer International Publishing*, 2018.

[13] A. Chakrabarti, S. Banerjea, B. N. Mandal, and T. Sahoo. A unified approach to problems of scattering of surface water waves by vertical barriers. *The ANZIAM Journal*, 39(1):93–103, 1997.

[14] P. G. Chamberlain and D. Porter. The modified mild-slope equation. *Journal of Fluid Mechanics*, 291:393–407, 1995.

[15] P. G. Chamberlain and D. Porter. On the solution of the dispersion relation for water waves. *Applied Ocean Research*, 21(4):161–166, 1999.

[16] A. Chanda and S. N. Bora. Effect of a porous sea-bed on water wave scattering by two thin vertical submerged porous plates. *European Journal of Mechanics-B/Fluids*, 84:250–261, 2020.

[17] A. Chanda and S. N. Bora. Investigation of water wave scattering by an elastic sea-bed of varying depth in two superposed fluids covered by an ice-sheet. *Ocean Engineering*, 221:108510, 2021.

[18] A. Chanda and S. N. Bora. Investigation of oblique flexural gravity wave scattering by two submerged thin vertical porous barriers with different porosities. *Journal of Engineering Mechanics*, 148(2):04021145, 2022.

[19] A. Chanda and S. N. Bora. Scattering of flexural gravity waves by a pair of submerged vertical porous barriers located above a porous sea-bed. *Journal of Offshore Mechanics and Arctic Engineering*, 144(1):011201, 2022.

[20] A. T. Chwang. A porous-wavemaker theory. *Journal of Fluid Mechanics*, 132:395–406, 1983.

[21] A. D. D. Craik. *Wave Interactions and Fluid Flows*. Cambridge University Press, 1988.

[22] A. D. D. Craik. The origins of water wave theory. *Annual Review of Fluid Mechanics*, 36:1–28, 2004.

[23] R. A. Dalrymple, M. A. Losada, and P. A. Martin. Reflection and transmission from porous structures under oblique wave attack. *Journal of Fluid Mechanics*, 224:625–644, 1991.

[24] G. Das and R. Chakraborty. Effect of porosity on wave scattering by a vertical porous barrier over a rectangular trench. *Journal of Marine Science and Application*, 23(1):85–100, 2024.

[25] S. Das and S. N. Bora. Damping of oblique ocean waves by a vertical porous structure placed on a multi-step bottom. *Journal of Marine Science and Application*, 13(4):362–376, 2014.

[26] S. Das and S. N. Bora. Reflection of oblique ocean water waves by a vertical porous structure placed on a multi-step impermeable bottom. *Applied Ocean Research*, 47:373–385, 2014.

[27] S. Das and S. N. Bora. Reflection of oblique ocean water waves by a vertical rectangular porous structure placed on an elevated horizontal bottom. *Ocean Engineering*, 82:135–143, 2014.

[28] S. Das and S. N. Bora. Wave damping by a vertical porous structure placed near and away from a rigid vertical wall. *Geophysical & Astrophysical Fluid Dynamics*, 108(2):147–167, 2014.

[29] S. Das and S. N. Bora. Oblique water wave damping by two submerged thin vertical porous plates of different heights. *Computational and Applied Mathematics*, 37:3759–3779, 2018.

[30] W. R. Dean. On the reflexion of surface waves by a submerged plane barrier. In *Mathematical Proceedings of the Cambridge Philosophical Society*, volume 41, pages 231–238. Cambridge University Press, 1945.

[31] M. W. Dingemans. *Water wave propagation over uneven bottoms (in 2 parts)*, volume 13. World Scientific, 1997.

[32] S. Earnshaw. The mathematical theory of the two great solitary waves of the first order. *Transactions of the Cambridge Philosophical Society*, 8:326–341, 1847.

[33] R. Gayathri, P. Kar, H. Behera, and T. Sahoo. Oblique wave scattering by a floating bridge in the presence of a vertical permeable flexible barrier. *Journal of Offshore Mechanics and Arctic Engineering*, 143(2):021701, 2021.

[34] G. Green. On the motion of waves in a variable canal of small depth and width. *Transactions of the Cambridge Philosophical Society*, 6:457–462, 1838.

[35] Z. Huang. An experimental study of wave scattering by a vertical slotted barrier in the presence of a current. *Ocean Engineering*, 34(5-6):717–723, 2007.

[36] Z. Huang, Y. Li, and Y. Liu. Hydraulic performance and wave loadings of perforated/slotted coastal structures: A review. *Ocean Engineering*, 38(10):1031–1053, 2011.

[37] M. Isaacson, S. Premasiri, and G. Yang. Wave interactions with vertical slotted barrier. *Journal of Waterway, Port, Coastal, and Ocean engineering*, 124(3):118–126, 1998.

[38] C. Jiang, P. Xu, X. Bai, Z. Zhao, O. el Moctar, and G. Zhang. A review of advances in modeling hydrodynamics and hydroelasticity for very large floating structures. *Ocean Engineering*, 285:115319, 2023.

[39] D. Karmakar and C. G. Soares. Wave transformation due to multiple bottom-standing porous barriers. *Ocean Engineering*, 80:50–63, 2014.

[40] D. Karmakar and C. G. Soares. Propagation of gravity waves past multiple bottom-standing barriers. *Journal of Offshore Mechanics and Arctic Engineering*, 137(1):011101, 2015.

[41] P. Kelland. On the theory of waves. *Report of the British Association for the Advanced of Science*, pages 50–52, 1840.

[42] S. Koley and T. Sahoo. Integral equation technique for water wave interaction by an array of vertical flexible porous wave barriers. *ZAMM-Journal of Applied Mathematics and Mechanics/Zeitschrift für Angewandte Mathematik und Mechanik*, 101(5):e201900274, 2021.

[43] U. V. Kumar, S. Saha, and S. Koley. A comparative study of wave scattering by non-porous and porous flexible plates in the presence of a submerged porous structure. *Meccanica*, 58(7):1329–1346, 2023.

[44] M. M. Lee and A. T. Chwang. Scattering and radiation of water waves by permeable barriers. *Physics of Fluids*, 12(1):54–65, 2000.

[45] Y. Liu and Y. Li. Wave interaction with a wave absorbing double curtain-wall breakwater. *Ocean Engineering*, 38(10):1237–1245, 2011.

[46] Y. Liu, Y. C. Li, and B. Teng. The reflection of oblique waves by an infinite number of partially perforated caissons. *Ocean Engineering*, 34(14-15):1965–1976, 2007.

[47] Y. Liu, Y. C. Li, and B. Teng. Interaction between obliquely incident waves and an infinite array of multi-chamber perforated caissons. *Journal of Engineering Mathematics*, 74:1–18, 2012.

[48] O. S. Madsen. Wave transmission through porous structures. *Journal of the Waterways, Harbors and Coastal Engineering Division*, 100(3):169–188, 1974.

[49] P. A. Madsen. Wave reflection from a vertical permeable wave absorber. *Coastal Engineering*, 7(4):381–396, 1983.

[50] R. Magne, V. Rey, and F. Ardhuin. Measurement of wave scattering by topography in the presence of currents. *Physics of Fluids*, 17(12), 2005.

[51] P. Maiti and B. N. Mandal. Water wave scattering by an elastic plate floating in an ocean with a porous bed. *Applied Ocean Research*, 47:73–84, 2014.

[52] S. C. Martha, S. N. Bora, and A. Chakrabarti. Oblique water-wave scattering by small undulation on a porous sea-bed. *Applied Ocean Research*, 29(1-2):86–90, 2007.

[53] P. McIver. Wave forces on adjacent floating bridges. *Applied Ocean Research*, 8(2):67–75, 1986.

[54] F. J. Mendez and I. J. Losada. A perturbation method to solve dispersion equations for water waves over dissipative media. *Coastal Engineering*, 51(1):81–89, 2004.

[55] B. Michel, R. J. Marc, and C. Guillaume. Perforated breakwaters, dieppe harbour jarlan caisson: General schedule and acquired experience. *In Proceedings of 13th International Offshore and Polar Engineering Conference*, pages 850–857, 2003.

[56] M. Muniyappan, R. R. Dora, and S. K. Mohanty. Wave resonances in the presence of current and the frequency and time-domain interconnection. *Wave Motion*, 119:103128, 2023.

[57] M. A. Mustapa, O. B. Yaakoba, M. A. Yasser, K. R. Chang, K. K. Kohb, and A. A. Faizul. Wave energy device and breakwater integration: A review. *Renewable and Sustainable Energy Reviews*, 77:43–58, 2017.

[58] J. N. Newman. *Marine hydrodynamics*. The MIT Press, 2018.

[59] H. P. Nguyen, H. Liang, and V. H. Luong. Finite element-dual boundary element method for hydroelastic analysis of very large floating structures protected by perforated barrier. *Ocean Engineering*, 268:113511, 2023.

[60] T. J. O'Hare and A. G. Davies. A new model for surface wave propagation over undulating topography. *Coastal Engineering*, 18(3-4):251–266, 1992.

[61] E. Otaola, A. J. Garrido, J. Lekube, and I. Garrido. A comparative analysis of self-rectifying turbines for the mutriku oscillating water column energy plant. *Complexity*, 2019(1):6396904, 2019.

[62] D. Porter and D. J. Staziker. Extensions of the mild-slope equation. *Journal of Fluid Mechanics*, 300:367–382, 1995.

[63] M. Rahman. *Water waves: relating modern theory to advanced engineering applications*. Oxford University Press, 1995.

[64] B. Rayleigh. On waves. *Philosophical Magazine*, 5:257–279, 1876.

[65] V. Rey, R. Capobianco, and C. Dulou. Wave scattering by a submerged plate in presence of a steady uniform current. *Coastal Engineering*, 47(1):27–34, 2002.

[66] R. Roy, S. De, and B. N. Mandal. Water wave scattering by three thin vertical barriers arranged asymmetrically in deep water. *Fluid Dynamics Research*, 51(4):045508, 2019.

[67] J. S. Russell and S. J. Robinson. Report on waves. *Report of the British Association for the Advancement of Science*, pages 417–496, 1837.

[68] S. Saha, S. Das, and S. N. Bora. Trapped waves within the blocking frequency under compressed sea ice and two-dimensional current. *Marine Structures*, 87:103336, 2023.

[69] S. Saha, S. K. Mohanty, and S. N. Bora. Flexural gravity wave resonance in the presence of current. *Journal of Waterway, Port, Coastal, and Ocean Engineering*, 148(3):04022003, 2022.

[70] G. Sahoo, S. Singla, and S. C. Martha. Scattering of oblique water waves by thick porous structure and thin elastic plate. *Ocean Engineering*, 248:110526, 2022.

[71] G. Sahoo, S. Singla, and S. C. Martha. Interaction of surface water waves with partial porous structure and floating elastic plate in the presence of sea wall. *Ships and Offshore Structures*, pages 1–18, 2024.

[72] T. Sahoo. On the scattering of water waves by porous barriers. *ZAMM-Journal of Applied Mathematics and Mechanics/Zeitschrift für Angewandte Mathematik und Mechanik: Applied Mathematics and Mechanics*, 78(5):364–370, 1998.

[73] T. Sahoo, A. T. Chan, and A. T. Chwang. Scattering of oblique surface waves by permeable barriers. *Journal of Waterway, Port, Coastal, and Ocean Engineering*, 126(4):196–205, 2000.

[74] A. Sarkar and S. N. Bora. Hydrodynamic forces due to water wave interaction with a bottom-mounted surface-piercing compound porous cylinder. *Ocean Engineering*, 171:59–70, 2019.

[75] A. Sarkar and S. N. Bora. Water wave diffraction by a surface-piercing floating compound porous cylinder in finite depth. *Geophysical & Astrophysical Fluid Dynamics*, 113(4):348–376, 2019.

[76] A. Sarkar and S. N. Bora. Hydrodynamic coefficients for a floating semi-porous compound cylinder in finite ocean depth. *Marine Systems & Ocean Technology*, 15:270–285, 2020.

[77] A. Sarkar and S. N. Bora. Hydrodynamic forces and moments due to interaction of linear water waves with truncated partial-porous cylinders in finite depth. *Journal of Fluids and Structures*, 94:102898, 2020.

[78] A. Sasmal and S. De. Hydroelastic analysis of surface gravity wave interaction with multiple flexible porous structures. *Journal of Fluids and Structures*, 120:103906, 2023.

[79] M. Sharma, R. B. Kaligatla, and T. Sahoo. Effect of bottom undulation for mitigating wave-induced forces on a floating bridge. *Wave Motion*, 89:166–184, 2019.

[80] V. I. Shrira and A. V. Slunyaev. Nonlinear dynamics of trapped waves on jet currents and rogue waves. *Physical Review E*, 89(4):041002, 2014.

[81] S. Singla, H. Behera, S. C. Martha, and T. Sahoo. Scattering of obliquely incident water waves by a surface-piercing porous box. *Ocean Engineering*, 193:106577, 2019.

[82] S. Singla, H. Behera, S. C. Martha, and T. Sahoo. Scattering of water waves by very large floating structure in the presence of a porous box. *Journal of Offshore Mechanics and Arctic Engineering*, 144(4):041904, 2022.

[83] C. K. Sollitt and R. H. Cross. Wave transmissions through permeable breakwaters. In *Coastal Engineering 1972*, pages 1827–1846. American Society of Civil Engineers, Virginia, USA, Proceedings of the 13th International Coastal Engineering Conference,Vancouver, 1972.

[84] O. W. Staff. Scottish wave energy project cancelled.

[85] G. G. Stokes. On the theory of oscillatory waves. *Transactions of the Cambridge Philosophical Society*, 8:441–455, 1847.

[86] H. Tavana and M. Khanjani. Reducing hydroelastic response of very large floating structure: a literature review. *International Journal of Computer Applications*, 71(5):13–17, 2013.

[87] B. Teng, X. T. Zhang, and D. Z. Ning. Interaction of oblique waves with infinite number of perforated caissons. *Ocean Engineering*, 31(5-6):615–632, 2004.

[88] C. C. Tsai, T. W. Hsu, and Y. T. Lin. On step approximation for roseau' s analytical solution of water waves. *Mathematical Problems in Engineering*, 2011(1):607196, 2011.

[89] S. W. Twu and D. T. Lin. On a highly effective wave absorber. *Coastal Engineering*, 15(4):389–405, 1991.

[90] S. W. Twu and D. T. Lin. Wave reflection by a number of thin porous plates fixed in a semi-infinitely long flume. In *Coastal Engineering 1990*, pages 1046–1059. 1991.

[91] F. Ursell. The effect of a fixed vertical barrier on surface waves in deep water. In *Mathematical Proceedings of the Cambridge Philosophical Society*, volume 43, pages 374–382. Cambridge University Press, 1947.

[92] C. M. Wang and Z. Y. Tay. Very large floating structures: applications, research and development. *Procedia Engineering*, 14:62–72, 2011.

[93] Y. Yang, L. Huang, and M. H. Meylan. Wave interaction with multiple floating elastic plates with arbitrary constraints near a sloping beach. *Physics of Fluids*, 37(3), 2025.

[94] Z. Yang, J. L. Hua, and L. Yong. Oblique wave scattering by a submerged porous breakwater with a partially reflecting sidewall. *Journal of Marine Science and Technology*, 25(4):383–392, 2017.

[95] X. Yu. Diffraction of water waves by porous breakwaters. *Journal of Waterway, Port, Coastal, and Ocean Engineering*, 121(6):275–282, 1995.

[96] X. Yu and A. T. Chwang. Wave motion through porous structures. *Journal of Engineering Mechanics*, 120(5):989–1008, 1994.

[97] Z. Zhai, J. Li, D. Liu, and J. Miao. Short-crested wave-current forces around a concentric multiple-cylinder structure. *Coastal Engineering Journal*, 65(2):295–308, 2023.

[98] E. Zhao, Y. Dong, Y. Tang, and X. Xia. Performance of submerged semi-circular breakwater under solitary wave in consideration of porous media. *Ocean Engineering*, 223:108573, 2021.

[99] H. Zhenhua, L. Yucheng, and L. Yong. Hydraulic performance and wave loadings of perforated/slotted coastal structures: A review. *Ocean Engineering*, 38(10):1031–1053, 2011.

[100] S. Zhu. Water waves within a porous medium on an undulating bed. *Coastal Engineering*, 42(1):87–101, 2001.

भारतीय प्रौद्योगिकी संस्थान गुवाहाटी
Indian Institute of Technology Guwahati

Status of manuscripts out of the thesis

A. Published:

1. S. Jain and S. N. Bora (2023), "Oblique water wave scattering by a floating bridge fitted with a rectangular porous structure and the resulting waveload mitigation." *Ocean Engineering*, 275: 114132, doi: 10.1016/j.oceaneng.2023.114132.
2. S. Jain and S. N. Bora (2024), "Impact of two vertical porous barriers in reflection of water waves and mitigation of wave forces on a rigid floating structure with consideration of uniform current over a porous sea-bed." *International Journal of Applied Mechanics*, 16(4): 2450049, doi: 10.1142/S1758825124500492.
3. S. Jain and S. N. Bora (2024), "Impact of a vertical porous barrier in the reflection of water waves and mitigation of wave forces on a rigid floating structure in the presence of an elevated bottom and a trench." *European Journal of Mechanics-B/Fluids*, 107: 29-39, doi: 10.1016/j.euromechflu.2024.06.003.
4. S. Jain and S. N. Bora (2025), "Scattering of oblique incident waves by a rigid floating structure in the presence of two surface-piercing thick porous breakwaters: pattern of reflection, dissipation and wave forces." *Journal of Fluids and Structures*, 135: 104285, doi: https://doi.org/10.1016/j.jfluidstructs.2025.104285.

B. Submitted:

1. S. Jain and S. N. Bora, "Scattering of oblique incident waves by a floating structure with a porous wall fitted on its vertical sides in the presence of a varying bottom topography."